

# **Combining SAR and optical satellite image time series for tropical forest monitoring**

Johannes Reiche

## **Thesis committee**

### **Promotor**

Prof. Dr M. Herold

Professor of the Laboratory of Geo-information Science and Remote Sensing  
Wageningen University

### **Co-promotor**

Dr D.H. Hoekman

Associate Professor, Earth System Science Group  
Wageningen University

Dr J.P. Verbesselt

Assistant Professor, Laboratory of Geo-information Science and Remote Sensing  
Wageningen University

### **Other members**

Dr D. Pflugmacher, Humboldt University of Berlin, Germany

Prof. Dr G.M.J. Mohren, Wageningen University

Prof. Dr C.E. Woodcock, Boston University, United States of America

Prof. Dr I.H. Woodhouse, The University of Edinburgh, United Kingdom

This research was conducted under the auspices of the C.T. de Wit Graduate School  
of Production Ecology & Resource Conservation (PE&RC)

# Combining SAR and optical satellite image time series for tropical forest monitoring

Johannes Reiche

## **Thesis**

submitted in fulfilment of the requirements for the degree of doctor  
at Wageningen University  
by the authority of the Academic Board  
in the presence of the  
Thesis Committee appointed by the Academic Board  
to be defended in public  
on Friday 19 June 2015  
at 1.30 p.m. in the Aula.

Johannes Reiche

**Combining SAR and optical satellite image time series for tropical forest monitoring**

151 pages

PhD thesis, Wageningen University, Wageningen, NL (2015)

With references, with summaries in English and Dutch

ISBN 978-94-6257-313-0

## Table of contents

Chapter 1	Introduction	1
Chapter 2	Feature level fusion of multi-temporal ALOS PALSAR and Landsat data for mapping and monitoring of tropical deforestation and forest degradation	11
Chapter 3	Multi-model radiometric slope correction of SAR images of complex terrain using a two-stage semi-empirical approach	37
Chapter 4	Fusing Landsat and SAR time series to detect deforestation in the tropics	59
Chapter 5	Combining Landsat and SAR time series in a Bayesian approach for near real-time deforestation detection in the tropics	91
Chapter 6	Synthesis	113
	References	125
	Summary / Samenvatting	138
	Acknowledgments	143
	List of publications	146
	Short biography	149
	PE&RC Training and Education Statement	150



Chapter

# 1

**Introduction**

## 1.1 Background

*“Among the scenes which are deeply impressed on my mind, none exceed in sublimity the primeval [tropical] forests, ... temples filled with the varied productions of the God of Nature. No one can stand in these solitudes unmoved, and not feel that there is more in man than the mere breath of his body.”*

— Charles Darwin, 1879

Tropical forests are the largest of the global forest biomes and cover approximately 16% of the Earth's land surface (2.4 billion hectares, FAO 2011). They play a crucial role in global carbon, hydrological, and biochemical cycles, and fundamentally contribute to the Earth's biological diversity, global economy and local welfare (Pan et al. 2011; Sasaki et al. 2011). The increasing global demand for resources has put increasing pressure on tropical forests (Ghazoul & Sheil 2010), and over the past four decades, deforestation and forest degradation have resulted in rapid changes in tropical forest cover (Achard et al. 2014; Stern 2007). After fossil fuel combustion, tropical forest degradation and deforestation is the second largest source of greenhouse gases in the atmosphere (Gullison et al. 2007; van der Werf et al. 2009).

Deforestation can be defined in different ways (Lund 1999). The United Nations Framework Convention on Climate Change (UNFCCC) describes it under the Marrakesh Accords as the 'direct human-induced conversion of forested land to non-forested land'. 'Forest' is hereby defined as a minimum area of land of 0.05 - 1.0 ha with tree canopy cover of more than 10 – 30 percent, and trees capable of reaching a minimum height of 2 – 5 m at maturity *in situ* (UNFCCC 2002). The latter definition for deforestation is commonly adapted by the earth observation community since remote sensing typically detects the reduction of tree canopy cover below a defined country specific threshold that is associated with the removal of forest. This definition is also used in this thesis. The main drivers of deforestation in the tropics are commercial logging (Ghazoul & Sheil 2010), agricultural expansion, mining, as well as infrastructure and urban expansion (Hosonuma et al. 2012). Forest degradation is generally regarded as the human intervention that causes a loss of carbon stocks within a forest that remains forest (Achard et al. 2010; Olander et al. 2008). It often leads to canopy cover damage that can be detected by remote sensing (Asner et al. 2004; Souza et al. 2005). In the tropics, forest degradation is mainly driven by selective logging, livestock grazing in forest and fuelwood collection (Hosonuma et al. 2012; Vargas et al. 2013). Tropical forest degradation is usually followed by forest regrowth within a few years due to fast regeneration, canopy

closure and understory re-vegetation (Asner et al. 2004; West et al. 2014). In some cases forest degradation is a catalyst for further logging activities and eventually leads to deforestation (Griscom et al. 2009; Pratihast et al. 2014).

Consistent and accurate detection of tropical forest cover change is fundamental to reliably estimate greenhouse gas emissions and successfully implement climate mechanisms such as REDD+ (*Reducing Emissions from Deforestation and Degradation, enhancement of carbon stocks, sustainable management of forest, and conservation of forest carbon stocks*). REDD+ is a UNFCCC endorsed mechanism aiming to mitigate climate change by rewarding tropical developing countries for reducing emissions by avoiding deforestation and forest degradation (Herold & Skutsch 2011; Pelletier et al. 2011; UNFCCC 2009). A successful REDD+ mechanism requires participating countries to design and implement an operational monitoring, reporting and verification (MRV) system to accurately and consistently report changes in forest and forest carbon stock (UNFCCC 2009); detected changes form the basis for receiving rewarding compensations (Herold & Skutsch 2011).

To assess historical and predict future changes in forest area and carbon stocks, satellite remote sensing at medium spatial resolution (10 - 30 m) supported by field observations is the appropriate tool for most tropical countries (Achard et al. 2010; De Sy et al. 2012). Remote sensing provides the area estimation of deforestation and degradation, the so-called activity data, while field observations provide carbon emission factors. The two are used in combination to calculate the respective carbon emissions from deforestation and degradation (GOF-C-GOLD 2014).

To improve the management and protection of tropical forest resources and to empower governments and communities to enact immediate law enforcement, near real-time (NRT) detection of illegal activities causing deforestation and degradation is crucial (Assunção et al. 2013; Hammer et al. 2014; Lynch et al. 2013; Wheeler et al. 2014). Illegal and unsustainable forest activities cause a wide range of negative environmental effects, significant financial losses among developing tropical countries and the depression of the world timber price (Nellermann 2012). Illegally extracted timber, for example, represents 5 to 10% of the commercial value of all wood products traded on the global market (Seneca Creek Associates 2004). Time series satellite imagery is the only data stream capable of providing repetitive observations of global tropical forest areas (Hansen et al. 2013; Lynch et al. 2013). Therefore, it is considered the primary data source to detect forest change in NRT (Lynch et al. 2013). In this context NRT forest change detection refers to the ability to detect changes in a satellite image once it is available.

A review on satellite-based tropical forest monitoring at medium spatial resolution scale including optical-based, SAR(*Synthetic Aperture Radar*)-based and SAR-optical multi-sensor approaches is provided in Section 1.2. Based on this review, Section 1.3 elaborates on the research needs in this field and defines the research questions of this thesis. An outline of the remaining chapters is given in Section 1.4.

## 1.2 Tropical forest monitoring using SAR and optical satellite remote sensing

Medium resolution satellite remote sensing constitutes a powerful tool for mapping and monitoring forest cover and forest cover change from local to global scales. These monitoring efforts rely on time series imagery provided by a number of satellite systems. Figure 1.1 depicts current and anticipated medium resolution optical and Synthetic Aperture Radar (SAR) satellite missions that were selected by the CEOS (*Committee on Earth Observation Satellites*) Space Data Coordination Group (CEOS 2014) as core missions to support systematic worldwide forest monitoring by providing long term medium resolution time series data with a free and open data policy (GFOI 2013).

With a data archive spanning over 40 years, Landsat provides the longest and most sophisticated record of medium spatial resolution satellite imagery (Roy et al. 2014). For many tropical countries, very limited coverage or no observations are available for the 1980s and 1990s due to a non-global observation strategy (Goward et al. 2006) and a lack of available ground receiving stations in the past (Arvidson et al. 2006). Since the mid-1990s a number of optical and C- and L-band SAR satellite constellations have provided an additional source of time series data. With the Landsat Data Continuity Mission (LDCM, Irons et al., 2012) and the planned launch of multiple optical and SAR satellite systems in the next decade, the continuation of these data streams is ensured. There has been some temporal overlap between optical and SAR satellite systems available for forest change assessments. However, varying overlapping periods, uncoordinated observation strategies, and user-unfriendly data policies and data access procedures have resulted in data from different satellite missions rarely being used in combination to track forest changes in the tropics (GCOS 2011; Hollmann et al. 2013). As a result, applied forest monitoring approaches are mainly based on optical remote sensing and infrequently include SAR or multi-sensor approaches (GOFC-GOLD 2014).

### 1.2.1 Optical-based approaches

The operational capabilities of optical medium resolution satellite imagery to detect changes and trends in tropical forest cover have been demonstrated by many studies (Achard et al. 2014; Carreiras et al. 2014; Griffiths et al. 2013; Hansen et al. 2013; Hirschmugl et al. 2014; Huang et al. 2010; Kim et al. 2014; Margono & Turubanova 2012; Margono et al. 2014; Masek et al. 2013; Souza et al. 2013; Potapov et al. 2012; Potapov et al. 2014). Catalysed by the opening of the Landsat archive (Woodcock et al. 2008), applications transitioned from local to global scales. Hansen et al. (2013) exploited the Landsat archive and derived the first global product of annual forest cover change for 2000 - 2012. This effort was followed by Kim et al. (2014) who released a further global Landsat-based forest change product covering 5-yearly change between 1990 - 2000.

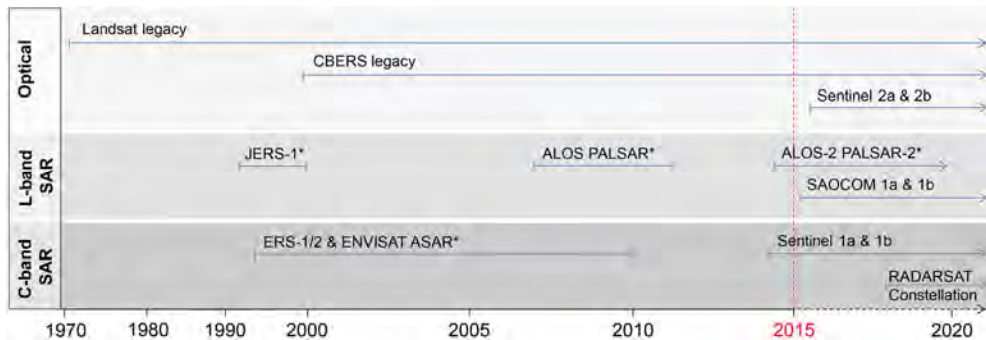


**Figure 1.1** Current and anticipated medium resolution optical and SAR satellite missions selected by CEOS Space Data Coordination Group as core missions to provide time series data in support of worldwide forest mapping. Important missions with non-core status due to restricted data access policy in 2014 are denoted with an asterisk (adapted from CEOS, 2014).

Monitoring tropical forest degradation is not yet operationally established, since it is more difficult and costly than deforestation monitoring (Defries et al. 2007; GOF-GOLD 2014; Souza et al. 2005). First, unlike deforestation, forest degradation is not associated with an entire removal of the forest canopy. Degradation instead causes a change in the structure of the forest, which often results in complex pixels that are difficult to analyze (GOF-GOLD 2014; Souza et al. 2005). Second, after degradation events occur, the change in the forest structure that causes a change in the remote sensing signal usually disappears within 1–3 years due to fast canopy closure and understory regeneration (Asner et al. 2004; Souza et al. 2005). Intensive research on tropical degradation monitoring has been conducted on the basis of Landsat data (Asner et al. 2005; Souza et al. 2005; Souza et al. 2013). In particular sub-pixel fraction approaches using spectral mixture analysis (Adams et al. 1993) were found to be useful for detecting degradation. The term sub-pixel fraction refers to the proportional information of pure spectral targets within the mixed spectral signal of the pixel. Derived non-photosynthetic vegetation, green vegetation and soil fraction information showed much higher sensitivity to degraded forest than whole pixel classifier (Souza 2003; Souza et al. 2005; Matricardi et al. 2010; Souza et al. 2013).

Current remote sensing based NRT monitoring systems such as the Brazilian DETER system (*Sistema de Detecção do Desmatamento em Tempo Real na Amazônia*) rely on coarse resolution MODIS (*Moderate Resolution Imaging Spectroradiometer*) time series imagery in order to provide fortnightly information on newly deforested areas (Shimabukuro et al. 2006; Hammer et al. 2009; Wheeler et al. 2014). Due to the low spatial resolution of 500 m, however, small-scale changes are missed (Anderson et al. 2005; Hammer et al. 2014). Therefore, this approach prevents the rapid response to many human interventions in tropical forest which tend to be small-scale (Tyukavina et al. 2013). Examples of satellite-based NRT monitoring systems at medium resolution scale are lacking.

The main limitation of optical remote sensing methods in tropical regions in general, is the restricted data availability due to frequent cloud cover (Asner 2001; Souza et al. 2013). In fact, some tropical countries experience cloud cover exceeding a long-term yearly average of 80% (Herold 2009). Persistent cloud cover inhibits full optical coverage from Landsat-like sensors even when compositing is performed over a period of one or two years. Certain regions are even affected in a stronger manner (Potapov et al. 2012; Sannier et al. 2014; Souza et al. 2013).

The increasing availability of freely available time series data for large areas over the previous years has led to a shift from traditional bi-temporal change detection approaches (Coppin et al. 2004; Lu et al. 2004), in which many changes are missing and the timing of changes is disregarded, to time series based methods (Hansen & Loveland 2012; Lu et al. 2014). A number of optical time series methods capable of analysing the entire temporal detail have been introduced in recent years and successfully applied to detect natural and human induced forest changes. (Verbesselt et al. 2010a; Verbesselt et al. 2012; Zhu et al. 2012; Zhu & Woodcock 2014). Several were designed especially for NRT forest change detection and often the Normalised Difference Change Index (NDVI) was utilized as the optical time series metric (Hammer et al. 2014; Verbesselt et al. 2012; Xin et al. 2013). However, a number of shortcomings have been identified for these methods. First, all introduced methods were demonstrated with imagery from a single optical sensor, and only in areas where a large number of observations were available. Second, the performance of the methods in tropical regions under persistent cloud cover was not investigated. Finally, annual mapping periods validated with independent reference data were not exceeded. Often the Landsat time series data itself has served as reference data. Providing annual deforestation information only, however, does not allow for rapid intervention to combat illegal forest activities (Lynch et al. 2013).

### 1.2.2 SAR-based approaches

Synthetic Aperture Radar (SAR; radar = *radio detection and ranging*) penetrates through clouds and can operate day and night, both major advantages over optical satellite data when monitoring tropical forest (Figure 1.2) (Lu et al. 2014; De Sy et al. 2012). Unlike optical sensors that only provide a signal from the top part of the canopy (Jensen 2013), SAR penetrates into the forest and thus provides a signal from its physical constituents. Because of its long wavelength (~25 cm), L-band SAR penetrates the tropical forest canopy and backscattering is primarily caused by branches and trunks. Double-bounce scattering in particular, where the SAR signal fully penetrates the canopy and is scattered back by the ground and trunks, results in high L-band SAR backscatter. After deforestation, the L-band backscatter strongly decreases causing a large contrast between forest and non-forest. In contrast, the shorter wavelength (~6cm) of C-band SAR only partially penetrates the forest canopy and mainly interacts with leaves and small branches. After forest removal, C-band interacts in a similar way with the remaining understory vegetation and bushes.

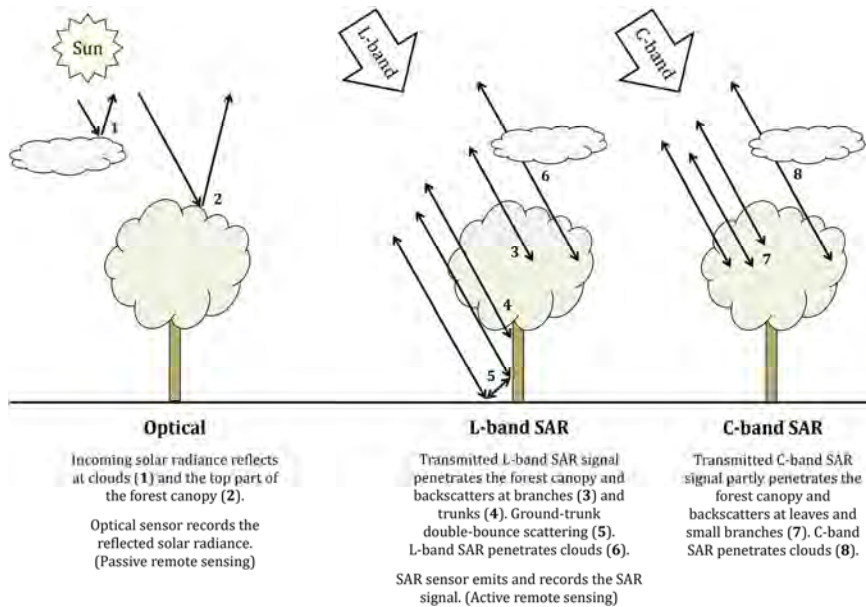


**Figure 1.2** Basic interactions of optical, C-band SAR and L-band SAR remote sensing over tropical forest.

C-band also largely responds to soil surfaces, which appear rougher in C-band compared to longer wavelengths. This leads to a lower forest/non-forest backscatter contrast when compared to L-band SAR (van der Sanden 1997; Ulaby et al. 1986; Woodhouse 2005). The potential of C- and L-band SAR backscatter for mapping and monitoring deforestation and degradation has been demonstrated by several studies. In particular multi-temporal L-band SAR data provided by JERS-1 (*Japan Earth Resources Satellite*) and ALOS (*Advanced Land Observing Satellite*) PALSAR (*Phased Array type L-band Synthetic Aperture Radar*) has been proven suitable for detecting tropical deforestation (Almeida-Filho et al. 2009; Motohka et al. 2014; Ryan et al. 2012; Rahman & Sumantyo 2012; Shimada et al. 2014; Simard et al. 2000; Thapa et al. 2013; Whittle et al. 2012). Shimada et al. (2014) made use of the global ALOS PALSAR archive and derived an annual forest cover change product for 2007 - 2010. Despite its lower sensitivity towards deforestation, C-band SAR was also used for deforestation mapping (Håme et al. 2009; Håme et al. 2013; Ribbes et al. 1997; Takeuchi & Oguro 2003). Although monitoring forest change using SAR has been demonstrated on an operational scale, the interpretation of the SAR signal over tropical forests is often more ambiguous than the optical signal; in particular when dealing with forest degradation. This often causes false alarm detections (Ryan et al. 2012; Quegan et al. 2009). A further limitation for most tropical countries is the low density of medium resolution C- and L-band SAR observations, with only a small number of images available per year (Rosenqvist et al. 2007).

Large fractions of the world's remaining pristine tropical forests are located on steep slopes (Aide et al. 2013), where topographic normalisation of SAR imagery is notoriously difficult to perform (Hoekman et al. 1994). Even when an accurate DEM (Digital Elevation Model) is available and an orthorectification has been achieved, slopes are often still visible. Approaches to handle slope effects for a variety of applications have been introduced, including forest land cover and change detection, and multi-sensor analysis (Atwood et al. 2012; Franklin et al. 1995; Castel et al. 2001; Stussi et al. 1995; Sun et al. 2002). Approaches may be divided into several categories, including (a) simple physical models (Hoekman 1990; Ulander 1996), (b) empirical models (Hinse et al. 1988; Franklin et al. 1995; Stussi et al. 1995) and (c) terrain type dependent or tuneable models. Hoekman (1990) proposed a simple physical model that assumes opaque volume scatter. It was validated for tropical forests (Hoekman et al. 1994) and often applied successfully for large-scale application in areas with dense vegetation (e.g. Hoekman et al. 2010). However, all approaches, including the latter model, have a limited range of application, and the general consensus is that a single-model will not suffice to describe SAR radiometric slope effects of multiple land cover types. The need for a multi-model approach was mentioned frequently and sometimes the need for stratification or pre-classification was indicated. However, to the authors knowledge, practical solutions for such an approach do not yet exist.

### **1.2.3 SAR-optical multi-sensor approaches**

Multi-sensor approaches that combine data from SAR and Landsat-like optical sensors have clearly demonstrated increased forest mapping accuracy (Almeida-Filho et al. 2007; Erasmi & Twele 2009; Hoan et al. 2013; Kuplich 2006; Vaglio Laurin et al. 2013; Lehmann et al. 2011; Lehmann et al. 2013; Rignot et al. 1997; Walker et al. 2010). The use of SAR-optical time series for detecting forest changes, however, has been rather limited to date and leaves lots of potential unexplored (Lu et al. 2014; Zhang 2010). By increasing the observation density such fusion approaches have the potential to target the problem of missing data in a time series (Dunsmuir & Robinson 1981; Racault et al. 2014), which may help to decrease the delay to detection of change events (Hussain et al. 2013; Zhang 2010). Various challenges including accurate co-registration, dealing with spectral variation in the time series (Zhang 2010) and the varying acquisition dates of images have to be addressed when designing a SAR-optical approach for detecting forest change (Lu et al. 2014). Bayesian classification frameworks (Strahler 1980) can combine optical and SAR time series for change detection (Lehmann et al. 2013; Lehmann et al. 2015; Huseby et al. 2008). Lehmann et al. (2013, 2015) applied a Bayesian multi-temporal processing framework to fuse annual Landsat and ALOS PALSAR mosaics and detected forest cover change. However, to date no approach exists that combines the advantages of medium resolution optical and SAR time series and utilizes their entire temporal detail for forest monitoring.

### 1.3 Research needs and research questions

Based on the review of optical and SAR based remote sensing for monitoring tropical forest change at medium spatial resolution (Section 1.2), the following points deserve emphasis. First, optical-based approaches for operational tropical forest monitoring exist, but restricted data availability due to frequent cloud cover limits their applicability. How persistent cloud cover in the tropics affects the accuracy of optical time series approaches is not well understood. Second, SAR-based approaches have demonstrated potential as tools for tropical forest monitoring, however they suffer from several drawbacks. They have a sparse observation frequency, the link between SAR signal and forest degradation can be unclear, and there are limited time series methods available. Slope correction of SAR images using single-model approaches show a limited applicability and may affect forest change detection in complex terrain. This raises the need for more investigations and a practical multi-model approach. Finally, the potential of multi-sensor methods to overcome the limitations of single-sensor approaches by combining the advantages of SAR and optical time series is well recognized, but the methods developed for their analysis to date are mainly restricted to mapping approaches.

To successfully implement mechanisms such as REDD+, satellite-based tropical forest monitoring must be significantly improved in order to provide spatially and temporally consistent information (Pelletier et al. 2011). To support timely action against illegal forest activities, satellite-based NRT monitoring at medium resolution scale is crucial. In order to use the impending stream of medium resolution optical and SAR time series data in a beneficial way, synergy across multiple SAR and optical data sources has been defined as a major research focus (e.g. GFOI 2013; Reiche & Herold 2012; Lu et al. 2014).

Motivated by the research needs addressed in this introduction, the overall objective of this thesis is to develop methods that advance tropical forest monitoring by combining satellite-based medium resolution SAR and optical time series imagery. The four research questions are:

1. How can we combine the advantages of multi-temporal SAR and optical information for detecting tropical deforestation and forest degradation?
2. How do slope-induced effects on the SAR signal impact forest change detection in complex terrain?
3. How can we fuse SAR and optical image time series, and what impact does persistent cloud cover have on the spatial and temporal accuracy of deforestation estimates?
4. How can we optimise SAR-optical fusion for near-real time deforestation monitoring?

## 1.4 Thesis outline

The core of this thesis is a series of four chapters, each of them addressing one research question. Figure 1.3 provides an overview of these core chapters.

In Chapter 2, we addressed research question 1 by developing an approach to map deforestation and forest degradation by fusing multi-temporal and medium resolution SAR with optical forest disturbance information. We demonstrated the approach with multi-temporal ALOS PALSAR and Landsat imagery of 2007 and 2010 acquired at a persistently cloud covered mining area in Guyana, where changes are primarily occurring in natural forest on flat terrain.

In Chapter 3, we addressed research question 2 by developing a multi-model approach for terrain type dependent slope correction of SAR images. We applied the multi-model approach to ALOS PALSAR imagery of two topographically complex sites in Fiji (study site of Chapter 4 and 5) and Brazil. Remaining slope effects were assessed and compared with results from a standard single-model approach.

In Chapter 4, we addressed research question 3 by developing an approach for fusing SAR and optical time series. We applied the approach to fuse Landsat NDVI and ALOS PALSAR time series, and subsequently used the fused time series in a change detection framework to detect deforestation between 2008 and 2010 at a managed forest site in Fiji. To assess the effect of persistent cloud cover, we increased the per-pixel missing data percentage of the NDVI time series stepwise and validated the spatial and temporal accuracy for the Landsat-only, PALSAR-only and the fused Landsat-PALSAR case, using three-monthly reference data.

In Chapter 5, we addressed research question 4 by developing a Bayesian-based approach to combine multi-sensor SAR and optical time series for NRT deforestation detection. We simulated a NRT scenario using Landsat NDVI and ALOS PALSAR time series from 2008 to 2010 and validated the approach at a managed forest site in Fiji.

Finally, Chapter 6 synthesises the main results of this thesis and provides an outlook and suggestions for further research efforts.

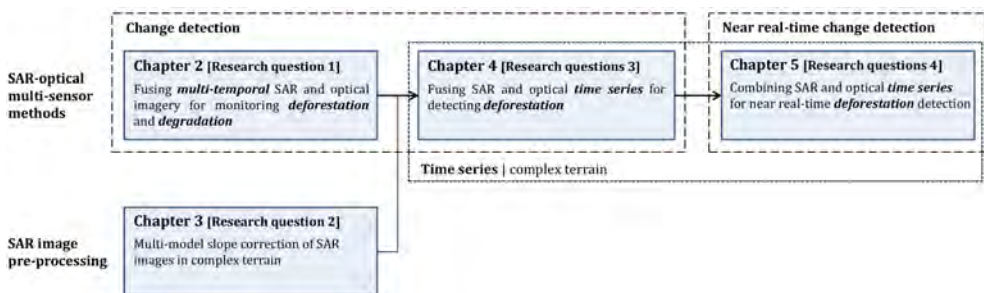


Figure 1.3 Overview of and links between the four core chapters of this thesis.

Chapter

# 2

## **Feature level fusion of multi-temporal ALOS PALSAR and Landsat data for mapping and monitoring of tropical deforestation and forest degradation**

Johannes Reiche, Carlos M. Souza, Jr., Dirk H. Hoekman, Jan Verbesselt,  
Haimwant Persaud and Martin Herold

*Published in IEEE Journal of Selected Topics in Applied Earth Observation and  
Remote Sensing, 6 (2013), 5, 2159–2173, DOI: 10.1109/JSTARS.2013.2245101*

## **Abstract**

*Many tropical countries suffer from persistent cloud cover inhibiting spatially consistent reporting of deforestation and forest degradation for REDD+. Data gaps remain even when compositing Landsat-like optical satellite imagery over one or two years. Instead, medium resolution SAR is capable of providing reliable deforestation information but shows limited capacity to identify forest degradation. This paper describes an innovative approach for feature fusion of multi-temporal and medium resolution SAR and optical sub-pixel fraction information. After independently processing SAR and optical input data streams the extracted SAR and optical sub-pixel fraction features are fused using a decision tree classifier. ALOS PALSAR Fine Beam Dual and Landsat imagery of 2007 and 2010 acquired over the main mining district in Central Guyana have been used for a proof-of-concept demonstration observing overall accuracies of 88% and 89.3% for mapping forest land cover and detecting deforestation and forest degradation, respectively. Deforestation and degradation rates of 0.1% and 0.08% are reported for the observation period. Data gaps due to mainly clouds and Landsat ETM+ SLC-off that remained after compositing a set of single-period Landsat scenes, but also due to SAR layover and shadow could be reduced from 7.9% to negligible 0.01% while maintaining the desired thematic detail of detecting deforestation and degradation. The paper demonstrates the increase of both spatial completeness and thematic detail when applying the methodology, compared with potential Landsat-only or PALSAR-only approaches for a heavy cloud contaminated tropical environment. It indicates the potential for providing the required accuracy of activity data for REDD+ MRV.*

---

## 2.1 Introduction

Tropical forest, the largest of the global forest biomes, plays a crucial role in the global carbon, hydrological and biochemical cycle, and contributes fundamentally to the Earth's biological diversity, the global economy and local welfare (Pan et al. 2011; Sasaki et al. 2011). An increasing global demand for food, timber and biofuels (Ghazoul & Sheil 2010) rapidly increases the pressure on tropical forests and leads to deforestation and forest degradation rates that currently account for up to 20% of global greenhouse gas emissions (Gullison et al. 2007; IPCC 2007; Stern 2007; van der Werf et al. 2009).

REDD+, is a UNFCCC endorsed mechanism aiming to mitigate climate change in the tropics by rewarding tropical developing countries for reducing emissions by avoiding deforestation and forest degradation (Asner 2011). Successful implementation of REDD+ requires country-wide-consistent and accurate monitoring, reporting and verification (MRV) systems (UNFCCC 2009; Herold & Skutsch 2009). For the majority of the developing countries, satellite-based remote sensing supported by field observations constitutes the appropriate tool for assessing historical and future changes in forest carbon stocks. Thereby, remote sensing provides the area estimation, the so called activity data, and field observations provide carbon emission factors that are used in combination to calculate the respective carbon emissions (GOF-C-GOLD 2014; Maniatis & Mollicone 2010). In order to make REDD+ viable, the accuracy and the spatial consistency of satellite based monitoring systems needs to be significantly improved to provide accurate and consistent activity data; the basis for a reliable carbon emissions mechanism (Pelletier et al. 2011).

Both, SAR and optical remote sensing at Landsat-like scale have been proven to be capable of operationally mapping and monitoring forest cover and forest cover change at different spatial scales, from local to pan tropical, with accuracies between 80 – 95% (GOF-C-GOLD 2014). However, applied monitoring approaches are mainly based on optical remote sensing and consider SAR or multi-sensor approaches only marginal (GOF-C-GOLD 2014).

Monitoring tropical forest degradation is not considered operational yet, because it is more difficult and cost intensive to perform than deforestation monitoring (Defries et al. 2007; Souza et al. 2005; GOF-C-GOLD 2014). Unlike deforestation, forest degradation is not associated with a change in land cover. Degradation instead causes a change in the structure of the forest, which results in complex pixels that are difficult to analyse (Souza et al. 2005; GOF-C-GOLD 2014). After a degradation event occurs, the change in forest structure that causes a change in the canopy cover and in the remotely sensed signal usually disappears within 1 – 3 years due to fast regeneration, canopy closure and understory re-vegetation (Asner et al. 2004; Souza et al. 2005). Intensive research on tropical degradation monitoring has been conducted on the basis of Landsat based data (Asner et al. 2005; Souza et al. 2005). In particular sub-pixel fraction approaches using spectral mixture analysis (SMA,

Adams et al. 1993) were found to be capable of detecting degradation. Thereby, the term sub-pixel fraction refers to the proportional information of pure spectral targets (endmembers) within the mixed spectral signal of the pixel and not to spatial resolution. Derived non-photosynthetic vegetation (NPV), green vegetation (GV) and soil fraction information showed much higher sensitivity to degraded forest than whole pixel classifier (Souza 2003; Souza et al. 2005; Matricardi et al. 2010). The Normalised Difference Fraction Index (NDFI) combines NPV, GV and soil fraction information in one synthetic band that enhances forest canopy damage, and proves to be capable of monitoring selective logging events in the Amazon (Souza et al. 2005; Souza et al. 2009). The main constraint of optical remote sensing techniques in tropical regions is restricted data availability due to frequent cloud cover, which limits the applicability of the developed methods (Souza et al. 2009). Some tropical countries, such as Guyana, experience cloud cover exceeding the long-term yearly average frequency of 80% (Herold 2009). This inhibits full optical coverage from Landsat-like sensors even in the case when compositing is performed over a period of 1 - 2 years. Certain areas are even affected in a stronger manner. Overcoming this problem for monitoring deforestation and degradation is still an open research issue and requires advanced processing techniques (Romijn et al. 2012).

Synthetic Aperture Radar (SAR) is not affected by cloud cover and provides continuous time series information. Unlike optical sensors that only provide a signal from the top of the canopy, SAR penetrates into the forest canopy and thus provides a signal from its physical structure. Several studies have demonstrated the potential of C- and L-band SAR backscatter (Almeida-Filho et al. 2009; Hoekman et al. 2010; Häme et al. 2009) and SAR coherence (Ribbes et al. 1997; Takeuchi & Oguro 2003) for (i) forest/non-forest mapping and (ii) monitoring deforestation indicating that SAR-based methods can potentially complete or replace optical forest monitoring systems in the tropics. In particular, multi-temporal L-band SAR backscatter provided by JERS and ALOS PALSAR has been proven suitable for detecting tropical deforestation due to the high penetration depth of L-band into the canopy enhancing disturbed and undisturbed forest using SAR difference ratios (Almeida-Filho et al. 2007; Almeida-Filho et al. 2009), temporal standard deviation (Quegan et al. 2009) and decision tree approaches (Simard et al. 2000). However, the interpretation of SAR signals over tropical forest is more ambiguous than of optical signals. This often causes false alarm detection of deforestation and degradation events (Quegan et al. 2009; Ryan et al. 2012). In particular the detection of degradation events is affected by very high uncertainties (Ryan et al. 2012).

Multi-sensor approaches that combine the advantages of SAR and Landsat-like optical sensors in order to overcome the above described limitations of the single-sensor systems have clearly demonstrated an increase in forest mapping accuracy (Almeida-Filho et al. 2007; Erasmi & Twele 2009; Kuplich 2006; Lehmann et al. 2011; Lehmann et al. 2012; Walker et al. 2010). However, multi-sensor and multi-temporal approaches that combine optical and SAR data for monitoring deforestation and forest degradation are lacking. Multi-sensor fusion of optical and

SAR data can be performed at data, feature and decision level, referring to the level of processing at which the fusion is undertaken (Pohl & Genderen 1998). Data fusion, the fusion at the lowest processing level, is generally performed to merge different input data layers into a single data set that is subsequently used for classification (Pohl & Genderen 1998). Decision fusion refers to the fusion at the highest processing level. The different SAR and optical input data sets are independently classified and subsequently combined in a decision fusion process (Pohl & Genderen 1998; Waske & van der Linden 2008). Feature level fusion is considered the fusion at the intermediate processing level between data and decision fusion. It requires the extraction of characteristics (features) from the initial (SAR and optical) input images that are subsequently fused using a decision tree classifier, a Bayesian classifier or an Artificial Neuronal Network (ANN) (Pohl & Genderen 1998). Optical-SAR feature level fusion has been performed in several applications like urban mapping remote sensing (Wegner et al. 2009) and land cover mapping (Chureesampant & Susaki 2011), however, applications for improved tropical forest monitoring are lacking.

The present paper proposes an innovative approach for feature level fusion of multi-temporal, medium resolution SAR and optical sub-pixel fraction information (NDFI) for mapping tropical forest land cover (FLC) and monitoring FLC change. FLC is hereafter defined as including the classes' forest, non-forest, water and degraded forest, whereas FLC change covers both, deforestation and forest degradation. The complementarities of SAR and optical remote sensing are analysed and subsequently used to overcome the specific limitations of the single-sensor systems in terms of thematic and spatial completeness aiming for provision of consistent and reliable activity for both, deforestation and forest degradation. To demonstrate the feasibility of the approach followed in this paper, ALOS PALSAR and Landsat data from 2007 and 2010 is used for a pilot study covering the main mining area in Central Guyana that is of high importance for Guyana's REDD+ program. Within the framework of a bilateral REDD agreement with Norway, Guyana needs to report its forest status on an annual basis and also its historical forest cover change. Persistent cloud cover led to spatially incomplete monitoring of the first two yearly interim measures reports (2010, 11) that were primarily based on optical remote sensing (Pöyry Management Consulting (NZ) Limited 2011; Indufor Asia Pacific Ltd 2012). Degraded forest was only accounted in the last interim report for 2011, wherefore an indirect manual approach was employed that visually interprets high and medium resolution optical imagery within a buffer zone around non-forest areas and roads (Indufor Asia Pacific Ltd 2012). The main objective of the pilot study is to evaluate the increase of spatial completeness and thematic detail of the proposed PALSAR-Landsat feature level fusion product compared to potential Landsat-only or PALSAR-only approaches for a heavy cloud contaminated tropical environment. The improvement of overall accuracy by incorporating optical and SAR data compared to single-sensor approaches was not included in this paper, since it has already been proven (Almeida-Filho et al. 2007; Lehmann et al. 2012; Walker et al. 2010).

## **2.2 Material and methods**

### **2.2.1 Methodological concept**

Based on the literature review of satellite-based mapping and monitoring of deforestation and forest degradation, the following points can be summarized:

- (i) Medium resolution SAR features provide reliable and spatially consistent forest/non-forest and deforestation information, but have very limited capabilities for identifying degraded forest/degradation
- (ii) Optical (Landsat-like) sub-pixel fraction features are capable of detecting degraded forest/degradation, but have restricted data availability due to frequent cloud cover that prohibits spatial completeness

Figure 2.1 presents the overview of the proposed feature level fusion approach. Medium resolution SAR and optical sub-pixel fraction features in a complementary way. After independently processing SAR and optical input data streams and subsequently extracting SAR and optical sub-pixel fraction features, fusion at feature level is performed in a final step to classify FLC and/or FLC change. For FLC mapping, single-date SAR and optical input data are processed and single-date SAR (e.g. backscatter, backscatter ratios) and optical sub-pixel fraction features (e.g. NDFI) are extracted.

A set of optical images acquired in a short period, so called single-period data is processed and subsequently merged to maximize cloud-free coverage. In case multiple single-period SAR images are available multi-temporal filtering can be applied for SAR speckle reduction. For FLC change detection, the optical and SAR processing is expanded to multiple dates and SAR and optical change features are extracted in addition to single-date features.

For feature level fusion, the above described optical and SAR data constraints are considered in the following way. SAR features are favoured for the provision of FLC classes' of forest, non-forest and water and deforestation information to account for the spatial inconsistency of optical data. Due to their capability of detecting forest degradation, optical sub-pixel fraction features are employed to ensure the desired thematic detail, although full coverage is not given. In addition, optical features, instead of SAR features, are considered for the distinction of FLC in areas affected by SAR layover and shadow. For this pilot study, a decision tree classifier was employed for feature level fusion. To address Guyana's REDD+ obligations for reporting yearly forest status and historical change, the proposed concept was applied to ALOS PALSAR and Landsat data for the reference years 2007 and 2010 to (i) map single year FLC status and (ii) to detect deforestation and degradation for the period of 2007 - 10.

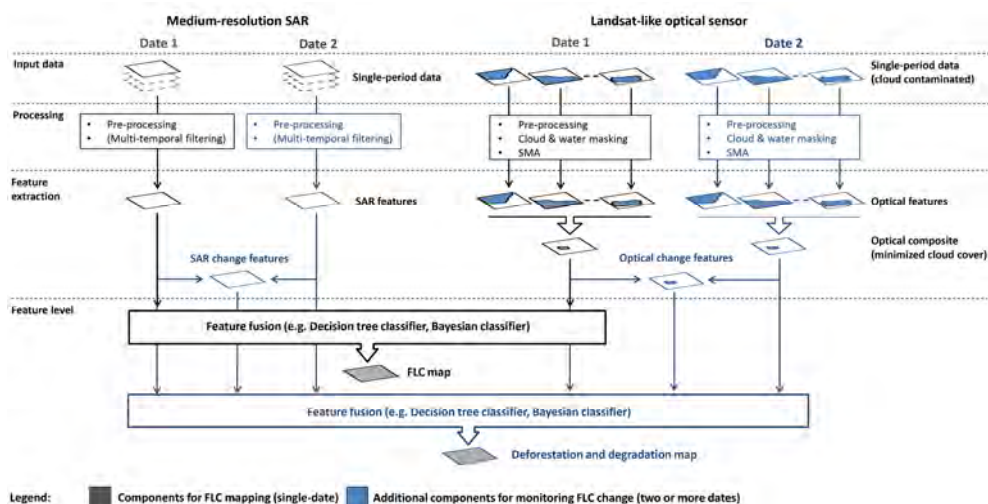


**Figure 2.1** Schematic overview of the proposed feature level fusion approach for (i) mapping tropical forest land cover (FLC) including degraded forest, and (ii) for monitoring tropical deforestation and forest degradation (FLC change). The components required for single-date FLC mapping are kept in dark grey. The additional components required for FLC change detection are kept in blue.

The remaining part of the paper is structured as follows. Section 2.2.2 presents the pilot study site. Section 2.2.3 comprises data and processing description of Landsat and ALOS PALSAR as well as the presentation of reference and training data. The feature level fusion process using a decision tree classifier is examined in Section 2.2.4. In Section 2.2.5 an explanation of the assessment and evaluation method is done. Section 2.3 presents the results and provides an assessment in terms of the aimed objectives. Finally, conclusions are given in Section 2.4.

## 2.2.2 Pilot study site

The pilot study was carried out in the central part of the South American Republic of Guyana. Guyana is widely covered by tropical rain forest (~ 87%, 18.5 million ha) (Pöyry Management Consulting (NZ) Limited 2011) and is considered as one of the cloudiest countries in the world characterized by a very high mean annual cloud cover of > 80% (Herold 2009). Central Guyana has a tropical climate with average daily temperatures of 25.9°C, high annual rainfall (2772 mm/year) and two distinct wet (April - June (primary); November - January (minor)) and dry seasons (van Dam 2001). The study area is located in Central Guyana within the main mining district of Mahdia. It extends approximately 130 x 60 km (746716 ha) and is covered by two adjacent ALOS PALSAR tiles with the track/frame 116/90 in the east and 117/90 in the west (Figure 2.2).

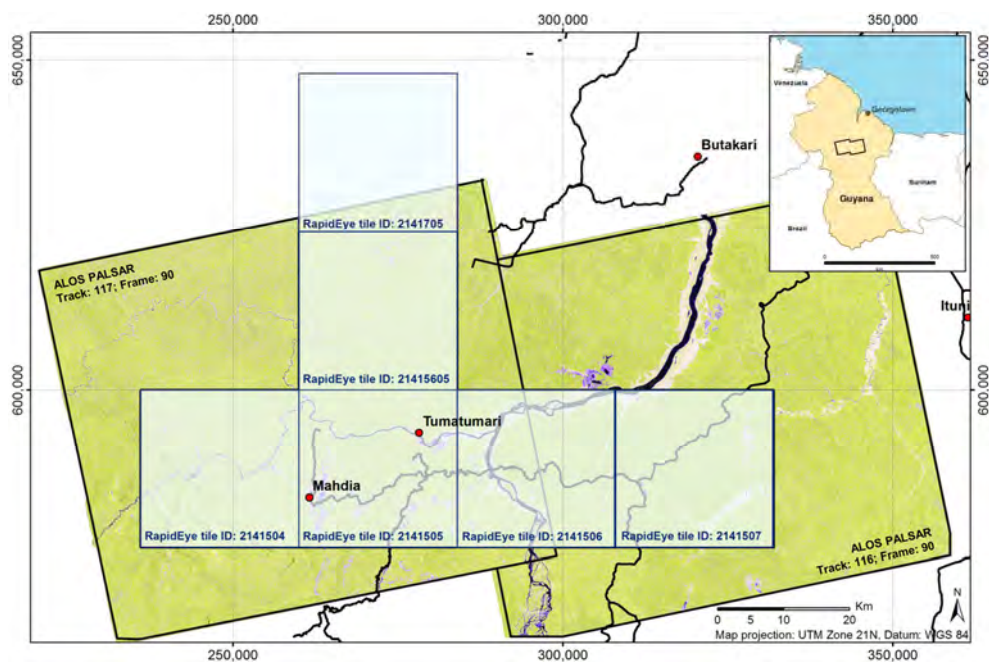


**Figure 2.2** Pilot study area around Mahdia (Central Guyana) covering two ALOS PALSAR tiles (Track/Frame: 117/90 (west); 116/90 (east)). The RapidEye coverage consisting of 6 tiles is shown in blue. Main roads and settlements are overlaid.

Within the framework of Guyana's REDD+ program, Guyana reports relatively low yearly deforestation rates of 0.02%/year for the period of 2006 - 2009, 0.056% for 2010 and 0.053% for 2011 (Indufor Asia Pacific Ltd 2012). Around Mahdia, deforestation and forest degradation rates are much higher. The main drivers of deforestation and forest degradation occurring in Guyana are active, including agriculture expansion, forestry and in particular small- and medium-scale open pit gold mining (Clifford 2011; Pöry Management Consulting (NZ) Limited 2011). The practiced method of mining is 'land dredging' (Clifford 2011). Throughout the last decade, gold mining increased rapidly in Guyana and accounts for 46% of the total export earnings in 2011, which is more than triple the value of second-ranked sugar (Guyana Bureau of Statistics 2012). Significant topographic variations can be found across the study site with the terrain elevation varying between -119 m (mining pit) and 1118 m above sea level. Land is defined as forest according to the Marrakech Accords by meeting the following criteria: Tree cover of minimum 30%, at a minimum height of 5 m, and over a minimum area of 1 ha. Degraded forest comprises disturbed forest areas, but also shifting cultivation and roads smaller 10 m (Indufor Asia Pacific Ltd 2012; Pöry Management Consulting (NZ) Limited 2011).

## 2.2.3 Data processing

### 2.2.3.1 ALOS PALSAR data

Multi-temporal L-band SAR data for 2007 and 2010 was obtained from the phased array L-band synthetic aperture radar sensor aboard the advanced land observing satellite (ALOS PALSAR) acquired in Fine Beam Dual (FBD) mode (Shimada et al. 2010). All images were acquired in ascending mode with an incidence angle of  $34.3^\circ$  and were provided in Level 1.1 format. The swath width of FBD data is 70 km. The data set covers Track/Frame 116/90 and 117/90 (Figure 2.2) and consists of two FBD images per frame for 2007 and 2010 (Table 2.1). The ALOS PALSAR FBD images were pre-processed independently using the Gamma software package (Werner & Strozzi 2000), combined with SRTM (*Shuttle Radar Topography Mission*) version 4 DEM information (<http://srtm.csi.cgiar.org/>). Pre-processing included multi-looking, radiometric calibration using standard calibration coefficients (Shimada et al. 2009), topographic normalization as described in (Hoekman et al. 2010) as well as geocoding to 25 m pixel resolution (WGS84, UTM 21N). Visual comparison with Landsat and high resolution RapidEye as reference showed very good geocoding accuracy (around 1 pixel error, 25 m). Among the different pre-processed images for one tile no significant geolocation differences are visible. In addition to the general SAR pre-processing steps, adaptive multi-temporal SAR filtering (Quegan & Yu 2001) has been applied separately to the FBD image pairs (HH - horizontal transmit and horizontal receive polarisation; HV - horizontal transmit and vertical receive polarisation) for 2007 and 2010. In contrast to conventional bi-dimensional SAR speckle filter that result in a trade-off between speckle-reduction and decreased spatial resolution, multi-temporal SAR filter reduce the SAR speckle without losing radiometric accuracy and spatial resolution of the single channels (Trouvé et al. 2003; Quegan et al. 2000; Quegan & Yu 2001). A measured increase of the equivalent number of looks (ENL) from  $4.58 \pm 0.03$  to  $8.45 \pm 0.46$  for HH and from  $5.13 \pm 0.35$  to  $9.05 \pm 0.51$  for HV indicates a clear reduction of SAR speckle in the data. This is crucial for analysing the data at pixel level or small segment level. In addition, no significant changes in the mean radiometric characteristics were observed.

**Table 2.1** ALOS PALSAR data specifications.

Track/Frame	Date	Mode (Polarisation)	Incidence angle	Orbit
116/90	05-07-2007	FBD (HH and HV)	$34.3^\circ$	Ascending
	20-08-2007			
	13-07-2010			
	28-08-2010			
117/90	22-07-2007	FBD (HH and HV)	$34.3^\circ$	Ascending
	06-09-2007			
	30-07-2010			
	14-09-2010			

For this study only basic SAR features were considered. Besides the single-date HH and HV backscatter and the HH-HV backscatter ratio (HVHH), the dual-date difference change index (DCI) has been computed for HH and HV polarisation based on the processed PALSAR data for 2007 and 2010:

$$DCI_{pq} = \gamma_{pq, year1}[dB] - \gamma_{pq, year2}[dB] \quad (2.1)$$

with  $\gamma$  as the radar backscatter parameter ( $\gamma = \sigma^0 / \cos\theta_i$  with  $\sigma^0$  = the normalised radar cross section,  $\theta_i$  = incidence angle) and  $pq$  as the polarisation (HH or HV).

### 2.2.3.2 Landsat data

Multi-temporal Landsat Thematic Mapper 5 (TM 5) and Landsat Enhanced Thematic Mapper (ETM+) images with 30 m spatial resolution were acquired for the reference years 2007 and 2010 through the USGS (*United States Geological Survey*) GLOVIS (*Global Visualization Viewer*) portal (<http://glovis.usgs.gov/>). The Landsat path/row: 231/56 covers the Mahdia mining area and further parts of Central Guyana. Due to persistent cloud cover, the Landsat archive contains only 22 images with cloud cover < 40% and only 8 images with cloud cover < 30% for 5 years of observation between 2006 and 2010 (Figure 2.3) referring to only 19% and 7% of the acquired images, respectively. With a few exceptions, the less cloud contaminated images area acquired at the beginning of the main dry season in July – September. Analysing the Landsat archive shows that Central Guyana experiences primarily scattered clouds evenly distributed over the entire area. Thus, large areas are affected by small cloud shadows. Due to the failure of the scan line corrector (SLC) of Landsat ETM+ in 2003, all acquired ETM+ images (SLC-off) are missing around 22% of their information as result of horizontal gaps (Zhang et al. 2007). In order to provide a sufficient cloud-free coverage, the 5 most suitable (cloud free) images have been acquired for each reference year (Table 2.2).

**Table 2.2** Landsat data specifications and cloud cover for Landsat path/row: 231/56 (Central Guyana).

Date	Landsat Sensor	Cloud cover [%]
02-09-2006	TM5	21
10-09-2006	ETM+ (SLC-off)	26
26-09-2006	ETM+ (SLC-off)	31
21-03-2007	ETM+ (SLC-off)	44
27-07-2007	ETM+ (SLC-off)	36
29-07-2010	ETM+ (SLC-off)	44
28-08-2010	TM5	35
05-09-2010	ETM+ (SLC-off)	38
07-10-2010	ETM+ (SLC-off)	23
23-10-2010	ETM+ (SLC-off)	34

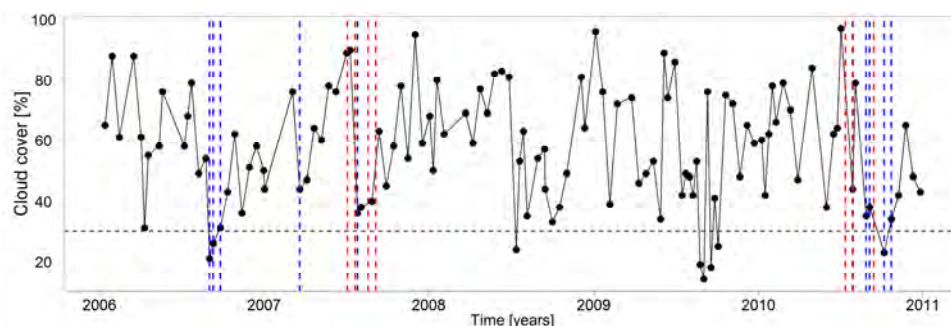


**Figure 2.3** Landsat (TM and ETM+) cloud cover for path/row 231/56 (Central Guyana) acquired for the period from 2006 to 2010. The dotted lines show (i) 30% cloud cover level (black), (ii) the 10 Landsat images (in blue with 5 images for each of 2007 and 2010) and (iii) the 8 acquired ALOS PALSAR FBD images (in red with 2 images by 2 tiles for each of 2007 and 2010).

The Landsat data was processed with the *ImgTools* software (V1.0 beta) developed by Imazon (<http://www.imazon.org.br/>). *ImgTools* is IDL-based toolbox that provides components for pre-processing, SMA, cloud and water masking, NDFI calculation, decision tree based classification and accuracy assessment for several medium and low resolution optical sensors. For the SMA of Landsat data end member for NPV, GV, soil and shade are available that was derived from images of the Brazilian Amazon using the pixel purity index (Souza et al. 2005).

Landsat digital numbers (DN<sub>s</sub>) were converted to reflectance through a stepwise approach for each of the available images. First, the DN<sub>s</sub> were converted to radiance using the gains and offsets provided in the Landsat image metafile. Haze correction was performed using the technique introduced by Carlotto (1999, (Carlotto 1999)) and is described in detail in Souza et al. (2005). To finally convert radiance to reflectance, atmospheric correction was performed using ENVI FLAASH (Exelis Visual Information Solutions 2009); a MODTRAN4-based (*MODerate resolution atmospheric TRANsmi*sion 4) atmospheric correction package that provides physics-based derivations of surface reflectance. A tropical atmospheric model, a rural aerosol model and for aerosol retrieval the 2-Band Kaufman-Tanre Aerosol Retrieval (Kaufman et al. 1997) has been used as settings.

SMA (Adams et al. 1993) was performed to decompose the Landsat reflectance data into fractions of NPV, GV, soil and shade fraction as described in Souza et al. (2005). Water, cloud and cloud shadow were masked by applying thresholds on the pixel fractions. GV, shade and soil fractions were used to detect water, whereas cloud and shade fractions were used for cloud and cloud shadow masking. A buffer (of 2 pixels) was applied around detected clouds to ensure that cloud edges are masked completely. A visual control showed no remaining unmasked cloud parts within the images. The Normalised Difference Fraction Index (NDFI) combines NPV, GV and soil fraction information in one synthetic band that enhances forest canopy damage.

The NDFI is calculated as:

$$NDFI = \frac{GV_{Shade} - (NVP + Soil)}{GV_{Shade} + NVP + Soil} \quad (2.2)$$

With  $GV_{Shade}$  is the shade-normalised  $GV$  fraction given by:

$$GV_{Shade} = \frac{GV}{100 - Shade} \quad (2.3)$$

The NDFI ranges from -1 to 1, where undisturbed forest has a high NDFI. Due to a lower proportion of  $GV$  and a higher proportion of  $NPV$ , soil and shade content within a pixel as a result of canopy gaps, degraded forest features a lower NDFI (Souza 2003). The 5 Landsat NDFI images processed for each reference year were merged to reduce cloud and SLC-off gaps. In case of a multiple-coverage, the maximum NDFI value was applied as a rule for merging input images. The last processing step consisted of rescaling the NDFI images from 30 m to the 25 m resolution; the resolution of the processed ALOS PALSAR features. The same spatial resolution is required to fuse at feature level.

### 2.2.3.3 Training and reference data

The study used four sources of reference data: (i) high resolution optical satellite imagery; (ii) a comprehensive GIS (*Geographic information system*) dataset available from the Guyana Forestry commission; (iii) ground truth information; and (iv) aerial photographs. High resolution multi-spectral image data from RapidEye featuring a ground sampling distance (nadir) of 6.5 m and orthorectified to 5 m pixel resolution was acquired for 6 tiles (footprint: 25 x 25 km) for 2010/11 (Table 2.3, Figure 2.2). The 6 tiles cover approximately one third of the ALOS PALSAR FBD image data and for each tile two scenes are obtained in order to minimize data gaps due to varying cloud cover between 25 – 44%. Half tiles are created, whereby one half of is used to select training samples and the second half is saved to assess the map accuracies. This ensures a statistically robust accuracy assessment (Korting et al. 2010).

**Table 2.3** RapidEye data overview and cloud cover.

Tile ID	Acquisition dates	Cloud cover [%]
2141504	17-10-2010; 08-08-2011	27; 26
2141505	15-08-2011; 20-08-2011	25; 27
2141506	16-10-2010; 20-08-2011	26; 34
2141507	11-08-2011; 23-12-2011	26; 31
2141605	15-08-2011; 20-08-2011	34; 44
2141705	17-12-2010; 15-08-2011	25; 26

For Guyana, the RapidEye archive currently represents the only data source for high resolution optical satellite images with reasonable spatial coverage, reasonable cloud cover (< 50% cloud cover) and image quality. High resolution optical image data acquired before the launch of RapidEye in 2009 is not available. However, an almost cloud-free (2% cloud cover) Landsat TM 5 image from 01-10-2005 (path/row: 231/56), the only Landsat image with < 10% cloud covers in the entire Landsat archive, suits as historical reference information. The GIS dataset is continuously maintained by the Guyana Forestry Commission (GFC) and includes spatial information for several data groups such as managed forests (e.g. harvesting areas, logging camps, logging blocks, timber sales agreements, state forest permit boundaries), mining areas (e.g. mining areas, mining permits), agricultural leases, soil and vegetation, administrative boundaries, and roads.

Ground truth information were collected during a survey where 58 GPS points were visited in October 2011, land cover and change was interpreted by international (Dirk Hoekman, Johannes Reiche) and national (Haimwant Persaud) experts. In addition, photographs of areas affected by different drivers of deforestation and forest degradation, as well as aerial photographs (September 2010, October 2011) have been used in the reference data interpretation. A set of 20 training samples (10 - 25 pixel/sample) per FLC class was manually extracted from the RapidEye (2010/11) data in combination with the GPS ground truth information. As deforestation training samples, 20 areas (10 - 25 PALSAR pixel/sample) were manually extracted from combined analysis of the Landsat (2005) and RapidEye (10/11) data. Local expert knowledge from the GFC and the GFC GIS layer (mining pits, permits and logging pits) were used to consolidate the reference samples and area and to delete inappropriate ones.

#### **2.2.4 Feature level fusion using decision tree classifier**

A decision tree classifier was used to fuse the extracted SAR and optical features. Decision tree classifiers are non-parametric and therefore require no probabilistic descriptions of the desired classes to be distinct. The lack of comprehensive training data inhibits the assessment of accurate probability density functions (Hoekman et al. 2010). It instead consists of a set of explicit hierarchical conditions (rules, feature thresholds) applied to intervals of input data, in our case SAR and optical features. Decision tree classifiers have been successfully applied for forest mapping and also change detection (e.g. Korting et al. 2010; Simard et al. 2000).

For feature and feature threshold selection, a signature and separability analysis of the extracted features (2007 and 2010) was conducted using the training sample areas available for the FLC classes and deforestation. Figure 2.4 shows the signatures (mean and standard deviation) of the PALSAR backscatter features HH, HV, HHHV and the Landsat NDFI for forest (F), non-forest (NF), degraded forest (DF) and water (W). The normalised Jeffreys-Matusita distance (JM) was used as measure for pair-wise class separability. The normalised JM has a finite dynamic range from 0

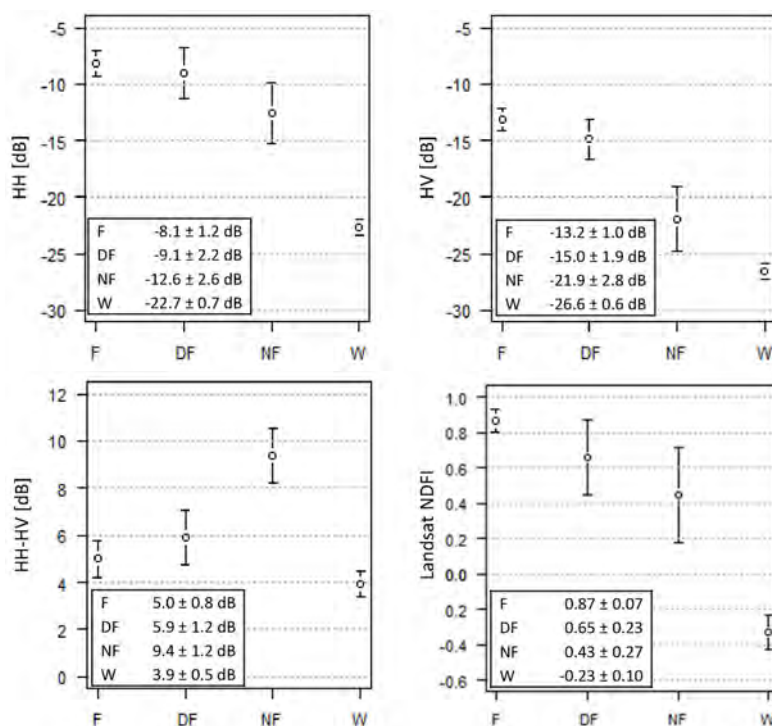


**Figure 2.4** Signatures (mean and standard deviation) of the PALSAR backscatter features HH, HV, HHHV and the Landsat NDFI for the FLC classes forest (F), degraded forest (DF), non-forest (NF), water (W). Signatures were derived from training sample areas.

(inseparable) to 2 (separable) which allows for an objective comparison (Laliberte et al. 2012).

Table 2.4 depicts the JM separability measures of (i) the FLC class combinations observed for the PALSAR backscatter features HH, HV and HHHV and the Landsat NDFI; and (ii) between F and DF combined and NF representing a F/NF only classification; and (iii) for the FLC change class combination deforestation – NoChange observed for the HH- and HV-DCI 2007 - 2010. The features with the highest separability per class were identified (Table 2.4, highlighted in grey) and used to design a straightforward decision trees. The corresponding feature thresholds were identified qualitatively by evaluating the signatures of the training data and subsequently tuned. The spatial incompleteness of the NDFI was taken into account and only PALSAR feature were selected to distinct FLC classes F, NF and W and to detect deforestation.

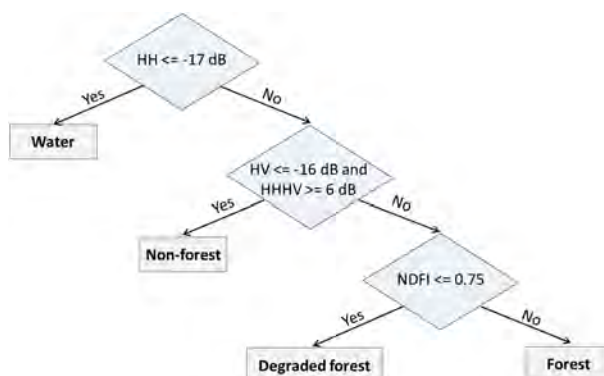


**Figure 2.5** Decision tree classifier for PALSAR-Landsat based single-date FLC mapping of 2007 and 2010, using single-date PALSAR backscatter features and the Landsat NDFI.

Figure 2.5 depicts the decision tree classifier used for single-date FLC mapping of 2007 and 2010. HH backscatter was used to distinguish W from other FLC classes. NF was separated from F by their difference in HV backscatter and HHHV backscatter ratio. Compared to F, NF is characterized by a lower backscatter in HV due to much less volume scattering contribution. DF was identified using the NDFI. In areas of PALSAR data gaps (SAR layover and shadow) where Landsat information was available, FLC was classified by a straightforward thresholding of the NDFI (F: NDFI > 0.75, DF: NDFI > 0.55, NF: NDFI > 0, W: NDFI ≤ 0). The latter step can be enhanced by integrating further Landsat features and employing a more sophisticated classification. After the decision tree classification, a post-classification is applied to reduce isolated single pixels.

**Table 2.4** Normalised JM between the FLC classes: forest (F), degraded forest (DF), non-forest (NF), water (W); between (F+DF) and NF representing a F-NF only separation; and between the FLC change classes deforestation (DEF) and no change. Figures highlighted in grey mark the best separability per class combination linked to the features that were used to classify FLC and FLC change.

Feature	Class combination							DEF - NoChange
	F-NF	(F+DF)-NF	F-DF	F-W	NF-DF	NF-W	DF-W	
HH	1.72	1.43	0.41	2.0	1.06	1.98	2.0	-
HV	1.99	1.88	0.61	2.0	1.72	1.89	1.97	-
HHHV	1.95	1.76	0.75	1.04	1.68	1.98	1.71	-
NDFI	1.89	1.61	1.62	1.99	1.12	1.96	1.99	-
HH-DCI (2007-10)	-	-	-	-	-	-	-	1.64
HV-DCI (2007-10)	-	-	-	-	-	-	-	1.98

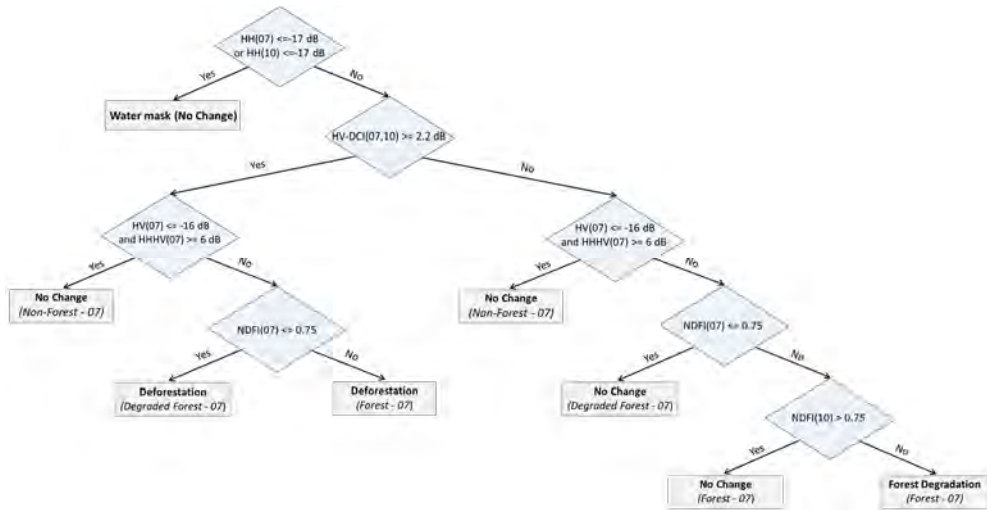


**Figure 2.6** Decision tree classifier for PALSAR-Landsat based deforestation and forest degradation detection (FLC change) between 2007 (07) and 2010 (10), using the HV difference change index (HV-DCI) calculated for 07-10, single-date PALSAR backscatter features from 07 and 10 and the NDFI from 07 and 10. For each FLC change class the respective FLC class of 07 is given in brackets (*italic*), indicating the class transition.

Figure 2.6 depicts the decision tree classifier for detecting deforestation and degradation between 2007 and 2010. Water bodies are masked in a first step using HH backscatter before the HV-DCI is used to detect possible deforestation pixels. The results of the signature and separability analysis of the HH- and HV-DCI calculated using the dual-date PALSAR data of 2007 and 2010 (1) confirmed the expected higher sensitivity of the HV-DCI to forest cover change (Table 2.4). Deforestation events result in a significant drop of the HV backscatter over forest due to the decrease of volume scattering from the canopy. For the case of forest areas converted to open mining pits where sandy soils are mixed with small water ponds, a drop of up to 6 - 7 dB was observed. No significant temporal variability of the HH and HV backscatter over stable forest areas between 2007 and 2010 has been observed. An HV-DCI of 2.2 dB was found to be a suitable threshold to detect deforestation without too many false alarms. Values below 2.2 dB can be explained by the natural variability over forest due to changes in soil and canopy moisture for example (Quegan et al. 2009). In case a possible deforestation pixel is found, the left side of the decision tree distinguishes deforestation from non-forest areas that are in consequence classified as no change. The last level separates deforestation pixel into deforestation either related to the conversion of forest to non-forest or of degraded forest to non-forest, respectively. The same features and thresholds that are utilized for FLC mapping are applied. The right side of the decision tree identifies for forest degradation. After separating possible degradation pixel from non-forest that are consequently classified as no change, new degradation is

distinguished from stable forest (no change) and already degraded forest in 2007 at the last two levels using the NDFI of 2007 and 2010. Forest degradation has only been monitored at areas where Landsat coverage was available for both reference years. This avoids an overestimation of degradation in case degraded areas were not detected in 2007 due to cloud cover, but instead were detected as new degradation in 2010.

### **2.2.5 Assessment of map accuracy and thematic and spatial completeness**

Measuring the thematic map accuracy is crucial to assess the usefulness of the mapping approach for a particular application, in this case REDD+. A statistically robust accuracy assessment design is crucial to derive reliable measures of user's, producer's, overall accuracy and kappa statistic from an error matrix (Congalton 1991; Foody 2002). Thereby, user's accuracy refers to the probability that a pixel classified as a certain class does in fact belong to the class on the ground, whereas the producer's accuracy refers to the probability that a certain class on the ground is classified as such. A stratified random sampling with the equal number of reference samples per class (50 per class) has been used to address the unequal class appearance of the FLC and FLC change classes in the study area (Congalton 1991). In order to assess the desired per-pixel classification of FLC and change the pixel resolution of 25 m has been defined as the sample unit size. The response design consisted of class labelling of each sample by applying the forest and forest degradation definition applied in Guyana's REDD+ MRVS interim reports. To demonstrate the FLC mapping accuracy, only the FLC map of 2010 was validated since for 2007 no appropriate high resolution reference data (RapidEye) was available. Landsat (2005), RapidEye (2010/11) data in combination with expert knowledge gained during the field visit (2011) and GIS data was used to evaluate the FLC change detection accuracy. The increase of spatial completeness and thematic detail of the proposed PALSAR-Landsat feature level fusion products compared to potential Landsat-only or PALSAR-only approaches for a heavy cloud contaminated tropical environment is assessed in addition to the map accuracy to address the main objective of the present study. This is done by jointly analysing and discussing the class and the data gap statistics with respect to the requirements of a meaningful REDD+ MRV system that aims at full spatial coverage and high thematic detail including both, deforestation and forest degradation information.

## 2.3 Results and Discussions

### 2.3.1 Assessing data gaps

For each reference period, the 5 processed Landsat TM/ETM+ images were merged together to maximize the spatial coverage. Figure 2.7 visualizes the merging process for 2010 by the NDFI. Due to masked clouds and ETM+ SLC-off areas for which no valid information was available from any of the 5 Landsat input images, gaps remained for 5.1% (382 km<sup>2</sup>) and 3.1% (237 km<sup>2</sup>) of the entire study area for 2007 and 2010, respectively (Table 2.5). It has to be mentioned here that open mining pits were partly masked as clouds because of a strong spectral overlap (Landsat fractions) between clouds and the very bright sandy soil in the open mining pits. In addition, few very dark cloud shadow areas were not detected by the masking algorithm and cause artifacts within the degraded forest class. These problems, however, are well known and can be solved by a cloud detection algorithm that additionally incorporates thermal information (e.g. FMASK, (Zhu & Woodcock 2012)). Combining the Landsat data set of 2007 and 2010 only a marginal part of the data gaps are overlapping (0.3%, 22 km<sup>2</sup>) and for 7.9% (597 km<sup>2</sup>) of the study area no dual-date information is available (Table 2.5). The results shows that in a heavy cloud contaminated environment, a series of Landsat images is required to produce a dataset with a reasonable spatial coverage. In our case, Landsat images acquired throughout an entire year had to be merged to get 95% coverage. This prohibits a meaningful intra-annual analysis using only Landsat information. Although Landsat images acquired over a period of up to 11 month (reference year 2007) were combined, only dry season observations were selected to avoid major seasonal variations that otherwise need to be corrected to provide consistent data. SAR layover and shadow effects in mountainous parts of the study area lead to data gaps that account for 0.05% (3.81 km<sup>2</sup>) of the study area. In contrast to the Landsat data gaps, SAR layover and shadow areas have always the same location for a certain SAR acquisition specification (sensor, orbit, mode and associated incidence angle). In the present case, almost the entire SAR layover and shadow areas are covered by Landsat information and only a negligible part of ~0.01% is missing in both datasets (Table 2.5).

**Table 2.5** Landsat and ALOS PALSAR data gaps and remaining ALOS PALSAR data gaps that are not covered by Landsat data for the reference years 2007, 2010 and for 2007 and 2010 combined.

<i>Total area: 746716 ha</i> Reference year	Landsat data gap (clouds & SLC-off)	PALSAR data gap (layover & shadow)	Remaining PALSAR data gap (not covered by Landsat)
<b>2007</b>	5.1% (38212 ha)	0.05% (381 ha)	0.01% (53 ha)
<b>2010</b>	3.1% (23756 ha)	0.05% (381 ha)	< 0.01% (13 ha)
<b>2007 &amp; 2010 (combined)</b>	7.9% (59708 ha)	0.05% (381 ha)	0.01% (63 ha)

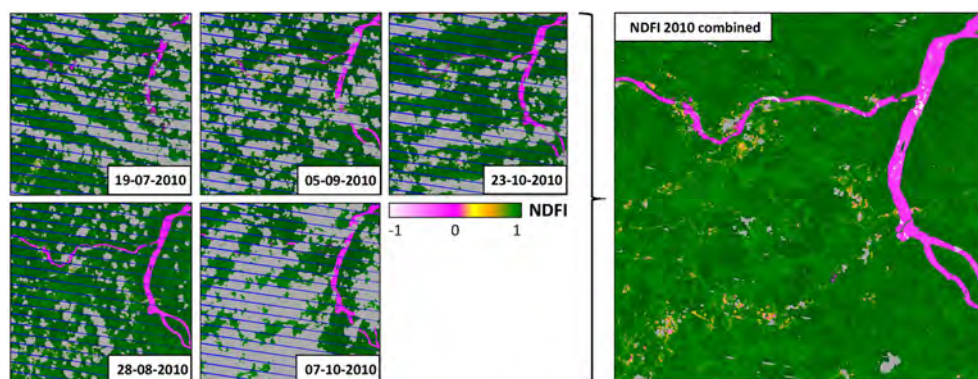


**Figure 2.7** Merging the 5 individually processed Landsat TM/ETM+ NDFI images from 2010 to reduce data gaps due to clouds (grey) and ETM+ SLC-off.

### 2.3.2 Mapping forest land cover

The PALSAR-Landsat feature level fusion approach has been applied for mapping FLC for the reference years 2007 and 2010. Table 2.6 depicts the accuracy assessment results for the FLC classification 2010 including the entire confusion matrix. An overall accuracy of 88% and a Kappa coefficient of 0.84 were found. Misclassification mainly occurred due to confusions with the DF expressed by a relatively low user's (omission error) and producer's accuracy (commission error). This can be partly explained by the single NDFI threshold that was applied and might not cover the entire variety of forest types present in the study area. A spatially stratified NDFI threshold associated to different forest types is a promising approach to increase the degradation mapping accuracy.

**Table 2.6** Confusion matrix for the PALSAR-Landsat 2010 FLC classification, including user's and producer's accuracy, overall accuracy (OA) and Kappa coefficient (Kappa).

	Forest	Degraded forest	Non-forest	Water	
<b>PALSAR-Landsat FLC, 2010</b>					
<b>Forest</b>	47	2	1	0	94%
<b>Degraded forest</b>	4	39	6	1	78%
<b>Non-forest</b>	1	6	41	2	82%
<b>Water</b>	0	0	1	49	98%
<b>Producer's accuracy</b>	90.3%	82.9%	83.6%	94.2%	

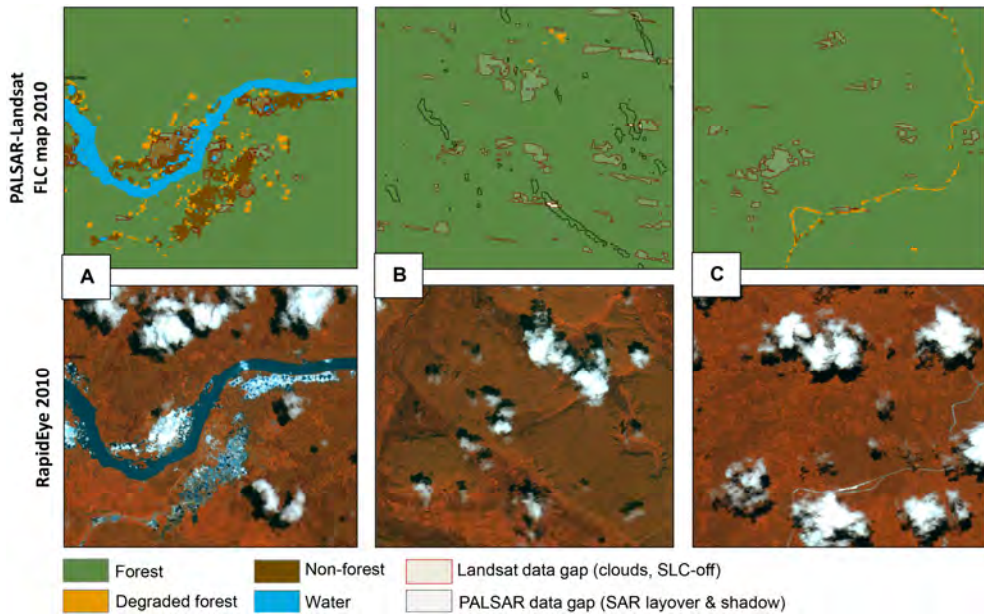
Because DF also comprises Amerindian shifting cultivation following the definitions applied in Guyana’s REDD+ MRVS report, recently burned forest patches (slash-and-burn) caused a commission error in the NF class. Guyana’s definitions for DF led also to the classification of any kind of disturbed forest areas as DF. Consequently, in this study it was assumed that all visible disturbances are caused by degradation since Central Guyana is mainly covered by primary forest. This could be considered as limitation of the proposed classification scheme when trying to apply to other countries. However, following and adapting classification schemes and classes to the country requirements and definitions is always necessary when conducting remote sensing work for REDD+ MRV. Taking Guyana’s (Indufor Asia Pacific Ltd 2012; Pöyry Management Consulting (NZ) Limited 2011) and many other countries REDD+ MRVS into account which commonly assess F, DF and NF with W included in the NF class, an overall accuracy of 86% and a Kappa coefficient of 0.79 can be found for the 2010 FLC map. By only considering a F/NF and W classification, where DF is defined as part of forest, a high overall accuracy of 96.6% and a Kappa coefficient of 0.95 was observed. This clearly demonstrates the capability of medium resolution L-band SAR for mapping tropical forest cover with high thematic accuracy confirming the results of previous studies (e.g. Almeida-Filho et al. 2007; Almeida-Filho et al. 2009).

Table 2.7 depicts the area statistics per class. A decrease in undisturbed forest area from 98% to 97.6% representing 2898 ha was observed for 2010 compared to 2007 due to an increase of non-forest and degraded forest areas from 0.43% to 0.62% and from 0.27% to 0.44%, respectively. The observed small increase of water areas of 0.02% is caused by mainly flooded open mining pits, but also (seasonal) water level fluctuations of rivers.

Figure 2.8 shows three details of the PALSAR-Landsat FLC classification for 2010, emphasizing the increase of spatial completeness and thematic detail compared to potential Landsat-only or PALSAR-only approaches. Figure 2.8A shows overlaid (red outline, transparent grey) the remaining Landsat data gaps that account for 3.1% of

**Table 2.7** Area statistics per FLC class for 2007 and 2010.

<i>Total area: 746716 ha</i>	<b>Area per class, 2007</b>		<b>Area per class, 2010</b>	
<b>Forest</b>	98.0%	732048 ha	97.6%	729150 ha
<b>Degraded forest</b>	0.27%	1883 ha	0.44%	3359 ha
		<i>[94.9% coverage]</i>		<i>[96.9% coverage]</i>
<b>Non-forest</b>	0.43%	3227 ha	0.62%	4609 ha
<b>Water</b>	1.27%	9505 ha	1.29%	9686 ha
<b>NoData</b>	0.01%	53 ha	< 0.01%	13 ha



**Figure 2.8** Details of the PALSAR-Landsat FLC map 2010 and corresponding RapidEye 2010 reference imagery. The FLC map is overlaid with Landsat gaps (red outline, transparent grey) and PALSAR layover&shadow areas (black outline). (A) NF and degraded forest (DF) areas within a mining area, (B) SAR layover&shadow areas (outlined in black) filled with optical information, (C) Road network classified as DF.

the total investigation area.. A Landsat-only classification would not cover these areas resulting in spatially inconsistent results. Figure 2.8B illustrates the complementary potential of Landsat data to improve spatial completeness through providing FLC information to fill PALSAR data gaps caused by SAR layover and shadow (black outline). For the FLC classification of 2010, data gaps were reduced to a negligible area ( $< 0.1\%$ ). A PALSAR-only classification could provide reliable FLC information with (almost) complete spatial coverage at any time of acquisition, but the desired thematic detail would lack since the PALSAR-based detection of degraded forest is limited. Figure 2.8C shows parts of the road network as an example for degraded forest areas that were not detected by PALSAR due to sensitivity and resolution constraints. A quality flag consisting of the remaining Landsat gaps (Figure 2.8A) indicate areas where potential degraded forest areas were not assessed. In the case of the FLC classification of 2010, degraded forest accounts for 42% of the disturbed area (Table 2.7). This area would stay unreported or associated with lower class accuracy for a PALSAR-only approach.

### 2.3.3 Monitoring deforestation and forest degradation

The proposed PALSAR-Landsat feature level fusion approach was successfully applied for detecting deforestation and forest degradation (FLC change) between the reference years 2007 and 2010 (Figure 2.9). Comparing the FLC change map with the FLC map of 2007 and 2010 (Figure 2.9-detail map) proves visually the validity of the proposed method. Table 2.8 depicts the accuracy assessment results for which the two distinct types of deforestation (F → NF and DF → NF) were considered as one class. An overall accuracy of 89.3% and a Kappa coefficient of 0.84 were observed. The majority of the class confusion was introduced by the forest degradation class. False alarm rates of 10% and 22% were found for deforestation and forest degradation. The relatively high forest degradation false alarm rate can be partly explained by non-masked cloud shadow areas. The two most obvious examples are located in the south-western part of the study area where two larger incorrectly detected degradation areas, surrounded by dense forest, can be found Figure 2.9. Area statistics depicted in Table 2.9 shows a forest loss (deforestation) of 2223 ha within the observation period representing 0.3% of the total area mainly driven by the expansion of small to large-scale open mining sites. The majority of the forest loss is related to the direct transformation from undisturbed forest to non-forest and only 20% to the conversion of already degraded forest to non-forest. The latter mainly represents degraded forest areas located at edges of mining pits that were eventually deforested due to the expansion of the mining pits. As expected, the observed deforestation rate of 0.1%/year for the Mahdia strongly exceeds the reported country average rates (0.02% - 0.056%/year) (Indufor Asia Pacific Ltd 2012). Also degradation that accounts for 0.25% (1871 ha) of the total area corresponding to a yearly degradation rate of 0.08% clearly exceeds the reported country average rate of 0.024%/year for 2011. Compared to a potential Landsat-only or PALSAR-only approach a reduction of missing deforestation information from 7.9% and 0.05% to negligible 0.01% (63 ha) was achieved by the combined PALSAR-Landsat approach, respectively (Table 2.5).

**Table 2.8** Confusion matrix for PALSAR-Landsat FLC change map of 2007 – 2010, including user’s and producer’s accuracy, overall accuracy (OA) and Kappa coefficient (Kappa).

<i>OA: 89.3% / Kappa: 0.84</i>				
PALSAR-Landsat FLC change, 2007 - 2010	Reference			User’s accuracy
	Deforestation	Degradation	No Change	
Deforestation	45	1	4	90%
Degradation	4	39	5	78%
No Change	0	0	50	100%
<b>Producer’s accuracy</b>	88.2%	97.5%	84.7%	

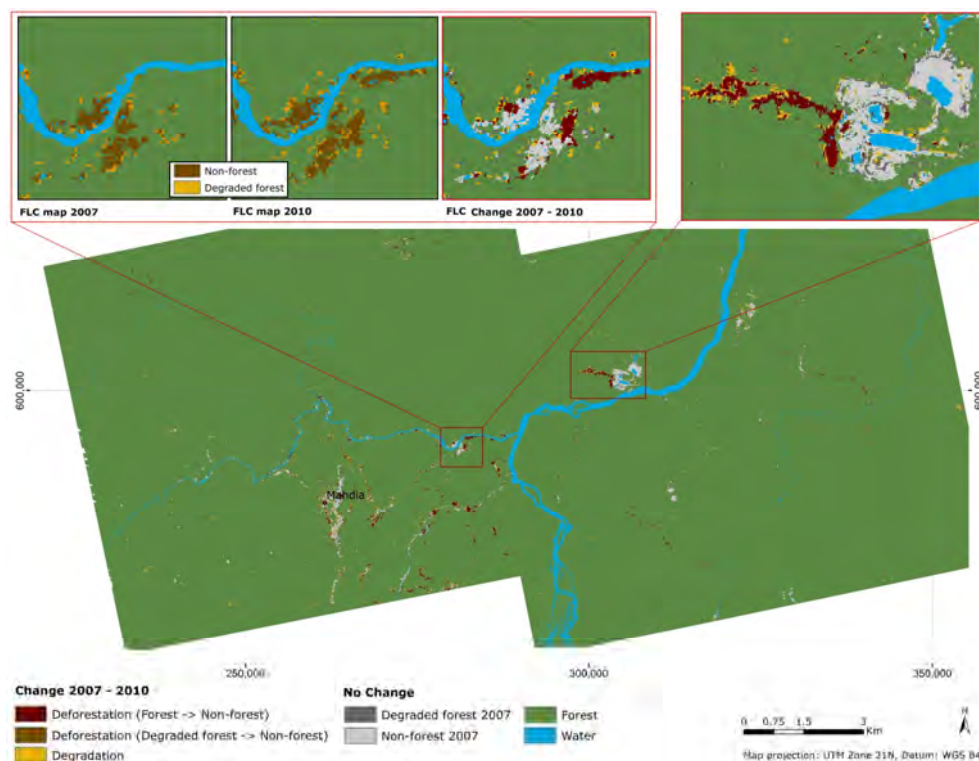


**Figure 2.9** PALSAR-Landsat FLC change map 2007 - 2010 of Mahdia mining district, including 2 detail maps. For comparison, the PALSAR-Landsat FLC maps for 2007 and 2010 are depicted in addition with the left detailed map.

Due to Landsat data gaps degradation information is missing for 7.9% of the area. A potential PALSAR-only would be capable of reliably detecting deforestation, but 45% of the detected change information that corresponds to forest degradation would be either missing or be associated with a much higher false detection rate due to the lower sensitivity of L-band backscatter compared to the Landsat NDFI. However, the observed signatures of degraded forest show lower HV and increased HH-HV values compared to undisturbed forest. This is explained by a decrease in canopy cover that in turn results in reduced volume scattering. The overlap between both classes expressed by low JM measures of 0.61 and 0.75 is also due to a limited spatial resolution of 25 m prohibits the clear identification of degraded forest and forest degradation using only very few PALSAR backscatter images. Analysing L-band time series is promising to increase the sensitivity to degraded forest which in turn would decrease the false detection rate (Quegan et al. 2009). The main focus of the presented case study was to provide more reliable and spatially complete deforestation and forest degradation activity data required for carbon emission estimation within Guyana's REDD+ MRV (Indufor Asia Pacific Ltd 2012).

**Table 2.9** Area statistics for the FLC change classification of 2007 – 2010.

<i>Total area: 746716 ha</i>		
	<b>Area change statistics</b>	<b>2007 - 2010</b>
<b>Deforestation</b> (Forest -> Non-forest)	0.24%	1920 ha
<b>Deforestation</b> (Degraded Forest -> Non-forest)	0.06%	303 ha
<b>Degradation</b>	0.25%	1871 ha
	<i>[92.1% coverage]</i>	
<b>No Change</b>	99.45%	742542 ha
<b>NoData</b>	0.01%	63 ha

By expanding the presented feature fusion approach with more observations or preferable with time series data, will allow to monitor forest dynamics such as forest regrowth and re-vegetation of deforested or degraded forest areas. It should be emphasized that the latter is one of the main challenges to be addressed in future studies.

## 2.4 Conclusions

The paper describes an innovative approach for feature level fusion of multi-temporal and medium resolution SAR and optical sub-pixel fraction information for mapping tropical FLC and detecting deforestation and forest degradation (FLC change). Multi-temporal ALOS PALSAR and Landsat imagery of 2007 and 2010 acquired for the main Guyanese mining district was used for demonstration. The overall accuracies are 88% and 89.3% for mapping FLC and deforestation and degradation, respectively. Central Guyana, like many other tropical regions, is affected by persistent cloud resulting in a very poor Landsat coverage. Landsat images acquired over an entire year were merged to provide reasonable coverage (~95%), which is prohibiting meaningful and consistent intra-annual analysis. In particular, change detection schemes are affected since cloud and ETM+ SLC-off data gaps of composited Landsat images showed to be unevenly distributed leading to accumulated data gaps by analysing multi-temporal datasets. The interoperable use of Landsat and PALSAR led to a reduction of Landsat (cloud cover, SLC-off) and PALSAR data gaps (SAR layover and shadow) to negligible 0.01% of the entire study area while maintaining the desired thematic detail of detecting deforestation and forest degradation, whereby a quality flag indicates remaining areas where potential forest degradation areas were not assessed. The combined improvement of both, thematic detail and spatial completeness compared to a potential Landsat- or PALSAR-only approach directly addresses the open requirements for a successful implementation of REDD+. The reported high yearly deforestation (0.1%) and degradation rates (0.08%) for the period of 2007 to 2010 that are mainly caused by

the drastic expansion of mining are clearly exceeding the reported country average and emphasizing the importance of the region for Guyana's REDD+ program. This in turn stresses the need for a spatially complete remote sensing based monitoring system for the provision of activity data. Therefore, the proposed SAR-optical fusion approach contributes directly to Guyana's REDD+ plans for employing SAR data for its REDD+ MRVS to tackle the country's persistent high cloud cover (Indufor Asia Pacific Ltd 2012); and provides opportunities/an option for other developing tropical countries. Further developments are stressed by (i) the need for multi-sensor time series methods and (ii) the increasing number of available satellite image time series in the near future. Besides the Landsat Data Continuity Mission (LDCM) and ALOS-2 PALSAR (L-band SAR) in particular ESA's (*European Space Agency*) Sentinel-1 (C-band SAR) and Sentinel-2 (optical) satellite constellations are of great interest. Since Sentinel-1 and Sentinel-2 data will be free of charge and developing countries are relying on cost efficient MRV systems, future work will aim to adapt the concept to a Sentinel based REDD+ monitoring system.

## **Acknowledgment**

This work was undertaken and funded as part of the EU Framework Program 7 project ReCover (grant agreement no 263075), and is supporting the ALOS Kyoto and Carbon and GEO FCT initiative. ALOS PALSAR data have been provided by JAXA EORC. RapidEye data has been provided by RapidEye AG. The authors thank the two anonymous reviewers for their careful critique, and comments that substantially improved the manuscript. The authors acknowledge Jagdesh Singh and Pradeepa Bholanath from the Guyana Forestry Commission for providing reference information and support during the field visit. We are also grateful to Joao Victor Siqueira for his technical support concerning the ImgTools software package.



**Chapter**

# 3

## **Multi-model radiometric slope correction of SAR images of complex terrain using a two-stage semi-empirical approach**

Dirk H. Hoekman and Johannes Reiche

*Published in Remote Sensing of Environment, 156 (2015), 1-10,  
DOI: 10.1016/j.rse.2014.08.037*

---

## **Abstract**

*Practical approaches for the implementation of terrain type dependent radiometric slope correction for SAR data are introduced. Radiometric slope effects are modelled as the products of two models. The first is a simple physical model based on the assumption of a uniform opaque layer of isotropic scatterers, which is independent of terrain type, frequency and polarisation. It accounts for the slope-induced variation in the number of scatterers per resolution cell. The second is a semi-empirical model, which accounts for the variation in scattering mechanisms, dependent on terrain type, frequency and polarisation. PALSAR FBD (L-band, HH- and HV polarisation) data are used at two test sites in Brazil and Fiji. Results for the Brazilian area, which has slopes up to 25 degrees, show that remaining slope effects for the multi-model case are much smaller than 0.1 dB, for all land cover types. This is much better than the best single-model approach where remaining slope effects can be very small for forests but be as large as 1.77 dB for woodland in HH polarisation. Results for the Fiji area, which has different vegetation types, are very similar. The potential large improvement, using this multi-model approach, in the accuracy of biomass estimation for transparent or open canopies is discussed. It is also shown that biomass change on slopes can be systematically under- or overestimated because of associated change in scattering mechanism.*

---

### 3.1 Introduction

Steep slopes in SAR images are notoriously difficult to handle. Even when an accurate DEM (Digital Elevation Model), is available and a proper orthorectification has been achieved, slopes are still visible. Slopes modulate the radar backscatter level in a complex way depending on slope steepness, slope aspect, land cover type, radar observation geometry, radar frequency band and polarisation. Many applications of radar monitoring require a proper handling of slope effects. For forests, for example, this is the case because a large fraction of the remaining pristine forests are located on steep slopes. For agricultural crop monitoring, for example, this is the case because dense time series are required and images from different look directions and incidence angles need to be combined. For accurate biomass estimation proper handling of slope effects is critical since slope effects, or remaining slope effects, can be of similar magnitude as the biomass induced backscatter modulation.

Slope effects are mentioned by many authors as they affect applications such as bio-physical parameter estimation (biomass, soil moisture), land cover classification and complicate the combination of ascending and descending images and multi-sensor analysis, including Atwood et al. (2012); Franklin et al. (1995); Castel et al. (2001); Luckman (1998); Sun et al. (2002). These authors also provide approaches to handle the slope effects. Several categories of approaches may be distinguished, such as (a) simple physical models, (b) empirical models and (c) terrain type dependent or tunable models.

Simple physical models with exact solutions were introduced by Hoekman (1990) and Ulander (1996). These models compensate for slope induced variation in the amount of scatterers in a resolution cell and will be described in more detail in Section 2. Both models assume uniform isotropic scattering. In Hoekman (1990) the terrain is described as an opaque volume scatterer and in Ulander (1996) as a surface scatterer, which leads to different expressions. The opaque isotropic volume scatterer model was validated for tropical forests in Hoekman et al. (1994) and often successfully applied for large-scale application in areas with dense vegetation such as in Hoekman et al. (2010). Both models have a limited range of applicability, however are independent of frequency and polarisation. In Ulander (1996) it is noted that alternative equations can be found in literature but that these are only approximations of the exact solution presented in Ulander (1996), such as Holecz et al. (1994), based on local incidence angle, and van Zyl et al. (1993) and Goering et al. (1995), based on slope tilt angles. Many empirical models, many of which may be regarded as approximate solutions of Ulander (1996), have been proposed. These empirical models have a limited range of applicability as they depend on terrain type, frequency and polarisation, however, may perform satisfactorily when tuned properly for the (dominating) terrain type and the sensor used. The models introduced by Hinse et al. (1988); Franklin et al. (1995) and Stussi et al. (1995) can be regarded as approximate solutions of Ulander (1996), based on the use of the

local incidence angle. In Kellndorfer et al. (1998) another empirical solution based on the local incidence angle is proposed. Sun et al. (2002) compares the model of Kellndorfer et al. (1998) and several other simple empirical models and concludes that none of these models provides a close approximation of the real scattering behaviour. Sun et al. (2002) states that terrain slope changes the local radar incidence angle, as well as the forest structure perceived by the radar and, consequently, the dependence of radar backscattering on slope steepness and slope direction is very complex.

More recently Loew & Mauser (2007) applied the model of Ulander (1996) and concluded it worked well for a test site in Germany. Akatsuka et al. (2009) applied a simple empirical model for PALSAR data. Shimada (2010) applied an empirical for PALSAR and concluded it did not perform well on steep slopes. Small (2011) applied a slope normalization model for ASAR and PALSAR. In Atwood et al. (2012) polarimetric PALSAR data are normalised for slope effects by applying the same normalization factor to each element of the coherency matrix. However, it is noted that this method presupposes that each scatter mechanism is equally affected by slope while, in fact, the proportions of surface, volume and double bounce, scattering are affected by slope and, moreover, these proportions are polarisation dependent. Therefore, future developments should address the complex interplay between look angle, topography and land cover. Atwood et al. (2012) also states that such an approach would entail an *a priori* knowledge of the land cover classification.

The notion that a single-model is not sufficient is not new. Teillet et al. (1985); Hinse et al. (1988) and Bayer et al. (1991) state that slope corrections must be class specific and introduced terrain type dependent correction functions. These simple and local incidence angle dependent corrections should be applied on pre-classified images. Stussi et al. (1995) remarks that relationships are polarisation and frequency dependent. Franklin et al. (1995) states that a single formulation is unlikely to adequately cover the whole range of topographic effects and that stratification may be needed. In Sun et al. (2002) several models were used, none of them capable of dealing with the whole range of variation. In Leclerc et al. (2001) a single semi-empirical model was used, however, it was noted that a single-model is unlikely to cover all types of terrain. Separate models would be needed, for example for terrain behaving as a Lambertian surface or terrain with a specular surface.

A single semi-empirical model with diffuse-Lambertian and specular components was used by Goering et al. (1995) for ERS-1 scenes of an Arctic landscape. The reduction of slope effects was demonstrated by comparing ascending and descending passes. It was noted that the proportions of the two model components depends on terrain characteristics, thus suggesting a stratification of the area. A semi-empirical radiative transfer model with a single parameter describing the optical thickness that should be tuned to local conditions was introduced by Castel et al. (2001). Encouraging results were obtained except for very steep slopes and open canopies. The effects of topography on backscatter mechanism change, and its dependence on frequency band and polarisation, were discussed by many authors

(van Zyl et al. 1993; Luckman 1998; Franklin et al. 1995). In summary, there is a general consensus that a single-model will not suffice to describe SAR radiometric slope effects. The need for a multi-model approach was mentioned frequently and sometimes the need for stratification or pre-classification was indicated. However, practical solutions for such an approach were never offered.

In this paper an approach is introduced that can handle a wide range of terrain and topographic conditions. Moreover, a practical solution for the implementation of the stratification is offered.

Section 2 describes the observation geometry, derives the exact solutions for normalization according Hoekman (1990) and Ulander (1996), and shows their relation. Under certain conditions these normalizations may be sufficient. In Section 3 two small case studies are used to illustrate that certain land cover types and polarisations require additional corrections. A semi-empirical approach to accomplish this is introduced. The complete correction follows from successive application of the general applicable physical normalization model and the class and polarisation dependent semi-empirical model. Section 4 discusses two approaches to implement the stratification. To illustrate its feasibility a fully multi-model corrected SAR image is shown. The large accuracy improvement obtained for biomass estimation of sparse vegetation cover is discussed.

## 3.2 Theory

### 3.2.1 Observation geometry and definitions

#### 3.2.1.1 Radar geometry

The radar look direction can be described by *two angles*: the (nominal) incidence angle  $\theta_i$  and the range (or look) direction  $\phi_i$ . The incidence angle  $\theta_i$  is defined as the angle between the flat earth's normal direction and backscatter direction, and increases with range distance. The range direction is the angle in the horizontal plane with respect to true North, and varies with latitude. For side-looking radar in near-polar orbit, the variation of  $\phi_i$  near the equator is very small. For the PALSAR FBD image of Guyana used here the incidence angle range is  $36.6^\circ - 40.9^\circ$ , while the look direction is East, closely around  $78.1^\circ$  with respect to North (for more details see Section 3.3.1).

#### 3.2.1.2 Terrain geometry

The terrain geometry is modelled by a DEM, such as the SRTM DEM. It can be described by *two angles*: the slope steepness angle  $\alpha_s$  and the slope aspect angle (uphill direction)  $\phi_s$  relative to true North. Note that these values follow from the height values of a pixel and its neighbouring pixels by interpolation. Methods commonly used include cubic interpolation, cubic spline interpolation or Lanczos interpolation (Conejero 2011).

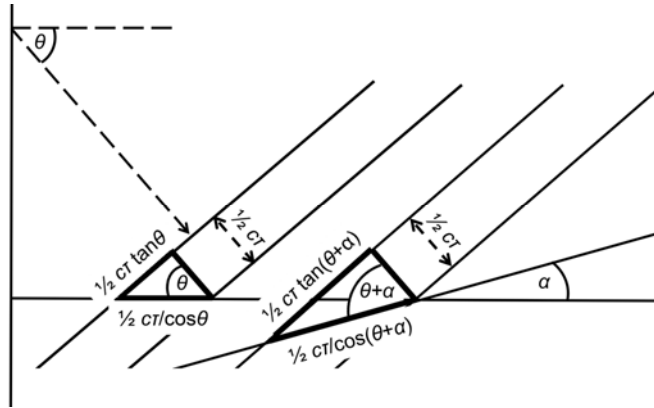


**Figure 3.1** Geometry of resolution cell in range direction: for flat terrain (left triangle) and facing slope (right triangle). The angle of slope steepness in range direction is  $\alpha$  (or  $\alpha_r$ ); the incidence angle  $\theta_i$  equals  $90^\circ - \theta$ , as is illustrated in Figure 3.2; the range resolution is  $\frac{1}{2} c \tau$  (or half pulse length; where pulse length is the product of speed of light  $c$  and pulse duration  $\tau$ ).

### 3.2.1.3 Model geometry

To describe radar backscatter relative to the terrain these four angles can be reduced to three angles. These are the above-mentioned  $\theta_i$  and  $\alpha_s$ , and the slope direction relative to range (or look) direction  $\phi_r$ :

$$\phi_r = \phi_i - \phi_s \quad (3.1)$$

In addition two dependant angles should be defined (depending on  $\alpha_s$  and  $\phi_r$ ), which are the slope steepness angle in range direction:  $\alpha_r$  which follows from

$$\tan(\alpha_r) = \tan(\alpha_s) \cos(\phi_r) \text{ or } \alpha_r = \arctan(\tan(\alpha_s) \cos(\phi_r)) \quad (3.2)$$

and the slope steepness angle in azimuth direction:  $\alpha_{az}$  which follows from

$$\tan(\alpha_{az}) = \tan(\alpha_s) \sin(\phi_r) \text{ or } \alpha_{az} = \arctan(\tan(\alpha_s) \sin(\phi_r)) \quad (3.3)$$

Now, the local incidence angle  $\theta_\Delta$ , defined here as the angle between the backscatter direction and the (tilted) surface normal direction, can be described as:

$$\cos(\theta_\Delta) = \cos(\alpha_{az}) \cos(\theta_i - \alpha_r) \quad (3.4)$$

Note that in case the surface is not tilted (i.e.  $\alpha_{az} = \alpha_r = 0$ ,  $\theta_\Delta = \theta_i$ ).

### 3.2.2 Physical reference models for isotropic scattering

The modulation of backscatter by terrain slope depends on terrain type. Backscatter will be described by the backscattering coefficient  $\gamma^0$  ( $\gamma^0 = \sigma^0/\cos(\theta_i)$ ;  $\sigma^0$  is the normalised radar cross section). The ratio between backscatter on tilted terrain  $\gamma^0$  and the backscatter on flat terrain  $\gamma_f^0$  can be modelled using physical models of the terrain-wave interaction.

There are two models of particular relevance, which can be regarded as reference models. The first describes the terrain as an opaque volume of isotropic scatterers, with a constant scatterer density per volume unit Hoekman (1990). The second describes the terrain as a surface of isotropic scatterers, with a constant scatterer density per (tilted) surface unit Ulander (1996). The relief modulation factors for these two reference models simply follow from the geometry of a resolution cell in range direction, as depicted in Figure 3.1.

For reference Model 1,

$$\gamma^0 = \gamma_f^0 \frac{\tan(90^\circ - \theta_i + \alpha_r)}{\tan(90^\circ - \theta_i)} = \gamma_f^0 N_1(\theta_i, \alpha_r) \quad (3.5)$$

which is the ratio between the observed volume on tilted terrain in a particular range cell (right triangle in Figure 3.1) and the volume that would have been observed in case the terrain is flat (left triangle in Figure 3.1). The volume equals the illuminated area (within the resolution cell) multiplied by the penetration depth in a direction normal to the surface of this volume. Consequently, this penetration depth depends on the orientation of the surface of the volume element with respect to the backscatter direction. Note that this ratio equals the ratio of the surfaces (of these volumes) as projected in the backscatter direction.

For reference Model 2,

$$\gamma^0 = \gamma_f^0 \frac{\cos(90^\circ - \theta_i)}{\cos(\alpha_{az})\cos(90^\circ - \theta_i + \alpha_r)} = \gamma_f^0 N_2(\theta_i, \alpha_r, \alpha_{az}) \quad (3.6)$$

which is the ratio between the observed tilted surface in a particular range cell (right triangle in Figure 3.1) and the surface that would have been observed in case the terrain is flat (left triangle in Figure 3.1). In this case the tilt in azimuth direction has to be included, which accounts for the extra factor  $\cos(\alpha_a)$  in the denominator of Eq. 3.6.

These two reference models normalise the backscatter of tilted terrain in different ways. It can be shown that the normalization of reference Model 1 equals the normalization of reference Model 2 when the latter is multiplied by a factor  $\cos(\theta_A)/\cos(\theta_i)$ .

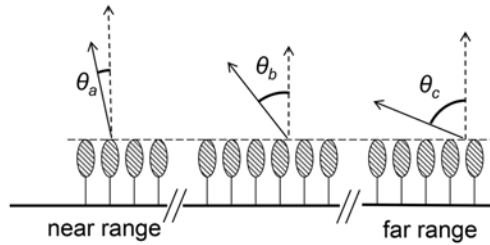


**Figure 3.2a** Example of change in scattering mechanism in (open) forest as a function of incidence angle: (a) At near range the incidence angle  $\theta_i = \theta_a$  is small, the vertical penetration depth is large, and the soil surface may be visible through openings in the canopy. (b) At medium incidence angle  $\theta_i = \theta_b$  the vertical penetration is less, but may be sufficiently high to cause a strong contribution from double bounce scattering between soil surface and trunk. (c) At far range the incidence angle  $\theta_i = \theta_c$  is large and the vertical penetration depth can be low; backscatter may originate from the crown layer exclusively.

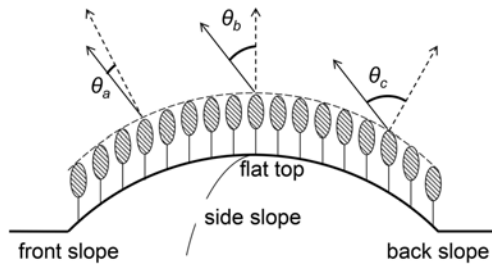


**Figure 3.2b** Example of change in scattering mechanism in (open) forest as a function of local incidence angle: In comparison with flat terrain, changes in backscatter mechanisms in hilly terrain can occur at short distances, even at identical incidence angles. Moreover, backscatter mechanisms can differ from those found on flat terrain. (a) At the front slope the local incidence angle  $\theta_{\Delta} = \theta_a$  can be small, and the vertical penetration depth can be large, however, the double bounce contribution is absent because of the tilt of the soil surface. (b) At the flat top the local incidence angle  $\theta_{\Delta} = \theta_b$  has a medium value and the double bounce contribution is present. However, at the side slope similar values for the local incidence angle are found, but here the double bounce contribution is absent. (c) At the back slope the local incidence angle  $\theta_{\Delta} = \theta_c$  has a large value, the vertical penetration can be low, and, even though the double bounce contribution is absent, the situation may be comparable to the flat terrain case where the incidence angle  $\theta_i = \theta_c$ .

### 3.2.3 Semi-empirical models for non-isotropic scattering

The reference models normalise the backscatter for the slope-induced variation in the amount of scatterers per resolution cell. In addition, as is illustrated in Figure 2 for an open forest area, slopes can also change the type of scattering. Open forest, as compared to closed forest, features increased exposure of trunks and soil surface through gaps. In uniform flat terrain the backscatter changes slowly as a function of incidence angle (Figure 3.2a). In uniform hilly terrain backscatter can change over short distances because the backscatter mechanism also depends on the two slope steepness angles (Figure 3.2b). The latter is also true when normalization for the amount of scatterers (with one of the reference models) already has taken place.

There are two exceptions, both related to the two theoretical cases described above. For an opaque isotropic volume scatterer the backscatter is independent of incidence angle in flat terrain, and stays independent of incidence angle and the two slope angles after normalization with reference Model 1. The same is true for a theoretical isotropic surface scatterer on flat terrain, or on hilly terrain after application of reference Model 2. In real SAR images the first case is well approximated by many closed canopy forests on hills, and is very common. Good approximations of the second case in real SAR images, to the authors' knowledge, are rare. In general, backscattering is non-isotropic, meaning that the two reference models not suffice to describe the slope induced backscatter variation found in hilly terrain with uniform land cover. To describe non-isotropic behaviour an extra modulating factor  $M$  is introduced here as:

$$\gamma^0 = \gamma_f^0 N_1(\theta_i, \alpha_r) M_1(\theta_i, \alpha_r, \alpha_{az}) \quad (3.7)$$

$$\text{or } \gamma^0 = \gamma_f^0 N_2(\theta_i, \alpha_r, \alpha_{az}) M_2(\theta_i, \alpha_r, \alpha_{az}) \quad (3.8)$$

It is noted that since the normalization factors  $N$  for reference models 1 and 2 differ by a factor  $\cos(\theta_\Delta)/\cos(\theta_i)$  the corresponding modulation factors  $M$  differ by the reverse, i.e. by a factor  $\cos(\theta_\Delta)/\cos(\theta_i)$ . In this paper the semi-empirical two-step approach, i.e. the product  $N_1M_1$  (or the identical product  $N_2M_2$ ) is referred to as Model 3.

### 3.3 Case studies

#### 3.3.1 Rupununi Savannah, Brazil

##### 3.3.1.1 Test site and radar data

A small case study is appropriate to elucidate the theory and its ramifications. The selected 27 km x 21 km study area is located in the Rupununi savannah in Brazil near the Pakaraima Mountains and near the border with Guyana (59.60W; 4.03N). It features mountainous areas with dense closed canopy forest and open woodland; and flat areas with grassland. The vegetation in the adjacent Guyanese part of this area is described by Huber et al. (1995) as tall/medium pre- and lower montane evergreen forest, with forest height in the range of 24 m – 36 m, and terrain height up to 800 m, and as upland shrub savannah, up to 5 m tall. The selected radar image is a fine beam dual-polarisation PALSAR image acquired at August 13, 2009. The SRTM 3 arc-second (90 m) DEM was used to derive slope angles. The slopes in this area are relatively long and steep, with slope angles up to 25, and slope direction distribution. The error in slope angle for low curvature terrain depends on the

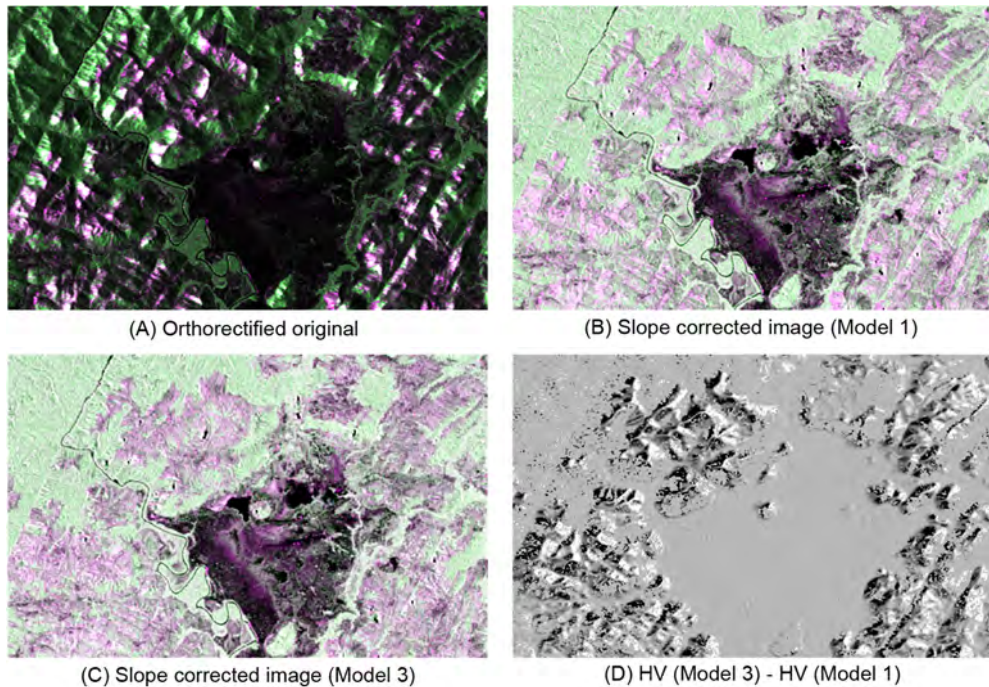


**Figure 3.3** Original and slope corrected PALSAR FBD images. (A) Orthorectified original; (B) Slope corrected image using Model 1; (C) Slope corrected image using Model 3; (D) Model 3 HV minus Model 1 HV backscatter difference. In image a, b and c the HH backscatter ( $\gamma^0$ ) is in the range of -15.8 dB to -5.8 dB (magenta) and the HV backscatter ( $\gamma^0$ ) is in the range of -22.3 dB to -12.3 dB (green). In image d the HV backscatter difference is in the range of -1.0 dB to 0.4 dB (grey). The area shown is a 22 km x 14.3 km area located in the Rupununi savannah in Brazil, featuring (in image c) dense hilly forest (green), hilly woodlands (shades of magenta), and flat grasslands (dark). Date of acquisition is August 13, 2009. PALSAR data courtesy: ALOS K&C © JAXA/METI.

relative height error for SRTM (Brown et al. 2005) and the interpolation technique used and is estimated at about 1 degree.

A section of this radar image is shown in Figure 3.3A. In this image the facing slopes are very bright. After normalization using reference Model 1 (or  $N_1$ ) the different land cover types show up clearly in Figure 3.3B: forest in green, woodlands in purple, and the grassland savannah in black.

### 3.3.1.2 Modelling results

The effect of normalization ( $N_1$ ) for a section of the woodland area, for HH polarisation, is shown graphically in Figure 3.4. Numerical results for woodland (in HH polarisation) are summarized in Table 3.1, as well as results for woodland in HV polarisation and forest (HH and HV polarisation). These results are described as follows.

The selected woodland and forest sections are sufficiently large to cover the complete range of slope aspect angles ( $\phi_s$ ) and slope steepness angles ( $\alpha_s$ ). Figure 3.4 shows backscatter as a function of slope aspect ( $\phi_s$ ; left column) and slope steepness in range ( $\alpha_r$ ; right column). Backscatter dependency as a function of slope aspect shows a sinusoidal type of behaviour with the maximum backscatter when uphill direction and radar look direction match. This effect is arbitrarily quantified by the amplitude ( $A$ ) of the sine best fitting the data. Backscatter dependency as a function of slope steepness in range shows a linear type of behaviour, with negative values for the back slope, and positive values for the facing slope. This effect is arbitrarily quantified by the slope ( $S$ ) of a straight line best fitting the data. The values  $A$  and  $S$  are summarized in Table 3.1, together with the mean ( $m$ ) and standard deviation ( $sd$ ) of the data. These four values are used to evaluate the performance of the models. For a good model  $A$  and  $S$  should decrease to a value approaching zero, while the  $sd$  of the backscatter should decrease to a value approaching the  $sd$  of the same land cover type on flat terrain.

Table 3.1 shows the following results for Model 1 ( $N_1$ ) and Model 2 ( $N_2$ ). For forests Model 1 is clearly better than Model 2. For HV polarisation Model 1 is near perfect. For HH polarisation small values for  $A$  (0.21 dB) and  $s$  remain, which in most practical cases may be acceptable. Though Model 2 also gives a large improvement, slope effects are still prominent. This result may be expected because dense closed forest acts as a volume scatterer, especially for HV polarisation. Also for woodland Model 1 is clearly better than Model 2. However, even for Model 1 the remaining slope effects are too large to be acceptable ( $A$  is 1.77 dB for HH polarisation, and 0.58 dB for HV polarisation). It can be noted that the offset in mean backscatter level is much lower for Model 1 as compared to Model 2. The effect of applying Model 1 is well illustrated by comparing the images in Figure 3.3A and Figure 3.3B.

**Table 3.1** Slope effect statistics for forest and woodland for HH and HV polarisation (HH and HV pol.) at the Rupununi test area. Mean backscatter ( $m$ ); standard deviation of backscatter ( $sd$ ); backscatter increase per degree slope steepness in range ( $s$ ); amplitude of backscatter modulation as a function of slope aspect angle ( $A$ ); for original data, after application of Model 1 ( $N_1$ ), Model 2 ( $N_2$ ) and (woodland only) Model 3 ( $N_3/M_1$ ).

Forest									
HH pol.	$m$	$sd$	$s$	$A$	HV pol.	$m$	$sd$	$s$	$A$
Original	-9.58	2.76	0.1840	3.61	Original	-14.00	2.57	0.1727	3.36
Model 2	-10.14	1.43	0.0664	1.36	Model 2	-14.56	1.23	0.0551	1.15
Model 1	-9.71	1.05	0.0061	0.21	Model 1	-14.13	0.93	-0.0052	-0.03
Woodland									
HH pol.	$m$	$sd$	$s$	$A$	HV pol.	$m$	$sd$	$s$	$A$
Original	-9.01	3.89	0.2634	5.15	Original	-17.18	3.15	0.2046	3.96
Model 2	-9.55	2.49	0.1450	2.93	Model 2	-17.72	1.85	0.0862	1.76
Model 1	-9.07	1.92	0.0824	1.77	Model 1	-17.24	1.54	0.0236	0.58
Model 3	-9.32	1.55	-0.0008	0.06	Model 3	-17.50	1.46	-0.0050	0.01

Results for Model 1 for woodland in HH polarisation are shown graphically in Figure 3.4 (middle row). The next step is the development of Model 3, which is either the product  $N_1M_1$  or the identical product  $N_2M_2$ . Since (in this case)  $N_1$  performs better and is already sufficient for forests, it is easier to use  $N_1$ , determine  $M_1$  for woodland, and set  $M_1$  for forest to unity.

$M_1$  introduced in Eq. 3.7 can be written as the ratio between two identical functions of the incidence angle and the two slope angles where, for the function in the denominator, the two slope angles are set to zero (Eq. 3.9).

$$M_1(\theta_i, \alpha_r, \alpha_{az}) = \frac{f(\theta_i, \alpha_r, \alpha_{az})}{f(\theta_i; \alpha_r=0, \alpha_{az}=0)} \quad (3.9)$$

The function in the nominator should be fitted from image data after normalisation  $N_1$  is applied. In the next a simple heuristic procedure to achieve this is suggested, which proved to be very efficient (also for other land cover classes in other images). The first step is to take a data sample representative for the land cover class comprising the whole range of variation for the two slope angles  $\alpha_r$  and  $\alpha_{az}$ , in such a way that the incidence angle variation is small (e.g. less than  $1^\circ$ ). The second step is to plot the data sample as a function of the local incidence angle  $\theta_\Delta$  and fit a function of the form:

$$f_\Delta = \cos^a(\theta_\Delta) + c \cdot \cos^b(\theta_\Delta) \quad (3.10a)$$

The third step is to use Eq. 3.10a as a preliminary version of  $f$ , apply the preliminary Model 3 ( $N_1M_1$ ), plot the data as a function of the slope angle in azimuth  $\alpha_{az}$ , and fit the residual slope dependence with a function of the form:

$$f_{az} = \cos^d(\alpha_{az}) \quad (3.10b)$$

This completes the procedure and  $f$  can be written as the product of two marginal functions:

$$f = f_\Delta \cdot f_{az} \quad (3.10c)$$

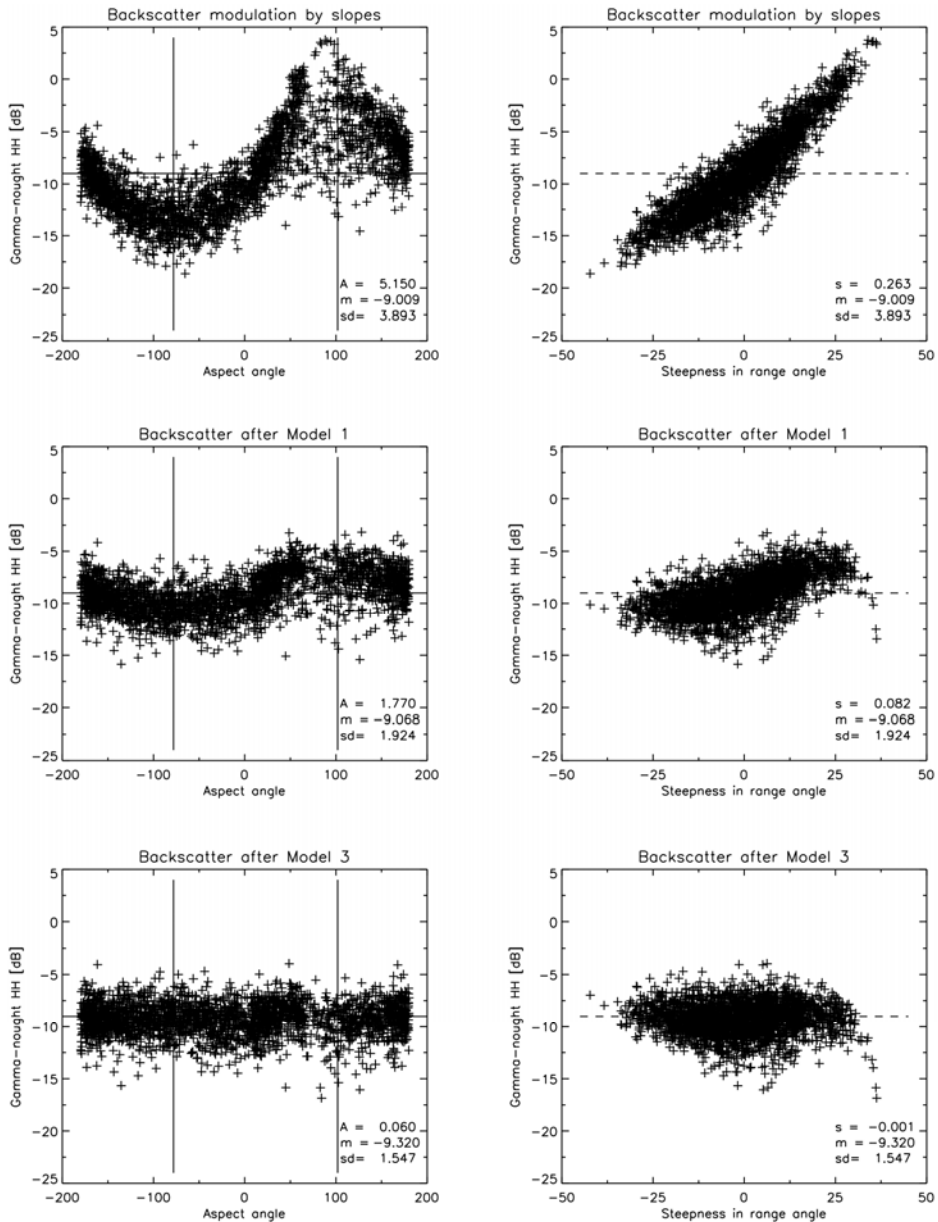


**Figure 3.4** HH backscatter ( $\gamma$ -axis) for woodlands as a function of aspect (left column) and steepness in range angles (right column) for: (top row) original data; (middle row) after correction for isotropic opaque volume scattering (or Model 1;  $N_i$ ), and; (bottom row) after tuning for additional (anisotropic) scattering effects (or Model 3;  $N_iM_j$ ). The vertical lines in the left three images indicate the backscatter and forward scattering directions; the horizontal lines in all six images indicate the mean backscatter level in the original data. The numbers in the bottom left stand for amplitude (A), slope (s), mean (m), and standard deviation (sd) of the backscatter coefficient  $\gamma$  [dB]. The parameters A and s are defined in the text.

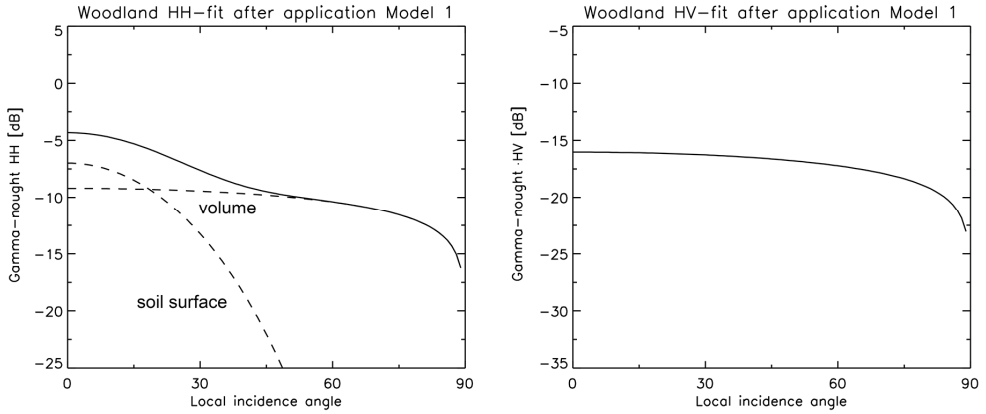


**Figure 3.5** After normalization for the variation in the amount of scatterers using reference Model 1, the backscatter of woodland still has a dependency on the slope angles caused by a change in scattering behaviour. This dependency can be modelled by simple semi-empirical relationships. (Left) The dependency as a function of local incidence angle for HH polarisation can be modelled as the sum of a medium rough soil surface component (prominent at small angles) and a volume component (relatively angle independent). (Right) For HV polarisation the surface component is negligible, while the volume component is comparable in shape, but has a lower level. Backscatter is shown in dB.

The shape of  $f_{\Delta}$  has similarities with the shape of the backscatter as a function of incidence angle (on flat terrain) as can be seen in Figures 3.5. For HV polarisation, where backscatter mainly originates from volume scattering, the angular response is flat, with a drop at high angles. For HH polarisation there is an additional strong component from the soil surface, which is much stronger at steep incidence angles, and decreases much faster. Backscatter behaviour of flat terrain is well known and usually can be described well with a function of the type  $f_{\Delta}$ .

The final results are the following. For woodland, for HH polarisation:

$$f = f_{HH} = \left( \cos^{10}(\theta_{\Delta}) + 0.60 \cdot \cos^{0.4}(\theta_{\Delta}) \right) \cdot \cos^{-2.0}(\alpha_{az}) \quad (3.11a)$$

and  $M_i$  follows (using Eq. 3.9) as

$$M_1 = M_{1,HH} = \frac{\cos^{10}(\theta_{\Delta}) + 0.60 \cdot \cos^{0.4}(\theta_{\Delta})}{\cos^{10}(\theta_i) + 0.60 \cdot \cos^{0.4}(\theta_i)} \cdot \cos^{-2.0}(\alpha_{az}) \quad (3.11b)$$

For woodland, for HV polarisation:

$$f = f_{HV} = \cos^{0.4}(\theta_{\Delta}) \cdot \cos^{-2.0}(\alpha_{az}) \quad (3.11c)$$

For forest, for HH and HV polarisation:

$$f = f_{HH} = f_{HV} = 1 \quad (3.11d)$$

Using these final results for  $M_i$ , the Model 3 ( $N_iM_i$ ) can be applied. Table 3.1 shows that the slope dependence for woodlands (expressed by the parameters  $A$  and  $s$ ) is now almost completely removed. This is shown graphically in the bottom row of Figure 3.2 (for HH polarisation); and in the image in Figure 3.3C. Section 3.4 of this paper will discuss how the image in Figure 3.3C is made. The improvement obtained by Model 3 is nicely illustrated in Figure 3.3D, which shows the difference of Model 1 (Figure 3.3B) and Model 3 (Figure 3.3C) for HV polarisation. In forest areas there is no difference because Model 1 suffices; for the grassland savannahs there is no difference because the terrain is flat; but for the woodlands a prominent residual pattern shows up.

### 3.3.1.3 Evaluation for Rupununi test site

Application of Model 3 obviously is far more complex than application of Model 1 (see also Section 3.4). Comparing Figure 3.3B and Figure 3.3C shows that the images are almost identical, and for some applications the normalization provided by Model 1 may be sufficient. The only clear differences occur on the steep slopes of the woodlands. This effect may be quantified as follows. In case  $\alpha_{az} = 0$  the error (defined here as the difference between Model 3 and Model 1) is less than  $\pm 0.1$  dB when  $\alpha_r$  is in the range of  $-1.01^\circ$  to  $+0.96^\circ$  for HH polarisation and  $-3.84^\circ$  to  $+4.45^\circ$  for HV polarisation. In case  $\alpha_r = 0$  the error is less than  $\pm 0.1$  dB when  $\alpha_{az}$  is in the range of  $\pm 16.7^\circ$  for HH polarisation and  $\pm 9.7^\circ$  for HV polarisation. In other words: (a) steep slopes in range are much more problematic than steep slopes in azimuth and; (b) the effects are much larger for HH polarisation than for HV polarisation. The latter result is a consequence of the better performance of Model 1, i.e. the better compliance to a volume scattering model, for HV polarisation. The former result confirms the appropriateness of making the fit of  $M_i$  for slope angle in range direction (Eq. 3.10a), before the fit for slope angle in azimuth direction (Eq. 3.10b).

## 3.3.2 Lololo Fiji Pine site, Fiji Islands

### 3.3.2.1 Test site and radar data

A second case study in an area with entirely different land cover characteristics is used to evaluate the validity and portability of the approach. The second test site is a softwood forest plantation (*Pinus caribaea*) located in the north-western part of the Viti Levu Island, Fiji (Lat.  $17.32^\circ$  S, Lon.  $177.37^\circ$  E) managed by Lololo Fiji Pine Ltd. Detailed spatial inventory data of 623 forest stands (9570 ha) is available for this concession, comprising exact information on forest extent and logging activities. Fully-grown pine stands without any logging activities during the last 15 years were selected as forest reference data. Recently logged (within the last year) areas were

selected as non-forest reference data. These non-forest areas comprise a mix of grassland, exposed rocks and bare soil. The terrain in the 10 km x 10 km test site is very rugged with elevations between 10 m and 570 m and slopes up to 48 degrees. For the reference data slopes are up to 40 degrees. The ALOS PALSAR Fine Beam Dual-Polarisation image dates from September 29, 2010, and has the same incidence angle range as for the Rupununi test site. Use is made of a local 30 m DEM. This allows processing at 25 m pixel size while for Rupununi, where only the 90 m SRTM DEM was available, processing was done at the 50 m pixel size.

### 3.3.2.2 Modelling results

Like for Rupununi, the selected pine forest and grassland areas are sufficiently large to cover the entire range of slope aspect angles and slope steepness angles. Results are summarised in Table 3.2. The backscatter level of the Fiji pine forest is much lower than the level of the Rupununi forest but has almost the same high HVHH-ratio (-4.58 dB for Fiji and -4.42 dB for Rupununi). Such a high HVHH-ratio is indicative for a pure volume scatterer. The backscatter level of the Fiji grasslands is much lower than the level of the Rupununi woodland but, again, has almost the same low HVHH-ratio (-8.1 dB for Fiji and -8.2 dB for Rupununi). Such a low HVHH-ratio is indicative for areas with a much lower fraction of volume scattering. The level of standard deviation is much higher for the Fiji cases because processing was done at 25 m, which results in a much higher speckle level. The modelling results are comparable. For pine forest Model 1 suffices to yield good slope correction results. For grasslands additional slope corrections using Model 3 are necessary. The grasslands areas show up well in Figure 3.6D, which shows the difference of Model 1 (Figure 3.6B) and Model 3 (Figure 3.6C) for HH polarisation. Figure 3.6A shows the original image. Section 4 will discuss how the image in Figure 3.6C is made. The values of the fitting parameters  $a$ ,  $b$ ,  $c$  and  $d$  in Eq. 3.10a-c and 3.11a-c for Fiji grassland are exactly the same as for Rupununi woodland.

**Table 3.2** Slope effect statistics for pine forest and grassland for HH and HV polarisation (HH and HV pol.) at the Fiji test area. Mean backscatter ( $m$ ); standard deviation of backscatter ( $sd$ ); backscatter increase per degree slope steepness in range ( $s$ ); amplitude of backscatter modulation as a function of slope aspect angle ( $A$ ); for original data, after application of Model 1 ( $N$ ) and (grassland only) Model 3 ( $N;M$ ).

Pine forest									
HH pol.	$m$	$sd$	$s$	$A$	HV pol.	$m$	$sd$	$s$	$A$
Original	-11.19	3.19	0.1618	3.15	Original	-15.77	2.95	0.1387	2.69
Model 1	-10.27	2.44	-0.0066	0.21	Model 1	-14.86	2.40	-0.0297	-0.24
Grassland									
HH pol.	$m$	$sd$	$s$	$A$	HV pol.	$m$	$sd$	$s$	$A$
Original	-13.77	4.16	0.2495	4.03	Original	-21.91	3.56	0.1812	2.86
Model 1	-13.61	3.17	0.0796	1.55	Model 1	-21.75	2.90	0.0113	0.36
Model 3	-13.72	2.99	-0.0111	0.15	Model 3	-21.82	2.93	-0.0163	-0.04

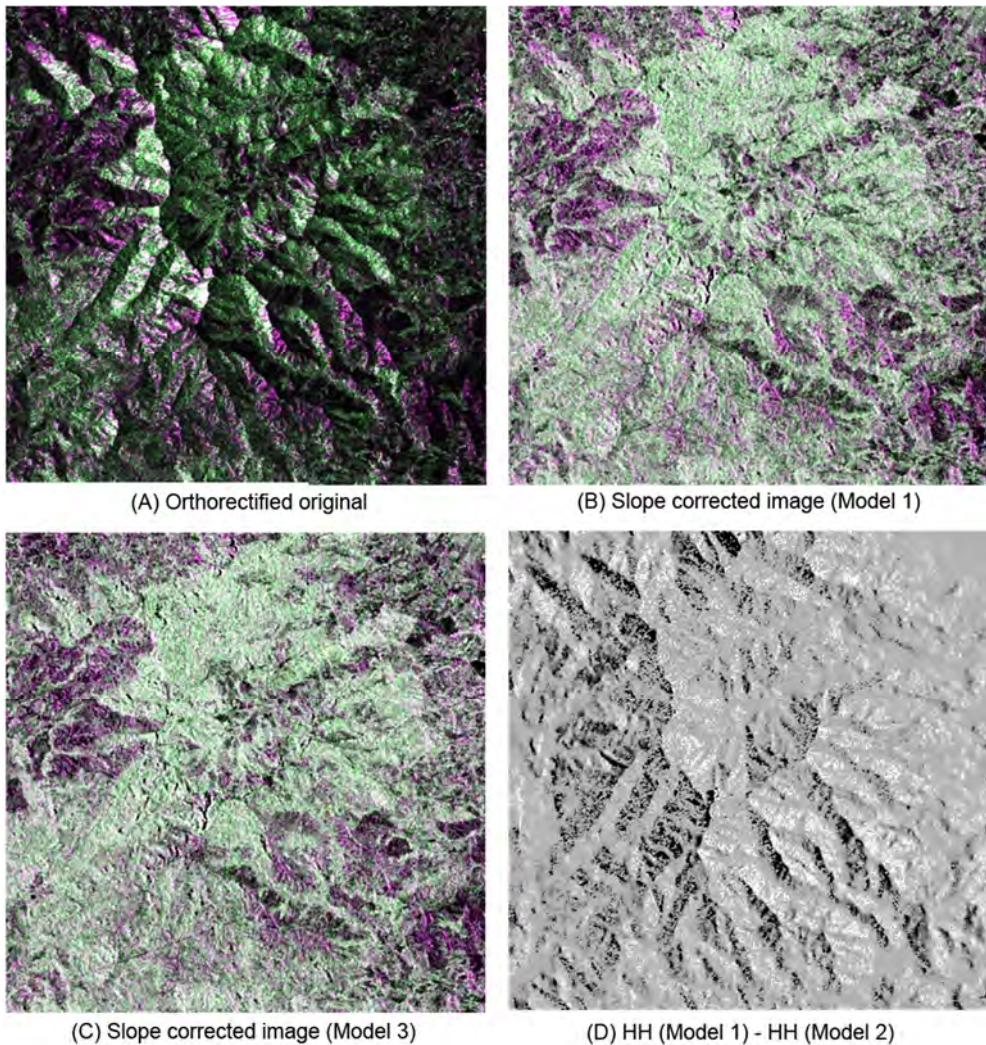


**Figure 3.6** Original and slope corrected PALSAR FBD images. (A) Orthorectified original; (B) Slope corrected image using Model 1; (C) Slope corrected image using Model 3; (D) Model 3 HH minus Model 1 HH backscatter difference. The area shown is a 10 km x 10 km area located in the Lololo Fiji Pine estate in Fiji, featuring (in image c) dense pine forest (green) and hilly grasslands (shades of magenta). Date of acquisition is September 29, 2010. PALSAR data courtesy: ALOS K&C © JAXA/METI.

Slightly different values do not cause noticeable overall effects, and better fits cannot be obtained with other values. The reason identical values for the fitting parameters are obtained for an entirely different land cover class may be related to a similarity in the fraction of the volume scattering component, for which the identical HVHH-ratio is an indication.

### 3.3.3 Steps of fitting procedure

The procedure to fit the parameters  $a$ ,  $b$  and  $c$  in Eq. 3.10a and parameter  $d$  in Eq. 3.10b, both for Rupununi and Fiji, has been the following:

- Step 1: Apply Model 1 to all data.
- Step 2: Select data that sufficiently covers the entire range of slope aspect angles and slope steepness angles for each land cover type to be modelled.
- Step 3: Plot backscatter data corrected by Model 1 as a function of the slope angle in range direction and use Eq. 3.10a to fit parameters  $a$ ,  $b$  and  $c$  (for each land cover type).
- Step 4: Apply Model 3 (with a default value for parameter  $d$ ), for each land cover type separately.
- Step 5: Plot backscatter data corrected by Model 3 (with default value for  $d$ ) as a function of slope angle in azimuth direction and use Eq. 3.10b to fit parameter  $d$  (for each land cover type).

## 3.4 Application approaches

### 3.4.1 Classification

For a uniform land cover class on flat terrain the backscatter level  $\gamma^0$  has a mean  $\overline{\gamma^0}$  and a stochastic variation depending on speckle and textural characteristics. This is usually described with a probability density function, which is used in classification procedures or biophysical parameter estimation procedures. In case there is a significant incidence angle range between near and far range and the incidence angle effects cannot be ignored, this is usually described by a modulation of  $\overline{\gamma^0}$  as  $\overline{\gamma^0} = \overline{\gamma^0}(\theta_i)$ . When, in addition, slope effects cannot be ignored the modulation can be described as  $\overline{\gamma^0} = \overline{\gamma^0}(\theta_i, \alpha_r, \alpha_{az})$ . This modulation is class and polarisation dependant and can be modelled as described in the previous two sections. Several approaches to handle slope effects can be followed. Since the polarisation, incidence angle and the two slope angles are known, the only unknown is the land cover class. Land cover class in this context should be understood in its relation to its slope modulating behaviour. With respect to the theory introduced three fundamentally different situations exist:

- (i) The terrain is flat. For example, a coastal plain with many different wetland classes falls in this category. In this case a single-model for slope modulation, *any model*, or no model at all, would be adequate.

- (ii) The terrain has significant slopes, but all land cover on the slopes has the same modulating behaviour. Land cover on flat parts of the area may have different behaviour. In this case a *single-model* would still be adequate. Often, in case of densely forested terrain, this is Model 1.
- (iii) The terrain has significant slopes, but not all land cover on slopes has the same modulating behaviour, just like the situation in the Rupununi as described above. In this case only a *multi-model* approach would be appropriate.

Situations 1 and 2 can be handled straightforward. Situation 3 is more complicated and can be handled in two different ways. Suppose the objective is to make a land cover map and for each class a slope modulation model has been determined (cf. the procedure outlined in Section 3.3). Then, in case probabilistic classification methods are used, such as Markov Random Field classification, the classification can be done directly. Therefore, in this case, in principal, there is no need to remove slope effects from the image. However, the difficulty is that the slope correction models are based on samples of the relevant land cover classes, which are very hard to delineate on the original image because of the slope effects (as in Figure 3.3A). It would be much easier to make this delineation on the transformed image (as in Figure 3.3C) but this image cannot be made before all slope modulation models are determined. The strength of the methodology proposed in this paper is that the slope modulation is described as a two-step approach. After the first step, i.e. the normalization  $N_1$  (or  $N_2$ ), slope effects are mitigated strongly and, for some classes, even absent (as in Figure 3.3B). The first step is easy to apply, and samples for the development of the models for the second step of the slope modulation ( $M_1$  or  $M_2$ ) can be obtained much easier.

When the slope modulation models are determined the land cover classification can be made. To remove the slope effects from the radar image itself the following approach based on stratification in feature space is suggested. All land cover classes that occur on flat terrain only, such as wetland classes, can be ignored. The remaining classes should have a low degree of overlap in feature space. This is best done after application of Model 1, since it reduces the size of land cover clusters in feature space. Note that the alternative, i.e. Model 2, may give much less reduction (as shown in Section 3). For the example shown in Figure 3.3C the flat savannahs could be ignored and a boundary in HH-HV feature space was drawn between the forest cluster and the woodland cluster. A simple approach would be to apply Model 3 for forest for all pixels that lie on the forest side of this boundary and to apply Model 3 for woodland for pixels at the other side of the boundary. Since there is a small overlap in feature space (i.e. after applying Model 1), and to avoid the introduction of artefacts, a transition zone was designed with a width of  $\pm 0.35$  dB. In this transition zone a weighted mixture of Model 3 for woodland and Model 3 for forest was applied. In case such stratification cannot be made (e.g. when the overlap

is too high) the feature space could be extended (e.g. with an optical image). In case all slope modulations can be removed from the image, the classification can be made in a much simpler way.

For the Fiji test area a simpler stratification procedure was applied based on the HVHH backscatter ratio only. This stratification, at exactly the same levels for the transition zone, would also be appropriate for the Rupununi case.

In summary, there are two classification approaches. (a) No removal of slope effects using class statistics modulated by models of the type  $N_i M_i(\theta_i, \alpha_r, \alpha_{az})$  or global removal of slope effects with a single-model such as Model 1 (or  $N_i$ ) using class statistics modulated by models of the type  $M_i(\theta_i, \alpha_r, \alpha_{az})$ . (b) Multi-model slope effect removal (when this is possible) using class statistics derived from the multi-model transformed image, which have little or none dependence on the angles  $\theta_i$ ,  $\alpha_r$ ,  $\alpha_a$ . The latter method is somewhat different because the image transformation procedures may introduce artefacts but, on the other hand, subtle landscape ecological patterns that would otherwise be obscured by slope effects may now become visible. This actually is the case in Figure 3.3C, where patterns in the woodlands landscape become more pronounced. Both multi-model methods give considerable improvement over the single-model method. In a follow-on paper this will be addressed explicitly and these two multi-model methods will be compared.

### 3.4.2 Biomass estimation

Another type of application of the multi-model approach is the improvement of biomass estimation. A simple example will be given first. Suppose the HV backscatter level is used to estimate biomass, for example as described for PALSAR by Mitchard et al. (2009). When a single-model is used to account for slope effects Model 1 may be the most appropriate choice, since it is near perfect for closed forest. Only a multi-model approach can account for all slope effects the landscape comprises both closed and open types of forest. This is illustrated in Figure 3.3D where the difference between the single-model and multi-model HV images are shown. This difference, only prominent in the woodlands, is the remaining error present in the HV backscatter level. Next, suppose that the same relationship between biomass and HV backscatter exist as given by Mitchard et al. (2009; Figure 3.2), i.e. an approximately 1.34 dB backscatter increase when biomass level doubles. Then, using Eq. 3.11b, on the facing slope, the biomass would be overestimated by 21.6% at a +25° range steepness angle (for a 0° azimuth steepness angle). On the back slope the underestimation is 39.7% at a -25° range steepness angle (at 0° azimuth steepness angle). For example, when the biomass is 50 ton/ha the single-model estimation could deviate between approximately 30 and 60 ton/ha. Similar effects may occur for any open forest type where the relation between backscatter level and biomass is linear. When biomass levels go up, and consequently the canopy closes, the relation is less steep, or even may become 'saturated', the errors are less or absent. At the same time Model 3 would become more similar or identical to

Model 1. In other words, for the single-model approach, in the biomass range where backscatter is most sensitive to biomass variation, the largest errors occur. For P-band this would be at a higher biomass range (Hoekman & Quiriones 2000). Carbon monitoring systems focus on accurate estimation of biomass change, rather than elimination of small systematic errors. In this context it is important to note that the overestimation in range at facing slopes reduces when biomass increases, because the forest becomes a more 'pure' volume scatterer. Consequently, the biomass increase is underestimated for the single-model approach. Vice-versa, biomass increase on back slopes is overestimated. A simple technique to quantify how well single or multi-model approaches eliminate slope effects is to compare images taken from different directions (see also Goering et al. 1995). For PALSAR this could be observations from ascending and descending mode (nearly East and West looking at Equator). These should be near identical for all land cover types on steep slopes.

### 3.5 Discussion and conclusion

The modulation of backscatter by slopes is described by three angles (incidence angle, slope steepness angle in range and slope steepness angle in azimuth), from which the local incidence angle can be derived (Section 3.2.1.3). Many of the radiometric slope correction models to date only use the local incidence angle, and fail to provide good solutions valid for a wide range of terrain type and topographic conditions. The method introduced here is a two-step approach. The first step normalises for slope-induced variation of the amount of scatterers. Since uniform isotropic (volume or surface) scattering is assumed, this step is independent from terrain type, frequency band and polarisation. The second step takes the (variation in) scatter mechanisms into account, and depends on terrain type, frequency band and polarisation. Since the first step already mitigates slope effects to a large extent, depending on the terrain types, the image resulting from application of the first step is a good basis to extract samples to derive the (semi-empirical) models for the second step. Moreover, as was shown, such an image may be used as a basis for stratification to apply a multi-model correction on the image itself. Results (Table 3.1) for an area with slopes up to 25 degrees, show that the remaining slope effects are much smaller than 0.1 dB for the multi-model case (two steps), while for the best single-model case (first step only, model  $N_7$ ) the slope effects can be as large as 1.77 dB (woodland, HH polarisation). The multi-model approach can be used to improve classification (accuracy and number of sub-classes) but is also very important for biomass estimation. In the example given here, in case the first step single-model result was used instead of the multi-model two-step approach, a +20% to -40% error range was estimated for the low biomass open woodland on steep slopes. For dense opaque volume scatterers a simple normalization (the first step, model  $N_7$ ) may be sufficient, especially for HV polarisation. For more open and less opaque vegetation the second-order terrain-type dependent correction is necessary to obtain good biomass estimations. Therefore the longer the wavelength, the more

prominent these effects become. For X- and C-band the effects may be less, however, for P-band, the second-order correction may be necessary for even more land cover types as compared to L-band, and of special concern for ESA's BIOMASS mission (ESA 2012). Since carbon monitoring systems focus on accurate estimation of biomass change, rather than elimination of small systematic errors, it is important to note that over- and underestimation of biomass increase can occur, because the forest changes in a more 'pure' volume scatterer. Combined use of ascending and descending passes or right- and left-looking observations may help to detect such phenomena and may further increase the accuracy of biomass estimation.

A point of concern is the resolution of the SRTM DEM. In areas with long steep slopes such as the Rupununi, the SRTM DEM suffices to get reliable values for the slope steepness angles. However in other areas, such as parts of Borneo, featuring very dissected landscapes with short steep slopes, a higher resolution DEM may be needed. This was also the case for the Fiji test site. Another point of concern is the provision by space agencies of 'terrain-corrected' images or image mosaics. In case a single-model type of radiometric slope compensation was applied (to mitigate slope effects), it is important to provide in addition the model that was used and a data layer with the three angles (such as incidence angle, slope steepness angle in range and slope steepness angle in azimuth). In this way full flexibility is kept and the correction applied can be reversed or extended with a multi-model correction.

## **Acknowledgments**

This work has been undertaken in part within the framework of the ALOS Kyoto & Carbon Initiative. ALOS PALSAR data have been provided by JAXA EORC.

**Chapter**

# **4**

## **Fusing Landsat and SAR time series to detect deforestation in the tropics**

Johannes Reiche, Jan Verbesselt, Dirk H. Hoekman and Martin Herold

*Published in Remote Sensing of Environment, 156 (2015), 276-293,  
DOI: 10.1016/j.rse.2014.10.001*

## **Abstract**

*Fusion of optical and SAR time series imagery has the potential to improve forest monitoring in tropical regions, where cloud cover limits optical satellite time series observations. We present a novel pixel-based Multi-sensor Time series correlation and Fusion approach (MulTiFuse) that exploits the full observation density of optical and SAR time series. We model the relationship of two overlapping univariate time series using an optimized weighted correlation. The resulting optimized regression model is used to predict and fuse two time series. Using the MulTiFuse approach we fused Landsat NDVI and ALOS PALSAR L-band backscatter time series. We subsequently used the fused time series in a multi-sensor change detection framework to detect deforestation between 01/2008 - 09/2010 at a managed forest plantation in the tropics (*Pinus caribea*; 2859 ha). Three-monthly reference data covering the entire study area was used to validate and assess spatial and temporal accuracy. We tested the impact of persistent cloud cover by increasing the per-pixel missing data percentage of the NDVI time series stepwise from ~53% (~6.5 observations/year) up to 95% (~0.5 observation/year) while fusing with a consistent PALSAR time series of ~2 observations/year. A significant linear correlation was found between the Landsat NDVI and ALOS PALSAR L-band SAR time series observables for logged forest. The multi-temporal filtered PALSAR HVHH backscatter ratio time series ( $HVHH_{mt}$ ) was most strongly correlated with the NDVI time series. While for Landsat-only the spatial and temporal accuracy of detected deforestation decreased significantly with increasing missing data, the accuracies for the fused NDVI-PALSAR case remained high and were observed to be above the NDVI- and PALSAR-only cases for all missing data percentages. For the fused NDVI- $HVHH_{mt}$  time series the overall accuracy was 95.5% with a 1.59 month mean time lag of detected changes. The MulTiFuse approach is robust and automated, and it provides the opportunity to use the upcoming data streams of free-of charge, medium resolution optical and SAR satellite imagery in a beneficial way for improved tropical forest monitoring.*

---

## 4.1 Introduction

Forest change is one of the major processes of global land cover change (Foley et al. 2005). In particular tropical regions have been undergoing rapid changes in forest cover since the 1980s (Achard et al. 2010; Achard et al. 2014; Gullison et al. 2007; Hansen et al. 2008; Hansen et al. 2013; Stern 2007; van der Werf et al. 2009). These changes are regarded as one of the major sources of greenhouse gas emissions (Harris et al. 2012; Zarin 2012). Consistent and accurate detection of tropical forest changes is fundamental to reliably estimating greenhouse gas emissions and successful implementation of climate mechanisms such as REDD+ (Herold & Skutsch 2011; Pelletier et al. 2011; UNFCCC 2009). To assess historical and future changes in forest area and carbon stocks, satellite-based remote sensing at medium spatial resolution (10 – 30 m) supported by field observations is the appropriate tool for most tropical countries (De Sy et al. 2012) that currently lack sufficient national forest monitoring capacities (Romijn et al. 2012).

Current and anticipated optical and SAR satellite missions (Figure 4.1) have been listed as core missions by the CEOS Space Data Coordination Group (CEOS 2014). Their aim is to support systematic worldwide forest monitoring by providing long term medium resolution time series data with a free and open data policy (GFOI 2014). There has been some temporal overlap between different optical and SAR satellite systems available for forest change assessments. However, varying overlapping periods, uncoordinated observation strategies, and user-unfriendly data policies and data access procedures have resulted in data from different satellite missions rarely being used in combination to track forest changes in the tropics.

With a data archive spanning over 40 years, Landsat provides the longest and most sophisticated record of medium spatial resolution satellite imagery (Roy et al. 2014). For many tropical countries, very limited or no observations are available for

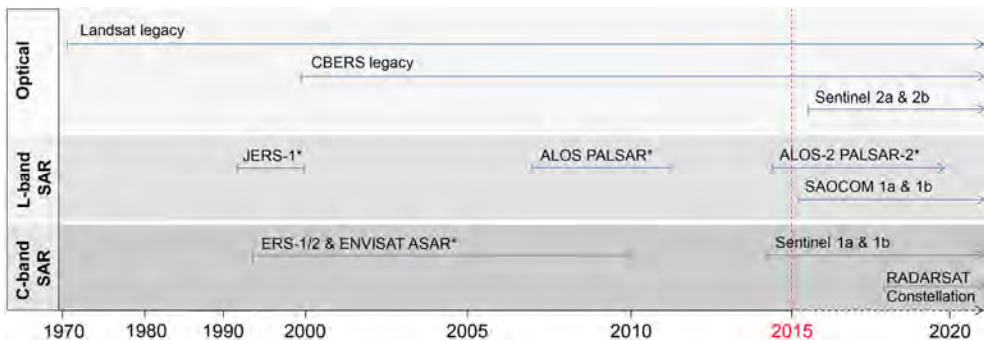


**Figure 4.1** Current and anticipated medium resolution optical and SAR satellite missions selected by CEOS Space Data Coordination Group as core missions to provide time series data in support of worldwide forest mapping. Important missions with non-core status due to restricted data access policy in 2014 are denoted with an asterisk (adapted from CEOS, 2014).

the 1980s and 1990s due to a non-global observation strategy (Goward et al. 2006) and a lack of available ground stations in the past (Arvidson et al. 2006). Since the mid-1990s a number of optical and C- and L-band radar satellite constellations have provided an additional source of time series data. With the Landsat Data Continuous Mission (Irons et al. 2012) and the planned launch of a multiple optical and SAR satellite systems in the next decade, the continuation of these data streams will be ensured and synergy across multiple data sources encouraged. Such efforts on multi-sensor synergies support the clearly defined goal of the responsible space agencies to increase the detail and accuracy of time series to assess forest changes in the tropics (Drusch et al. 2012; Irons et al. 2012; Suzuki et al. 2013; Torres et al. 2012). After the opening of the Landsat archive (Woodcock et al. 2008) many studies demonstrated the operational capabilities of optical medium resolution satellite imagery for detecting changes and trends in forest cover from local to global scales (Achard et al. 2014; Carreiras et al. 2014; Griffiths et al. 2013; Hansen et al. 2013; Hirschmugl et al. 2014; Huang et al. 2010; Kennedy et al. 2010; Lehmann et al. 2013; Margono & Turubanova 2012; Margono et al. 2014; Schmidt et al. 2013; Potapov et al. 2012; Zhu et al. 2012; Zhu & Woodcock 2014). The main limitation of optical remote sensing methods in tropical regions is the restricted data availability due to frequent cloud cover (Asner 2001; Hirschmugl et al. 2014; Souza et al. 2013). In fact, some tropical countries experience cloud cover exceeding the long-term yearly average frequency of 80% (Herold 2009). Persistent cloud cover inhibits full optical coverage from Landsat-like sensors even when compositing is performed over a period of 1 - 2 years (Reiche et al. 2013; Souza et al. 2013). Overcoming this problem in forest change monitoring is still an open research issue (Romijn et al. 2012) that requires deliberate attention in order to provide more accurate and spatially consistent forest activity data which is key to making climate mechanisms such as REDD+ viable (Pelletier et al. 2011).

The increasing availability of freely available time series data for large areas provides the opportunity to benefit from multiple satellite observation sources. In order to fully realize the potential of these time series and to tackle the problem of frequent cloud cover in the tropics, a shift is needed from traditional bi-temporal change detection approaches (Coppin et al. 2004; Lu et al. 2004), in which many changes are missing and the timing of changes is disregarded, to time series based change detection methods (Hansen & Loveland 2012; Lu et al. 2014) which are capable of exploiting the full temporal detail of available archives (Irons et al. 2012; Verbesselt et al. 2012). A number of methods for analysing the entire temporal detail of optical time series have been introduced in recent years and successfully applied to detect natural and human induced forest change (Kennedy et al. 2010; Potapov et al. 2012; Verbesselt et al. 2010a; Verbesselt et al. 2012; Zhu et al. 2012; Zhu & Woodcock 2014). However, a number of shortcomings have been identified for these methods. First, all introduced methods were demonstrated with imagery from a single optical sensor, and only in areas where a large number of observations

were available. Second, the performance of the methods in tropical regions under persistent cloud cover was not investigated. Finally, annual mapping resolution validated with independent reference was not exceeded. Often the Landsat time series data itself has served as reference data.

Synthetic Aperture Radar (SAR) data are not affected by cloud cover and provide continuous time series information. For most tropical countries, however, the density of C- and L-band observations is low, with only a small number of images available per year (Rosenqvist et al. 2007). Unlike optical sensors, SAR penetrates into the forest canopy and thus returns signal derived from its physical structure. In particular, multi-temporal L-band SAR backscatter provided by JERS (1992 - 1998) and ALOS PALSAR (2006 - 2011) have been proven suitable for detecting tropical deforestation (Almeida-Filho et al. 2007; Almeida-Filho et al. 2009; Motohka et al. 2014; Reiche et al. 2013; Rosenqvist et al. 2014; Simard et al. 2000; Thapa et al. 2013; Whittle et al. 2012), even at a global-scale (Shimada et al. 2014). Due to the high penetration depth of L-band into the canopy, disturbed and undisturbed forest are more enhanced compared to C-band (Luckman et al. 1997; Ribbes et al. 1997). The main degrading factor for SAR data is SAR speckle resulting in poor radiometric resolution which negatively affects classification results (Quegan & Toan 1998; Quegan & Yu 2001). The most common method to reduce SAR speckle is bi-dimensional (spatial domain) SAR speckle filtering (Oliver & Quegan 1998; Trouvé et al. 2003). Having time series data available allows additional speckle reduction in the temporal domain using a multi-temporal SAR filter. In contrast to conventional bi-dimensional SAR speckle filters that result in a trade-off between speckle-reduction and decreased spatial resolution, multi-temporal SAR filters reduce the SAR speckle with minimal loss of radiometric accuracy and spatial resolution of single channels (Quegan & Yu 2001; Quegan et al. 2000; Trouvé et al. 2003).

Multi-sensor data fusion (Zhang 2010) approaches that combine SAR and Landsat-like optical sensors have clearly demonstrated an increase in forest mapping accuracy (Almeida-Filho et al. 2007; Erasmi & Twele 2009; Kuplich 2006; Vaglio Laurin et al. 2013; Lehmann et al. 2011; Lehmann et al. 2012; Reiche et al. 2013; Walker et al. 2010). Approaches that combine optical and SAR time series imagery for detecting forest changes (Lehmann et al. 2012; Reiche et al. 2013), however, are rather limited to date (Lu et al. 2014). Various challenges including accurate co-registration, dealing with spectral variation in the time series (Zhang 2010) and with images acquired at different dates have to be addressed when designing a SAR-optical time series approach (Lu et al. 2014). Fusion approaches can target the problem of missing data in a time series (Dunsmuir & Robinson 1981; Honaker & King 2010; Racault et al. 2014) by increasing the observation density. Considering the impending stream of free-of-charge medium resolution optical and SAR imagery, there is clearly a need for further research in SAR-optical fusion methods (Reiche & Herold 2012; Lu et al. 2014) in order to support consistent global forest monitoring (GFOI 2013).

We propose a novel pixel-based Multi-sensor Time series Fusion approach (MultiFuse). We apply MultiFuse to Landsat NDVI and ALOS PALSAR dual-polarisation L-band backscatter time series and use the fused time series in a change detection framework to detect abrupt human-induced forest changes (deforestation). Here we:

- (i) assess how Landsat NDVI and ALOS PALSAR L-band SAR time series are correlated, and investigate how the PALSAR backscatter observables (HV, HV, HVHH backscatter ratio) are correlated with the NDVI.
- (ii) evaluate how fused NDVI-PALSAR image time series improve the spatial and temporal accuracy of deforestation detection, compared to individual NDVI- and PALSAR-only change detection.
- (iii) investigate how the main factors degrading optical (cloud cover) and SAR time series (SAR speckle) in tropical environments affect analysis (i) and (ii) by simulating NDVI time series with increasing amounts of missing data, and applying a multi-temporal SAR speckle filter, respectively.

The output is a deforestation map that is validated with quarterly (three-monthly) reference data covering the entire study area.

## 4.2 Data and study area

### 4.2.1 Study area and reference data

The *Lololo* Fiji Pine Ltd. lease is a fully managed softwood forest plantation (*Pinus caribea*) located in the north western part of the Viti Levu Island, Fiji (Lat. 17.32° S, Lon. 177.37° E) (Figure 4.2). Viti Levu, the main island of the Fijian archipelago, lies in the seasonal tropics and experiences persistent and strongly varying cloud cover (Ash 1992). For the *Lololo* Fiji Pine Ltd. lease, detailed spatial inventory data of 623 forest stands (9570 ha) are available, comprising quarterly (three-monthly) harvesting information from 2000 - 2013 and replanting information going back to 1975. Logging cycles have an average turn-over rate of 15 - 20 years. During logging activities, forest stands are fully harvested within a very short period and stems are removed immediately after logging. Subsequently, forest stands are replanted entirely. Forest stands remaining unlogged over a long period (greater than 10 years) are covered with fully grown pine. The period from 01/2008 (January 2008) - 09/2010 (September 2010) serves as monitoring period for this study. During this period deforestation is detected. As validation area (and reference data set), a forest mask was derived from the inventory data for the start of the monitoring period. The forest mask accounts for 2859 ha and includes all forest stands planted before 01/2000 (January 2000), and not logged before 01/2008. Of those forest stands, 1395 ha were logged during 01/2008 - 09/2010 and 1464 ha remained forest.

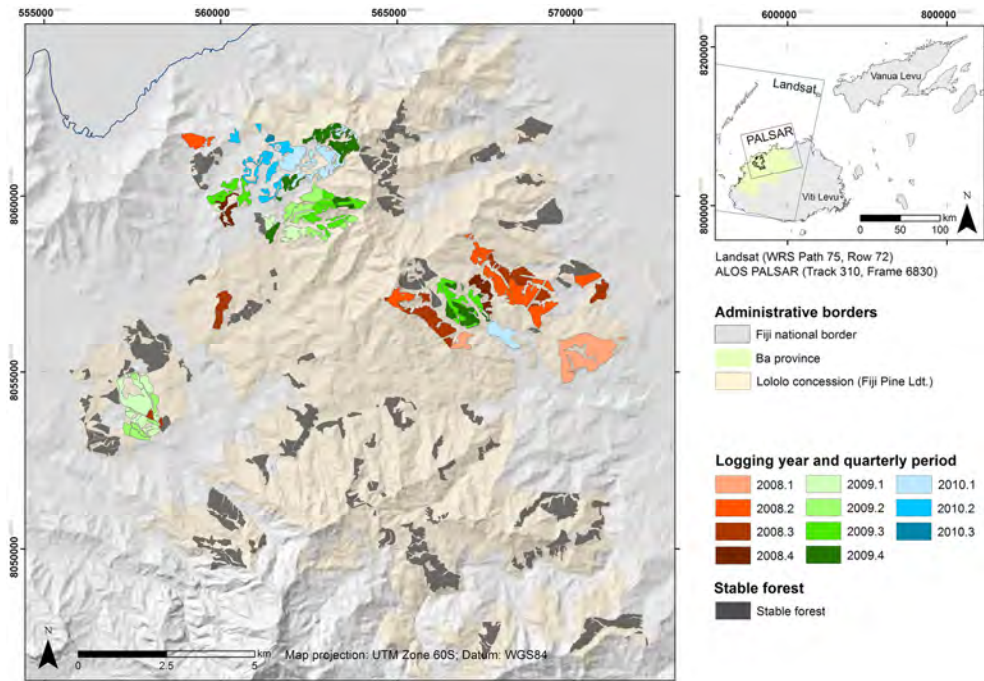


**Figure 4.2** The *Lololo* softwood plantation (*Pinus caribea*) located in north western part of the Viti Levu, Fiji. Depicted stable forest and logged forest stands with quarterly period logging information for the monitoring period 01/2008 – 09/2010 serve as validation area.

#### 4.2.2 Landsat NDVI data

All available 111 Level 1 Terrain (corrected) (L1T) Landsat 7 ETM+ images (Quality: 9) for the Worldwide Reference System (WRS) Path 75 and Row 72 acquired between 2004 and 2012 were used (downloaded from USGS GLOVIS portal) (Table 4.1). Landsat time series processing was performed using a standard processing chain consisting of Fmask and LEDAPS, a procedure which has been successfully applied in a number of recent studies dealing with large amounts of Landsat time series data (Hansen et al. 2013; Xin et al. 2013; Zhu et al. 2012; Zhu & Woodcock 2014).

**Table 4.1** Frequency by year of the Landsat 7 ETM+ (WRS Path 75, Row 72) and ALOS PALSAR FBD (Track 310, Frame 6830) observations for 2004 - 2010.

Year	2004	2005	2006	2007	2008	2009	2010	2011	2012
Nr. of Landsat images	15	12	14	13	16	14	13	5	9
Nr. of ALOS PALSAR FBD images				3	3	1	2		

**Table 4.2.** Approximate number of per-pixel observations per year for the original (org, mean 53%) Landsat NDVI time series, and for Landsat NDVI time series with increased 70, 80, 90, and 95% missing data.

Per-pixel MD	Approximate number of per-pixel observations per year
No MD (0%)	12.3
org (35 – 69%) (mean 53%)	3.8 – 9.25 (mean 6.5)
70%	3.8
80%	2.5
90%	1.2
95%	0.6

Each Landsat image was processed individually. Based on the uncorrected Landsat data in digital numbers, Fmask (Function of mask, Zhu & Woodcock 2012) was used to mask clouds, cloud shadow and Landsat-7 SLC-off-data gaps. Fmask is a fully automated object oriented approach that uses the optical and thermal Landsat bands. When dealing with consistent cloud cover and/or scatter clouds, some cloud edges may remain after masking (Zhu & Woodcock 2012; Xin et al. 2013). Atmospheric correction was performed using the Landsat Ecosystem Disturbance Adaptive Processing System (LEDAPS) tool (Vermote et al. 1997; Masek et al. 2006; Schmidt et al. 2013) to convert digital numbers to surface reflectance. The processed images (30 m spatial resolution) were re-projected to WGS 84 / UTM zone 60S. Clouds, cloud shadow and SLC-off were masked as missing data.

Per-pixel missing data (MD) was calculated based on the processed NDVI stack (WRS Path 75 Row 72) that covers the western part of Viti Levu (Table 4.2). It varies from 35% to 69% and averages 53% for the validation area, but increases up to 96% for other areas covered by the NDVI stack. By randomly excluding observations on a pixel basis, we increased the per-pixel percentage of MD from an average of 53% for the original (org) Landsat time series stack to 70, 80, 90 and 95%. Table 4.2 lists the approximate number of per-pixel observations per year for the original (org) and the increased MD Landsat time series stacks. It ranges from ~6.5 to ~0.5 observations/year for 53% (org) to 95% MD, respectively.

### **4.2.3 ALOS PALSAR data**

Multi-temporal L-band SAR data was obtained from the phased array L-band synthetic aperture radar sensor aboard the advanced land observing satellite (ALOS PALSAR) for 2007 - 2010 (Shimada et al. 2010). All archived data acquired in Fine Beam Dual (FBD) mode for Track 310 and Frame 6830 (Table 4.1) was used for time series processing. The time series consists of 9 dual-polarized FBD images (HH- and HV polarisation). All images were acquired in ascending mode with an incidence angle of 34.3° and were provided in Level 1.1 format. Pre-processing of ALOS PALSAR FBD images was done independently for each image, using the Gamma software package (Werner & Strozzi 2000).

Pre-processing included multi-looking, radiometric calibration using standard calibration coefficients (Shimada et al. 2009), topographic normalization as described by Hoekman et al. (2010), and geocoding to 25 m pixel resolution (WGS84, UTM 60S) using a local 30 m DEM. Visual comparison with Landsat and high resolution satellite imagery showed very good geocoding accuracy (around 0.5 pixel error). Among the different pre-processed images, no significant geolocation errors were visible. The individual HH and HV images were stacked to create HV- and HH time series stacks. The stacks are subsequently resampled to the 30 m Landsat pixel cells. The same spatial resolution and overlapping pixels are required to fuse at pixel level. By subtracting the HV and HH backscatter time series, a HVHH backscatter ratio time series is derived (HVHH). Steep topography in the validation area ranging from 0 to 48 degree, resulted in SAR layover and shadow areas that account for 0.73 ha. In addition to the general SAR pre-processing steps, adaptive multi-temporal SAR filtering (Quegan & Yu 2001) was applied to the pre-processed FBD time series in a sequential manner, where images acquired within 12 months were included in the multi-temporal filtering process. A measured increase of the equivalent number of looks indicated a clear reduction of SAR speckle in the data. This is crucial for analysing the data at pixel level. In addition, no significant changes in the mean radiometric characteristics were observed. An unfiltered and a multi-temporal filtered version of the HV and HH backscatter time series is available. Multi-temporal filtered backscatter are hereafter referred to as  $HH_{mt}$ ,  $HV_{mt}$ , and  $HVHH_{mt}$  for the HVHH backscatter ratio.

## 4.3 Methods

### 4.3.1 The MultiFuse approach for detecting deforestation

#### 4.3.1.1 Overview

Here, we present a novel pixel-based multi-sensor fusion approach. Figure 4.3 illustrates the main steps of applying the MultiFuse approach to two univariate optical and SAR image time series. First, a weighted time series correlation is performed (Section 4.3.1.2; step 1). To maximise the statistical significance of the correlation and to take exceptional cases into account, correlation weight optimization is done before the relationship of the two time series is modelled through a weighted regression analysis. The optimized regression model is utilized in a second step for regression-based prediction of time series observation to fuse the SAR and optical time series (Section 4.3.1.3; step 2). A practical multi-sensor change detection framework is proposed in Section 3.1.4 (step 3). Criteria are outlined to decide whether MultiFuse is applied to fuse the time series or whether one of the original SAR or optical time series is to be selected for time series analysis to detect deforestation. For time series analysis BFAST-monitor (Verbesselt et al. 2012) is used.

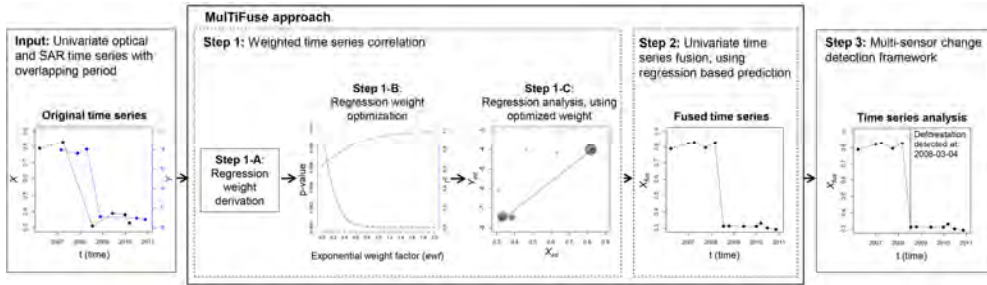


Figure 4.3 Schematic overview of MultiFuse to fuse optical and SAR image time series.

### 4.3.1.2 Weighted time series correlation (step 1)

Because of the specific characteristics of optical and SAR remote sensing time series observations, direct correlation and fusion is not feasible. In general medium resolution optical and SAR remote sensing time series share the following characteristics: (i) they are temporally discrete, (ii) their individual observations are non-equidistant in time, (iii) their observation times are not identical and (iv) their scales/unit are not directly compatible (e.g. NDVI versus SAR backscatter).

Figure 4.4A shows two univariate example time series  $X$  and  $Y$  that meet these characteristics and cover an abrupt change. For example,  $X$  and  $Y$  could be a Landsat NDVI and ALOS PALSAR backscatter time series, respectively, covering a deforestation event. Due to different revisit rates (16 days for Landsat and 46 days for PALSAR) and data gaps as a result of cloud cover (Landsat) and changing observation density (PALSAR) their observation times are not identical.

A straightforward way to determine the correlation between the  $X$  and  $Y$  time series is to first interpolate the  $Y$  time series observations and then correlate the  $X$  observations with the interpolated  $Y$  observations. Each  $X$  time series observation (large black dots in Figure 4.4A) forms a correlation pair with an interpolated  $Y$  observation (small blue dots in Figure 4.4A). After interpolation, the interpolated  $Y$  time series ( $Y_{int}$ ) consists of the original and the interpolated  $Y$  observations.

Similarly, the interpolated  $X$  time series ( $X_{int}$ ) consists of the original and the interpolated  $X$  observations. We can now correlate  $X_{int}$  and  $Y_{int}$  and derive their relationship by regression analysis. When plotting the interpolated time series against each other in a correlation plot, we expect two main clusters representing observation pairs under forests conditions before the change and observations pairs under non-forest conditions after the deforestation event, respectively. We assume that the paired  $X_{int}$  and  $Y_{int}$  observations are linearly related for abrupt forest changes and assess the linearity assumption in the validation section for Landsat NDVI and ALOS PALSAR backscatter time series. The simple interpolation-based time series correlation approach may introduce outliers in the following circumstance. Considering a case where two consecutive  $Y$  observations enclose the abrupt deforestation event (3<sup>rd</sup> and 4<sup>th</sup>  $Y$  observation, large blue dots in Figure 4.4B),

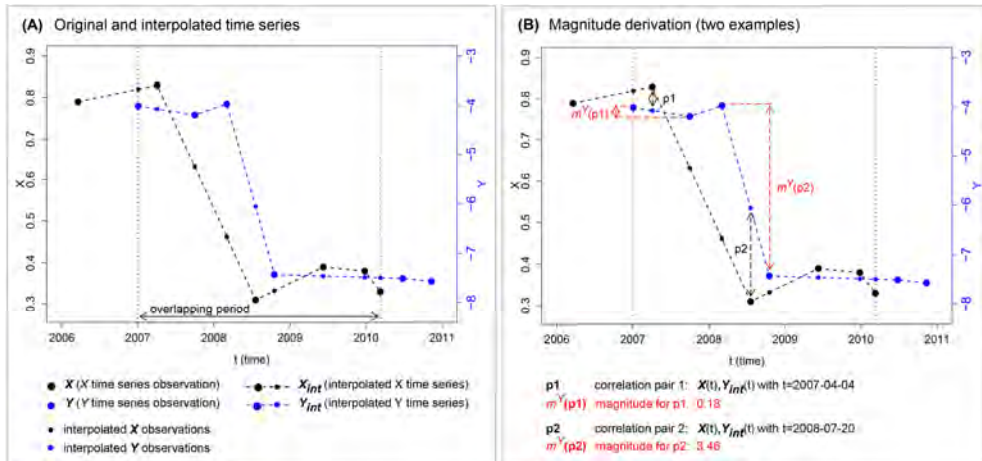


**Figure 4.4** A) Two hypothetical univariate time series  $X$  and  $Y$  (large dots) spanning an abrupt change event.  $X_{int}$  and  $Y_{int}$  are the interpolated  $X$  and  $Y$  time series, respectively, and consist of original (large dots) and interpolated time series observations (small dots). B) Magnitude derivation for two correlation pairs p1 and p2, referring to two  $X$  time series observations correlated to two interpolated  $Y$  time series observations. For  $X$  observations, the  $Y$  magnitude ( $m^Y$ ) is calculated as the magnitude difference between the neighboring  $Y$  time series observations enclosing  $X$ . The example data set used to derive the figures is given in Table 4.3.

the first having been acquired during dense forest conditions and the second acquired after the deforestation at non-forest conditions. A  $X$  observation (3<sup>rd</sup>  $X$  observation, large black dots, Figure 4.4B) acquired between the two  $Y$  observations either represents forest or non-forest, depending on whether it was acquired before or after the event. The  $X$  observation is now correlated to an interpolated observation  $Y_{int}$  with a value somewhere between the values of forest and non-forest (p2, Figure 4.4B). This correlation pair will be an outlier. Particularly when dealing with very sparse time series, such outliers may strongly affect the time series correlation.

To mitigate the negative effect of these outliers on the time series correlation, we introduce the magnitude between two consecutive  $Y$  observations as regression weight for the correlation pair formed by  $X$  and the interpolated  $Y$  observation ( $Y_{int}$ ). The larger the absolute magnitude value, the lower the regression weight. In the case described above (p2, Figure 4.4B), the absolute magnitude difference ( $m^Y(p2)$ ) of the two  $Y$  observation is very large since the  $Y$  observation at forest conditions is subtracted from a  $Y$  observation at non-forest condition. For this case the derived regression weight is very low. For correlation pairs before (p1, Figure 4.4B) and after the event, high weights can be expected due to low magnitude changes ( $m^Y(p1)$ ). Both cases are schematically depicted in Figure 4.4B. The example data set for Figure 4.4A and Figure 4.4B is given in Table 4.3. Next, we mathematically describe (i) the derivation of the regression weight and (ii) examine how the weight can be optimised.

**(i) Derivation of the time series regression weight**

We describe the concept of the introduced weighting approach generically and by referring to Figure 4.4A and Figure 4.4B. Let  $X$  and  $Y$  be two temporally discrete time series that are non-equally spaced in time and of which the observation times are non-identical. Let  $X$  and  $Y$  have a common overlapping time period. We can take the observation times of  $X$  and  $Y$  to be  $T_X = \{t^{X_1}, t^{X_2}, \dots, t^{X_{k_X}}\}$  and  $T_Y = \{t^{Y_1}, t^{Y_2}, \dots, t^{Y_{k_Y}}\}$  with  $k_X$  and  $k_Y$  being the number of  $X$  and  $Y$  observations, respectively. Now the observed time series  $X$  and  $Y$  can be expressed as  $X = \{X(t) : t \in T_X\}$  and  $Y = \{Y(t) : t \in T_Y\}$ , respectively. A straightforward approach for correlation is to first interpolate  $X$  and  $Y$ , and subsequently correlate the interpolated time series at the observation times of  $X$  and  $Y$  ( $T_X \cup T_Y$ ). The interpolated time series  $X_{int}$  and  $Y_{int}$  based on  $X$  and  $Y$ , respectively, are defined as follows:

$$X_{int}(t) = \begin{cases} X(t) & : t \in T_X \\ X_{lin}(t) & : t \in T_Y \end{cases} \quad (4.1)$$

$$Y_{int}(t) = \begin{cases} Y(t) & : t \in T_Y \\ Y_{lin}(t) & : t \in T_X \end{cases} \quad (4.2)$$

, with  $X_{lin}$  and  $Y_{lin}$  being the linearly interpolated  $X$  and  $Y$  time series, respectively. Next, we derive the magnitude that is subsequently inverted and normalised. First, the absolute magnitude  $m^Y$  for all correlation pairs at  $t^{X_i}, i = 1, \dots, k_X$  is derived as:

$$m^Y(t^{X_i}) = \begin{cases} \text{NA} & , \text{ if } t^{Y_{k_Y}} \leq t^{X_i} \\ \text{NA} & , \text{ if } t^{Y_1} \geq t^{X_i} \\ \left| Y(\min\{t^{Y_j} \in T_Y \mid t^{Y_j} \geq t^{X_i}\}) - Y(\max\{t^{Y_j} \in T_Y \mid t^{Y_j} \leq t^{X_i}\}) \right| & , \text{ otherwise} \end{cases} \quad (4.3)$$

, with  $t^{Y_{k_Y}} \leq t^{X_i}$  and  $t^{Y_1} \geq t^{X_i}$  representing the cases that the  $Y$  time series starts before or after the  $X$  observation at  $t^{X_i}$ , respectively. For these cases no magnitude weight is derived at  $t^{X_i}$ , and therefore  $m^Y(t^{X_i})$  is NA. The terms  $Y(\min\{t^{Y_j} \in T_Y \mid t^{Y_j} \geq t^{X_i}\})$  and  $Y(\max\{t^{Y_j} \in T_Y \mid t^{Y_j} \leq t^{X_i}\})$  represent the  $Y$  observations acquired closest in time before and after the  $X$  observation at  $t^{X_i}$ . By subtracting the two  $Y$  observations, the magnitude  $m^Y$  for the  $X$  observation at  $t^{X_i}$  is derived. Next the inverted and normalised magnitude is derived ( $m^Y_I$ ):

$$m^Y_I(t^{X_i}) = \frac{\max\{m^Y(t^{X_j}), t^{X_j} \in T_X\} + \min\{m^Y(t^{X_j}), t^{X_j} \in T_X\} - m^Y(t^{X_i})}{\sum m^Y(t^{X_j}), t^{X_j} \in T_X} \quad (4.4)$$

$$m^Y_{I'}(t^X_i) = \frac{m^Y_{I'}(t^X_i)}{\sum m^Y_{I'}(t^X_i), t^X_i \in T_X} \quad (4.5)$$

Let  $m^X$ ,  $m^X_{I'}$  and  $m^X_{I''}$  be defined analogously to  $m^Y$ ,  $m^Y_{I'}$  and  $m^Y_{I''}$ , respectively. For using  $m^X_{I'}$  and  $m^Y_{I'}$  jointly to calculate a regression weight, the possibility of unequal number of  $X$  and  $Y$  observations in the overlapping time period needs to be taken into account. Therefore, an additional normalisation of  $m^X_{I'}$  and  $m^Y_{I'}$  to the number of  $X$  and  $Y$  observations that are within the overlapping period ( $I_X$  and  $I_Y$ ) is carried out:

$$m^Y_{I''}(t^X_i) = \frac{m^Y_{I'}(t^X_i) * I_X}{I_X + I_Y} \quad (4.6)$$

$$m^X_{I''}(t^Y_j) = \frac{m^X_{I'}(t^Y_j) * I_Y}{I_X + I_Y} \quad (4.7)$$

, with  $I_X$  denoting the number of time points  $t^X_i$  where  $m^Y(t^X_i)$  is not NA, and  $I_Y$  denoting the number of time points  $t^Y_j$  where  $m^X(t^Y_j)$  is not NA. The regression weight  $\varpi(X_{int}, Y_{int})$  used to correlate the interpolated time series  $X_{int}$  and  $Y_{int}$  is calculated as:

$$\varpi(X_{int}, Y_{int})(t) = \begin{cases} m^Y_{I''}(t) & : t \in T_X \\ m^X_{I''}(t) & : t \in T_Y \end{cases} \quad (4.8)$$

An exponential weight function (*ewf*) is introduced to regulate the strength of the weight:

$$\varpi^{ewf} = (\varpi(X_{int}, Y_{int})(t))^{ewf} \quad (4.9)$$

, where an  $ewf=0$ ,  $ewf=1$ , and  $ewf=2$  represents no weight, a simple weight, or a squared weight, respectively. The relationship between the interpolated  $X_{int}$  and  $Y_{int}$  time series is determined using weighted least square regression (Seber & Lee 2003) with  $\varpi^{ewf}$  (Eq. 4.9) as weights. A linear fitting model is used:

$$Y_{int} = a + bX_{int} \quad (4.10)$$

, where  $a$  and  $b$  are constants of the linear model calculated by fitting the model to the  $X_{int}$  (predictor's variable) and  $Y_{int}$  (response variable) data.

**Table 4.3** Example time series  $X$  and  $Y$ , used for Figures 2, 3, 4 and 5. Interpolated time series ( $X_{int}, Y_{int}$ ), magnitudes ( $m^X, m^Y$ ), the normalised inverted magnitudes ( $m^Y_r, m^X_r$ ), the regression weight ( $\omega^{ewf}$ ), and the fused time series ( $X_{fus}$ ) are given.

t (time)	$X$	$X_{int}$	$Y$	$Y_{int}$	$m^Y$	$m^X$	$m^X_r$	$m^Y_r$	$\omega^{ewf}(ewf=1)$	$X_{fus}(ewf=1)$
2006-03-20	0.79	0.79			NA		NA		NA	0.79
2007-01-03		0.82	-4.01	-4.01		0.04		0.481	0.214	0.80
2007-04-04	0.83	0.83		-4.07	0.18		0.243		0.135	0.83
2007-10-01		0.63	-4.19	-4.19		0.52		0.037	0.016	0.78
2008-03-04		0.46	-3.97	-3.97		0.52		0.037	0.016	0.81
2008-07-20	0.31	0.31		-6.06	3.46		0.006		0.003	0.31
2008-10-18		0.33	-7.43	-7.43		0.08		0.044	0.197	0.36
2009-06-10	0.39	0.39		-7.46	0.08		0.250		0.139	0.39
2009-12-26	0.38	0.38		-7.48	0.08		0.250		0.139	0.38
2010-03-11	0.33	0.33		-7.50	0.08		0.250		0.139	0.33
2010-06-26			-7.51	-7.51		NA		NA	NA	
2010-11-11			-7.57	-7.57		NA		NA	NA	

**(ii) Regression weight optimization**

Applying the regression weight (Eq. 4.9) to correlate univariate remote sensing time series covering an abrupt change will in most cases improve the correlation between the time series and, more importantly, the statistical significance of the derived relationship (Eq. 4.10). The p-value is a widely recognised measure of statistical significance, and by testing the null hypothesis the p-value indicates if changes in the predictor’s variable ( $X_{int}$ ) are associated with the changes in the response variable ( $Y_{int}$ ) (Seber & Lee 2003). A p-value smaller than a significance level  $\alpha$  indicates a statistically significant relationship between the predictor(s) and the response variable. For larger p-values no significant relationship is found, which

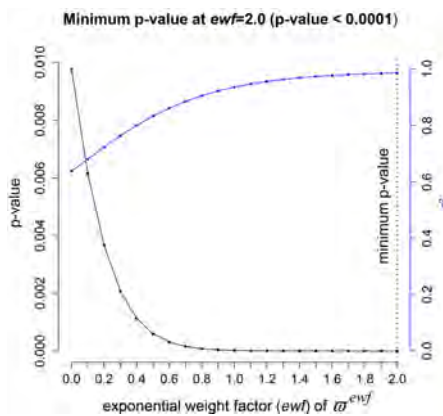


**Figure 4.5** Weight optimization plot. p-value (black dots) and  $r^2$  (blue dots) are plotted against an increasing exponential weight factor ( $ewf$ ) of the regression weight ( $\omega^{ewf}$ , Eq. 4.9) for the interpolated time series  $X_{int}$  and  $Y_{int}$ . The example data set used to derive the weight optimization plot is given in Table 4.3.

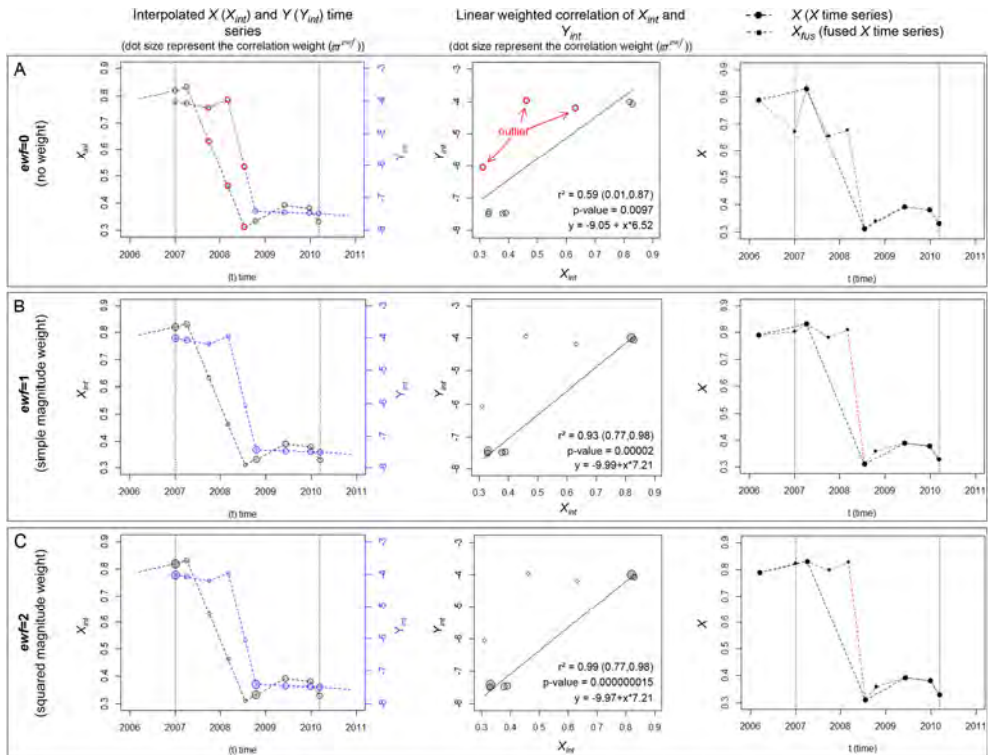


**Figure 4.6** Effect of an increasing  $ewf$  on the derived relationship. For  $ewf=0$  (A),  $ewf=1$  (B) and  $ewf=2$  (C), the interpolated time series  $X_{int}$  (black dots) and  $Y_{int}$  (blue dots) (left) as well as the correlation plots (centre) are shown (dot size represents regression weight). Additionally, the fused time series ( $X_{fus}$ , Eq. 4.12) is overlaid with the original  $X$  time series (right). The red dots in A represent outliers of the correlation that also apply for B and C.

also indicates a non-reliable coefficient of determination,  $r^2$ . Although there is no direct relationship between the p-value and the  $r^2$ , a decreasing p-value below the significance level  $\alpha$  commonly results in an increasing  $r^2$  (Seber & Lee 2003). The influence of the regression weight on the significance of the regression analysis can be assessed by plotting the p-value against an increasing exponential weight factor ( $ewf$ ). Figure 4.5 shows the weight optimization plot for the example case. The  $r^2$  (blue dots) is plotted in addition to the p-value (black dots). The p-value decreases exponentially for an increasing  $ewf$  starting from  $ewf=0$ , but begins to saturate as  $ewf$  approaches 1. The minimum p-value is found at  $ewf=2$ , indicating the optimized regression weight.

To better understand the effect of an increasing  $ewf$  on the determined relationship, Figure 4.6 depicts the interpolated time series  $X_{int}$  and  $Y_{int}$ , the correlation plot and the fused time series separately for  $ewf=0$ ,  $ewf=1$  and  $ewf=2$ . The dot size represents the regression weight ( $\omega^{ewf}$ ). In addition, the fused time

series ( $X_{fus}$ , derivation is explained in the next Section 4.3.1.3) is overlaid with the original  $X$  observations. For  $ewf=0$  (no weight, Figure 4.6A), all observations pairs receive an equal weight. The two clusters in the correlation plot represent observations before and after the abrupt change. The outliers (red dots) are related to the observations during the period of the change, where observations of a stable period (before or after the change) of one time series are correlated to an interpolated observation of the second time series that are derived from an observation before and after the event. These outliers weaken the correlation (p-value = 0.0097,  $r^2 = 0.59$ ). The relatively poor relationship strongly affects the quality of the fused time series (Figure 4.6A-right). The value range of the predicted observations (small dots) deviates from the range value of the original observations (large dots).

For  $ewf=1$  (simple weight, Figure 4.6B), the significance and the correlation of the relationship strongly increase (p-value =  $2.0 \cdot 10^{-6}$ ,  $r^2 = 0.93$ ) due to a reduced importance of the outliers (small weight) and an increased importance (high weight) of the observations acquired under stable conditions before and after the abrupt change. As a result, the value range of the predicted new observations in the fused time series corresponds more closely with original observations, strongly increasing the quality of the fused time series.

For  $ewf=2$  (squared weight, Figure 4.6C), the significance and the correlation of the relationship increases further compared to  $ewf=1$  (p-value =  $1.5 \cdot 10^{-8}$ ,  $r^2 = 0.99$ ), due to amplification of the weights, which also has a positive effect on the quality of fused time series.

The positive effect of an increasing  $ewf$  on the correlation, and thus on the quality of the fused time series is not valid for all circumstances. Three key scenarios can be distinguished. Figure 4.7 illustrates them using Landsat NDVI and ALOS PALSAR backscatter (multi-temporal filtered HVHH-ratio:  $HVHH_{mt}$ ) single pixel time series taken from the reference data set. The original overlapping time series (left), the weight optimization plot (p-value against  $ewf$ ) (second from left), and three correlation plots for the cases  $ewf=0$ ,  $ewf=1$  and  $ewf=2$  (centre to right) are shown.

- (i) The first case (Figure 4.7A) represents the common case identical to the case outlined in the previous paragraph and shown in Figure 4.6.
- (ii) The second case (Figure 4.7B) represents two time series where the abrupt change occurs at the beginning (shown here) or at the end of the overlapping period. In this case, only the  $HVHH_{mt}$  time series covers both forest and non-forest in the overlapping period, whereas the first NDVI observation in the overlapping period is already acquired after the event. Note that the shown NDVI (black line) and  $HVHH_{mt}$  time series (blue line) are identical to the ones shown in Figure 4.7A, but here (Figure 4.7B) the NDVI time series has an increased missing data percentage of 95% (MD=95). Also note that none of the NDVI observations under forest conditions are part of the overlapping

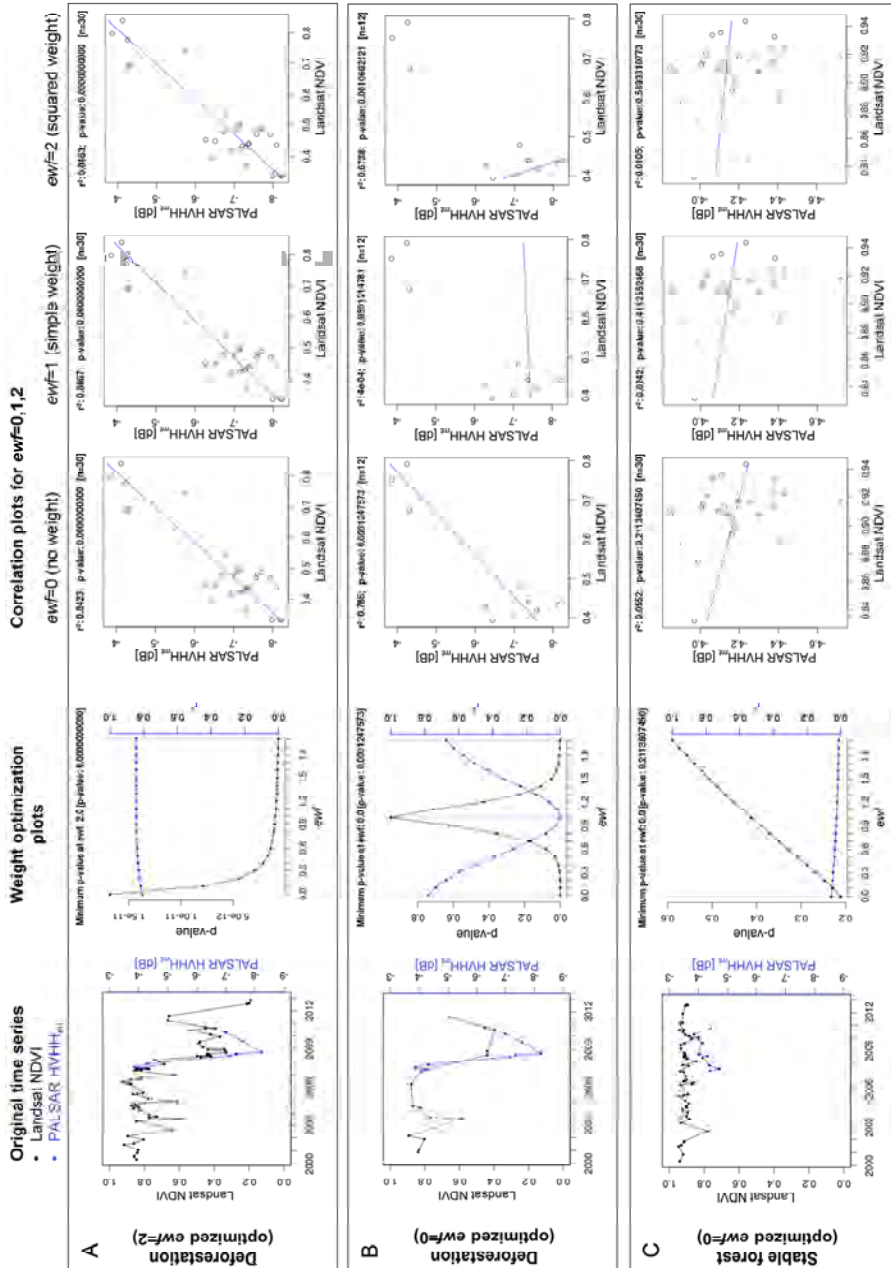


**Figure 4.7** Regression weight optimization key scenarios. The original overlapping time series (left), the weight optimization plot (p-value against  $ewf$ ) (second from left), and three correlation plots including regression line for the cases  $ewf=0$ ,  $ewf=1$  and  $ewf=2$  (centre to right) are depicted. A: deforestation event with optimized  $ewf=2$ , B: deforestation event with optimized  $ewf=0$ , C: stable forest with optimized  $ewf=0$ .

period, because they were acquired before the first HVHH<sub>mt</sub> observation. The three correlation pairs in the upper right corner of the correlation plots represent three HVHH<sub>mt</sub> observations acquired under forest conditions and correlated to interpolated NDVI observations. Due to the large magnitude of NDVI observations enclosing the HVHH<sub>mt</sub> observations, the correlation pairs receive very small regression weights. Thus, only observations after the change at non-forest conditions receive high weights. An increasing *ewf* starting from *ewf*=0 leads to an increasing p-value until it peaks at *ewf*=1 (local maxima) and starts decreasing afterwards. The correlation plots indicate that an increase of the *ewf* leads to a decrease of the positive relation between NDVI and HVHH<sub>mt</sub> until *ewf*=1. For *ewf*>1 the correlation is in the opposite direction. This is driven by an increasing weight of correlation pairs in the non-forest cluster. The optimized weight for this case is therefore *ewf*=0 (no weight).

- (iii) The third case (Figure 4.7C) illustrates two time series covering a stable forest where only the variance of the SAR and optical time series signals are correlated and a high p-value is observed for all *ewf*. No *ewf* is selected as the optimized weight and fusion is not performed. The same is valid for a stable non-forest period. Over such stable land cover classes, the variance of SAR signal can be related to speckle and environmental effects such as moisture differences (Salas et al. 2002; Lucas et al. 2010; Motohka et al. 2014), while seasonal and atmospheric effects can explain the variability for optical measurements (Verbesselt et al. 2010b).

To account for these exceptions, the optimized regression weight is determined by detecting the minimum p-value for *ewf* starting from *ewf*=0. In case a local maximum p-value occurs, the *ewf* that results in the minimum p-value before the local maxima is selected. When the p-value continuously increases, saturation was always found to occur around *ewf*=1 or 1.5, thus the maximum value of *ewf* was set to 2 in this work.

#### 4.3.1.3 Univariate time series fusion (step 2)

The optimized regression model is used to fuse the original  $X$  and  $Y$  time series within the overlapping period by predicting new  $X$  observations at the observation times of the  $Y$  time series. The fused time series  $X_{fus}$  consists of the original  $X$  observations and the additional predicted  $X$  observations. To avoid incorrect predictions using observations outside the overlapping period that have not been used to derive the correlation, only predictions during the overlapping period are fused. Figure 4.6C-right depicts  $X_{fus}$  for the example case. In the same manner  $Y$  time series observations can be predicted based on the  $X$  observations. Next, the mathematical description of the fusion process is explained. Based on Eq. 4.10,  $Y$  observations can be predicted based on  $X$  observations at  $T_x$ .

In case  $X$  observation are predicted based on  $Y$  observations, Eq. 4.10 rearranges to:

$$\hat{X}(t_i^Y) = \frac{Y(t_i^Y) - a}{b} \quad (4.11)$$

, where  $\hat{X}$  is the predicted  $X$  value at  $t_i^Y$ . The fused  $X$  time series  $X_{fus}$  consists of  $X$  observations and  $\hat{X}$  predictions belonging to the overlapping period and is defined to be:

$$X_{fus}(t) = \left\{ \begin{array}{ll} X(t) & : t \in T_X \\ \hat{X}(t) & : t \in T_Y \mid m^Y(t) \neq NA \end{array} \right\} \quad (4.12)$$

#### 4.3.1.4 Multi-sensor change detection framework (step 3)

Fusion using the proposed method is only meaningful if a strong and statistically significant relationship (p-value) exists between the SAR and optical time series. Two simple rules are proposed to decide whether the fused SAR-optical time series is to be used for detecting deforestation instead of either the original SAR or optical time series:

- (i) The significance level  $\alpha$  is used as decision rule to safeguard a meaningful fusion based on a strong relationship between the two time series. By studying (e.g. through plotting) the relationship of the overall accuracy of detected deforestation versus the p-value for p-value < 0.1,  $\alpha$  can be determined as the p-value for which the overall accuracy is highest. The study can be conducted at a subset of the validation area. For p-value <  $\alpha$  the fused time series is used.
- (ii) For p-value >  $\alpha$ , either the original optical or SAR time series needs to be selected. We select the time series in which the observations span the largest period within a defined monitoring period. This decision rule is used because the accurate detection of all changes is more important than the accurate determination of the time of change. Assuming an equal detection sensitivity of the optical and SAR time series for the desired type of change, the time series of which the observations spans the largest period (within a defined monitoring period) has the highest probability of detecting a possible change. Cases in which the detection capabilities of the two time series differ are discussed in the results and discussion.

To detect deforestation in the time series we use BFAST-monitor (BFM) (Verbesselt et al. 2012), an automated time series detection method that addresses the problem of frequent cloud cover by automatically dealing with data gaps. BFM analyses the full temporal frequency of the time series and is based on the BFAST concept for

detecting and characterizing breaks in satellite image time series (Verbesselt et al. 2010a; de Jong et al. 2011). BFM models the seasonal-trend variations of a defined historical period, and detects changes in a defined monitoring period (Verbesselt et al. 2012). Here, we only model underlying trends, since the Landsat and PALSAR time series data over stable tropical forests shown only minor seasonal variability (see original time series in Figure 4.6A-C).

For each detected change, BFM provides the time of change. The magnitude of the forest changes is estimated by calculating the difference between the median of the fitted trend model and the median of the observations in the monitoring period acquired at and after the detected change. A magnitude threshold is used to identify a detected BFM change as negative forest cover change. Only detected BFM changes with a magnitude less than the defined threshold are labelled as deforestation.

## 4.3.2 Validation

### 4.3.2.1 Correlating time series

We apply the weighted time series correlation, the first part of MultiFuse, to ALOS PALSAR L-band SAR and Landsat NDVI time series data and compare the results with a non-weighted time series correlation. The effects of increasing per-pixel MD in the NDVI time series, different SAR polarisations and SAR speckle reduction are analysed.

Firstly, an area-wide correlation is performed to (i) validate the assumption of a linear relationship between NDVI and L-band SAR time series when covering abrupt forest cover changes (deforestation), and (ii) to identify the PALSAR time series observable showing the strongest correlation with NDVI. Therefore, the relationship between all existing correlation pairs of the validation site is derived separately by linear weighted regression for the logged forest and stable forest validation areas. Weighted linear regression is compared for  $ewf=0$  (no regression weight) and for  $ewf=opt$  (optimized regression weight). A maximum  $ewf=2$  is defined for the regression weight optimization. The PALSAR time series observables HV, HH, HVHH and  $HV_{mt}$ ,  $HH_{mt}$ ,  $HVHH_{mt}$  are correlated with  $NDVI_{MD}$  for MD=org, 70, 80, 90 and 95%, whereby org refers to an average MD of 53%. In this manner, the consistency of the relationship for increasing MD can be validated for the different PALSAR observables. The remaining validation results are shown for the PALSAR observables that proved to have the strongest and most consistent correlation with NDVI.

Secondly, a pixel-based weight optimization is proposed as part of MultiFuse. We validate the proposed weight optimization approach for MD=org and MD=95, and compare the results with non-weighted correlation and static regression weights. Per-pixel, the p-value and  $r^2$  are compared for  $ewf=0,1,2$  and  $ewf=opt$ . The results are presented in box-and-whisker plots separately for logged forest and stable forest areas.

**Table 4.4** Parameterisation for the validation study.

<b>Time periods</b>	Landsat NDVI time series	01/2004 - 12/2012
	PALSAR time series	06/2007 - 09/2010
	Monitoring period	01/2008 - 09/2010
<b>Parameter for MultiFuse</b>	Maximum <i>ewf</i>	2
<b>Parameter for the change detection framework</b>	Significance level $\alpha$	0.001
	Sequential monitoring periods	01/2008 - 12/2008
		01/2009 - 12/2009
		01/2010 - 09/2010

### 4.3.2.2 Detecting deforestation

We apply MultiFuse to fuse PALSAR and Landsat NDVI time series. The fused NDVI-PALSAR time series is used in the multi-sensor change detection framework to detect deforestation for the monitoring period 01/2008 – 09/2010. The results are compared with NDVI-only and PALSAR-only results by assessing the spatial and temporal accuracy of the detected changes. We also compare the results for increasing MD in the Landsat NDVI time series. In the processed NDVI time series, remaining cloud edges and haze as a result of an imperfect Fmask cloud mask (Xin et al. 2013; Zhu et al. 2012; Zhu & Woodcock 2014) result in spikes of low values comparable to observations over non-forest land cover types. In the case of a deforestation event, however, the non-forest signal is expected to remain for a number of observations, even for very sparse NDVI time series. To avoid commission errors due to falsely detected changes, changes detected by BFM are only accepted if the change is also detected in the subsequent observations. Table 4.4 lists the time periods, the parameterisation for MultiFuse and the parameterisation for the change detection framework. Even though the overlapping period of NDVI and PALSAR ranges from 06/2007 – 09/2010, the monitoring period is restricted to 01/2008 – 09/2010 because the PALSAR observations acquired in 2007 are used by BFM to model the history. The fused time series is denoted as “fused NDVI<sub>org</sub>-HVHH<sub>mt</sub> (*ewf*=opt)” when the NDVI time series with original MD percentage (MD=53%) is fused with HVHH<sub>mt</sub>, using *ewf*=opt. The significance level  $\alpha$  was determined as  $\alpha = 0.001$  for this study. As BFM magnitude threshold to identify detected changes as deforestation -0.05 is used for NDVI<sub>MD</sub> and fused NDVI<sub>MD</sub>-HVHH<sub>mt</sub>, while -1 dB is applied for HVHH<sub>mt</sub>. The change detection framework is applied in a sequential manner with yearly monitoring periods. For each sequential period, the framework is applied to detect deforestation. Detected changes are masked and not considered in subsequent sequential periods. The result is a deforestation map showing the time of change for each detected change pixel.

We assess both the spatial and temporal accuracy of the deforestation map. Spatial accuracy is defined as the overall accuracy, which is inversely related to omission and commission error of detected changes. The temporal accuracy refers to

the extent to which timing of the detected changes are correct. Available reference data that covers the entire study area allows a map comparison. A major advantage of map comparison compared to common probabilistic sampling methods is that no sampling errors are introduced (Stehman 2009), since the number of pixels in the deforestation map represents the sample unit. To account for mixed pixels on the edges of the reference polygons, we only include a pixel if at least two-thirds of the pixel covers the reference polygon. To assess the spatial accuracy, a confusion matrix is derived (Foody 2002; Olofsson et al. 2013; Olofsson et al. 2014) from the deforestation and no-change class. We calculate the overall accuracy (OA), the omission error (OE) and commission error (CE) of the deforestation class following (Olofsson et al. 2014). Temporal accuracy is assessed by calculating the the mean time lag (MTL) of correctly detected changes. For each correctly detected change pixel, the time of change is converted to quarterly periods, before the time difference with the validation data is calculated. The MTL is calculated as the mean of all time differences and is given in months. It is important to analyze the MTL jointly with the OE, because the MTL is calculated based on correctly detected changes only.

## 4.4 Results

### 4.4.1 Correlating time series

#### 4.4.1.1 Area-wide correlation of logged and stable forest

Table 4.5 depicts the area-wide correlation ( $r^2$ ) between the PALSAR time series observables HH, HV, HVHH and  $HH_{mt}$ ,  $HV_{mt}$  and  $HVHH_{mt}$  with Landsat  $NDVI_{MD}$  time series for MD=org (53), 70, 80, 90 and 95%, separately for logged forest and stable forest areas. The  $r^2$  was compared for  $ewf=0$  and for the optimized regression weight, which was found to be  $ewf=2$  for all cases. We therefore denote the optimized regression weight as  $ewf=2=opt$  for the area wide-correlation only. Due to the large number of correlation pairs ( $n > 70000$  for logged forest,  $n > 65000$  for stable forest) a high statistical significance (p-value) was found for all cases. For logged forest, the strongest correlation was found between the  $NDVI_{org}$  and  $HVHH_{mt}$  ( $r^2 = 0.641$ ,  $ewf=2=opt$ ,  $n = 294028$ ). A slightly lower correlation was obtained for  $HV_{mt}$  ( $r^2 = 0.586$ ,  $ewf=2=opt$ ), and only a weak relationship was found for  $HH_{mt}$  ( $r^2 = 0.333$ ,  $ewf=2=opt$ ).

For all PALSAR time series, multi-temporal SAR filtering led to very strong increase of the correlation with  $NDVI_{MD}$  as a results of reduced SAR speckle effects. The absolute increase was found to be the highest for HVHH, for which the correlation increased from  $r^2 = 0.348$  ( $ewf=2=opt$ ) to  $0.641$  ( $ewf=2=opt$ ) when correlating HVHH and  $HVHH_{mt}$  with  $NDVI_{org}$ , respectively. Compared to a non-weighted time series correlation ( $ewf=0$ ), a strong increase in the strength of the

**Table 4.5** Area-wide correlation between PALSAR time series observables HH, HV, HVHH and HH<sub>mt</sub>, HV<sub>mt</sub> and HVHH<sub>mt</sub> with Landsat NDVI<sub>MD</sub> time series for MD=org (53), 70, 80, 90 and 95%. All correlation pairs of the validation site were considered. The  $r^2$  was derived for  $ewf=0$  (no weight) and  $ewf=2=opt$  (squared weight = optimized weight). \* indicates correlations shown as density scatter plots in Figure 4.9.

Correlation pair			$r^2$		
			logged forest	stable forest	
HH	-	vs. NDVI [MD=org(53), 70, 80, 90, 95%]	$ewf=0$	0.226, 0.221, 0.218, 0.205, 0.142	< 0.01
			$ewf=2=opt$	0.241, 0.235, 0.232, 0.218, 0.164	< 0.01
HH <sub>mt</sub>	-	NDVI [...]	$ewf=0$	0.327, 0.325, 0.325, 0.320, 0.303	< 0.01
			$ewf=2=opt$	0.333, 0.330, 0.329, 0.327, 0.313	< 0.01
HV	-	NDVI [...]	$ewf=0$	0.312, 0.311, 0.302, 0.264, 0.231	< 0.01
			$ewf=2=opt$	0.327, 0.323, 0.311, 0.282, 0.259	< 0.01
HV <sub>mt</sub>	-	NDVI [...]	$ewf=0$	0.557, 0.553, 0.552, 0.529, 0.413	< 0.01
			$ewf=2=opt$	0.586, 0.579, 0.576, 0.551, 0.474	< 0.01
HVHH	-	NDVI [...]	$ewf=0$	0.338, 0.337, 0.331, 0.305, 0.256	< 0.02
			$ewf=2=opt$	0.348, 0.346, 0.340, 0.321, 0.292	< 0.02
HVHH <sub>mt</sub>	-	NDVI [...]	$ewf=0$	0.583, 0.581, 0.584, 0.539, 0.460	< 0.07
			$ewf=2=opt$	0.641*, 0.634, 0.639, 0.607, 0.557*	< 0.07*

relationship between NDVI<sub>MD</sub> and all PALSAR time series was observed for the  $ewf=2=opt$ . For HVHH<sub>mt</sub>, the  $r^2$  increased from 0.583 to 0.641 for  $ewf=0$  and  $ewf=2=opt$ , respectively. An increasing MD led to decreasing correlations between all PALSAR time series and NDVI<sub>MD</sub>. As an example, the correlation between NDVI<sub>MD</sub> and HVHH<sub>mt</sub> decreased from  $r^2 = 0.641$  ( $ewf=2=opt$ ) for MD=org to  $r^2 = 0.557$  ( $ewf=2=opt$ ) for MD=95%. For stable forest, the correlation between the NDVI and all PALSAR backscatter polarisation was found to be very weak in all cases ( $r^2 < 0.07$ )

Figure 4.8 depicts density correlation plots of HVHH<sub>mt</sub> against NDVI<sub>org</sub> (A) and NDVI<sub>MD95</sub> (B) for logged forest (left) and stable forest areas (right) for  $ewf=2=opt$ . For logged forest, the strong linear relationship connecting two clusters of observations under stable forest conditions and logged forest conditions is clearly visible for NDVI<sub>org</sub> and NDVI<sub>MD95</sub>. Both clusters form a long ellipse following the regression line and partly connect, indicating that a linear correlation might be valid for even more graduate changes. For stable forest, an expected negligible correlation was found for MD=org and MD=95. The remaining results are presented and discussed for HVHH<sub>mt</sub>, since it was found to have the strongest and consistent correlation with the NDVI<sub>MD</sub>.

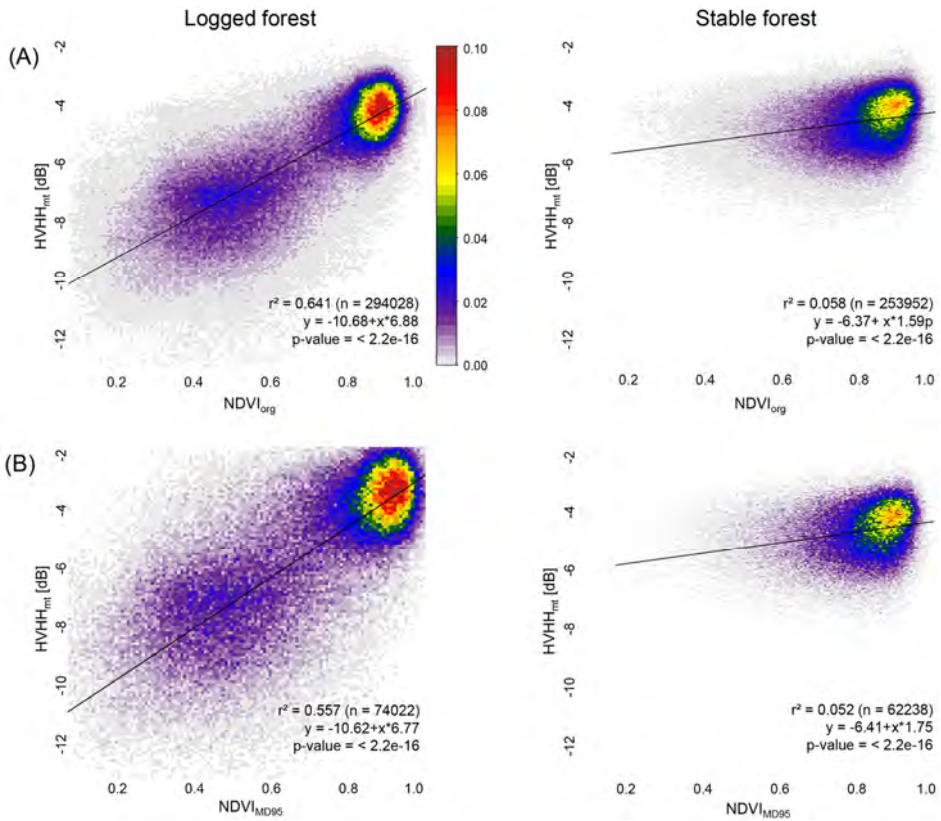


**Figure 4.8** Density correlation plots of HVHH<sub>mt</sub> against NDVI<sub>org</sub> (A) and NDVI<sub>MD95</sub> (B) for logged forest (left) and stable forest (right). All correlation pairs of the validations area were considered.

#### 4.4.1.2 Per-pixel correlation of logged and stable forest

Figure 4.9 shows box-and-whisker plots depicting per-pixel p-value and  $r^2$  for the correlation HVHH<sub>mt</sub> - NDVI<sub>org</sub> (Figure 4.9A) and HVHH<sub>mt</sub> - NDVI<sub>MD95</sub> (Figure 4.9B), separately for logged forest and stable forest. The results are compared for the static regression weights  $ewf=0$ ,  $ewf=1$ ,  $ewf=2$  and the optimized regression weight  $ewf=opt$ . The significance level  $\alpha = 0.001$  is indicated by a red line. Only pixels with p-value  $< \alpha$  were fused in the change detection framework. For HVHH<sub>mt</sub> and NDVI<sub>org</sub> (Figure 4.9A) the highest statistical significance was obtained for  $ewf=opt$ .

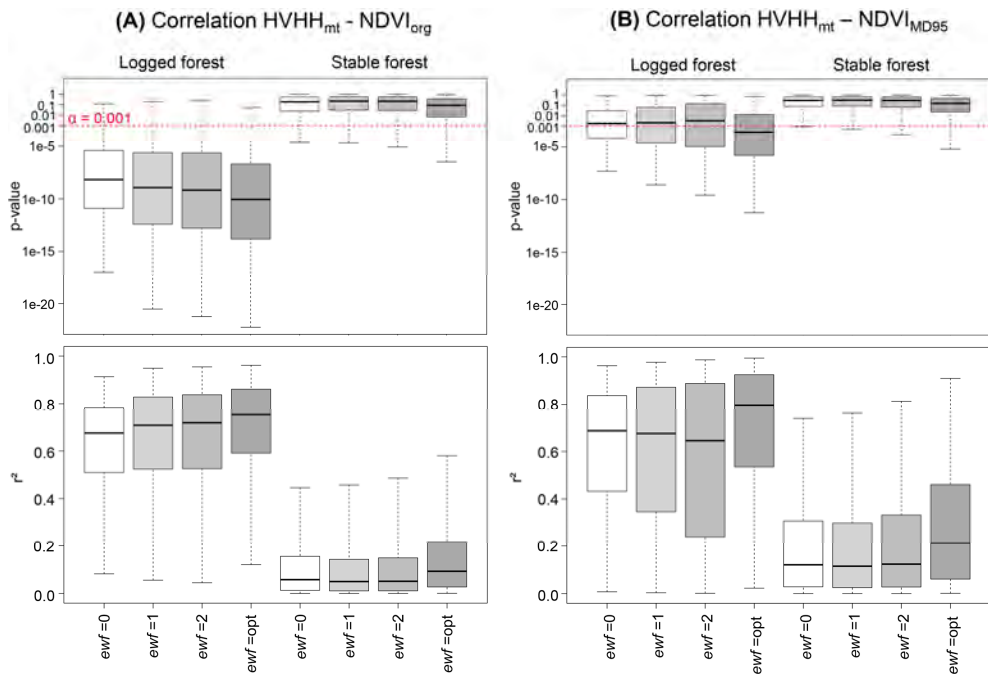


**Figure 4.9** Box-and-whisker plots depicting per-pixel  $r^2$  (top) and p-value (bottom) for the correlation  $HVHH_{mt} - NDVI_{org}$  (MD=53) (A) and  $NDVI_{MD95}$  (B) for logged forest and stable forest, compared for  $ewf=0$  (no weight),  $ewf=1$  (simple weight),  $ewf=2$  (squared weight) and  $ewf=opt$  (optimized weight). The p-value is given in logarithmic scale. The significance level = 0.001 used as threshold in the change detection framework is indicated as dotted red line.

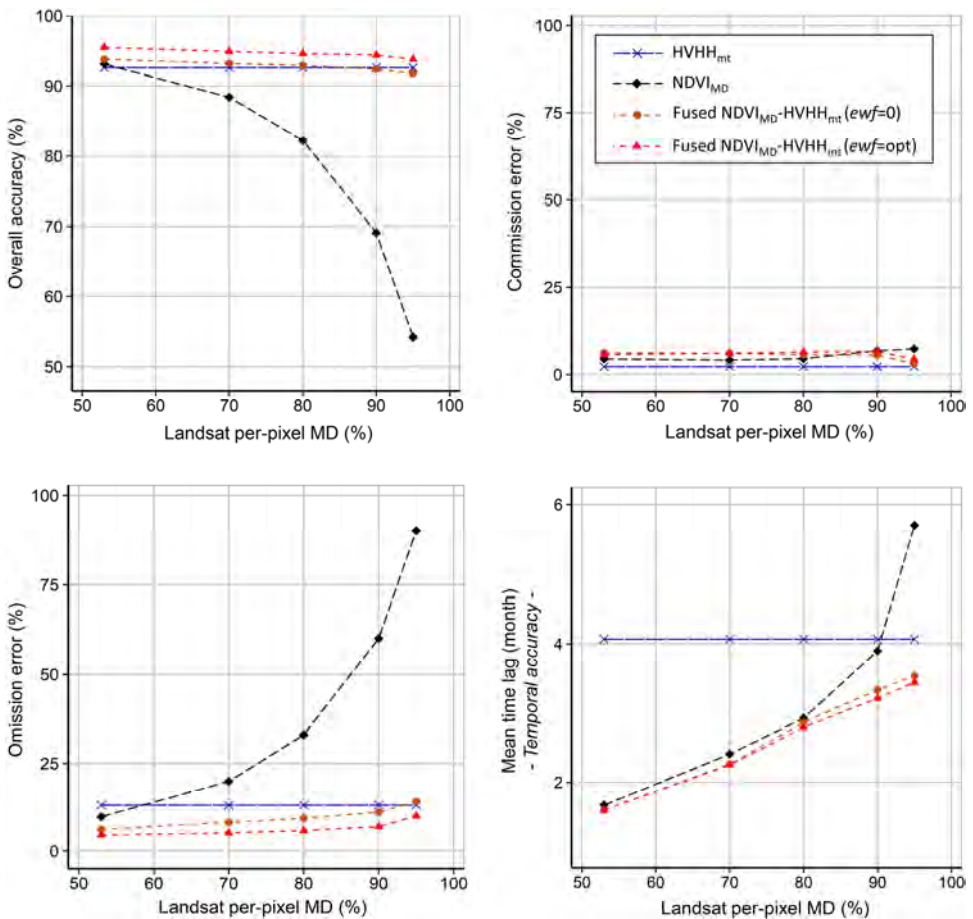
The p-values decrease consistently from  $ewf=0$ ,  $ewf=1$ ,  $ewf=2$  to  $ewf=opt$ . Nevertheless, for all cases the vast majority of the pixels featured a p-value less than  $\alpha$ . For  $HVHH_{mt} - NDVI_{MD95}$  (Figure 4.9B) when the NDVI time series density is strongly decreased, and thus the number of correlation pairs reduced, a different effect was observed. For the static regression weights  $ewf=1$  and  $ewf=2$ , the p-values increased compared to  $ewf=0$ . Weight optimisation ( $ewf=opt$ ), however, resulted in a decreased p-value and an increased  $r^2$ . As a result, the number of pixel with p-value  $< \alpha$  only increased when  $ewf=opt$ . For stable forest, a negligible correlation and a very low statistical significance was found for all values of  $ewf$ . These results reveal that the proposed pixel-based weight optimization ( $ewf=opt$ ) is required to increase the statistical significance (and the correlation) of the relationship between  $HVHH_{mt}$  and  $NDVI_{MD}$  consistently for increasing MD.

#### 4.4.2 Detecting deforestation

Figure 4.10 shows the spatial accuracy (OA, OE, CE) and the temporal accuracy (MTL) as a function of MD for the NDVI<sub>MD</sub>-only, HVHH<sub>mt</sub>-only, fused NDVI<sub>MD</sub>-HVHH<sub>mt</sub> ( $ewf=0$ ) and the fused NDVI<sub>MD</sub>-HVHH<sub>mt</sub> ( $ewf=opt$ ) cases. Their accuracy assessment results can be summarised as follows:

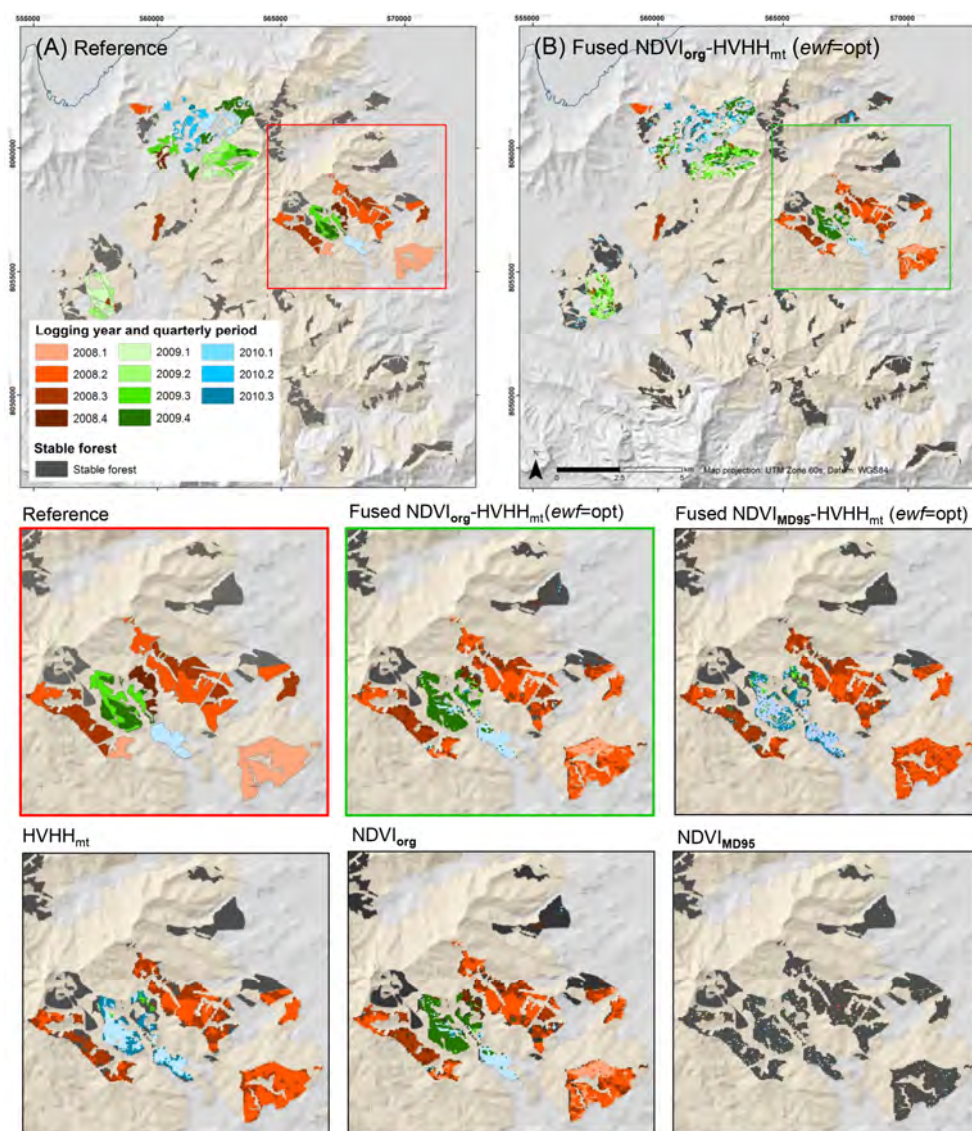
- (i) For HVHH<sub>mt</sub>-only, we obtained a high spatial accuracy (OA = 92.6%, OE = 13.2%, CE = 2.3%), but due to the fact that only 6 PALSAR observations were available in the monitoring period, a weak temporal accuracy (MTL = 4.07 month) was found. For HVHH-only, a much weaker spatial accuracy was found (OA = 63.5%, OE = 67.5%, CE = 17.6%) due to the strong effect of SAR speckle.
- (ii) For NDVI<sub>MD</sub>-only, a strong decrease in the spatial and temporal accuracy was observed with increasing MD. Compared to HVHH<sub>mt</sub>-only, however, a slightly higher spatial accuracy and a much higher temporal accuracy (MTL=1.67 month) was found for MD=org due to the large number of observations in the original NDVI time series. The OA dropped from 93.1% for MD=org to 54.2% for MD=95, mainly due to increasing omitted changes. For MD=95, the omission error almost reached 90%. The strong decrease in temporal accuracy can be explained by a reduced observation density. The MTL dropped from 1.67 months (MD=org) to 5.7 months (MD=95).
- (iii) For fused NDVI<sub>MD</sub>-HVHH<sub>mt</sub> ( $ewf=opt$ ), an improved spatial and temporal accuracy for all MD was found compared to NDVI<sub>MD</sub> and HVHH<sub>mt</sub>-only. For MD=org, the OA increased to 95.5% and the MTL decreased to 1.59 months. The increased OA accuracy was mainly caused by a reduced OE. While, the spatial and temporal accuracies decreased slightly but continuously for an increasing MD, they always exceeded the single-sensor accuracies. This was not found to be true for the fused NDVI<sub>MD</sub>-HVHH<sub>mt</sub> ( $ewf=0$ ) case, where no regression weight was used for MultiFuse. Although a slight improvement in the results was observed until MD=80, compared to HVHH<sub>mt</sub>-only, the OA dropped to 91.8% for MD=95. This can be explained by the fact that without regression weight a number of pixel time series have p-values that are below significance level  $\alpha$ , but the relatively weak correlation leads to a fused time series in which the value range does not fit the value range of the original NDVI time series.

Figure 4.11 illustrates the map results for the fused NDVI<sub>org</sub>-HVHH<sub>mt</sub> ( $ewf=opt$ ) case (Figure 4.11B) compared to the reference data (Figure 4.11A). For a subset, the map results obtained for the NDVI<sub>org</sub>, NDVI<sub>MD95</sub> cases (both NDVI-only) are compared to the map results of the fused NDVI<sub>org</sub>-HVHH<sub>mt</sub> ( $ewf=opt$ ) and fused NDVI<sub>MD95</sub>-HVHH<sub>mt</sub> ( $ewf=opt$ ) cases, respectively. In addition, the map results are illustrated for HVHH<sub>mt</sub>-only.



**Figure 4.10** Spatial (OA, OE, CE) and temporal accuracy (MTL) for NDVI<sub>MD</sub>-only, HVHH<sub>mt</sub>-only, fused NDVI<sub>MD</sub>-HVHH<sub>mt</sub> ( $ewf=0$ , no weight) and fused NDVI<sub>MD</sub>-HVHH<sub>mt</sub> ( $ewf=opt$ ) as a function of MD.

Due to the dense NDVI<sub>org</sub> time series used for the fused NDVI<sub>org</sub>-HVHH<sub>mt</sub> ( $ewf=opt$ ) case, a statistically significant relationship could be determined for the majority of the logged forest area. Thus, the map results for logged forest areas are mainly composed of fused pixels (92.9%), with only minor contribution of NDVI<sub>org</sub> (3.3%) and HVHH<sub>mt</sub> pixels (3.8%). Due to the minor contribution of HVHH<sub>mt</sub> time series observations the result is almost identical when compared to the NDVI<sub>org</sub>-only case. In contrast, the NDVI<sub>MD95</sub>-HVHH<sub>mt</sub> ( $ewf=opt$ ) case appears almost identical to the HVHH<sub>mt</sub>-only case. The only sparse NDVI<sub>MD95</sub> lead to mainly weak relationships and this prohibited the fusion for most of the logged forest area. Therefore the map results mainly consist of HVHH<sub>mt</sub> pixels (94.3%) and only a few NDVI<sub>MD95</sub> (0.9%) and fused NDVI<sub>MD95</sub>-HVHH<sub>mt</sub> ( $ewf=opt$ ) pixels (4.8%).



**Figure 4.11** Map results showing detected deforestation between 01/2008 – 09/2010 for the fused NDVI<sub>org</sub>-HVHH<sub>mt</sub> (*ewf=opt*) case (B) compared to the reference data (A). For a subset (squared box in A and B), the map results obtained for the NDVI<sub>org</sub>, NDVI<sub>MD95</sub> cases (both NDVI-only) are compared to the map results of the fused NDVI<sub>org</sub>-HVHH<sub>mt</sub> (*ewf=opt*) and fused NDVI<sub>MD95</sub>-HVHH<sub>mt</sub> (*ewf=opt*) cases, respectively. In addition, the map results are illustrated for HVHH<sub>mt</sub>-only.

## 4.5 Discussion and conclusion

Fusing optical and SAR image time series has the potential to improve forest monitoring in tropical regions, where cloud cover is a frequent challenge, when compared to single-sensor optical and SAR time series approaches. In this study, we developed a novel approach for optimized weighted Multi-sensor Time series correlation and Fusion (MulTiFuse). We applied MulTiFuse to single band Landsat NDVI and ALOS PALSAR time series imagery. The fused NDVI-PALSAR time series was used in a change detection framework to detect deforestation at a managed forest site in the tropics (*Pinus caribea*; size = 2859 ha). Three-monthly reference data covering the entire study area were used to assess the spatial and temporal accuracy. For the NDVI-only case, the validation data revealed a strong decrease of the spatial and temporal accuracy when the MD percentage was increased. The OA decreased from 93.1% for MD=org (~6.5 observations/year) to 54.2% for MD=95% (~0.5 observations/year), while the MTL increased from 1.67 to 5.7 months, respectively. In contrast, the accuracies for the fused NDVI-PALSAR case remained high with increasing MD and were observed to be above the NDVI- and PALSAR-only cases for all MD percentages due to consistent PALSAR time series of ~2 observations/year. For fused NDVI<sub>org</sub>-HVHH<sub>mt</sub> the OA increased to 95.5% and the MTL decreased to 1.59 month, which is close to the precision of the reference data.

For the first time, an optical-SAR time series fusion approach which exploits the entire temporal detail has shown significant improvements in deforestation detection accuracy in the tropics. Results shown here confirm previous studies that have highlighted the potential of SAR and optical data fusion (Lehmann et al. 2012; Reiche et al. 2013). We demonstrate that fusing single band Landsat and PALSAR time series using MulTiFuse always improves the accuracies of the single-sensor systems, even when dealing with persistent cloud cover. By increasing the observation density in the fused time series, MulTiFuse provides an opportunity to tackle the problem of missing data in SAR and optical time series.

Using the normalised inverted magnitude as a regression weight can improve the statistical significance and the correlation of the relationship between NDVI and PALSAR time series for most cases. However, a pixel-based weight optimization is required to account for exceptional cases where the weight does not result in an improved correlation. The p-value has proven to be a useful measure for the goodness of the correlation. A strong linear correlation was found for deforestation, whereas a weak correlation was observed for stable forest conditions.

Multi-temporal SAR filtering was found to strongly improve the correlation of the PALSAR time series observables with the NDVI time series, and in turn the accuracy of the deforestation map. Multi-temporal SAR filtering was found to be a mandatory pre-processing step when applying MulTiFuse to SAR data. Because of the relatively low observation frequency of medium resolution Landsat (~6.5 observations/year) and PALSAR (~2 observations/year) observations common to most tropical regions, the marginal seasonality of evergreen forest could not be modelled. This confirms

the results of previous studies (Zhang et al. 2009; Zhu et al. 2012). (Zhang et al. 2009) found that an observation density of ~25-60 (6 - 16 days temporal resolution) is necessary to reliably estimate vegetation phenology in remote sensing time series. A linear interpolation of time series observations was therefore found to be adequate (Eq. 4.2). However, given time series with a higher frequency of available observations, the interpolation of time series observations (Eq. 4.1 and 4.2) could also be done using a season-trend model after decomposing the time series (Verbesselt et al. 2010a).

The HVHH<sub>mt</sub> time series was observed to have the strongest correlation with the NDVI time series. The stronger correlation of HVHH<sub>mt</sub> with NDVI compared to that of HH<sub>mt</sub> and HV<sub>mt</sub> may be explained by the fact that the backscatter ratio of HV and HH partially compensates for environmental effects, such as changing moisture conditions. Increasing moisture over forest and open areas after a rainfall event, for example, leads to an increase of the backscatter for both HV and HH (Lucas et al. 2010). As a result, the optimized magnitude regression weight derived for HVHH<sub>mt</sub> is influenced to a lesser degree by environmental effects and therefore more robust. BFAST-monitor (BFM, Verbesselt et al. 2012) confirmed its capabilities as a tool for detecting changes in remote sensing time series, even when dealing with sparse Landsat-like and PALSAR time series. BFM, however, is designed for rapid detection of single change events in time series only. When dealing with monitoring periods much longer than the 2.75 years analysed here, the change detection framework needs to be expanded to detect multiple changes in a time series. Using BFAST instead of BFM enables the detection of e.g. multiple consecutive deforestation events. PALSAR HVHH<sub>mt</sub> and Landsat NDVI were shown to have a comparable sensitivity to deforestation, underlining the potential of upcoming L-band SAR missions (ALOS-2 PALSAR-2, SAOCOM-1, Tandem-L) as contributors to tropical forest monitoring. Future research should focus on how MulTiFuse and the proposed change detection framework performs when dealing with other metrics such as texture (Kuplich et al. 2005; Rakwatin et al. 2012), and time series that feature different detection sensitivities. This is of particular interest when making use of C-band SAR time series in combination with Landsat. C-band is less sensitive to forest cover changes compared to L-band (Mitchell et al. 2014), but the temporal resolution is higher for many tropical countries. The launch of ESA's Sentinel-1 mission (Torres et al. 2012) in 2014 and its free-of-charge data policy ensures the continuation of historical C-band SAR time series imagery from ERS-1/2 and ENVISAT ASAR (1992 - 2010) (Bonano et al. 2012).

We applied MulTiFuse to detect deforestation in cases where stems were removed immediately after logging. This practice causes a sharp decrease of both the NDVI and the HVHH<sub>mt</sub> signal resulting in a strong correlation of the time series signals. Varying harvest practices and unexpected natural disasters give rise to more complex dynamics. After a major storm event, for example, where fallen trees remain for a long period of time before removal, the HVHH<sub>mt</sub> signal increases immediately and remains at a higher level until the trees are removed. In the same manner, the

NDVI signal drops to a lower level. Because the direction of change in the NDVI and HVHH<sub>mt</sub> time series does not influence their correlation, a rather strong relationship may be expected. This enables the fusion of both time series and the subsequent detection of deforestation. In cases where stems remain only for a short period after logging, the HVHH<sub>mt</sub> signal initially increase before dropping to a low level after removal (Almeida-Filho et al. 2009, Whittle et al. 2012). When both time series cover the entire period of stable forest, logging, stems remaining on the ground and stem removal, a significant correlation may still be expected. The small number of HVHH<sub>mt</sub> observations acquired during the short period in which the stems remained on the ground may not have a large influence on the correlation. After fusion, however, a delayed detection is to be expected. Research is required to fully investigate the performance of MulTiFuse with respect to latter scenario and more subtle changes, such as forest degradation.

Although we applied MulTiFuse to Landsat and PALSAR data, it is not restricted to medium resolution optical and SAR data and can be used to fuse a variety of time series. Considering the multiple upcoming medium resolution optical, L- and C-band time series data sources, further research will focus on expanding MulTiFuse to fuse more than two univariate time series in parallel. A forest monitoring system combining historical and upcoming optical, C- and L-band SAR data streams of Landsat, Sentinel-1, Sentinel-2, SAOCOM-1 (*Microwave Earth Observation Satellites*) and ALOS-2 PALSAR-2 could address major problems faced by remote sensing in tropical countries, for example when implementing a consistent monitoring system for REDD+ (Herold & Skutsch 2011; Pelletier et al. 2011). Such a multi-sensor monitoring system may compensate for persistent cloud cover and for unexpected failures experienced by certain systems (e.g. ALOS failure in 2011; Rosenqvist et al. 2014). To use the upcoming data streams in the most beneficial way, addressing the need of a near-real time deforestation alert system based on medium spatial resolution (Xin et al. 2013), MulTiFuse should be further developed towards near-real time fusion capabilities.

## Acknowledgment

This work was funded by the European Community's Seventh Framework Programme (FP7) funded ReCover project (grant agreement 263075) and a Marie-Curie IRG grant within the FP7 to Jan Verbesselt (grant agreement 268423). We acknowledge Wolf Forstreuter from the Applied Geoscience and Technology Division of the Secretariat of the Pacific Community (SOPAC) for providing the local DEM and Fiji Pine Ltd. for providing the reference data set. Thanks to Dr. Oliver Kley from Technische Universität München for mathematical advice, Johannes Eberenz from Wageningen University for data pre-processing support, Ben DeVries and Christina May from Wageningen University for proof-reading the manuscript. The anonymous reviewers are thanked for their remarks.



**Chapter**

# 5

## **Combining Landsat and SAR time series in a Bayesian approach for near real-time deforestation detection in the tropics**

Johannes Reiche, Sytze de Bruin, Jan Verbesselt, Dirk H. Hoekman and Martin Herold

*Under Review in Remote Sensing of Environment*

## **Abstract**

*Detecting deforestation in near real-time (NRT) is essential for timely action against illegal logging in tropical regions. We present a novel Bayesian-based approach to combining multi-sensor SAR and optical time series for NRT deforestation detection. We estimated the normalised forest and non-forest probabilities for each individual time series observation using sensor specific forest and non-forest probability density functions. Potential deforestation was flagged in cases where the probability of forest became lower than 0.5. The probability of deforestation given the previous observations, the current observation, and upcoming observations was computed by Bayesian updating to confirm or reject a deforestation event. We applied the approach to Landsat NDVI and ALOS PALSAR L-band backscatter ratio (HVHH) time series to detect deforestation in a NRT scenario from 01/2008 to 09/2010 over a managed tropical forest plantation in Fiji (Pinus caribea, 2859 ha). The probability of deforestation of unconfirmed changes and the time of change of detected deforestation was provided at each time step. Three-monthly reference data (plantation operations) covering the entire study area was used to validate and assess spatial and temporal accuracy. We tested the impact of persistent cloud cover by increasing the per-pixel missing data percentage of the NDVI time series stepwise from ~53% (~6.5 observations/year) up to 95% (~0.5 observations/year) while combining with a consistent PALSAR time series of ~2 observations/year. While the spatial and temporal accuracy of detected deforestation decreases significantly with increasing missing data for the Landsat NDVI-only time series, the accuracy for the fused NDVI-HVHH case remained high and was observed to be above the NDVI- and HVHH-only cases for all missing data percentages. For the fused NDVI-HVHH case, the overall accuracy was between 87.4% and 90.6% with a mean time lag between 1.3 and 2.9 months for increasing NDVI missing data percentages. The presented approach is capable of combining observations from multiple time series and provides the opportunity to use upcoming free-of-charge, medium resolution optical and SAR satellite images data streams to improve NRT deforestation detection in the tropics.*

---

## 5.1 Introduction

Tropical deforestation accounts for 12% of global greenhouse gas emissions (Harris et al. 2012; van der Werf et al. 2009). The fundamental contribution of tropical forests to the Earth's biological diversity, the global economy and local welfare justifies its protection (Pan et al. 2011). Illegal and unsustainable logging activities cause a wide range of negative environmental effects, significant financial losses for developing tropical countries, and depression of the world timber price (Nellermann 2012). To reduce illegal and unsustainable deforestation activities, near real-time (NRT) detection of tropical deforestation is crucial for enabling governments and communities to enact immediate law enforcement (Assunção et al. 2013; Lynch et al. 2013; Wheeler et al. 2014).

Remote sensing based time series imagery is the only data stream capable of providing repetitive observations of global tropical forest areas in NRT (Hansen et al. 2013; Lynch et al. 2013). Here, NRT deforestation detection refers to the capacity to detect change in a satellite image once it is available. Current remote sensing based NRT monitoring systems are the Brazilian DETER system (Shimabukuro et al. 2006) and FORMA (Hammer et al. 2009), which is employed by the World Resources Institute Global Forest Watch platform (Showstack 2014). DETER uses MODIS time series imagery in order to provide fortnightly information on newly deforested areas at a resolution of 500 m. Due to the low spatial resolution, however, small-scale changes are missed (Anderson et al. 2005; Hammer et al. 2014), precluding a rapid response to many human-induced deforestation activities which tend to be small-scale (DeVries et al. 2015; Tyukavina et al. 2013).

Medium (Landsat-like) resolution time series imagery have been proven to be capable of operationally detecting smaller scale changes in forest cover from local to global scales (Achard et al. 2014; Griffiths et al. 2013; Hansen et al. 2013; Hirschmugl et al. 2014; Huang et al. 2010; Kennedy et al. 2010; Lehmann et al. 2013; Masek et al. 2013; Pflugmacher et al. 2012; Souza et al. 2013; Potapov et al. 2012; Zhu et al. 2012; Zhu & Woodcock 2014). However, most studies in tropical regions fail to exceed annual resolution. Missing data due to frequent cloud cover is the main factor limiting optical remote sensing methods in tropical regions (Asner 2001; Hirschmugl et al. 2014; Souza et al. 2009; Souza et al. 2013). Increasing missing data is related to a strong decrease in spatial and temporal deforestation detection accuracy (Reiche et al. 2015). Sparse observations prohibit rapid change detection and in turn the provision of more frequent deforestation information. (Assunção et al. 2013) found that a 17% increase in cloud cover in DETER data leads to an 11% decrease in environmental fines, proving that monitoring systems relying on optical data only are not consistent. Several time series approaches for NRT change detection have been developed to exploit the full temporal detail of time series (Hammer et al. 2014; Verbesselt et al. 2012; Zhu et al. 2012; Xin et al. 2013). However, a number of shortcomings have been identified in these methods. First, all introduced methods were demonstrated with imagery from optical sensors, and only

in areas where a large number of observations were available. Second, the performance of the methods in tropical regions and under persistent cloud cover was not investigated. Finally, temporal accuracy of available deforestation monitoring methods has only been assessed on a yearly basis. Often the Landsat time series data itself has served as reference data. Providing annual deforestation information only, however, does not allow for rapid responses to illegal logging activities (Lynch et al. 2013).

Synthetic Aperture Radar (SAR) is not affected by cloud cover and can provide continuous time series information. Therefore SAR data are seen ideal complement to optical-based forest monitoring systems (Herold 2009; Lu et al. 2014; De Sy et al. 2012). In particular, multi-temporal L-band SAR backscatter imagery have been proven suitable for detecting tropical deforestation (Almeida-Filho et al. 2007; Almeida-Filho et al. 2009; Motohka et al. 2014; Reiche et al. 2013; Rosenqvist et al. 2014; Simard et al. 2000; Thapa et al. 2013; Whittle et al. 2012), even at a global-scale (Shimada et al. 2014). Due to the high penetration depth of L-band into the canopy, disturbed and undisturbed forest are more contrasted than in C-band data (Luckman et al. 1997; Ribbes et al. 1997). For most tropical countries, however, the density of medium resolution C- and L-band SAR observations is low, with only a small number of images available per year (Rosenqvist et al. 2007). This challenges effective NRT forest monitoring.

Fusing SAR and Landsat time series imagery has been shown to increase deforestation detection accuracy (Lehmann et al. 2012; Lehmann et al. 2015; Reiche et al. 2013; Reiche et al. 2015). Fusion approaches can be used to address the problem of missing data in a time series (Dunsmuir & Robinson 1981; Honaker & King 2010; Racault et al. 2014) by increasing the observation density, which helps to decrease the delay to detection of deforestation (Hussain et al. 2013; Zhang 2010; Reiche et al. 2015). Various challenges, including accurate co-registration and dealing with spectral variation in the time series (Zhang 2010), have to be addressed when designing a SAR-optical time series approach (Lu et al. 2014). Medium resolution optical and SAR remote sensing time series observations share specific characteristics that inhibit direct correlation, integration and/or fusion. They are discrete, their individual observations are non-equidistant in time, their observation times are not identical and their scales/units are not directly compatible (Reiche et al. 2015). A pixel-based Multi-sensor Time series correlation and Fusion approach (MultiFuse) to fuse optical and SAR time series for detecting deforestation has been proposed to combine the advantages of optical and SAR observations for forest change detection (Reiche et al. 2015). MultiFuse has been used to fuse Landsat NDVI and PALSAR backscatter time series. The fused time series were used in a change detection framework to detect deforestation. Spatial and temporal accuracies for the fused NDVI-PALSAR case were consistently higher than those of the NDVI- and PALSAR-only cases for increasing percentages of missing data in the NDVI time series. MultiFuse is not applicable for NRT detection/application, however.

Bayesian classification frameworks (Strahler 1980) have been shown to be widely applicable to the analysis of single-sensor time series and the fusion of optical and SAR time series. Single-sensor applications include monitoring of annual land cover changes (Symeonakis et al. 2012; Kiiveri & Caccetta 1998; Kiiveri et al. 2001; Lehmann et al. 2013), soil moisture (Notarnicola 2014; Pierdicca et al. 2010; Pierdicca et al. 2014) and lake dynamics (Eilander et al. 2014). Fusing multi-temporal Landsat and SAR data for land cover classification was demonstrated by Solberg et al. (1994) and Bruzzone et al. (1999). Solberg & Huseby (2008) used a Bayesian framework for fusing Landsat and SAR time series to monitor snow cover states. The authors proposed a Hidden Markov Model, where the probability of a SAR or Landsat observation being in a certain snow state was calculated by the observation itself and external transition probabilities. Lehmann et al. (2012; 2015) expanded an existing Bayesian multi-temporal processing framework (Kiiveri et al. 2001; Kiiveri & Caccetta 1998) that is operationally used for mapping annual land cover changes (Lehmann et al. 2013) to fuse annual Landsat with ALOS PALSAR mosaics.

To date, there is no approach that combines the advantages of medium resolution optical and SAR time series and utilizes the entire temporal detail for NRT deforestation detection. The impending stream of free-of-charge medium resolution optical and SAR imagery from sensors such as Landsat, Sentinel-1, Sentinel-2, SAOCOM-1 (CEOS 2014) and the continuation of L-band SAR imagery (ALOS 2 PALSAR 2) stresses the need for further research in SAR-optical fusion methods (Reiche & Herold 2012; Lu et al. 2014). In particular, research on NRT deforestation alert systems based on medium resolution data (Xin et al. 2013) is required in order to support consistent global forest monitoring (GFOI 2013). We propose a novel probability-based approach to combine multi-sensor time series for NRT deforestation detection. We apply the approach to Landsat NDVI and ALOS PALSAR L-band backscatter time series to detect deforestation in a NRT scenario, aiming for both timelier and more accurate detection. The output is a deforestation map that is validated with quarterly (three-monthly) reference data covering the entire study area.

## **5.2 Materials and methods**

### **5.2.1 Bayesian multi-sensor time series combination for NRT deforestation detection**

Here we present a novel Bayesian-based approach to combine multi-sensor optical and SAR time series for NRT deforestation detection. Figure 5.1 illustrates the main steps for applying the approach to multi-sensor time series, whereby we considered a NRT environment with past, current and future observations (Section 5.2.1.1). First (Step 1, Section 5.2.1.2), the normalised probabilities for forest and that of non-

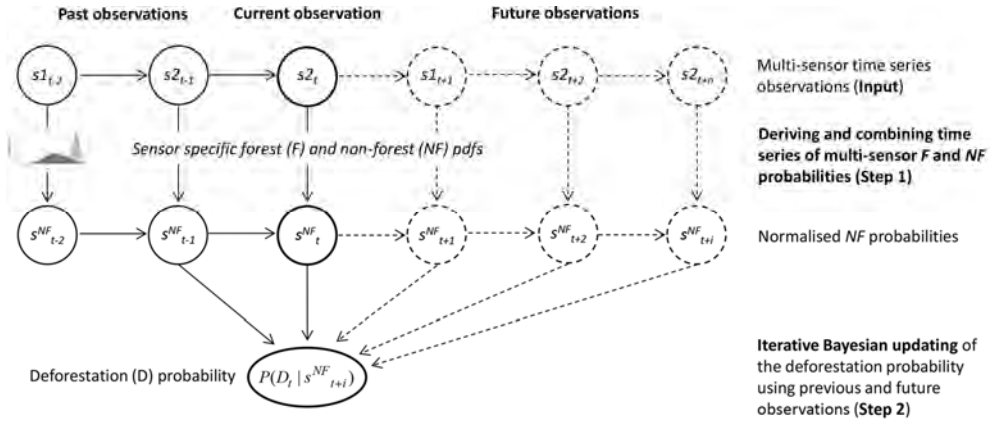


**Figure 5.1** Schematic overview of the proposed Bayesian approach to fuse two multi-sensor time series and detect deforestation in NRT.  $s1$  and  $s2$  refer to past, current and future time series observations from a sensor 1 (e.g. optical) and sensor 2 (e.g. SAR), respectively.

forest are estimated for each individual time series observation, using the corresponding sensor specific forest (F) and non-forest (NF) probability density functions (pdfs). Secondly, (Step 2, section 2.1.4) observations at time  $t$  are flagged to be potentially deforested in case the NF probability exceeds 0.5. For a flagged observation, the probability of deforestation is computed by iterative Bayesian updating, using the previous observation ( $t-1$ ), the current observation ( $t$ ), as well as  $i$  upcoming observations ( $t+i$ ) to confirm or reject a deforestation event at  $t$ .

### 5.2.1.1 Multi-sensor time series observations (Input)

Let  $s1, \dots, sn$  be discrete time series derived from *sensor-1, ..., sensor-n*, where observations are non-equally spaced in time and observation times are non-identical between sensors. Let assume that all images comprising the multi-sensor time series are co-registered and appropriately transformed into the same spatial resolution. We can express the observation times of  $s1, \dots, sn$  in the form  $T_{s1} = \{t^{s1}_1, t^{s1}_2, \dots, t^{s1}_{k_{s1}}\}$  and  $T_{sn} = \{t^{sn}_1, t^{sn}_2, \dots, t^{sn}_{k_{sn}}\}$  with  $k_{s1}$  and  $k_{sn}$  being the number of  $s1$  and  $sn$  observations, respectively. Similarly, time series observations are denoted  $s1_t, \dots, sn_t$  at  $t \in T_{s1}, \dots, T_{sn}$ . Newly acquired observations are immediately processed and appended to the respective time series for NRT detection.

### 5.2.1.2 Deriving and combining time series of multi-sensor F and NF probabilities (Step 1)

Sensor specific F and NF pdfs are fitted to F and NF training data using a maximum likelihood procedure. Next, the conditional densities of the time series observations,  $s1$ , given the presence of forest and non-forest,  $p(s1|F)$  and  $p(s1|NF)$  are computed. The normalised F probabilities,  $P(F|s1)$ , are computed from these conditional

densities as follows:

$$P(F|s1_t) = \frac{p(s1_t|F)}{p(s1_t|F) + p(s1_t|NF)} \text{ for } t \in T_{s1} \quad (5.1)$$

The normalised NF probabilities are computed as  $P(NF|s1) = 1 - P(F|s1)$ . Since  $P(NF|s1)$  is used in Bayesian updating using previous and future observations, we wanted to avoid extreme probabilities which imply absolute certainty about either state F or NF. Therefore we introduce a block weighting function that modifies the  $P(F|s1)$  at 0.1 and 0.9. Defining  $P(F|sn_t)$  analogously to  $P(F|s1_t)$ , the combined time series composed of normalised F probabilities,  $s^F$ , is computed as:

$$s^F_t = \begin{cases} P(F|s1_t) & : t \in T_{s1} \\ \vdots & \vdots \\ P(F|sn_t) & : t \in T_{sn} \end{cases} \quad (5.2)$$

The combined time series composed of normalised NF probabilities,  $s^{NF}$  is computed as  $s^{NF} = 1 - s^F$ .

### 5.2.1.3 Iterative Bayesian updating (Step 2)

Each new observation at time  $t$  is checked for potential deforestation and is assigned a flag  $\lambda = 1$  if  $s^{NF}_t > 0.5$  (deforestation) and a flag  $\lambda = 0$  (no deforestation) otherwise. If  $\lambda_t = 1$  at  $t = \text{current}$ , then the probability for a deforestation event ( $D$ ) at  $t$  is calculated using Bayesian probability updating by taking the previous observation  $t-1$  and the upcoming observations  $t+i$  into account:

$$P(D_t | s^{NF}_{t+i}) = \frac{P(s^{NF}_{t+i} | D)P(D_t | s^{NF}_{t+i-1})}{P(s^{NF}_{t+i} | D)P(D_t | s^{NF}_{t+i-1}) + P(s^{NF}_{t+i} | \bar{D})P(\bar{D}_t | s^{NF}_{t+i-1})} \quad (5.3)$$

, with  $i$  referring to the  $i$ -th future observation that can take values between  $i = 0, \dots, n$ , and  $\bar{D}$  denoting non-deforestation. The probability for deforestation at  $t$ ,  $P(D_t | s^{NF}_t)$  is repeatedly updated using (Eq. 5.3). For the initial step ( $n = 0$ ),  $P(D_t | s^{NF}_t)$  is calculated with the normalised NF probability at  $t = \text{current}$  ( $s^{NF}_t$ ) being the new evidence for deforestation and the NF probability at the previous time step ( $s^{NF}_{t-1}$ ) being the *prior* probability. In the subsequent steps ( $n > 0$ ), the *posterior*  $P(D_t | s^{NF}_{t+i})$  is repeatedly updated using future observations ( $s^{NF}_{t+i}$ ) along with the *posterior* of the previous iteration as *prior*  $P(D_t | s^{NF}_{t+i-1})$ .

The iterative Bayesian updating is stopped and deforestation is detected in case  $P(D_t | s^{NF}_{t+i}) \geq \chi$ , with  $\chi$  being a defined threshold. In case  $P(D_t | s^{NF}_{t+i})$  decreases below 0.5 after it has been flagged ( $i > 0$ ), we assume a false detection and set  $\lambda_t = 0$ . The next observation is then checked for possible deforestation.

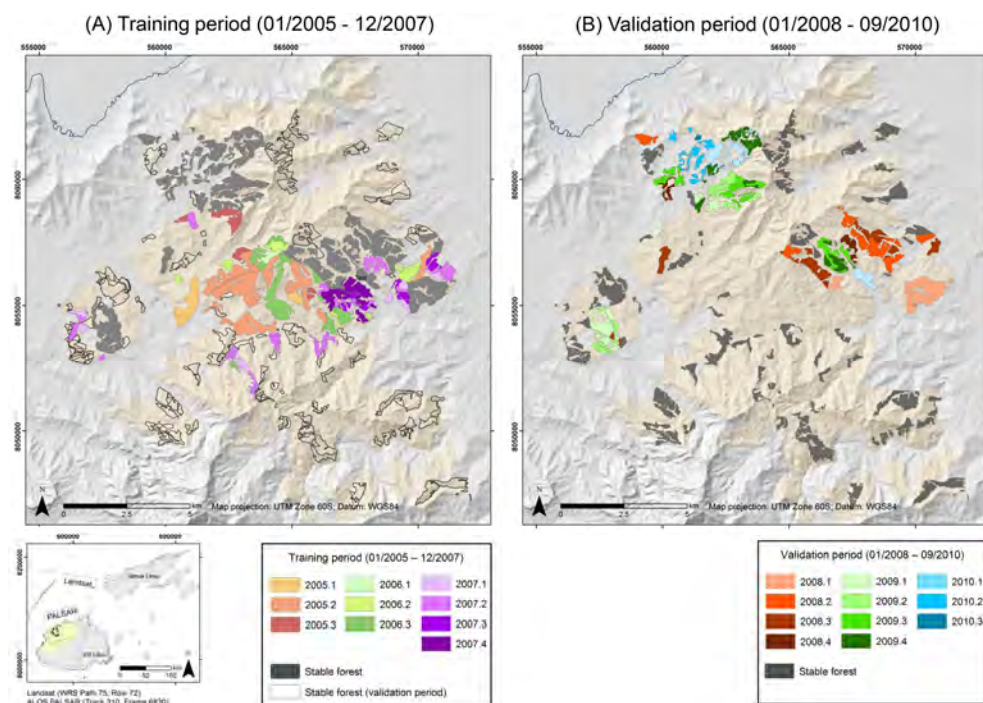


**Figure 5.2** The *Lololo* softwood concession (*Pinus caribea*) located in north western part of the Viti Levu, Fiji islands. Stable forest and logged forest stands with logging information at quarterly intervals are depicted for the training period (A, 01/2005 - 12/2007) and the validation period (B, 01/2008 - 09/2010). The stable forest areas of the validation area are also outlined for the training period.

## 5.2.2 Validation

### 5.2.2.1 Study area

The Lololo Fiji Pine Ltd. lease is a fully managed softwood forest plantation (*Pinus caribea*) located in the north western part of the Viti Levu Island, Fiji (Lat. 17.32° S, Lon. 177.37° E) (Figure 5.2). Viti Levu, the main island of the Fijian archipelago, lies in the seasonal tropics and experiences persistent and strongly varying cloud cover (Ash 1992). For the Lololo Fiji Pine Ltd. lease, detailed spatial inventory data of 623 forest stands (9570 ha) are available, comprising quarterly (three-monthly) harvesting information from 2000 - 2013 and replanting information dating back to 1975. The quarterly periods are denoted as 2008.1 and 2008.2 for the periods 01/2008 - 03/2008 (day of year (DOY): 2008.1 - 2008.90) and 04/2008 - 06/2008 (DOY: 2008.91 - 2008.181), respectively. Logging cycles have an average turnover rate of 15 - 20 years. During logging activities, forest stands are fully harvested within a very short period and stems are removed immediately after logging. Subsequently, forest stands are replanted entirely. Forest stands remaining

unlogged over a long period (greater than 10 years) are covered with full-grown pine. For this study, we define a training period (01/2005 - 12/2007) and a validation period (01/2008 – 09/2010). During the training period, sensor specific F and NF pdfs are derived to parameterise the proposed approach to subsequently detect deforestation in the validation period. For both periods, separate forest masks were derived from the inventory data. The forest mask for the training period (Figure 5.2A) accounts for 3020 ha and includes forest stands planted before 01/1995, and not logged before 01/2005. Of those forest stands, 1464 ha were logged during the training period (01/2005 - 12/2007). The forest mask for the validation period (Figure 5.2B, 01/2008 - 09/2010) accounts for 2859 ha and includes all forest stands planted before 01/2000, and not logged before 01/2008. Of those forest stands, 1395 ha were logged during the validation period and 1464 remained forest. Stable forest areas for the validation period do not overlap with the stable forest areas of the training period, ensuring an independent validation of the deforestation results. In Figure 5.2A, stable forest areas of the validation period are overlaid with the training period dataset.

### 5.2.2.2 Landsat NDVI data

All available Level 1 Terrain (corrected) (L1T) Landsat 7 ETM+ images (Quality: 9) for the Worldwide Reference System (WRS) Path 75 and Row 72 acquired between 01/2005 and 09/2010 were used (downloaded from USGS GLOVIS portal) (Table 5.1). In total, 82 images were used. Landsat time series processing was performed using a standard processing chain consisting of Fmask and LEDAPS, a procedure which has been successfully applied in a number of recent studies dealing with large amounts of Landsat time series data (Hansen et al. 2013; Xin et al. 2013; Zhu et al. 2012; Zhu & Woodcock 2014). Each Landsat image was processed individually. Based on the uncorrected Landsat data in digital numbers, Fmask (Function of mask, Zhu & Woodcock 2012) was used to mask clouds, cloud shadow and Landsat-7 SLC-off-data gaps. Fmask is a fully automated object oriented approach that uses the optical and thermal Landsat bands. When dealing with consistent cloud cover and/or scatter clouds, some cloud edges may remain after masking (Zhu & Woodcock 2012; Xin et al. 2013; Zhu & Woodcock 2014). Atmospheric correction was performed using the Landsat Ecosystem Disturbance Adaptive Processing System (LEDAPS) tool (Vermote et al. 1997; Masek et al. 2006; Schmidt et al. 2013) to convert digital numbers to surface reflectance.

**Table 5.1.** Frequency by year of Landsat 7 ETM+ and ALOS PALSAR FBD observations for 2005-09/2010.

Year	Training period			Validation period		
	2005	2006	2007	2008	2009	09/2010
Nr. of Landsat images	12	14	13	16	14	13
Nr. of ALOS PALSAR FBD images			3	3	1	2

**Table 5.2** Approximate number of per-pixel observations per year for the original (org, mean 53%) Landsat NDVI time series, and for Landsat NDVI time series with increased 70, 80, 90, and 95% missing data (MD).

Per-pixel MD	Approximate number of per-pixel observations per year
No MD (0%)	12.3
org (35 – 69%) (mean 53%)	3.8 – 9.25 (mean 6.5)
70%	3.8
80%	2.5
90%	1.2
95%	0.6

The processed images (30 m spatial resolution) were re-projected to WGS 84 / UTM zone 60S. Clouds, cloud shadows and SLC-off gaps were masked as missing data.

Per-pixel missing data (MD) was calculated based on the processed NDVI stack (WRS Path 75 Row 72) that covers the western part of Viti Levu (Figure 5.2). MD varies from 35% to 69% and averages 53% for the validation area, but increases up to 96% for other areas covered by the NDVI stack. By randomly excluding observations on a pixel basis, we increased the per-pixel percentage of MD from an average of 53% for the original (org) Landsat time series stack to 70, 80, 90 and 95%. Table 5.2 lists the approximate number of per-pixel observations per year for the original (org) and the increased MD Landsat time series stacks, ranging from 6.5 to 0.6 observations/year for 53% (org) and 95% MD, respectively.

### 5.2.2.3 ALOS PALSAR data

Multi-temporal L-band SAR data were obtained from the phased array L-band synthetic aperture radar sensor aboard the advanced land observing satellite (ALOS PALSAR) for 2007 - 2010 (Shimada et al. 2010). All archived data acquired in Fine Beam Dual (FBD) mode for Track 310 and Frame 6830 were used for time series processing. The time series consists of 9 dual-polarized FBD images (HH and HV polarisation). All images were acquired in ascending mode with an incidence angle of 34.3° and were provided in Level 1.1 format.

Pre-processing of ALOS PALSAR FBD images was done independently for each image, using the Gamma software package (Werner & Strozzi 2000). Pre-processing included multi-looking, radiometric calibration using standard calibration coefficients (Shimada et al. 2009), topographic normalization as described by Hoekman et al. (2010), and geocoding to 25 m pixel resolution (WGS84, UTM 60S) using a local 30 m DEM. Visual comparison with Landsat and high resolution satellite imagery showed very good geocoding accuracy (around 0.5 pixel error). Among the different pre-processed images, no significant geolocation errors were visible. The individual HH and HV images were stacked to create HV and HH time series stacks. The stacks were subsequently resampled to the 30 m Landsat pixel cells. Overlapping pixels with the same spatial resolution are required to fuse at pixel level. By subtracting the HV and HH backscatter time series, a HVHH backscatter

ratio time series was derived (HVHH). Steep topography in the validation area ranging from 0 to 48 degrees resulted in SAR layover and shadow areas accounting for 0.73 ha. In addition to the general SAR pre-processing steps, adaptive multi-temporal SAR filtering (Quegan & Yu 2001) was applied to the pre-processed FBD time series. A measured increase in the equivalent number of looks indicated a clear reduction of SAR speckle in the data. This reduction is crucial for analysing the data at pixel level. In addition, no significant changes in the mean radiometric characteristics were observed. Multi-temporal filtered backscatter ratio is hereafter referred to as  $HH_{mt}$ ,  $HV_{mt}$ , and  $HVHH_{mt}$ .

For the remaining analysis we only considered  $HVHH_{mt}$ , as previous results have shown that the  $HVHH$  backscatter ratio is more sensitive to deforestation than  $HH$  or  $HV$  (Reiche et al. 2015; Zeng et al. 2014). This may be explained by the fact that the ratio of  $HV$  and  $HH$  ( $HVHH$ ) partially compensates for environmental effects, such as changing moisture conditions (Reiche et al. 2015). Increasing moisture over forest and open areas after a rainfall event, for example, leads to an increase in the backscatter for both  $HV$  and  $HH$  (Lucas et al. 2010).

#### 5.2.2.4 Deriving F and NF pdfs

F and NF distributions were derived separately for Landsat  $NDVI_{MD}$  ( $MD=org, 70, 80, 90$  and  $95\%$ ) and ALOS PALSAR  $HVHH_{mt}$  using stable forest and change areas in the training period. To derive F distributions, all-time series observations covered by stable forest were considered. To derive NF distribution, only time series observations acquired at non-forest conditions immediately after deforestation events were used. To account for the precision of the reference data (0.25 years), only observations acquired between 0.25 – 0.75 years after logging were considered. During this period, NF conditions can be expected, even in the case of immediate replanting. We considered observations acquired during the entire year to derive F and NF distributions. Because of the low observation frequency of Landsat (~6.5 observations/year) and PALSAR (~2 observations/year), a situation commonly encountered in most tropical regions, only marginal seasonality of evergreen forest is visible. Therefore, we assumed non-seasonality over stable forest, which is justified by other studies (Zhang et al. 2009; Zhu et al. 2012) and previous work using the same dataset (Reiche et al., 2015). Images affected by remaining clouds over F and NF areas as a result of an imperfect cloud mask (Xin et al., 2013; Zhu and Woodcock, 2012, 2014) that would bias the distributions were removed manually. 12 of the 39 images available for the training period were removed. We evaluated the separability of the F and NF distributions for  $NDVI_{MD}$  and  $HVHH_{mt}$  using the normalised Jeffreys-Matusita distance (JM) (Laliberte et al. 2012). JM has a finite dynamic range from 0 (inseparable) to 2 (separable). A model was fitted separately to each of the derived univariate F and NF distributions by maximum-likelihood fitting using an iterative optimisation method (Venables & Ripley 2002). Gaussian, Gamma and Weibull models were tested and the Kolmogorov-Smirnov (K-S) test was

used for assessing goodness of fit (Conover 1971). The K-S test statistic D-values indicate the maximum distance between the cumulative pdfs to the modelled distribution and the sample distribution. The model resulting in the lowest D values was selected. The K-S test is available in the *stats* package for R.

### 5.2.2.5 Detecting deforestation in a NRT scenario

To validate the method for NRT deforestation detection we simulated a NRT scenario for the validation period. From the start of the validation period (01/2008) onwards, individual NDVI<sub>MD</sub> and HVHH<sub>mt</sub> observations were added chronologically to the time series until the end of the validation period (09/2010). For detecting deforestation, the proposed approach was applied to each newly added observation. Subsequent observations were handled as future observations. The output for each desired time step is a deforestation map showing the probability of deforestation for unconfirmed changes (soft information) and the time of change for confirmed changes (hard information).

First, we analysed the single-sensor results for increasing  $\chi$  from  $\chi = 0$  to  $\chi = 1$  in steps of 0.025 and compared them for HVHH<sub>mt</sub> and NDVI<sub>org</sub>. In addition, we analysed  $\bar{n}$ , the mean number of future observations used to confirm the change ( $n$ ). Based on these results, simple rules were defined for the fused NDVI<sub>MD</sub>-HVHH<sub>mt</sub> case with which we aimed for a high overall accuracy (OA) and rapid detection of change. We applied the same rules to NDVI<sub>MD</sub>-only and HVHH<sub>mt</sub>-only and fused NDVI<sub>MD</sub>-HVHH<sub>mt</sub> cases and compared them for increasing MD.

We assessed both the spatial and temporal accuracy of the detected deforestation. Spatial accuracy was defined as the overall accuracy, which is inversely related to omission and commission errors of detected changes. The temporal accuracy refers to the extent to which timing of the detected changes are correct. Available reference data that covers the entire study area allowed a map comparison. A major advantage of map comparison compared to common probabilistic sampling methods is that no sampling errors are introduced (Stehman 2009), since the number of pixels in the deforestation map represents the sample unit. To account for mixed pixels on the edges of the reference polygons, we only included a pixel if at least two-thirds of the pixel covers the reference polygon. To assess the spatial accuracy, a confusion matrix was derived (Foody 2002; Olofsson et al. 2013; Olofsson et al. 2014) from the deforestation and no-change class. We calculated the OA, the omission error (OE) and commission error (CE) of the deforestation class following (Olofsson et al. 2014). Temporal accuracy was assessed by calculating the mean time lag between the time at which correctly detected changes were initially flagged (MTL<sub>F</sub>) and the time at which the change was confirmed (MTL). For each correctly detected change pixel, the time at which the change was first flagged (T<sub>F</sub>) and the time at which it was confirmed (T) were

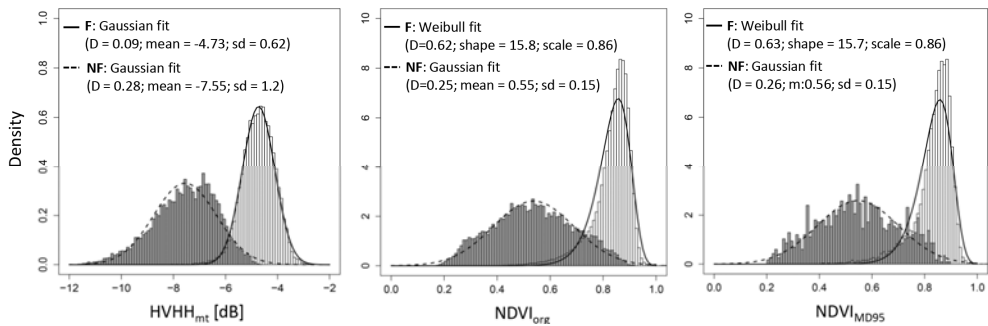


**Figure 5.3** HVHH<sub>mt</sub>, NDVI<sub>org</sub> and NDVI<sub>MD95</sub> distributions for F (dark grey) and NF (light grey) overlaid with the modelled pdfs. The K-S test statistic D values of the fitted distribution models are given. Mean and standard deviation (sd) of the Gaussian fit and shape and scale parameter of the Weibull fit are given.

converted to quarterly periods, after which the time differences with the validation data were calculated. The MTL<sub>F</sub> and MTL were calculated as the mean of the time differences of all correctly detected change pixels and was given in months. The MTL<sub>F</sub> provides the time lag until change events are indicated and allows identification of early detections. It is important to analyze the MTL<sub>F</sub> and MTL jointly with the OE, because the MTL<sub>F</sub> and MTL are calculated based on correctly detected changes only.

## 5.3 Results

### 5.3.1 Deriving F and NF pdfs

Figure 5.3 depicts the F and NF distributions for HVHH<sub>mt</sub>, NDVI<sub>org</sub> and NDVI<sub>MD95</sub> overlaid with fitted pdfs. HVHH<sub>mt</sub> was found to have the highest F - NF class separability (JM = 1.39) when compared to NDVI<sub>org</sub> (JM = 1.17) and NDVI<sub>MD95</sub> (JM = 1.13). The K-S test statistic D-values indicated a Gaussian model as the best fit for the HVHH<sub>mt</sub> F and NF distributions as well as for the NDVI<sub>org</sub> and NDVI<sub>MD95</sub> NF distributions. For NDVI<sub>org</sub> and NDVI<sub>MD95</sub> F distributions, a Weibull model resulted in the best fit for distributions with D-values slightly below the D-values for a Gaussian model (D = 0.62 for Weibull model vs. D = 0.65 for Gaussian model). Figure 5.3 also provides the mean and standard deviation (sd) describing the Gaussian pdfs and the shape and scale parameter describing the Weibull pdfs. The derived parameter for NDVI<sub>org</sub> and NDVI<sub>MD95</sub> were found to be consistent for increasing MD. Thus, we used the parameters found for NDVI<sub>org</sub> for all MD.

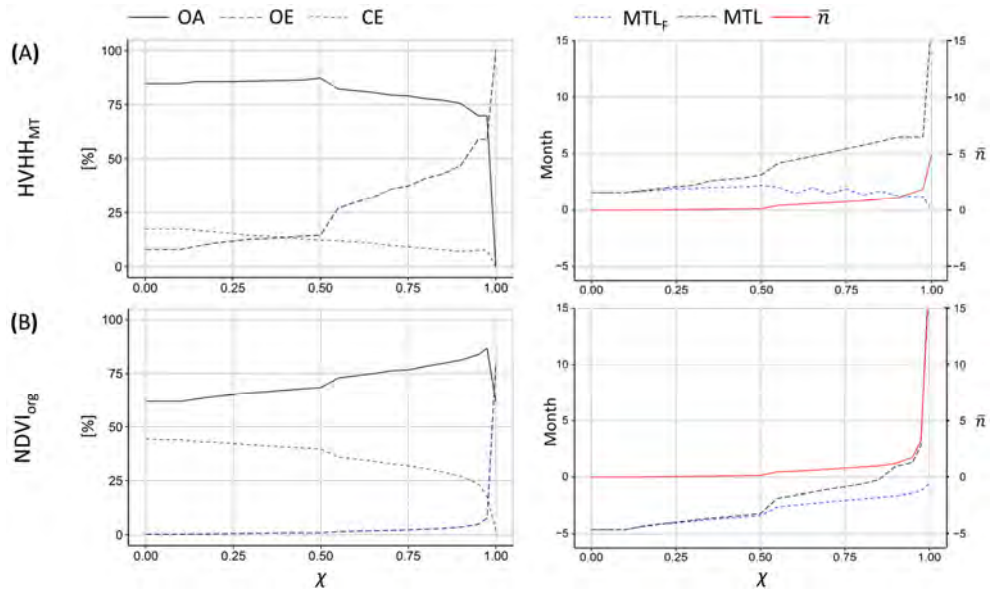


**Figure 5.4** Spatial accuracy (OA - overall accuracy, OE - omission error, CE - commission error), temporal accuracy (MTL<sub>F</sub> - mean time lag of flagged changes, MTL - mean time lag of confirmed changes) and the mean number of future observations used to confirm a deforestation event ( $\bar{n}$ ) as a function of  $\chi$  separately for HVHH<sub>mt</sub> and NDVI<sub>org</sub>.

### 5.3.2 Detecting deforestation in a NRT scenario

#### 5.3.2.1 Single-sensor results for increasing $\chi$

Figure 5.4 shows the spatial accuracy (OA, OE, CE) and the temporal accuracy (MTL<sub>F</sub>, MTL) as well as  $\bar{n}$  as a function of  $\chi$ , separately for HVHH<sub>mt</sub> and NDVI<sub>org</sub>. The results can be summarised as follows. For both, HVHH<sub>mt</sub> and NDVI<sub>org</sub>, an increasing  $\chi$  was observed to result in a decreasing CE and an increasing OE, MTL<sub>F</sub>, MTL and  $\bar{n}$ .

For HVHH<sub>mt</sub> (Figure 5.4A), the OA was found to slightly increase with increasing  $\chi$  from  $\chi = 0$  and was highest for  $\chi = 0.5$  (OA = 87.3%, OE = 14.5%, CE = 12.2%). For  $\chi = 0.5$  a MTL<sub>F</sub> and MTL of 2.2 and 3.2 months was observed, respectively and  $\bar{n}$  was found to be 0.12. For increasing  $\chi > 0.5$  the OA decreases consistently.

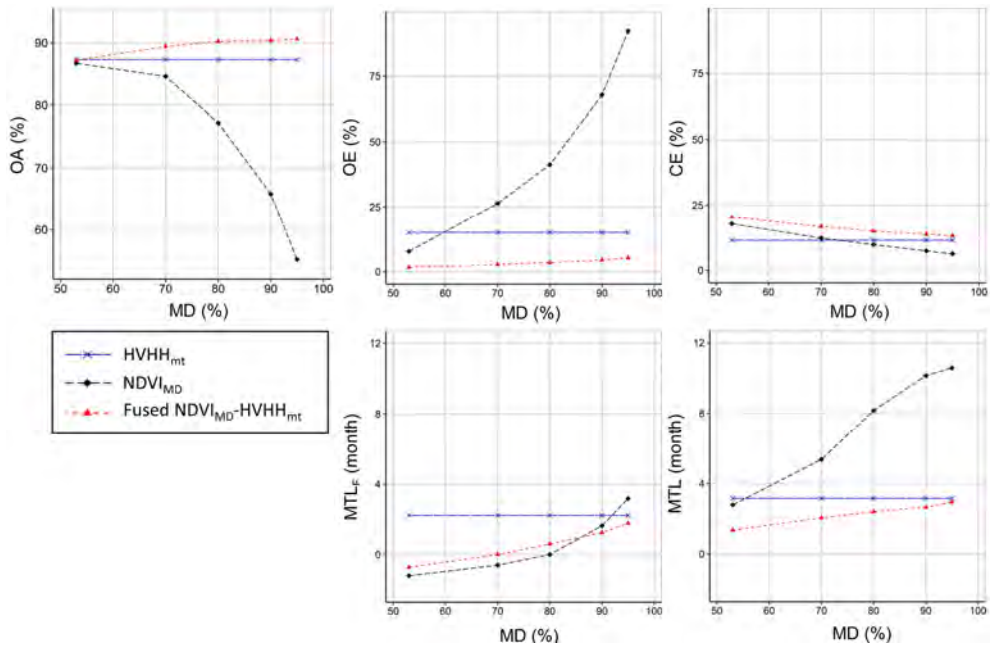
For NDVI<sub>org</sub> (Figure 5.4A), the OA was observed to consistently increase with increasing  $\chi$  and was highest for  $\chi = 0.975$  (OA = 86.7, OE = 7.8%, CE = 17.8%). For  $\chi > 0.975$ , the OA dropped due to a strongly increasing OE. At  $\chi = 0.975$ , a MTL<sub>F</sub> and a MTL of -1.2 and 2.8 months, respectively was observed and  $\bar{n}$  was found to be 1.75. The MTL<sub>F</sub> was observed to increase from -4.6 to -1.2 months with increasing values of  $\chi$  from 0 to 0.975, respectively. While MTL<sub>F</sub> of -1.2 month is within the precision of the reference data ( $\pm 1.5$  month), lower values clearly reflect an early detection, which is confirmed by a high CE. Early detections can be explained by spectral

variations in the NDVI time series and remaining clouds that results in low NDVI values. The results show that using a fixed value for  $\chi$  does not lead to consistent results for HVHH<sub>mt</sub> and NDVI<sub>org</sub> when aiming for the highest OA. The highest OA were found for a  $\chi$  for which the OE and CE are approximately equal, meaning that on the whole the map is unbiased. The changes in spatial and temporal accuracies for increasing  $\chi$  strongly depend on the time series metrics and their observation density and stability over time. Based on the findings described above and aiming for the highest OA, the following simple rules were defined for the fused NDVI<sub>MD</sub>-HVHH<sub>mt</sub> case. We used  $\chi = 0.5$  for new HVHH<sub>mt</sub> observations, and  $\chi = 0.975$  for new NDVI<sub>MD</sub> observations. In addition, a deforestation label was only assigned if  $s^{NF} > 0.5$  was found given the new observation. We applied the same rules to NDVI<sub>MD</sub> and HVHH<sub>mt</sub> and fused NDVI<sub>MD</sub>-HVHH<sub>mt</sub> cases and compared them for increasing MD. The results are presented in the next section.

### 5.3.2.2 Multi-sensor results

Figure 5.5 shows the spatial accuracy (OA, OE, CE) and the temporal accuracy (MTL<sub>F</sub>, MTL) as a function of MD for the NDVI<sub>MD</sub>-only, HVHH<sub>mt</sub>-only and fused NDVI<sub>MD</sub>-HVHH<sub>mt</sub> cases. The accuracy assessment results can be summarised as follows:

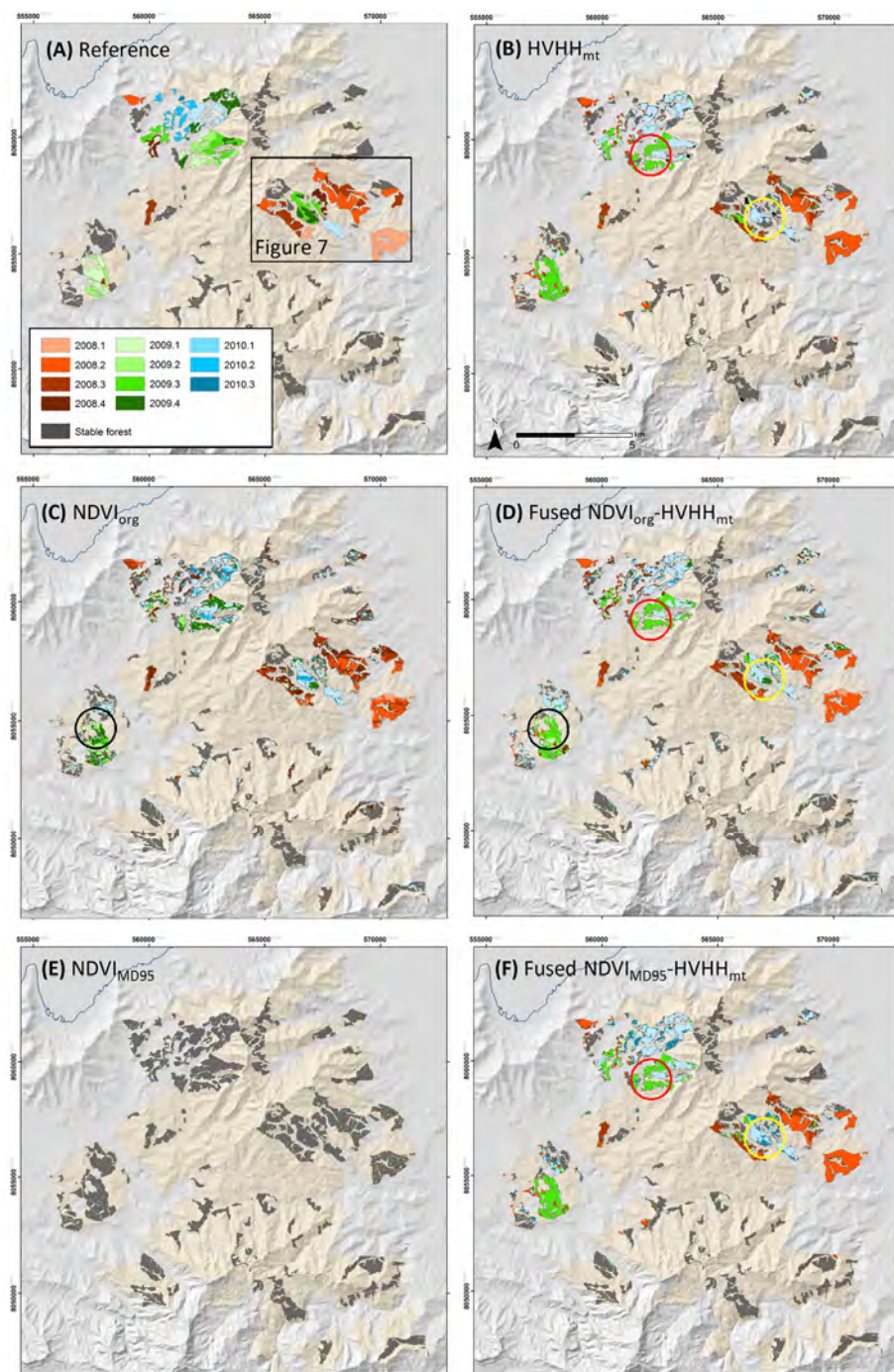
- (i) For HVHH<sub>mt</sub>-only the results are identical to the results observed for  $\chi = 0.5$  and outlined in the previous section (OA = 87.3%, OE = 14.5%, CE = 12.2%, MTL<sub>F</sub> = 2.2 month, MTL = 3.2 month).
- (ii) For NDVI<sub>MD</sub>-only, a strong decrease in the spatial and temporal accuracy was observed with increasing MD. Compared to HVHH<sub>mt</sub>-only, a slightly lower spatial accuracy (OA = 86.7, OE = 7.8%, CE = 17.8%) was observed for MD=org. The OA dropped from 86.7% for MD=org to 55.2% for MD=95, mainly due to increasing omitted changes. For MD=95, the OE reached 92.2% and the CE slightly decreased to 6.3%. The strong reduction of the observation density with increasing MD led to a strong decrease in temporal accuracy. The MTL<sub>F</sub> dropped from -1.2 (MD=org) to 3.2 months (MD=95) and the MTL decreased from 2.8 (MD=org) to 10,6 months (MD=95).
- (iii) For fused NDVI<sub>MD</sub>-HVHH<sub>mt</sub>, an improved spatial and temporal accuracy was found compared to NDVI<sub>MD</sub>- and HVHH<sub>mt</sub>-only. The MTL<sub>F</sub> and MTL decreased from -0.7 and 1.3 months (MD=org) to 1.8 and 2.9 months (MD=95). The OA was found to increase for increasing MD from 87.4% (MD=org) to 90.4% (MD = 95) due to a decreased CE as a result of the decreasing influence of the NDVI<sub>MD</sub> on the results. Though the CE is lower when compared to NDVI<sub>MD</sub>-only and decreased from 20.4% (MD=org) to 13.2% (MD=95), it was higher when compared to HVHH<sub>mt</sub>-only (CE = 12.2%). The OE improved compared to both single-sensor results due to an increased observation density, and was found to be only 1.7% for MD=org and slightly increased to 5.3% for MD=95%.



**Figure 5.5** Spatial accuracy (OA - overall accuracy, OE - omission error, CE - commission error) and temporal accuracy (MTL<sub>F</sub> - mean time lag of flagged changes, MTL - mean time lag of confirmed changes) for NDVI<sub>MD</sub>-only, HVHH<sub>mt</sub>-only and fused NDVI<sub>MD</sub>-HVHH<sub>mt</sub> as a function of NDVI per-pixel missing data (MD).

Figure 5.6 illustrates the map results for HVHH<sub>mt</sub>-only, NDVI<sub>org</sub>-only, and NDVI<sub>MD95</sub>-only cases compared to the fused NDVI<sub>org</sub>-HVHH<sub>mt</sub> case and fused NDVI<sub>MD95</sub>-HVHH<sub>mt</sub> case, respectively. Due to the strong contribution of both NDVI<sub>org</sub> and HVHH<sub>mt</sub> time series used for the fused NDVI<sub>org</sub>-HVHH<sub>mt</sub> case, the map results appear to be a combination of both, showing areas where deforestation is detected earlier when compared to HVHH<sub>mt</sub>-only (red circles in Figure 5.6) and NDVI<sub>org</sub>-only (black circles in Figure 5.6), respectively. Yellow circles in Figure 5.6 indicate areas of unconfirmed deforestation for the HVHH<sub>mt</sub>-only case that are confirmed in the fused NDVI<sub>org</sub>-HVHH<sub>mt</sub> case due to an increased number of observations. This explains the decreased OE for the fused case when compared to the single-sensor results. The NDVI<sub>MD95</sub>-HVHH<sub>mt</sub> case appears almost identical to the HVHH<sub>mt</sub>-only case due to the sparse contribution of NDVI<sub>MD95</sub>.

**Figure 5.6 (next page)** Map results showing detected deforestation between 01/2008 – 09/2010 for the HVHH<sub>mt</sub>-only (B), NDVI<sub>org</sub>-only (C) and NDVI<sub>MD95</sub>-only (E) cases compared to the fused NDVI<sub>org</sub>-HVHH<sub>mt</sub> (D) and NDVI<sub>MD95</sub>-HVHH<sub>mt</sub> cases (F). Reference data (A). Encircled areas indicate where deforestation was detected earlier for the fused NDVI<sub>org</sub>-HVHH<sub>mt</sub> when compared to HVHH<sub>mt</sub>-only (red circles) and NDVI<sub>org</sub>-only (black circles), respectively. Yellow circles: detected deforestation for the fused NDVI<sub>org</sub>-HVHH<sub>mt</sub>, but are not confirmed for HVHH<sub>mt</sub>-only. Subset used in Figure 5.7 is shown in (A).



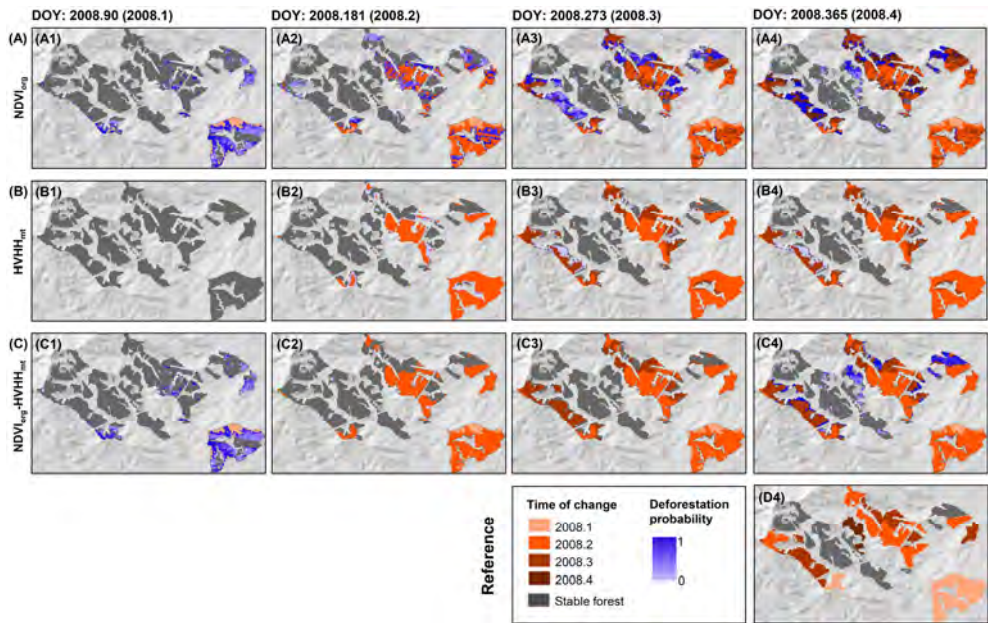


**Figure 5.7** Time sequence showing quarterly deforestation maps for 2008 for  $NDVI_{org}$ -only (A1-4),  $HVHH_{mt}$ -only (B1-4) and fused  $NDVI_{org}$ - $HVHH_{mt}$  (C1-4). The reference map is given in (D4). For each time step, the detected deforestation (MTL) and the deforestation probability of unconfirmed changes is given.

To better illustrate how the single-sensor time series are used complementarily to improve monitoring of deforestation in NRT when using the proposed approach, Figure 5.7 shows a sequence of quarterly deforestation maps over a subset of the study area for the year 2008 separately for  $NDVI_{org}$ -only (A),  $HVHH_{mt}$ -only (B) and fused  $NDVI_{org}$ - $HVHH_{mt}$  (C). For each time step, the MTL and the deforestation probability of unconfirmed changes are given. Comparing the quarterly map results for  $NDVI_{org}$ -only (Figure 5.7A-D) and  $HVHH_{mt}$ -only revealed that changes are flagged much earlier due to the dense observation density of  $NDVI_{org}$ , however, often are confirmed later. Although deforestation was already flagged at 2008.1 (A1) they were not confirmed until 2008.3 (A3). For  $HVHH_{mt}$  in contrast, deforestation was not flagged in 2008.1 (B1) but already confirmed in 2008.2 (B2). The fused results combine the advantages of both  $NDVI_{org}$  and  $HVHH_{mt}$  with deforestation events being flagged early and also confirmed early. As a result, deforestation is flagged in 2008.1 (C1) and confirmed in 2008.2 (C2).

Figure 5.8 and Figure 5.9 illustrate two single pixel examples showing the original  $NDVI_{org}$  and  $HVHH_{mt}$  time series (top) and the combined time series of F probabilities,  $s^F$  (bottom). Figure 5.8 shows a time series where deforestation was detected, with deforestation confirmed ( $T = 2008.266$ ) shortly after it has been flagged ( $T_F = 2008.219$ ). A remaining cloud at the beginning of 2008 was flagged as

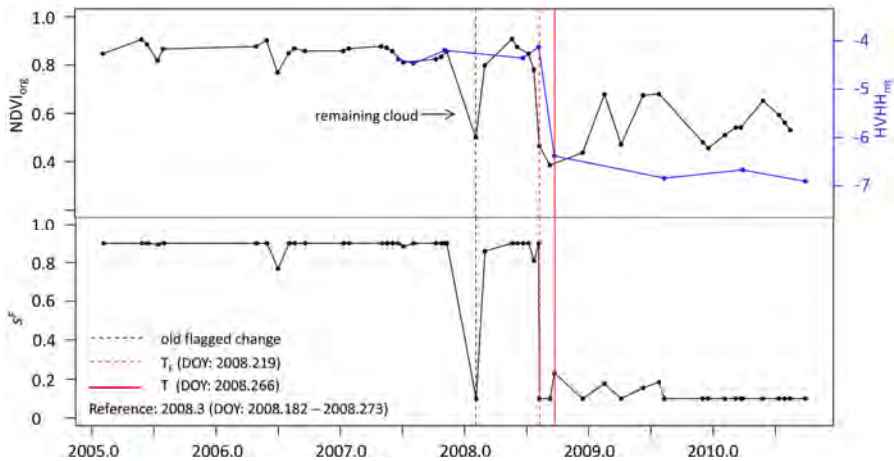


**Figure 5.8** Pixel example showing correctly detected deforestation for the fused  $NDVI_{org}$ - $HVHH_{mt}$  case. The  $NDVI_{org}$  and  $HVHH_{mt}$  time series (top) and the F probabilities,  $s^f$  (bottom) are shown. Time at which the change was first flagged ( $T_f$ ) and the time at which it was confirmed (T) are given.

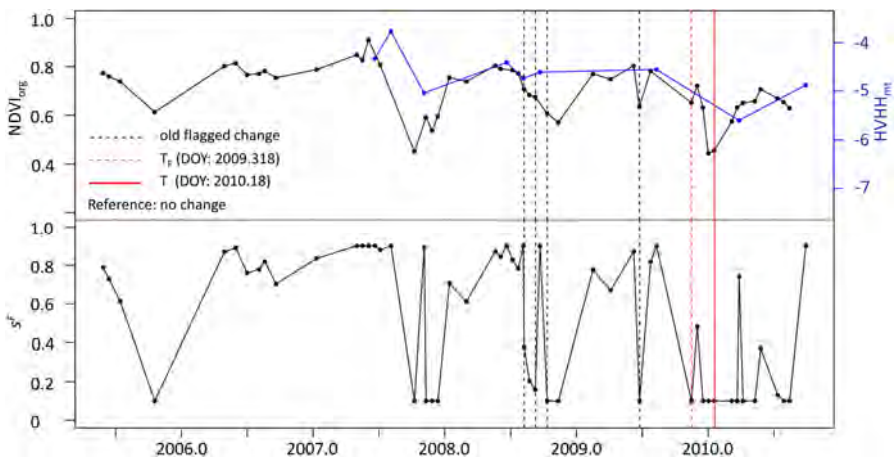


**Figure 5.9** Pixel example showing commission error in change detection for the fused  $NDVI_{org}$ - $HVHH_{mt}$  case. The  $NDVI_{org}$  and  $HVHH_{mt}$  time series (top) and the F probabilities,  $s^f$  (bottom) are shown. Time at which the change was first flagged ( $T_f$ ) and the time at which it was confirmed (T) are given.

possible deforestation, but not confirmed. Figure 5.9. shows a committed change. Since the forest seems to be disturbed and not stable at a high  $NDVI$  level as seen for the example in Figure 5.8 and typical for evergreen tropical forest,  $s^f$  varies strongly which causes a committed change. It should be noted that  $HVHH_{mt}$  does not show these fluctuations, and in the  $HVHH_{mt}$ -only results no change was detected. This explains the higher CE found for the fused results when compared to  $HVHH_{mt}$ -only.

## 5.4 Discussion and conclusion

Detecting deforestation in NRT is crucial for immediate law enforcement to combat illegal and unsustainable deforestation activities in the tropics. Fusing medium resolution optical and SAR image time series has the potential to improve NRT forest monitoring, when compared to single-sensor approaches. In this study, we developed a novel Bayesian multi-sensor time series combination approach for NRT deforestation detection. We applied the approach to univariate Landsat NDVI and ALOS PALSAR HVHH<sub>mt</sub> backscatter ratio time series imagery and detected deforestation between 01/2008 and 09/2010 in a NRT scenario at a managed forest site in the tropics (*Pinus caribea*; size = 2859 ha). For each time step the deforestation probability of unconfirmed changes and the time of change of detected deforestation is provided. Three-monthly reference data covering the entire study area were used to assess the spatial and temporal accuracy.

For the NDVI-only case, the validation data revealed a strong decrease in spatial and temporal accuracy as MD percentage increased. The OA decreased from 86.7% for MD=org (~6.5 observations/year) to 55.2% for MD=95% (0.6 observations/year), while the MTL increased from 3.2 months to 10.6 months, respectively. In contrast, the accuracies for the fused NDVI<sub>MD</sub>-HVHH<sub>mt</sub> case remained high with increasing MD and were observed to be above the NDVI<sub>MD</sub>- and HVHH<sub>mt</sub>-only cases for all MD percentages due to consistent PALSAR time series of ~2 observations/year. For fused NDVI<sub>org</sub>-HVHH<sub>mt</sub>, the OA was between 87.4% and 90.6% for increasing MD, while the MTL increased from 1.3 (MD=org) to 2.9 months (MD=95). An increased observation density led to a clear reduction of omitted changes. This result demonstrates that fusing single band Landsat and PALSAR time series using the proposed approach always improves the spatial and temporal accuracy of the single-sensor systems, even when dealing with dense cloud cover.

For the first time, an optical-SAR time series fusion approach designed for NRT deforestation detection which exploits the entire temporal detail has been introduced. Each newly acquired observation is immediately used as new evidence to update the deforestation probability and to confirm or reject a possible deforestation event. By providing the deforestation probability for flagged changes, a probability of a possible deforestation event is provided in NRT. Results shown here confirm previous studies that have highlighted the potential of SAR and optical data fusion (Lehmann et al. 2012; Lehmann et al. 2015; Reiche et al. 2013; Reiche et al. 2015). By providing a probabilistic framework to combine time series observations from multiple sensors, the observation density is increased, providing the opportunity to tackle the problem of missing data in optical and SAR time series.

Reiche et al. (2015) showed results for the same data set and validation period (01/2008-09/2010) using MultiFuse (see Section 1) to fuse NDVI<sub>MD</sub> and HVHH<sub>mt</sub> time series and a non-parametric time series analysis method (BFAST-monitor, Verbesselt et al. 2012) to detect historical deforestation. In contrast to this study, where a NRT scenario was simulated, the entire time series was available from the

beginning. Although the methods are not entirely comparable, the following differences are evident when comparing the results obtained for a historical scenario (Reiche et al. 2015) and a NRT scenario (this study). Results for the NRT scenario showed an improved temporal accuracy and less omitted changes, but a lower OA due to an increased CE. While the MTL was found to be 1.6 (MD=org) and 3.7 months (MD=95) for the historical scenario, an improved MTL of 1.3 (MD=org) and 2.9 (MD=95) months was found for the NRT scenario. In addition, potential changes are flagged and the probability for deforestation is provided. The much lower CE found for the historical scenario, which resulted in a higher OA, can be explained by the fact that the entire time series covering both stable forest and logged forest observations was available, allowing consideration of the variability of the entire time series.

Initial results from the HVHH<sub>mt</sub>- and NDVI<sub>MD</sub>-only time series for increasing  $\chi$  confirmed the results of previous studies (Whittle et al. 2012), which showed that the CE is always a compromise with the OE. In the same manner, an increasing MTL results in a decreased CE and increased OE as a result of more observations used to confirm a deforestation event. Using a sensor specific  $\chi$  for the fused case enabled us to account for the characteristics of the different time series observations of NDVI<sub>MD</sub> and HVHH<sub>mt</sub>. A  $\chi = 0.975$  resulted in the highest OA for NDVI<sub>org</sub>, showing that a high confidence linked to high number of future observations ( $\bar{n} = 1.75$ ) is needed to confirm a possible deforestation event using NDVI<sub>org</sub>-only. Remaining clouds and a rather strong varying spectral signal over time does result in false detection when using a lower  $\chi$ . In contrast,  $\chi = 0.5$  was found to result in the highest OA for HVHH<sub>mt</sub>-only (OA=87.3%), exceeding the OA for NDVI<sub>org</sub>-only. Only a very small number of observations are required to confirm a deforestation event ( $\bar{n} = 0.12$ ) showing the stability of the HVHH<sub>mt</sub> time series signal over evergreen tropical forest. These findings confirm the results of many studies showing the capabilities of L-band backscatter for detecting tropical deforestation (Motohka et al. 2014; Thapa et al. 2013; Reiche et al. 2015). These results underline the potential of upcoming L-band SAR missions (ALOS-2 PALSAR-2, SAOCOM-1, NISAR (*Nasa-Isro Synthetic Aperture Radar*, Rosen et al. 2014), Tandem-L) as contributors to tropical forest monitoring. In this study we deal with a forest practice in which stems are removed immediately after logging, causing a strong drop in the HVHH<sub>mt</sub> signal. This is confirmed by two clearly separated distributions found for F and NF. In the case of other forest practices, for example when fallen logs are left after logging (Almeida-Filho et al. 2009; Whittle et al. 2012) causing an initial increase of the signal, a second NF distribution should be added.

We demonstrated the derivation of F and NF distributions from univariate time series. Future research should focus on deriving F and NF distributions from multivariate information, for example, using all available Landsat bands and other metrics (e.g. Landsat band5 or band7, normalised burn ratio (NBR), tasseled cap wetness, texture) which already showed an improvement of class distinction (Jin & Sader 2005; Lehmann et al. 2015; Kuplich 2006; Zhu et al. 2012).

Providing a combination of spatially explicit hard and soft information, namely the time of change of confirmed changes and the deforestation probability for unconfirmed changes, is considered one of the major advantages of a probabilistic framework (Kiiveri & Caccetta 1998; Symeonakis et al. 2012). A disadvantage of probabilistic approaches when compared to non-parametric approaches is the need for training data to derive class specific distributions (Hoekman et al. 2010), such as in our case for F and NF. However, satellite-based medium resolution optical (Landsat) as well as C- (ERS-1, ENVISAT ASAR) and L-band SAR imagery (JERS-1, ALOS PALSAR) are available for most areas of the world. While Broich et al. (2011) demonstrated the derivation of time series of forest probabilities from Landsat time series for Sumatra and Kalimantan, Shimada et al. (2014) successfully demonstrated the extraction of F and NF distributions for PALSAR across global biomes.

The proposed approach is designed to use observations from multiple time series for NRT detection of changes. Since the F and NF probabilities are used to calculate and update the deforestation probability, the method directly accounts for different sensor specific class separabilities. This is of particular interest when making use of C-band SAR time series in combination with L-band and Landsat. C-band is less sensitive to forest cover changes compared to L-band (Mitchell et al. 2014) and therefore the F and NF distribution can be expected to overlap more. This leads to less extreme F and NF probabilities that in turn will reduce the impact on deforestation probabilities when compared to those derived from L-band. The higher temporal resolution of C-band for many tropical countries, however, promises to result in an improved temporal accuracy of detected deforestation. The continuation of historical C-band SAR time series imagery from ERS-1/2 and ENVISAT ASAR is ensured by the ESA's Sentinel-1 mission (Torres et al. 2012), which provides data under a free-of-charge data policy.

A NRT deforestation monitoring system combining historical and upcoming optical, C- and L-band SAR data streams of Landsat, Sentinel-1, Sentinel-2, SAOCOM-1 and ALOS-2 PALSAR-2 could address major problems faced by remote sensing in tropical countries, for example when implementing a consistent monitoring system for REDD+ (Herold & Skutsch 2011; Pelletier et al. 2011; De Sy et al. 2012). Such a multi-sensor system may compensate for persistent cloud cover and for unexpected failures experienced by certain systems (e.g. ALOS failure in 2011, Rosenqvist et al. 2014).

## **Acknowledgment**

This work was funded by the European Community's Seventh Framework Programme (FP7) funded ReCover project (grant agreement 263075) and a Marie-Curie IRG grant within the FP7 to Jan Verbesselt (grant agreement 268423). Thanks to Johannes Eberenz from Wageningen University for data pre-processing support, Ben DeVries and Christina May from Wageningen University for proof-reading the manuscript.

**Chapter**

# **6**

**Synthesis**

## 6.1 Main results

Satellite-based tropical forest monitoring needs to improve in order to provide timely and spatially accurate forest cover change information. Without this information, climate mechanisms such as REDD+ will be challenged. The restricted applicability of optical remote sensing for tropical forest monitoring due to cloud cover makes SAR of primary importance for continuously mapping changes in forest cover. However, SAR approaches and time series data are sparse. To overcome the limitations of the single-sensor systems and to make use of their complementarities for tropical forest monitoring, this thesis aimed to advance multi-sensor methods combining medium resolution SAR and optical satellite time series. Four research questions have been defined. For each of them, a synthesis of the main results is given in the remaining parts of this section. In Section 6.2 a general conclusion is provided followed by reflection and outlook of this PhD research in Section 6.3.

### ***1. How can we combine the advantages of multi-temporal SAR and optical information for detecting historical deforestation and forest degradation?***

Forest disturbance information derived from Landsat imagery have proven suitable for detecting forest degradation in tropical environments, but persistent cloud cover can lead to significant data gaps (Souza, Jr et al. 2013). For our study site in Central Guyana data gaps remained even when compositing Landsat imagery over one or two years. We showed that change detection schemes especially were affected. Because data gaps of annual Landsat composites were unevenly distributed, these data gaps accumulated during the multi-temporal analysis. In contrast, L-band SAR data demonstrated its capability to provide reliable deforestation information, but showed limited capacity to identify forest degradation.

To overcome the latter single-sensor limitations, Chapter 2 introduced an innovative approach for feature level fusion of multi-temporal L-band SAR and optical forest disturbance information. Using multi-temporal Landsat and dual-polarised ALOS PALSAR imagery (HH and HV polarisation) acquired for the years 2007 and 2010, we used the approach to map forest land cover and to detect deforestation and forest degradation. Adopting Guyana's country specific definitions for forest and degraded forest allowed a comparison of our results with other national products such as Guyana's REDD+ MRVS reports (Pöyry Management Consulting (NZ) Limited 2011; Indufor Asia Pacific Ltd 2012). Due to the persistent cloud cover in the region and the primary use of optical satellite data only, these reports suffered from spatially incomplete results. By making use of the complementarities of Landsat and ALOS PALSAR, we were able to reduce data gaps in Landsat (cloud cover, SLC-off) and PALSAR (SAR layover and shadow in mountainous area) data sets to a negligible amount. Compared to a potential Landsat- or PALSAR-only approach, thematic detail and spatial consistency improved significantly for the combined Landsat-PALSAR approach. We reported high annual deforestation and degradation rates of 0.1% and 0.08%, respectively for

the study site in Central Guyana, emphasizing the importance of the region for Guyana's REDD+ program. Extensive alluvial mining and agricultural expansion were the main drivers of these changes, which clearly exceeded the reported country averages.

Results of Chapter 2 stress the need for implementing SAR-optical approaches to support REDD+ in robustly reporting forest changes in areas with dense cloud cover.

## ***2. How do slope-induced effects on the SAR signal impact forest change detection in complex terrain?***

Driven by agricultural expansion and cost-efficient logging operations, the majority of tropical deforestation occurred in lowland areas (Aide et al. 2013) while large tracts of forest in mountainous terrain remained undisturbed. However, an increasing demand for timber and agricultural areas may shift deforestation operations towards mountainous areas. To manage and conserve these forests, robust satellite-based monitoring is required. Mountainous terrain, however, is notoriously difficult to handle when pre-processing SAR images. For pre-processing ALOS PALSAR data for Central Guyana (Chapter 2), a simple physical single-model (Hoekman 1990) was used that performed well for dense forest areas, but showed remaining slope-induced effects over other land cover when dealing with steep slopes (Hoekman et al. 1994; Hoekman et al. 2010). Since Chapter 2 dealt only with alluvial mining and agricultural expansion occurring in flat and gentle areas directly adjacent to rivers, change detection was not affected by remaining slope effects. Moving from the study site in Central Guyana (Chapter 2) to a managed evergreen forest site in Fiji (Chapter 4 and 5) where deforestation is occurring in complex terrain with steep slopes up to 40 degrees, slope-induced effects over non-forest land cover may negatively affect change detection.

To also account for varying land cover when correcting slope-induced effects on the SAR signal, Chapter 3 presented a two-step approach for multi-model land cover dependent slope correction. The first step uses the simple physical model (Hoekman 1990) used in Chapter 2, while the second step applies a semi-empirical model that accounts for the land cover (terrain type) dependent scatter mechanism. We corrected dual-polarised ALOS PALSAR images (HH and HV polarisation) of the site in Fiji and of an additional site in Brazil. Remaining slope effects were reduced to less than 0.1 dB for steep slopes. We showed that slope-induced effects were mitigated already to a large extent after the first step, but can remain as large as 1.77 dB for low biomass classes (woodland, HH). When estimating biomass this can lead to a systematic under- and/or overestimation purely related to slope effects, confirming the recent findings of Mermoz et al. (2015). When dealing with deforestation activities only, however, remaining slope effects are already sufficiently small after the first step when considering the large change in the L-band backscatter signal caused by the removal of forest. The single-model approach was therefore adequate to pre-process the ALOS PALSAR data of the Fiji site used for

time series analysis in Chapter 4 and 5. Although the multi-model approach is not required when dealing with deforestation only, for detecting forest degradation and distinguishing smaller biomass changes, implementation will strongly support the analysis.

A further point of concern is the resolution of the DEM used for slope correction. When dealing with long steep slopes, such as for the site in Brazil, the 90 m SRTM resolution is sufficient to retrieve necessary slope angles. However in other areas, such as parts of Guyana (Chapter 3) and Fiji (Chapter 4 and 5) featuring very dissected landscapes with short steep slopes, micro-topography may remain and distort the analysis. Having high resolution 30 m elevation information available for Fiji, enabled us to largely mitigate such effects. To enable remote sensing efforts to provide forest change information consistently at a medium resolution scale and for varying terrain, high resolution DEMs for the tropics like those available from Tandem-X (Zink et al. 2006) should be made available free-of-charge.

### ***3. How can we fuse SAR and optical image time series, and what impact does persistent cloud cover have on the spatial and temporal accuracy of deforestation estimates?***

Results of Chapter 2 confirmed the findings of several studies analysing optical time series, showing that annual image compositing decreases data gaps (Sannier et al. 2014; Pflugmacher et al. 2012; Hansen et al. 2013). Annual compositing, however, prohibits intra-annual analysis and remaining data gaps may accumulate when analysing a multi-temporal dataset. Related to this, missing data common in satellite-based medium resolution imagery, can potentially be compensated by fusing optical and SAR time series. We showed that the specific characteristics of optical and SAR time series, however, challenge a direct correlation and fusion.

We addressed these issue in Chapter 4 and introduced the Multi-sensor Time series Fusion (MulTiFuse) approach to fuse single band Landsat NDVI and ALOS PALSAR time series imagery. Introducing the normalised inverted magnitude as a regression weight and a corresponding optimization method provided a robust approach to improve the correlation between SAR and optical time series; the basis to predict and fuse the two time series in the final step. We found multi-temporal SAR speckle filtering (Quegan & Yu 2001) to strongly improve the correlation between the PALSAR and the Landsat NDVI time series, with the PALSAR HVHH backscatter ratio (HVHH<sub>mt</sub>) showing the highest correlation. This emphasises the importance of multi-temporal SAR speckle filtering when applying MulTiFuse.

The fused Landsat-PALSAR (NDVI-HVHH<sub>mt</sub>) time series was used in a change detection framework to detect deforestation at a managed evergreen tropical forest site in Fiji for the period between 01/2008 and 09/2010. BFAST-monitor (Verbesselt et al., 2012) was used for time series analysis and confirmed its usefulness as a tool for detecting changes in satellite time series. Evaluating the

results with three-monthly reference data revealed that fusing always improves spatial and temporal accuracies relative to the single-sensor systems.

We tested MulTiFuse in an area with a sufficient number of observations available; in a manner similar to the majority of studies introducing remote sensing based time series approaches (e.g. Verbesselt et al. 2010a; Verbesselt et al. 2012; Zhu et al. 2012; Zhu & Woodcock 2014). An average per-pixel missing data percentage (MD) of 50% due to cloud cover and SLC-off data gaps resulted in an average of 6.5 cloud free Landsat observations/year. In mountainous natural forest areas outside of the study area MD reached up to 96% (Landsat path/row: 75/72). This highlights the large local differences in cloud cover densities in the tropics (Asner 2001; Sannier et al. 2014; Potapov et al. 2012). To estimate the effect of persistent cloud cover on the spatial and temporal accuracies of resulting deforestation estimates, we increased the MD stepwise from ~50% (~6.5 observations/year) up to 95% (0.6 observation/year) and compared the results for the Landsat-only (NDVI), PALSAR-only (HVHH<sub>mt</sub>) and the fused Landsat-PALSAR cases. For the Landsat-only case, a very strong decrease in spatial and temporal accuracy was observed for increasing Landsat MD. In contrast, the accuracies for the fused case remained high with increasing MD and were above Landsat- and PALSAR-only cases for all Landsat MD due to a consistent PALSAR time series of ~2 observations/year. This demonstrated that even in the case of very few available Landsat observations (MD=95%) fusing improves the results.

For the first time the effect of increasing missing data on the spatial and temporal accuracy of detected deforestation has been quantified. The results highlight the vulnerability of tropical forest monitoring systems that rely on optical data only. At the same time, Chapter 4 demonstrated the capability of SAR-optical based forest monitoring to provide robust forest change information independent of varying cloud cover densities by mitigating the problem of missing data in SAR and optical time series.

#### ***4. How can we optimise SAR-optical fusion for near-real time deforestation monitoring?***

Chapter 4 introduced the MulTiFuse approach, which is designed to fuse SAR and optical satellite time series for historical deforestation monitoring. As fusing requires observations from both before and after the change event in both time series, MulTiFuse is not suited to detect changes in near real-time (NRT).

To address the need for a forest change alert system at medium resolution scale (Lynch et al. 2013), Chapter 5 introduced a Bayesian change detection approach that combines SAR and optical time series for NRT deforestation detection. We simulated a NRT scenario using the Landsat (NDVI) and ALOS PALSAR (HVHH<sub>mt</sub>) time series available for the Fiji site - the same data used in Chapter 4. Once a new image of either of the two time series was available, the probability of deforestation was calculated immediately and deforestation events were indicated. These NRT

detection capabilities are essential for timely law enforcement to combat illegal forest activities in tropical regions (Lynch et al. 2013; Wheeler et al. 2014). Future observations were then used to update the deforestation probability and thus to confirm or reject a possible deforestation event. Providing a combination of spatially explicit hard and soft information, namely: the time of change of confirmed changes and the deforestation probability for indicated changes, demonstrated the advantages of probabilistic frameworks (Kiiveri & Caccetta 1998; Symeonakis et al. 2012; Sexton et al. 2015). Results obtained for the fused Landsat-PALSAR case always improved the spatial and temporal accuracy of single-sensor systems. Both indicated and confirmed changes were detected earlier. The improvements were maintained even for increasing Landsat MD, which confirms the trends described in Chapter 4. This highlights the robustness of the NRT approach when dealing with cloud cover in the tropics and emphasises once more the weakness of forest monitoring systems relying on optical data only.

Because the implemented probabilistic approach directly accounts for the different sensor specific class separabilities, observations from multiple SAR and optical time series with varying sensitivities can be combined. This provides the opportunity to expand the approach to Sentinel-1 C-band imagery in combination with L-band SAR and optical time series. The lower sensitivity of C-band to forest cover changes when compared to L-band (Mitchell et al. 2014) is expected to result in more overlapping class distributions and thus less extreme class probabilities. A reduced impact of single C-band observations on the deforestation probability will be the result, however, this may be compensated by the increased observation frequency expected for Sentinel-1 (Torres et al. 2012).

## **6.2 Reflection and outlook**

This thesis addressed the need for advancing multi-sensor methods that combine time series imagery from medium resolution SAR and optical satellite data in order to improve forest monitoring in the tropics. The scientific contributions to the field of satellite-based forest monitoring include the introduction of three novel multi-sensor approaches to combine optical and SAR image time series for monitoring deforestation (Chapter 2, 4 and 5) and forest degradation (Chapter 2). All three showed strong improvements over single-sensor systems. For the first time, SAR-optical methods were presented that exploit the full observation density of time series data (Chapter 4 and 5). We demonstrated their robustness when dealing with persistent cloud cover in the tropics. This enabled the transition from annual to sub-annual change (Chapter 4) and NRT change detection (Chapter 5). Specific contributions to SAR remote sensing include the introduction of a practical approach for multi-model SAR slope correction that accounts for land cover dependent scatter mechanisms (Chapter 3). Furthermore, the effect of multi-temporal SAR speckle filtering when correlating and fusing SAR and optical time series was evaluated (Chapter 4). The following sections reflect on key aspects and limitations of the

introduced SAR-optical approaches and discuss further opportunities and developments.

### 6.2.1 Multi-sensor forest monitoring

This thesis introduced SAR-optical forest monitoring approaches that provide the opportunity to use impending data streams of medium resolution image time series from Landsat, Sentinel-1, Sentinel-2 and ALOS 2 PALSAR-2 in a beneficial way. When compared to single-sensor SAR- and optical-only results, fundamental improvements in spatial completeness, thematic detail, and spatial and temporal detection accuracy were achieved by applying the introduced SAR-optical approaches. Table 6.1 synthesises the main types of improvement and provides empirical examples from this thesis. By combining multiple optical and SAR data streams, even challenges such as irregular seasonal cloud cover, sudden data discontinuity from a satellite due to sensor failure, or unexpected changes in data policy may be compensated.

The great potential of SAR-optical approaches for tropical forest monitoring was highlighted by this thesis, but many steps still have to be taken to operationalize them. The main limitations of the presented research are:

- (i) All studies were conducted at local-scale, and only one of the introduced multi-sensor methods was applied in natural tropical forest conditions (Chapter 2). The remaining two Chapters (4 and 5) were evaluated at a managed evergreen plantation with forest stands being fully harvested within a very short period and stems removed immediately after logging. The existence of such regimented harvesting practices, in combination with the availability of three-monthly reference data covering the entire study area, greatly reduced the number of unknowns, providing an ideal situation for assessing the performance of novel methods. For operational use, however,

**Table 6.1** Main types of improvement demonstrated by the fused Landsat-PALSAR (Fused) approaches introduced in this thesis, when compared to results obtained with single-sensor PALSAR- or Landsat-only. For each type, an empirical example is provided from this thesis. Abbreviations: OA = overall accuracy; MTL = mean time lag of detected changes; \* and \*\* refer to results achieved with  $-2$  PALSAR observations/year in combination with (\*)  $-6.5$  or  $-0.5$  (\*\*) Landsat observations/year, respectively.

Improvement	Demonstrated in	Empirical example
Spatial completeness (data gaps)	Chapter 2, 4, 5	<i>Chapter 2; Table 2-5:</i> Data gaps decrease from 7.9% (Landsat) and 0.05% (PALSAR) to 0.01% (Fused)
Thematic detail	Chapter 2	<i>Chapter 2:</i> Detection of deforestation and forest degradation
Spatial accuracy	Chapter 4, 5	<i>Chapter 4; Figure 4.10:</i> * OA increased from 92.6% (PALSAR) and 93.1% (Landsat) to 95.5% (Fused) ** OA increased from 92.6% (PALSAR) and 54.2% (Landsat) to 93.8% (Fused)
Temporal accuracy	Chapter 4, 5	<i>Chapter 5; Figure 5.5:</i> * MTL decreased from 3.2 (PALSAR) and 2.8 (Landsat) to 1.3 months (Fused) ** MTL decreased from 3.2 (PALSAR) and 10.6 (Landsat) to 2.9 months (Fused)

the approaches need to be applied, tested and adapted to larger areas with varying harvesting practices, more complex forest dynamics, and tropical deciduous forest conditions.

- (ii) Only the detection of tropical deforestation (Chapter 2, 4 and 5) and forest degradation (Chapter 2) was considered in this thesis. Reforestation and regrowth dynamics were not tracked, but need to be considered for comprehensive monitoring of forest dynamics.
- (iii) All methods were demonstrated using dual-polarised (HH and HV) L-band SAR imagery only. Considering C-band imagery and better understanding its sensitivity towards tropical forest changes will be essential to making use of the impending stream of dense C-band SAR time series imagery expected from Sentinel-1.
- (iv) Although, multi-sensor approaches have been introduced that fully exploit optical and SAR time series with regard to their observation density (Chapter 4 and 5), only univariate (single band) optical and SAR time series were fused. In order to make use of the available reflectance and backscatter spectra of optical and SAR sensors as well, the approaches need to be expanded to allow multiple time series metrics as input from optical and SAR sensors. The Bayesian change detection approach presented in Chapter 5 is already designed to exploit such multivariate time series. A multivariate feature space instead of a univariate feature space (see Figure 5.3) can be used to derive the sensor specific class probabilities.
- (v) Only the effect of increasing missing data of optical time series on the spatial and temporal detection accuracy has been analysed. The impact of varying SAR observation densities on change detection accuracies was not investigated. The average observation frequency of PALSAR for many tropical countries - two L-band observations/year - does not allow an extensive analysis. The increasing observation frequency of C-band (Sentinel-1) and L-band (PALSAR-2, SAOCOM-1) time series observation in the near future, however, urges for a detailed assessment. Such knowledge is required to implement multi-sensor forest monitoring systems that are both robust and cost-efficient.

Besides the scientific developments presented in this thesis, very little progress has been made towards SAR-optical remote sensing approaches for forest monitoring over the past decade; despite many studies indicating its potential. In the same period optical remote sensing underwent major scientific breakthroughs that led to global Landsat-based forest change products for the past two decades (Hansen et al. 2013; Kim et al. 2014). Fewer advances were made in SAR remote sensing. This imbalance in the development of optical, SAR and multi-sensor SAR-optical approaches can be explained, for the most part, by the following three issues.

First, rapid developments in optical-based forest monitoring were catalysed by the opening of the Landsat archive after implementing a free-of-charge data policy in 2008 (Wulder et al. 2012). The sudden availability of medium resolution time series imagery for the past four decades, as well as an increase in affordable computer processing and storage capability (Lee et al. 2011) led to three major transitions in the field: (i) from bi-temporal to time series based change detection methods, (ii) from coarse resolution to medium resolution applications, and (iii) from local- to global-scale products. A broad acceptance of Landsat imagery as the major data source for large-area forest change detection and the implementation of REDD+ was the result (Birdsey et al. 2014).

Second, the large potential of L-band SAR for tropical forest monitoring is evident and has been highlighted once more by this thesis. However, the commercial data distribution of ALOS PALSAR and ALOS-2 PALSAR-2 delays full scientific exploitation and prohibits operational large area use of time series imagery. Since developing tropical countries avoid relying on costly remote sensing data for their REDD+ MRV (De Sy et al. 2012; Pelletier & Goetz 2015), only very few make use of L-band SAR data to assist their forest monitoring. To stimulate the wide-area use and acceptance of L-band SAR the commercial data policy for ALOS-2 PALSAR-2 should be changed. With the upcoming SAOCOM-1 (~2016) and NISAR (~2020) missions, however, free-of-charge L-band data is in sight.

Third, earth observation research groups traditionally emphasize either optical or SAR remote sensing and therefore multi-sensor SAR-optical developments are not a focal area. Only very few integrated SAR and optical research groups exist. More integrated groups and closer cooperation between research teams is necessary to exploit the full potential of SAR-optical remote sensing. These efforts are encouraged by the scientific community and stimulated by funding agencies such as European Space Agency, European Union and NASA (*National Aeronautics and Space Administration*), who are allocating major resources for multi-sensor remote sensing to support global forest monitoring. A successful implementation of multi-sensor systems also requires space agencies to further coordinate their acquisitions, a major effort stimulated by the Global Forest Observations Initiative (GFOI) (CEOS 2014).

In conclusion, the development towards multi-sensor systems combining optical, C- and L-band image time series will be the key for robust operational tropical forest monitoring. Quick scientific progress, large-scale applications, and wide-spread acceptance is expected to be catalysed largely by free-of-charge data policies and coordinated data acquisitions. This will also accelerate the transition from annual to sub-annual monitoring at medium resolution scale as has been demonstrated in this thesis. Providing sub-annual data may help to better understand the drivers and dynamics of change. Some drivers, for example, fires in Indonesia, are clearly season dependent (Achyar et al. 2014).

## 6.2.2 Near real-time forest change detection

The rapid detection of illegal activities in vast and inaccessible forest areas in the tropics is currently realized by monitoring systems that rely on coarse resolution optical MODIS data only (Shimabukuro et al. 2006; Hammer et al. 2009; Wheeler et al. 2014). These systems show limited detection capabilities during the rainy season when cloud free observations are rare (Assunção et al. 2013). Local experts also mentioned that small-scale illegal forest activity sometimes increased during the rainy season, a time at which cloud cover prevents existing Landsat-based annual monitoring systems from detecting such activities. In all cases, late and ineffective interventions impede effective forest management and conservation. To prevent the expansion of small-scale operations to larger areas, NRT monitoring systems that operate at medium resolution scale are required as otherwise these small-scale changes are either unseen or detected with a delay. Providing weather and seasonal independent forest change information at medium resolution and in NRT will only be accomplished by combining SAR and optical data streams. Although Chapter 5 introduces a SAR-optical approach capable of detecting deforestation in NRT, we acknowledge that more research is required.

Recently, Pratihast et al. (2014) demonstrated the potential of integrating Landsat-based and community-based (mobile phones) NRT forest change information. Adding SAR-optical based NRT information as well promises to improve the robustness of such systems and to better understand the complexity of change processes on the ground. Research is still needed on how to account for the varying quality and related uncertainties of satellite- and community-based information.

## 6.2.3 Regional optimisation of forest monitoring

Regional tuning at areas with sufficiently detailed reference data covering the classes of interest is essential for successful up-scaling of remote sensing approaches for forest monitoring (Vargas et al. 2013). Traditionally, such approaches are assessed and compared by spatial accuracy measures: overall accuracy (OA), commission error (CE) and omission error (OE) (Foody 2002; Olofsson et al. 2013). To optimise a method according for specific regional circumstances often a single-model parameter (e.g. band threshold) is tuned. Then, the model parameter is considered optimised when the highest OA is reached. In some cases user requirements are correct area statistics, the model parameter is tuned towards the smallest absolute area bias (area bias = CE - OE). A 2D plot is commonly used to visualise the relationship between the spatial accuracy measures (dependent variables) and the changing model parameter (independent variable). This thesis presented methods capable of detecting deforestation with sub-annual temporal accuracy (Chapter 4 and 5). For NRT monitoring in particular, the temporal accuracy becomes as important as spatial accuracy when tuning such methods and comparing results. A clear trade-off between spatial and temporal accuracy was found in Chapter 5, confirming the findings of Zhu et al. (2012) who evaluated the

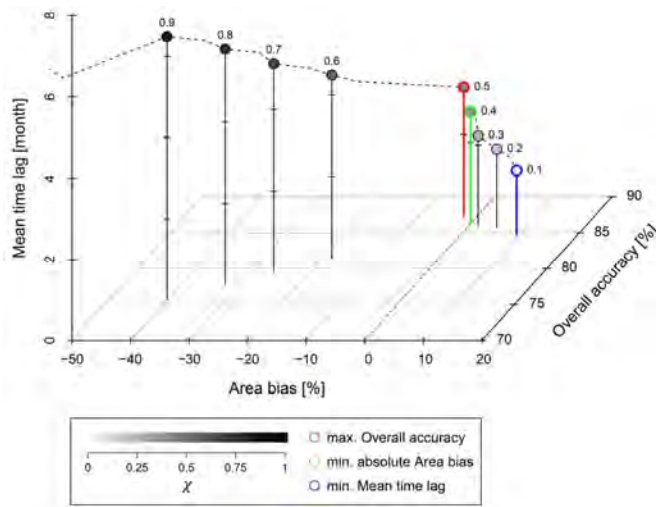


**Figure 6.1** 3D plot depicting area bias, OA and MTL as a function of the increasing threshold parameter  $\chi$  for PALSAR.  $\chi$  is derived in 0.025 steps (dotted line), and shown for 0.1 steps. Data is identical to Figure 5.4A.

performance of Landsat-based time series change detection. Increasing spatial accuracy was related to decreasing temporal accuracy in both cases. Separate 2D plots for spatial and temporal accuracy measures were used to visualise the effect of the changing model parameter (this thesis: Figure 5.4; Zhu et al. 2013; Figure 13). This often makes the interpretation and the subsequent selection of an optimised model parameter counterintuitive. To better understand and deal with the trade-off, a 3D plot showing the area bias, OA, and the temporal accuracy as a function of the independent variable is suggested for the purpose of regional method tuning (i) and method comparison (ii). Two examples from this thesis are provided:

- (i) As part of tuning the Bayesian approach presented in Chapter 5, the determining threshold parameter  $\chi$  needed to be optimised for PALSAR (HVHH<sub>mt</sub>). Figure 6.1 depicts the 3D plot consisting of the area bias, OA and MTL as a function of  $\chi$ . Figure 6.1 represents a transformed version of the two separate plots shown in Figure 5.4A. The OA slightly increased with increasing  $\chi$  from  $\chi = 0$  and was found to be highest for  $\chi = 0.5$ , whereby the smallest absolute area bias was obtained for  $\chi = 0.4$ . In contrast the minimum MTL was found for  $\chi = 0$  and  $\chi = 0.1$  and increased constantly for increasing  $\chi$ . No  $\chi$ -value exists that resulted in the highest OA and lowest MTL. Therefore, a  $\chi$ -value needs to be selected depending on user requirements. In case very rapid change detection is desired,  $\chi = 0.1$  may be used. However, high false alarm rates (CE) indicated by a large positive area bias need to be accounted for. In case a high detection accuracy is preferred the highest OA  $\chi = 0.5$  should be chosen, but a much weaker MTL needs to be considered.

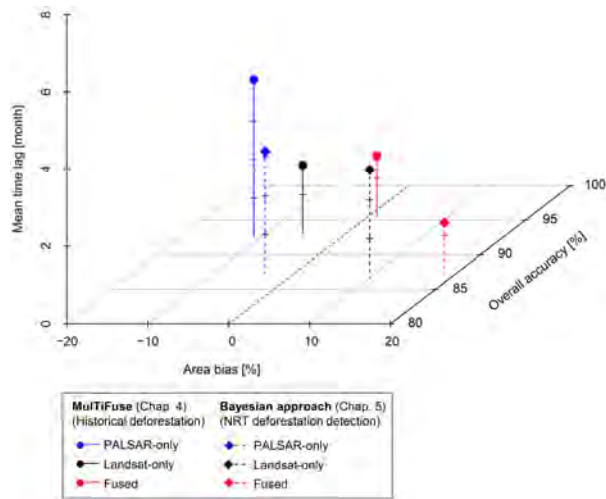


**Figure 6.2** 3D plot depicting area bias, OA and MTL for PALSAR-only (blue, HVH<sub>mt</sub>), Landsat-only (black, NDVI<sub>org</sub>) and fused PALSAR-Landsat (red, fused NDVI<sub>org</sub>-HVH<sub>mt</sub>) separately for MultiFuse (circle, Chapter 4) and the Bayesian approach (rhombus, Chapter 5). Data is identical to that used in Figure 4.10 and Figure 5.5.

- (ii) This thesis introduced two novel multi-sensor time series approaches designed for deforestation detection (MultiFuse, Chapter 4) and NRT deforestation detection (Bayesian approach, Chapter 5). Both were applied to the same reference data set in Fiji and compared for the Landsat-only, PALSAR-only and fused Landsat-PALSAR case. Using the suggested 3D plot (Figure 6.2) enables a meaningful comparison in terms of their spatial and temporal performance. The fused case obtained for the Bayesian approach (red dotted line) showed a lower MTL when compared to the MultiFuse results (red solid line) highlighting its capabilities for NRT deforestation detection. In contrast, a higher OA due to lower positive area bias makes MultiFuse more suitable for detecting historical deforestation.

In conclusion, there will be limitations for satellite-based monitoring to satisfy the requirements for both the reliable assessment of historical changes and NRT monitoring. For comprehensive countrywide implementation, and to effectively support REDD+, the Brazilian example in which two systems work in parallel could be followed. This is currently realised by a Landsat-based system optimised for historical forest change monitoring at medium resolution scale (PRODES), and a separate NRT deforestation alert system relying on coarse resolution MODIS data to provide frequent enough cloud-free observations (DETER) (Wheeler et al. 2014). The research on SAR-optical time series based tropical forest monitoring presented in this thesis paves the way to further advance these efforts and overcome current limitations towards their operational use at medium resolution spatial scale by combining the impending stream of 10 – 30 m optical and SAR time series data.

## References

- Achard, F., Beuchle, R., Mayaux, P., Stibig, H.-J., Bodart, C., Brink, A., Carboni, S., Desclee, B., Donnay, F., Eva, H. D., Lupi, A., Raši, R., Seliger, R., & Simonetti, D. (2014) Determination of tropical deforestation rates and related carbon losses from 1990 to 2010. *Global Change Biology*, 20(8), 2540–2054.
- Achard, F., Stibig, H. J., & Eva, H. D. (2010) Estimating tropical deforestation from Earth observation data. *Carbon Management*, 1(2), 271–287.
- Achyar, E., Schmidt-Vogt, D., & Shivakoti, G. P. (2014) Dynamics of the multi-stakeholder forum and its effectiveness in promoting sustainable forest fire management practices in South Sumatra, Indonesia. *Environmental Development*, 13, 4–17.
- Adams, J. B., Smith, M. O., & Gillespie, A. R. (1993) Imaging Spectroscopy: interpretation based on spectral mixture analysis. In C. M. Pieters & P. A. J. Englert, eds. *Remote Geochemical Analysis Elemental and Mineralogical Composition*. Cambridge University Press, pp. 145–166.
- Aide, T. M., Clark, M. L., Grau, H. R., López-Carr, D., Levy, M. a., Redo, D., Bonilla-Moheno, M., Riner, G., Andrade-Núñez, M. J., & Muñoz, M. (2013) Deforestation and Reforestation of Latin America and the Caribbean (2001-2010). *Biotropica*, 45(2), 262–271.
- Akatsuka, S., Takeuchi, W., Rakwatin, P., & Sawada, H. (2009) Evaluation of slope correction effects on ALOS PALSAR mosaic data set in forest mapping in Indonesia and Mala. In *Proceedings of the 2009 Asian Association on Remote Sensing (AARS)*. pp. 2–7.
- Almeida-Filho, R., Rosenqvist, A., Shimabukuro, Y. E., & Silva-Gomez, R. (2007) Detecting deforestation with multitemporal L-band SAR imagery: a case study in western Brazilian Amazônia. *International Journal of Remote Sensing*, 28(6), 1383–1390.
- Almeida-Filho, R., Shimabukuro, Y. E., Rosenqvist, A., & Sanchez, G. A. (2009) Using dual-polarized ALOS PALSAR data for detecting new fronts of deforestation in the Brazilian Amazonia. *International Journal of Remote Sensing*, 30(14), 3735–3743.
- Anderson, L. O., Shimabukuro, Y. E., DeFries, R. S., & Morton, D. (2005) Assessment of deforestation in near real time over the Brazilian Amazon using multitemporal fraction images derived from Terra MODIS. *IEEE Geoscience and Remote Sensing Letters*, 2(3), 315–318.
- Arvidson, T., Goward, S., Gasch, J., & Williams, D. (2006) Landsat-7 long-term acquisition plan: Development and validation. *Photogrammetric Engineering & Remote Sensing*, 72(10), 1137–1146.
- Ash, J. (1992) Vegetation ecology of Fiji: past, present, and future perspectives. *Pacific Science*, 46(2), 111–127.
- Asner, G. P. (2001) Cloud cover in Landsat observations of the Brazilian Amazon. *International Journal of Remote Sensing*, 22(18), 3855–3862.
- Asner, G. P. (2011) Painting the world REDD: addressing scientific barriers to monitoring emissions from tropical forests. *Environmental Research Letters*, 6(2), 021002.
- Asner, G. P., Keller, M., Pereira, Jr, R., Zweede, J. C., & Silva, J. N. M. (2004) Canopy Damage and Recovery After Selective Logging in Amazonia: Field and Satellite Studies. *Ecological Applications*, 14(4), 280–298.

- Asner,G.P., Knapp,D.E., Broadbent,E.N., Oliveira,P.J.C., Keller,M., & Silva,J.N. (2005) Selective logging in the Brazilian Amazon. *Science*, 310(5747), 480–482.
- Assunção,J., Gandour,C., & Rocha,R. (2013) DETERring Deforestation in the Brazilian Amazon: Environmental Monitoring and Law Enforcement., Rio De Janeiro: Climate Policy Initiative.
- Atwood,D., Small,D., & Gens,R. (2012) Improving PolSAR land cover classification with radiometric correction of the coherency matrix. *IEEE Journal of Selected Topics in Applied Earth Observations and Remote Sensing*, 5(3), 848–856.
- Bayer,T., Winter,R., & Schreier,G. (1991) Terrain influences in SAR backscatter and attempts to their correction. *IEEE Transactions on Geoscience and Remote Sensing*, 29(3), 451–462.
- Birdsey,R., Angeles-Perez,G., Kurz,W. a, Lister,A., Olguin,M., Pan,Y., Wayson,C., Wilson,B., & Johnson,K. (2014) Approaches to monitoring changes in carbon stocks for REDD+. *Carbon Management*, 4(5), 519–537.
- Bonano,M., Manunta,M., Marsella,M., & Lanari,R. (2012) Long-term ERS/ENVISAT deformation time-series generation at full spatial resolution via the extended SBAS technique. *International Journal of Remote Sensing*, 33(15), 4756–4783.
- Broich,M., Hansen,M.C., Potapov,P., Adusei,B., Lindquist,E., & Stehman,S. V. (2011) Time-series analysis of multi-resolution optical imagery for quantifying forest cover loss in Sumatra and Kalimantan, Indonesia. *International Journal of Applied Earth Observation and Geoinformation*, 13(2), 277–291.
- Brown,C., Sarabandi,K., & Pierce,L.E. (2005) Validation of the shuttle radar topography mission height data. *IEEE Transactions on Geoscience and Remote Sensing*, 43(8), 1707–1715.
- Bruzzone,L., Prieto,D.F., & Serpico,S.B. (1999) A neural-statistical approach to multitemporal and multisource remote-sensing image classification. *IEEE Transactions on Geoscience and Remote Sensing*, 37(3), 1350–1359.
- Carlotto,M. (1999) Reducing the effects of space-varying , wavelength-dependent scattering in multispectral imagery. *International Journal of Remote Sensing*, 20(17), 3333–3344.
- Carreiras,J.M.B., Jones,J., Lucas,R.M., & Gabriel,C. (2014) Land Use and Land Cover Change Dynamics across the Brazilian Amazon: Insights from Extensive Time-Series Analysis of Remote Sensing Data. *PLoS one*, 9(8), e104144.
- Castel,T., Beaudoin,A., & Stach,N. (2001) Sensitivity of space-borne SAR data to forest parameters over sloping terrain. Theory and experiment. *International Journal of Remote Sensing*, 22(12), 2351–2376.
- CEOS (2014) Global Baseline Data Acquisition Strategy for the Global Forest Observations Initiative (GFOI)., Geneva, Switzerland.
- Churesampant,K. & Susaki,J. (2011) Multi-temporal SAR and optical data fusion with texture measures for land cover classification based on the Bayesian theory. In *Proceedings of the ISPRS (Commission VI, WG VI/4)*. pp. 1–3.
- Clifford,M.J. (2011) Pork knocking in the land of many waters: Artisanal and small-scale mining (ASM) in Guyana. *Resources Policy*, 36(4), 354–362.
- Conejero,J. (2011) Interpolation Algorithms in PixInsight.
- Congalton,R.G. (1991) A review of assessing the accuracy of classifications of remotely sensed data. *Remote Sensing of Environment*, 37(1), 35–46.
- Coppin,P., Jonckheere,I., Nackaerts,K., Muys,B., & Lambin,E. (2004) Digital change detection methods in ecosystem monitoring: a review. *International Journal of Remote Sensing*, 25(9), 1565–1596.
- Van Dam,O. (2001) Forest filled with gaps: effects of gap size on water and nutrient cycling in tropical rain forest - A study in Guyana., Georgetown, Guyana: Tropenbos.
- Darwin,C. (1879) What Mr. Darwin Saw in his Voyage Round the World in the Ship “Beagle.”, New York: Harper & Brothers.

- Defries,R., Achard,F., Brown,S., Herold,M., Murdiyarto,D., Schlamadinger,B., & Desouzajr,C. (2007) Earth observations for estimating greenhouse gas emissions from deforestation in developing countries. *Environmental Science & Policy*, 10(4), 385–394.
- DeVries,B., Verbesselt,J., Kooistra,L., & Herold,M. (2015) Robust Monitoring of Small-Scale Forest Disturbances in a Tropical Montane Forest Using Landsat Time Series. *Remote Sensing of Environment*.
- Drusch,M., Del Bello,U., Carlier,S., Colin,O., Fernandez,V., Gascon,F., Hoersch,B., Isola,C., Laberinti,P., Martimort,P., Meygret, a., Spoto,F., Sy,O., Marchese,F., & Bargellini,P. (2012) Sentinel-2: ESA's Optical High-Resolution Mission for GMES Operational Services. *Remote Sensing of Environment*, 120, 25–36.
- Dunsmuir,W. & Robinson,P.M. (1981) Estimation of Time Series Models in the Presence of Missing Data. *Journal of the American Statistical Association*, 76(375), 560–568.
- Eilander,D., Annor,F., Iannini,L., & Giesen,N. van de (2014) Remotely Sensed Monitoring of Small Reservoir Dynamics: A Bayesian Approach. *Remote Sensing*, 6(2), 1191–1210.
- Erasmı,S. & Twele,A. (2009) Regional land cover mapping in the humid tropics using combined optical and SAR satellite data—a case study from Central Sulawesi, Indonesia. *International Journal of Remote Sensing*, 30(10), 2465–2478.
- ESA (2012) Report for mission selection: Biomass, ESA SP-1324/1 (3 volume series)., Noordwijk, The Netherlands: European Space Agency.
- Exelis Visual Information Solutions (2009) Atmospheric Correction Module: QUAC and FLAASH User' s Guide., Boulder, Colorado, USA: Exelis Visual Information Solutions.
- FAO (2011) State of the World's Forests 2011., Rome: Food and Agriculture Organization of the United Nations.
- Foley,J.A., Defries,R., Asner,G.P., Barford,C., Bonan,G., Carpenter,S.R., Chapin,F.S., Coe,M.T., Daily,G.C., Gibbs,H.K., Helkowski,J.H., Holloway,T., Howard,E.A., Kucharik,C.J., Monfreda,C., Patz,J. a, Prentice,I.C., Ramankutty,N., & Snyder,P.K. (2005) Global consequences of land use. *Science*, 309(5734), 570–574.
- Foody,G. (2002) Status of land cover classification accuracy assessment. *Remote Sensing of Environment*, 80(1), 185–201.
- Franklin,S., Lavigne,M., & Jr,E.H. (1995) Topographic dependence of synthetic aperture radar imagery. *Computers & Geosciences*, 21(4), 521–532.
- GCOS (2011) Systematic observation requirements for satellite-based products for climate, 2011 update., WMO GCOS Report 154, Geneva, Switzerland: World Meteorological Organization.
- GFOI (2014) Integrating remote-sensing and ground-based observations for estimation of emissions and removals of greenhouse gases in forests., Geneva, Switzerland: Group on Earth Observation (GEO).
- GFOI (2013) Review of Priority Research & Development Topics - R & D related to the use of Remote Sensing in National Forest Monitoring., Geneva, Switzerland: Group on Earth Observation (GEO).
- Ghazoul,J. & Sheil,D. (2010) Tropical Rain Forest Ecology, Diversity, and Conservation., Oxford: Oxford University Press.
- Goering,D.J., Hinzman,L.D., & Kane,D.L. (1995) Removal of terrain effects from SAR satellite imagery of Arctic tundra. *IEEE Transactions on Geoscience and Remote Sensing*, 33(1), 185–194.
- GOFC-GOLD (2014) A sourcebook of methods and procedures for monitoring and reporting anthropogenic greenhouse gas emissions and removals associated with deforestation, gains and losses of carbon stocks in forests remaining forests, and forestation. GOFC-GOLD Report versio., Wageningen University, The Netherlands: GOFC-GOLD Land Cover Project Office.
- Goward,S., Arvidson,T., & Williams,D. (2006) Historical record of Landsat global coverage: Mission operations, NSLRSDA, and international cooperator stations.

- Photogrammetric Engineering & Remote Sensing*, 72(10), 1155–1169.
- Griffiths,P., Kuemmerle,T., Baumann,M., Radeloff,V.C., Abrudan,I. V., Lieskovsky,J., Munteanu,C., Ostapowicz,K., & Hostert,P. (2013) Forest disturbances, forest recovery, and changes in forest types across the Carpathian ecoregion from 1985 to 2010 based on Landsat image composites. *Remote Sensing of Environment*, 151, 72–88.
- Griscom,B., Shoch,D., Stanley,B., Cortez,R., & Virgilio,N. (2009) Sensitivity of amounts and distribution of tropical forest carbon credits depending on baseline rules. *Environmental Science & Policy*, 12(7), 897–911.
- Gullison,R.E., Frumhoff,P.C., Canadell,J.G., Field,C.B., C.D., Hayhoe,K., Avissar,R., Curran,L.M., Friedlingstein,P., & D.C. (2007) Tropical Forests and Climate Policy. *Science*, 316(5827), 985–986.
- Häme,T., Kilpi,J., Ahola,H., Rauste,Y., Antropov,O., Rautiainen,M., Sirro,L., & Bounpone,S. (2013) Improved Mapping of Tropical Forests With Optical and SAR Imagery, Part I: Forest Cover and Accuracy Assessment Using Multi-Resolution Data. *IEEE Journal of Selected Topics in Applied Earth Observations and Remote Sensing*, 6(1), 74–91.
- Häme,T., Rauste,Y., Sirro,L., & Stach,N. (2009) Forest Cover Mapping in French Guiana since 1992 Using Satellite Radar Imagery. In *Proceedings of the 33rd International Symposium on Remote Sensing of Environment (ISRSE 33)*. Stresa, Italy.
- Hammer,D., Kraft,R., & Wheeler,D. (2014) Alerts of forest disturbance from MODIS imagery. *International Journal of Applied Earth Observation and Geoinformation*, 33, 1–9.
- Hammer,D., Kraft,R., & Wheeler,D. (2009) FORMA: Forest Monitoring for Action-Rapid Identification of Pan-Tropical Deforestation Using Moderate-Resolution Remotely Sensed Data., Rochester, New York: Centre for Global Development.
- Hansen,M., Potapov,P., Moore,R., Hancher,M., Turubanova,S.A., Tyukavina,A., Thau,D., Stehman,S. V., Goetz,S.J., Loveland,T.R., Kommareddy,A., Egorov,A., Chini,L., Justice,C.O., & Townshend,J.R.G. (2013) High-resolution global maps of 21st-century forest cover change. *Science*, 342, 850–853.
- Hansen,M.C. & Loveland,T.R. (2012) A review of large area monitoring of land cover change using Landsat data. *Remote Sensing of Environment*, 122, 66–74.
- Hansen,M.C., Stehman,S. V., Potapov,P. V., Loveland,T.R., Townshend,J.R.G., DeFries,R.S., Pittmann,K.W., Margono,B.A., Stolle,F., Steiner,M., Carroll,M., & DiMiceli,C. (2008) Humid tropical forest clearing from 2000 to 2005 quantified by using multitemporal and multiresolution remotely sensed data. *PNAS*, 105(27), 9439–9444.
- Harris,N.L., Brown,S., Hagen,S.C., Saatchi,S.S., Petrova,S., Salas,W., Hansen,M.C., Potapov,P. V., & Lotsch,A. (2012) Baseline Map of Carbon Emissions from Deforestation in Tropical Regions. *Science*, 336(6088), 1573–1576.
- Herold,M. (2009) An assessment of national forest monitoring capabilities in tropical non-Annex I countries: Recommendations for capacity building., Jena, Germany: Friedrich Schiller University Jena.
- Herold,M. & Skutsch,M. (2009) Measurement, reporting and verification for REDD+: Objectives, capacities and institutions. In *Measurement, reporting and verification in a post-2012 climate agreement*. CIFOR, pp. 85–100.
- Herold,M. & Skutsch,M. (2011) Monitoring, reporting and verification for national REDD+ programmes: two proposals. *Environmental Research Letters*, 6(1), 014002.
- Hinse,M., Gwyn,Q., & Bonn,F. (1988) Radiometric correction of C-band imagery for topographic effects in regions of moderate relief. *IEEE Transactions on Geoscience and Remote Sensing*, 26(2), 122–132.
- Hirschmugl,M., Steinegger,M., Gallaun,H., & Schardt,M. (2014) Mapping Forest Degradation due to Selective Logging by Means of Time Series Analysis: Case Studies in Central Africa. *Remote Sensing*, 6, 756–775.

- Hoan,N.T., Tateishi,R., Alsaaidh,B., Ngigi,T., Alimuddin,I., & Johnson,B. (2013) Tropical forest mapping using a combination of optical and microwave data of ALOS. *International Journal of Remote Sensing*, 34(1), 139–153.
- Hoekman,D.H. (1990) Radar remote sensing data for applications in forestry. Ph.D. Thesis, Wageningen Agricultural University.
- Hoekman,D.H. & Quiriones,M.J. (2000) Land cover type and biomass classification using AirSAR data for evaluation of monitoring scenarios in the Colombian Amazon. *IEEE Transactions on Geoscience and Remote Sensing*, 38(2), 685–696.
- Hoekman,D.H., van der Sanden,J.J., & Bijker,W. (1994) The AIRSAR-93 and SAREX-92 Campaigns in Guyana and Colombia. In *Proceedings of the 1994 IEEE Geoscience and Remote Sensing Symposium (IGARSS 1994)*. Pasadena, USA, pp. 1051–1053.
- Hoekman,D.H., Vissers,M.A.M., & Wielaard,N. (2010) PALSAR wide-area mapping of Borneo: methodology and map validation. *IEEE Journal of Selected Topics in Applied Earth Observations and Remote Sensing*, 3(4), 605–617.
- Holecz,F., Meier,E., Piesbergen,J., Nuesch,D., & Moreira,J. (1994) Rigorous derivation of backscattering coefficient. *IEEE Geoscience Remote Sensing Society Newsletter*, 92(1), 6–14.
- Hollmann,R., Merchant,C.J., Saunders,R., Downy,C., Buchwitz,M., Cazenave, a., Chuvieco,E., Defourny,P., de Leeuw,G., Forsberg,R., Holzer-Popp,T., Paul,F., Sandven,S., Sathyendranath,S., van Roozendaal,M., & Wagner,W. (2013) The ESA Climate Change Initiative: Satellite Data Records for Essential Climate Variables. *Bulletin of the American Meteorological Society*, 94(10), 1541–1552.
- Honaker,J. & King,G. (2010) What to Do about Missing Values in Time-Series Cross-Section Data. *American Journal of Political Science*, 54(2), 561–581.
- Hosonuma,N., Herold,M., De Sy,V., De Fries,R.S., Brockhaus,M., Verchot,L., Angelsen,A., & Romijn,E. (2012) An assessment of deforestation and forest degradation drivers in developing countries. *Environmental Research Letters*, 7(4), 044009.
- Huang,C., Goward,S.N., Masek,J.G., Thomas,N., Zhu,Z., & Vogelmann,J.E. (2010) An automated approach for reconstructing recent forest disturbance history using dense Landsat time series stacks. *Remote Sensing of Environment*, 114(1), 183–198.
- Huber,O., Gharbarran,G., & Funk,V.A. (1995) Preliminary vegetation map of Guyana., Washington DC: Biological Diversity of the Guianas Program, Smithsonian Institution.
- Huseby,R., Solberg,R., Koren,H., & Malnes,E. (2008) Time-series fusion of optical and SAR data for snow cover estimation using a Hidden Markov Model.
- Hussain,M., Chen,D., Cheng,A., Wei,H., & Stanley,D. (2013) Change detection from remotely sensed images: From pixel-based to object-based approaches. *ISPRS Journal of Photogrammetry and Remote Sensing*, 80, 91–106.
- Indufor Asia Pacific Ltd (2012) Guyana REDD + Monitoring Reporting & Verification System ( MRVS ) Interim Measures Report: 01 October 2010 – 31 December 2011 Version 1., Georgetown, Guyana: The Guyana Forestry Commission and Indufor.
- IPCC (2007) Summary for Policymakers. In S. Solomon et al., eds. *Climate Change 2007: The Physical Science Basis. Contribution of Working Group I to the Fourth Assessment Report of the Intergovernmental Panel on Climate change*. Cambridge, United Kingdom: Cambridge University Press.
- Irons,J.R., Dwyer,J.L., & Barsi,J. a. (2012) The next Landsat satellite: The Landsat Data Continuity Mission. *Remote Sensing of Environment*, 122, 11–21.
- Jensen,J.R. (2013) Remote Sensing of the Environment: An Earth Resource Perspective. 2nd ed., Pearson Education, Limited.
- Jin,S. & Sader,S.A. (2005) Comparison of time series tasseled cap wetness and the normalized difference moisture index in detecting forest disturbances. *Remote Sensing of Environment*, 94(3), 364–372.

- De Jong,R., de Bruin,S., de Wit,A., Schaepman,M.E., & Dent,D.L. (2011) Analysis of monotonic greening and browning trends from global NDVI time-series. *Remote Sensing of Environment*, 115(2), 692–702.
- Kaufman,Y.J., Wald,A.E., Remer,L.A., Gao,B., Li,R., & Flynn,L. (1997) The MODIS 2.1- $\mu\text{m}$  Channel — Correlation with Visible Reflectance for Use in Remote Sensing of Aerosol. *IEEE Transactions on Geoscience and Remote Sensing*, 35(5), 1286–1298.
- Kellndorfer,J., Pierce,L., Dobson,C.M., & Ulaby,T.F. (1998) Toward consistent regional-to-global-scale vegetation characterization using orbital SAR systems. *IEEE Transactions on Geoscience and Remote Sensing*, 36(5), 1396–1411.
- Kennedy,R.E., Yang,Z., & Cohen,W.B. (2010) Detecting trends in forest disturbance and recovery using yearly Landsat time series: 1. LandTrendr — Temporal segmentation algorithms. *Remote Sensing of Environment*, 114(12), 2897–2910.
- Kiiveri,H. & Caccetta,P. (1998) Image fusion with conditional probability networks for monitoring the salinization of farmland. *Digital signal processing*, 230(1998), 225–230.
- Kiiveri,H.T., Caccetta,P., & Evans,F. (2001) Use of conditional probability networks for environmental monitoring. *International Journal of Remote Sensing*, 22(7), 1173–1190.
- Kim,D.-H., Sexton,J.O., Noojipady,P., Huang,C., Anand,A., Channan,S., Feng,M., & Townshend,J.R. (2014) Global, Landsat-based forest-cover change from 1990 to 2000. *Remote Sensing of Environment*, 155, 178–193.
- Korting,T., Fonseca,L., & Câmara,G. (2010) Decision Trees to Detect Changes in Remote Sensing Image Time Series. In *Proceedings of the 2010 Reserach Symposium GIScience for Enviornmental Change (GeoChange 2010)*. Campos do Jordao, Brazil.
- Kuplich,T.M. (2006) Classifying regenerating forest stages in Amazônia using remotely sensed images and a neural network. *Forest Ecology and Management*, 234, 1–9.
- Kuplich,T.M., Curran,P.J., & Atkinson,P.M. (2005) Relating SAR image texture to the biomass of regenerating tropical forests. *International Journal of Remote Sensing*, 26(21), 4829–4854.
- Laliberte,A.S., Browning,D.M., & Rango,A. (2012) A comparison of three feature selection methods for object-based classification of sub-decimeter resolution UltraCam-L imagery. *International Journal of Applied Earth Observation and Geoinformation*, 15(April 2012), 70–78.
- Leclerc,G., Beaulieu,N., & Bonn,F. (2001) A simple method to account for topography in the radiometric correction of radar imagery. *International Journal of Remote Sensing*, 22(17), 3553–3570.
- Lee,C.A., Gasster,S.D., Plaza,A., Chang,C.I., & Huang,B. (2011) Recent developments in high performance computing for remote sensing: A review. *IEEE Journal of Selected Topics in Applied Earth Observations and Remote Sensing*, 4(3), 508–527.
- Lehmann,E., Caccetta,P., Zhou,Z., Mitchell,A., Tapley,I., Milne,A., Held,A., Lowell,K., & McNeill,S. (2011) Forest Discrimination Analysis of Combined Landsat and ALOS-PALSAR Data. In *Proceedings of the 34rd International Symposium on Remote Sensing of Environment (ISRSE 34)*. Sydney, Australia.
- Lehmann,E.A., Caccetta,P., Lowell,K., Mitchell,A., Zhou,Z.-S., Held,A., Milne,T., & Tapley,I. (2015) SAR and optical remote sensing: Assessment of complementarity and interoperability in the context of a large-scale operational forest monitoring system. *Remote Sensing of Environment*, 156(1), 335–348.
- Lehmann,E.A., Caccetta,P., Zhou,Z.-S., McNeill,S.J., Wu,X., & Mitchell,A.L. (2012) Joint Processing of Landsat and ALOS-PALSAR Data for Forest Mapping and Monitoring. *IEEE Transactions on Geoscience and Remote Sensing*, 50(1), 55–67.
- Lehmann,E.A., Wallace,J.F., Caccetta,P.A., Furby,S.L., & Zdunic,K. (2013) Forest cover trends from time series Landsat data for the Australian continent. *International Journal of Applied Earth Observation and Geoinformation*, 21, 453–462.
- Loew,A. & Mauser,W. (2007) Generation of geometrically and radiometrically terrain

- corrected SAR image products. *Remote Sensing of Environment*, 106(3), 337–349.
- Lu, D., Li, G., & Moran, E. (2014) Current situation and needs of change detection techniques. *International Journal of Image and Data Fusion*, 5(1), 13–38.
- Lu, D., Mausel, P., Brondizio, E., & Moran, E. (2004) Change detection techniques. *International Journal of Remote Sensing*, 25(12), 2365–2401.
- Lucas, R., Armston, J., Fairfax, R., Fensham, R., Accad, A., Carreiras, J., Kelley, J., Bunting, P., Clewley, D., Bray, S., Metcalfe, D., Dwyer, J., Bowen, M., Eyre, T., Laidlaw, M., & Shimada, M. (2010) An Evaluation of the ALOS PALSAR L-band backscatter—Above ground biomass relationship Queensland, Australia: Impacts of surface moisture condition and vegetation structure. *IEEE Journal of Selected Topics in Applied Earth Observations and Remote Sensing*, 3(4), 576–593.
- Luckman, A., Baker, J., Kuplich, T.M., da Costa Freitas Yanasse, C., & Frery, A.C. (1997) A study of the relationship between radar backscatter and regenerating tropical forest biomass for spaceborne SAR instruments. *Remote Sensing of Environment*, 60(1), 1–13.
- Luckman, A.J. (1998) The effects of topography on mechanisms of radar backscatter from coniferous forest and upland pasture. *IEEE Transactions on Geoscience and Remote Sensing*, 36(5), 1830–1834.
- Lund, H.G. (1999) A 'forest' by any other name... *Environmental Science & Policy*, 2(2), 125–133.
- Lynch, J., Maslin, M., Balzter, H., Sweeting, M., & Degrada, F. (2013) Choose satellites to monitor deforestation. *Nature*, 496(7445), 293–294.
- Maniatis, D. & Mollicone, D. (2010) Options for sampling and stratification for national forest inventories to implement REDD+ under the UNFCCC. *Carbon balance and management*, 5(1), 9.
- Margono, B. & Turubanova, S. (2012) Mapping and monitoring deforestation and forest degradation in Sumatra (Indonesia) using Landsat time series data sets from 1990 to 2010. *Environmental Research Letters*, 7(3), 034010.
- Margono, B.A., Potapov, P. V., Turubanova, S., Stolle, F., & Hansen, M.C. (2014) Primary forest cover loss in Indonesia over 2000–2012. *Nature Climate Change*, 4, 730–735.
- Masek, J.G., Goward, S.N., Kennedy, R.E., Cohen, W.B., Moisen, G.G., Schleeweis, K., & Huang, C. (2013) United States Forest Disturbance Trends Observed Using Landsat Time Series. *Ecosystems*, 16(6), 1087–1104.
- Masek, J.G.J., Vermote, E.F.E., Saleous, N.E., Wolfe, R., Hall, F.G., Huemmrich, K.F., Gao, F., Kutler, J., & Lim, T. (2006) A Landsat Surface Reflectance Dataset for North America, 1990–2000. *IEEE Geoscience and Remote Sensing Letters*, 3(1), 68–72.
- Matricardi, E.A.T., Skole, D.L., Pedlowski, M.A., Chomentowski, W., & Fernandes, L.C. (2010) Assessment of tropical forest degradation by selective logging and fire using Landsat imagery. *Remote Sensing of Environment*, 114(5), 1117–1129.
- Mermoz, S., Réjou-Méchain, M., Villard, L., Le Toan, T., Rossi, V., & Gourlet-Fleury, S. (2015) Decrease of L-band SAR backscatter with biomass of dense forests. *Remote Sensing of Environment*.
- Mitchard, E.T.A., Saatchi, S.S., Woodhouse, I.H., Nangendo, G., Ribeiro, N.S., Williams, M., Ryan, C.M., Lewis, S.L., Feldpausch, T.R., & Meir, P. (2009) Using satellite radar backscatter to predict above-ground woody biomass: A consistent relationship across four different African landscapes. *Geophysical Research Letters*, 36(23), L23401.
- Mitchell, A.L., Tapley, I., Milne, A.K., Williams, M.L., Zhou, Z.-S., Lehmann, E., Caccetta, P., Lowell, K., & Held, A. (2014) C- and L-band SAR interoperability: Filling the gaps in continuous forest cover mapping in Tasmania. *Remote Sensing of Environment*, 155, 58–68.
- Motohka, T., Shimada, M., Uryu, Y., & Setiabudi, B. (2014) Using time series PALSAR gamma nought mosaics for automatic detection of tropical deforestation: A test study in Riau, Indonesia. *Remote Sensing of Environment*, 155, 79–88.
- Nellermann, C. (2012) Green Carbon, Black Trade: Illegal Loggin, Tax Fraud and Laundering in

- the Worlds Tropical Forests. A rapid response assessment., INTERPOL Environmental Crime Programme, United Nations Environmental Programme, GRID-Arendal.
- Notarnicola,C. (2014) A Bayesian Change Detection Approach for Retrieval of Soil Moisture Variations Under Different Roughness Conditions. *IEEE Geoscience and Remote Sensing Letters*, 11(2), 414–418.
- Olander,L.P., Gibbs,H.K., Steining,M., Swenson,J.J., & Murray,B.C. (2008) Reference scenarios for deforestation and forest degradation in support of REDD: a review of data and methods. *Environmental Research Letters*, 3(2), 025011.
- Oliver,C.J. & Quegan,S. (1998) Understanding Synthetic Aperture Radar Images., Norwood, USA: Artech House.
- Olofsson,P., Foody,G., & Herold,M. (2014) Good practices for estimating area and assessing accuracy of land change. *Remote Sensing of Environment*, 148, 42–57.
- Olofsson,P., Foody,G.M., Stehman,S. V., & Woodcock,C.E. (2013) Making better use of accuracy data in land change studies: Estimating accuracy and area and quantifying uncertainty using stratified estimation. *Remote Sensing of Environment*, 129, 122–131.
- Pan,Y., Birdsey,R.A., Fang,J., Houghton,R., Kauppi,P.E., A.W., Phillips,O.L., Shvidenko,A., Lewis,S.L., Canadell,J.G., Ciais,P., Jackson,R.B., Pacala,S., Mcguire,A.D., Piao,S., Rautiainen,A., & Hayes,D. (2011) A Large and Persistent Carbon Sink in the World's Forests. *Science*, 333(6045), 988–993.
- Pelletier,J. & Goetz,S.J. (2015) Baseline data on forest loss and associated uncertainty: advances in national forest monitoring. *Environmental Research Letters*, 10(2), 021001.
- Pelletier,J., Ramankutty,N., & Potvin,C. (2011) Diagnosing the uncertainty and detectability of emission reductions for REDD+ under current capabilities: an example for Panama. *Environmental Research Letters*, 6(2), 024005.
- Pflugmacher,D., Cohen,W.B., & E. Kennedy,R. (2012) Using Landsat-derived disturbance history (1972–2010) to predict current forest structure. *Remote Sensing of Environment*, 122, 146–165.
- Pierdicca,N., Pulvirenti,L., & Bignami,C. (2010) Soil moisture estimation over vegetated terrains using multitemporal remote sensing data. *Remote Sensing of Environment*, 114(2), 440–448.
- Pierdicca,N., Pulvirenti,L., & Pace,G. (2014) A Prototype Software Package to Retrieve Soil Moisture From Sentinel-1 Data by Using a Bayesian Multitemporal Algorithm. *IEEE Journal of Selected Topics in Applied Earth Observations and Remote Sensing*, 7(1), 153–166.
- Pohl,C. & Genderen,J.L. Van (1998) Multisensor image fusion in remote sensing: concepts, methods and applications (Review article). *International Journal of Remote Sensing*, 19(5), 823–854.
- Potapov,P. V., Turubanova,S. a., Hansen,M.C., Adusei,B., Broich,M., Altstatt,A., Mane,L., & Justice,C.O. (2012) Quantifying forest cover loss in Democratic Republic of the Congo, 2000–2010, with Landsat ETM+ data. *Remote Sensing of Environment*, 122, 106–116.
- Potapov,P.V., Turubanova,S. a., Tyukavina, a., Krylov, a. M., McCarty,J.L., Radeloff,V.C., & Hansen,M.C. (2014) Eastern Europe's forest cover dynamics from 1985 to 2012 quantified from the full Landsat archive. *Remote Sensing of Environment*.
- Pöyry Management Consulting (NZ) Limited (2011) Guyana REDD+ Monitoring, Reporting and Verification System (MRVS) Interim Measures Report (Final, 16 March 2011)., Georgetown, Guyana: The Guyana Forestry Commission and Pöyry Management Consulting (NZ) Limited.
- Pratihast,A., DeVries,B., Avitabile,V., de Bruin,S., Kooistra,L., Tekle,M., & Herold,M. (2014) Combining Satellite Data and Community-Based Observations for Forest Monitoring. *Forests*, 5(10), 2464–2489.
- Quegan,S. & Toan,T. Le (1998) Analysing multitemporal SAR images. In *Proceedings of the Anais IX Simposio Brasileiro de*

- Sensoriamento Remoto*. Santos, Brasil, pp. 1183–1194.
- Quegan,S., Whittle,M., & Uryu,Y. (2009) K & C Science Report – Phase 1 Monitoring Indonesian Forests with ALOS-PALSAR., Kyoto & Carbon Initiative.
- Quegan,S. & Yu,J.J. (2001) Filtering of multichannel SAR images. *IEEE Transactions on Geoscience and Remote Sensing*, 39(11), 2373–2379.
- Quegan,S., Yu,J.J., & Le Toan,T.L. (2000) Iterative multi-channel filtering of SAR images. In *Proceedings of the 2000 IEEE Geoscience and Remote Sensing Symposium (IGARSS 2000)*. Honolulu, Hawaii, pp. 657–659.
- Racault,M.-F., Sathyendranath,S., & Platt,T. (2014) Impact of missing data on the estimation of ecological indicators from satellite ocean-colour time-series. *Remote Sensing of Environment*, 152, 15–28.
- Rahman,M.M. & Sumantyo,J.T.S. (2012) Quantifying deforestation in the Brazilian Amazon using Advanced Land Observing Satellite Phased Array L-band Synthetic Aperture Radar (ALOS PALSAR) and Shuttle Imaging Radar (SIR)-C data. *Geocarto International*, 27(6), 463–478.
- Rakwatin,P., Longépé,N., Isoguchi,O., Shimada,M., Uryu,Y., & Takeuchi,W. (2012) Using multiscale texture information from ALOS PALSAR to map tropical forest. *International Journal of Remote Sensing*, 33(24), 7727–7746.
- Reiche,J. & Herold,M. (2012) Concepts and Processing Techniques for a global Sentinel 1-3 Land Cover Dynamics and Change (LCDC) product. In *ESA SP-707, Proceedings of the Sentinel 2 Preparatory Symposium*. Frascati, Italy, p. 8.
- Reiche,J., Souza,C.M., Hoekman,D.H., Verbesselt,J., Persaud,H., & Herold,M. (2013) Feature Level Fusion of Multi-Temporal ALOS PALSAR and Landsat Data for Mapping and Monitoring of Tropical Deforestation and Forest Degradation. *IEEE Journal of Selected Topics in Applied Earth Observations and Remote Sensing*, 6(5), 2159–2173.
- Reiche,J., Verbesselt,J., Hoekman,D., & Herold,M. (2015) Fusing Landsat and SAR time series to detect deforestation in the tropics. *Remote Sensing of Environment*, 156, 276–293.
- Ribbes,F., Le Toan,T.L., Bruniquel,J., Floury,N., Stussi,N., & Wasrin,U.R. (1997) Deforestation monitoring in tropical regions using multitemporal ERS/JERS SAR and INSAR data. In *Proceedings of the 1997 IEEE Geoscience and Remote Sensing Symposium (IGARSS 1997)*. IEEE, pp. 1560–1562.
- Rignot,E., Salas,W., & Skole,D.L. (1997) Mapping deforestation and secondary growth in Rondonia, Brazil, using imaging radar and thematic mapper data. *Remote Sensing of Environment*, 59(2), 167–179.
- Romijn,E., Herold,M., Kooistra,L., Murdiyarso,D., & Verchot,L. (2012) Assessing capacities of non-Annex I countries for national forest monitoring in the context of REDD+. *Environmental Science & Policy*, 19-20(May–June 2012), 33–48.
- Rosen,P.A., Kim,Y., Hensley,S., Shaffer,S., Veilleux,L., Hoffman,J., Chuang,C.-L., Chakraborty,M., Sagi,V.R., Satish,R., Putrevu,D., & Bhan,R. (2014) An L- and S-band SAR Mission Concept for Earth Science and Applications. In *Proceedings of the 10th European Conference on Synthetic Aperture Radar (EUSAR 2014)*. Berlin, Germany.
- Rosenqvist,A., Shimada,M., Member,S., Ito,N., & Watanabe,M. (2007) ALOS PALSAR: A Pathfinder Mission for Global-Scale Monitoring of the Environment. *IEEE Transactions on Geoscience and Remote Sensing*, 45(11), 3307–3316.
- Rosenqvist,A., Shimada,M., Suzuki,S., Ohgushi,F., Tadono,T., Watanabe,M., Tsuzuku,K., Watanabe,T., Kamijo,S., & Aoki,E. (2014) Operational performance of the ALOS global systematic acquisition strategy and observation plans for ALOS-2 PALSAR-2. *Remote Sensing of Environment*, 155, 3–12.
- Roy,D.P., Wulder,M.A., Loveland,T.R., C.E.,W., Allen,R.G., Anderson,M.C., Helder,D., Irons,J.R., Johnson,D.M., Kennedy,R., Scambos,T.A., Schaaf,C.B., Schott,J.R., Sheng,Y., Vermote,E.F., Belward,A.S., Bindschadler,R., Cohen,W.B., Gao,F., et al. (2014) Landsat-8: Science and product vision for terrestrial global change

- research. *Remote Sensing of Environment*, 145, 154–172.
- Ryan,C.M., Hill,T., Woollen,E., Ghee,C., Mitchard,E., Cassells,G., Grace,J., Woodhouse,I.H., & Williams,M. (2012) Quantifying small-scale deforestation and forest degradation in African woodlands using radar imagery. *Global Change Biology*, 18(1), 243–257.
- Van der Sanden,J.J. (1997) Radar remote sensing to support tropical forest management., Georgetown, Guyana: Tropenbos-Guyana Programme.
- Sannier,C., McRoberts,R.E., Fichet,L.-V., & Makaga,E.M.K. (2014) Using the regression estimator with Landsat data to estimate proportion forest cover and net proportion deforestation in Gabon. *Remote Sensing of Environment*, 151, 138–148.
- Sasaki,N., Asner,G.P., Knorr,W., Durst,P.B., Priyadi,H.R., & Putz,F.E. (2011) Approaches to classifying and restoring degraded tropical forests for the anticipated REDD+ climate change mitigation mechanism. *iForest - Biogeosciences and Forestry*, 4(1), 1–6.
- Schmidt,G.L., Jenkerson,C.B., Masek,J., Vermote,E., & Gao,F. (2013) Landsat Ecosystem Disturbance Adaptive Processing System (LEDAPS) Algorithm Description.,
- Seber,G.A.F. & Lee,A.J. (2003) Linear Regression Analysis. 2nd ed., New Jersey, USA: Wiley & Sons.
- Seneca Creek Associates (2004) “Illegal” Logging and Global Wood Markets: The Competitive Impacts on the U.S. Wood Products Industry., Prepared for American Forest & Paper Association by Seneca Creek Associates and Wood Resources International.
- Sexton,J.O., Noojipady,P., Anand,A., Song,X.-P., McMahon,S., Huang,C., Feng,M., Channan,S., & Townshend,J.R. (2015) A model for the propagation of uncertainty from continuous estimates of tree cover to categorical forest cover and change. *Remote Sensing of Environment*, 156, 418–425.
- Shimabukuro,Y.E., Duarte,V., Anderson,L.O., Valeriano,D.M., Arai,E., Freitas,R.M. De, Rudorff,B.F.T., & Moreira,A.A. (2006) Near real time detection of deforestation in the Brazilian Amazon using MODIS imagery. *Revista Ambiente e Agua - An Interdisciplinary Journal of Applied Science*, 1(1), 37–47.
- Shimada,M. (2010) Ortho-Rectification and Slope Correction of SAR Data Using DEM and Its Accuracy Evaluation. *IEEE Journal of Selected Topics in Applied Earth Observations and Remote Sensing*, 3(4), 657–671.
- Shimada,M., Isoguchi,O., Tadono,T., & Isono,K. (2009) PALSAR Radiometric and Geometric Calibration. *IEEE Transactions on Geoscience and Remote Sensing*, 47(12), 3915–3932.
- Shimada,M., Itoh,T., Motooka,T., Watanabe,M., Shiraishi,T., Thapa,R., & Lucas,R. (2014) New global forest/non-forest maps from ALOS PALSAR data (2007–2010). *Remote Sensing of Environment*, 155, 13–31.
- Shimada,M., Tadono,T., & Rosenqvist,A. (2010) Advanced Land Observing Satellite (ALOS) and Monitoring Global Environmental Change. *Proceedings of the IEEE*, 98(5), 780–799.
- Showstack,R. (2014) Global Forest Watch Initiative Provides Opportunity for Worldwide Monitoring. *Transactions American Geophysical Union*, 95(9), 77–79.
- Simard,M., Saatchi,S.S., Grandi,G. De, & Member,S. (2000) The Use of Decision Tree and Multiscale Texture for Classification of JERS-1 SAR Data over Tropical. *IEEE Transactions on Geoscience and Remote Sensing*, 38(5), 2310–2321.
- Small,D. (2011) Flattening gamma: radiometric terrain correction for SAR imagery. *IEEE Transactions on Geoscience and Remote Sensing*, 49(9), 3081–3093.
- Solberg,A., Jain,A., & Taxt,T. (1994) Multisource classification of remotely sensed data: Fusion of Landsat TM and SAR images. *IEEE Transactions on Geoscience and Remote Sensing*, 32(4), 768–778.
- Solberg,R. & Huseby,R. (2008) Time-series fusion of optical and SAR data for snow cover area mapping. In *Proceedings of the EARSeL Land Ice and Snow Special Interest Group Workshop*. Berne, Switzerland, p. 9.

- Souza,C. (2003) Mapping forest degradation in the Eastern Amazon from SPOT 4 through spectral mixture models. *Remote Sensing of Environment*, 87(4), 494–506.
- Souza,C., Cochrane,M., Sales,M., Monteiro,A., & Mollicone,D. (2009) Case Studies on Measuring and Assessing Forest Degradation Integrating Forest Transects and Remote Sensing Data to Quantify Carbon Loss due to Degradation in the Brazilian Amazon., Forest Resources Assessment Working Paper 161, Rome: Food and Agriculture Organization of the United Nations.
- Souza,C., Roberts,D., & Cochrane,M. (2005) Combining spectral and spatial information to map canopy damage from selective logging and forest fires. *Remote Sensing of Environment*, 98(2-3), 329–343.
- Souza,C., Siqueira,J., Sales,M., Fonseca,A., Ribeiro,J., Numata,I., Cochrane,M., Barber,C., Roberts,D., & Barlow,J. (2013) Ten-Year Landsat Classification of Deforestation and Forest Degradation in the Brazilian Amazon. *Remote Sensing*, 5(11), 5493–5513.
- Stehman,S.V. (2009) Sampling designs for accuracy assessment of land cover. *International Journal of Remote Sensing*, 30(20), 5243–5272.
- Stern,N. (2007) The economics of climate change., Cambridge, United Kingdom: Cambridge University Press.
- Strahler,A.H. (1980) The use of prior probabilities in maximum likelihood classification of remotely sensed data. *Remote Sensing of Environment*, 10(2), 135–163.
- Stussi,N., Beaudoin,A., Castel,T., & Gigord,P. (1995) Radiometric correction of multiconfiguration spaceborne SAR data over hilly terrain. In *Proceedings of the International Symposium on Retrieval of Bio- and Geophysical Parameters from SAR Data for Land Applications*. Toulouse, France, pp. 457–466.
- Sun,G., Ranson,K.J., & Kharuk,V.I. (2002) Radiometric slope correction for forest biomass estimation from SAR data in the Western Sayani Mountains, Siberia. *Remote Sensing of Environment*, 79, 279–287.
- Suzuki,S., Kankaku,Y., & Osawa,Y. (2013) ALOS-2 current status and operation plan. In *Proceedings of the SPIE 8889, Sensors, Systems, and Next-Generation Satellites XVII, 888908*. Dresden, Germany.
- De Sy,V., Herold,M., Achard,F., Asner,G.P., Held,A., Kellndorfer,J., & Verbesselt,J. (2012) Synergies of multiple remote sensing data sources for REDD+ monitoring. *Current Opinion in Environmental Sustainability*, 4(6), 696–706.
- Symeonakis,E., Caccetta,P., Koukoulas,S., Furby,S., Karathanasis,N., & Taylor,P. (2012) Multi-temporal land-cover classification and change analysis with conditional probability networks: the case of Lesvos Island (Greece). *International Journal of Remote Sensing*, 33(13), 4075–4093.
- Takeuchi,S. & Oguro,Y. (2003) A comparative study of coherence patterns in C-band and L-band interferometric SAR from tropical rain forest areas. *Advances in Space Research*, 32(11), 2305–2310.
- Teillet,P.M., Guindon,B., Meunier,J.F., & Goodenough,D.G. (1985) Slope-aspect effects in synthetic aperture radar in imagery. *Canadian Journal of Remote Sensing*, 11(1), 39–49.
- Thapa,R.B., Shimada,M., Watanabe,M., & Motohka,T. (2013) The tropical forest in south east Asia: Monitoring and scenario modeling using synthetic aperture radar data. *Applied Geography*, 41, 168–178.
- Torres,R., Snoeij,P., Geudtner,D., Bibby,D., Davidson,M., Attema,E., Potin,P., Rommen,B., Floury,N., Brown,M., Traver,I.N., Deghaye,P., Duesmann,B., Rosich,B., Miranda,N., Bruno,C., L'Abbate,M., Croci,R., Pietropaolo,A., et al. (2012) GMES Sentinel-1 mission. *Remote Sensing of Environment*, 120, 9–24.
- Trouv e,E., Chambenoit,Y., Classeau,N., & Bolon,P. (2003) Statistical and Operational Performance Assessment of Multitemporal SAR Image Filtering. *IEEE Transactions on Geoscience and Remote Sensing*, 41(11), 2519–2530.
- Tyukavina,A., Stehman,S. V., Potapov,P. V., Turubanova,S. a, Baccini,A., Goetz,S.J., Laporte,N.T., Houghton,R. a, & Hansen,M.C. (2013) National-scale estimation of gross forest

- aboveground carbon loss: a case study of the Democratic Republic of the Congo. *Environmental Research Letters*, 8(4), 044039.
- Ulaby, T.F., Moore, R.K., & Fung, A.K. (1986) *Microwave remote sensing - Active and Passive*, Norwood, USA: Artech House.
- Ulander, L.M.H. (1996) Radiometric slope correction of synthetic-aperture radar images. *IEEE Transactions on Geoscience and Remote Sensing*, 34(5), 1115–1122.
- UNFCCC (2002) Land use, land-use change and forestry. *United National Framework Convention on Climate Change, The Marrakesh Accord Decision 11/CP.7*.
- UNFCCC (2009) Methodological guidance for activities relating to reducing emission from deforestation and forest degradation and the role of conservation, sustainable forest management of forests and enhancements of forest carbon stocks in developing countries. *United National Framework Convention on Climate Change Decision 4/CP.15*.
- Vaglio Laurin, G., Liesenberg, V., Chen, Q., Guerriero, L., Del Frate, F., Bartolini, A., Coomes, D., Wilebore, B., Lindsell, J., & Valentini, R. (2013) Optical and SAR sensor synergies for forest and land cover mapping in a tropical site in West Africa. *International Journal of Applied Earth Observation and Geoinformation*, 21, 7–16.
- Vargas, R., Paz, F., & Jong, B. De (2013) Quantification of forest degradation and belowground carbon dynamics: ongoing challenges for monitoring, reporting and verification activities for REDD+. *Carbon Management*, 4(6), 579–582.
- Venables, W.N. & Ripley, B.D. (2002) *Modern Applied Statistics with S*. 4th ed., New York, USA: Springer.
- Verbesselt, J., Herold, M., & Zeileis, A. (2012) Near real-time disturbance detection using satellite image time series. *Remote Sensing of Environment*, 123, 98–108.
- Verbesselt, J., Hyndman, R., Newnham, G., & Culvenor, D. (2010)(a) Detecting trend and seasonal changes in satellite image time series. *Remote Sensing of Environment*, 114(1), 106–115.
- Verbesselt, J., Hyndman, R., Zeileis, A., & Culvenor, D. (2010)(b) Phenological change detection while accounting for abrupt and gradual trends in satellite image time series. *Remote Sensing of Environment*, 114(12), 2970–2980.
- Vermote, E.F., El Saleous, N., Justice, C.O., Kaufman, Y.J., Privette, J.L., Remer, L., Roger, J.C., & Tanré, D. (1997) Atmospheric correction of visible to middle-infrared EOS-MODIS data over land surfaces: Background, operational algorithm and validation., NASA Publications, Paper 31.
- Walker, W.S., Stickler, C.M., KelIndorfer, J.M., Kirsch, K.M., & Nepstad, D.C. (2010) Large-Area Classification and Mapping of Forest and Land Cover in the Brazilian Amazon: A Comparative Analysis of ALOS/PALSAR and Landsat Data Sources. *IEEE Journal of Selected Topics in Applied Earth Observations and Remote Sensing*, 3(4), 594–604.
- Waske, B. & van der Linden, S. (2008) Classifying Multilevel Imagery From SAR and Optical Sensors by Decision Fusion. *IEEE Transactions on Geoscience and Remote Sensing*, 46(5), 1457–1466.
- Wegner, J.D., Thiele, A., & Soergel, U. (2009) Fusion of optical and InSAR features for building recognition in urban areas. In U. Stilla, F. Rottensteiner, & N. Paparoditis, eds. *Proceedings of the IAPRS (Commission III, WG III/4)*. Paris, France, pp. 169–174.
- Van der Werf, G.R., Morton, D.C., DeFries, R.S., Olivier, J.G.J., Kasibhatla, P.S., Jackson, R.B., Collatz, G.J., & Randerson, J.T. (2009) CO2 emissions from forest loss. *Nature Geoscience*, 2(11), 737–738.
- Werner, C. & Strozz, T. (2000) Gamma SAR and interferometric processing software. In *Proceedings of the 2000 ERS-ENVISAT Symposium*. Gothenburg, Sweden.
- West, T.A.P., Vidal, E., & Putz, F.E. (2014) Forest biomass recovery after conventional and reduced-impact logging in Amazonian Brazil. *Forest Ecology and Management*, 314, 59–63.
- Wheeler, D., Hammer, D., Kraft, R., & Steele, A. (2014) Satellite-based forest clearing detection in the

- Brazilian Amazon: FORMA, DETER, and PRODES., World Resources Institute.
- Whittle,M., Quegan,S., Uryu,Y., Stüewe,M., & Yulianto,K. (2012) Detection of tropical deforestation using ALOS-PALSAR: A Sumatran case study. *Remote Sensing of Environment*, 124, 83–98.
- Woodcock,C., Allen,R., Anderson,M., Belward,A., Bindschadler,R., Cohen,W., Gao,F., Goward,S.N., Helder,D., Helmer,E.H., Nemani,R., Oreopoulos,L., Schott,J., Thenkabail,P.S., Vermote,E.F., Vogelmann,J., Wulder,M.A., & Wynne,R. (2008) Free access to Landsat imagery. *Science*, 320(5879), 1011.
- Woodhouse,I.H. (2005) Introduction to Microwave Remote Sensing., CRC Press.
- Wulder,M.A., Masek,J.G., Cohen,W.B., Loveland,T.R., & Woodcock,C.E. (2012) Opening the archive: How free data has enabled the science and monitoring promise of Landsat. *Remote Sensing of Environment*, 122, 2–10.
- Xin,Q., Olofsson,P., Zhu,Z., Tan,B., & Woodcock,C.E. (2013) Toward near real-time monitoring of forest disturbance by fusion of MODIS and Landsat data. *Remote Sensing of Environment*, 135, 234–247.
- Zarin,D.J. (2012) Atmospheric science. Carbon from tropical deforestation. *Science*, 336(6088), 1518–9.
- Zeng,T., Hu,C., Quegan,S., Uryu,Y., & Dong,X. (2014) Regional tropical deforestation detection using ALOS PALSAR 50 m mosaics in Riau province, Indonesia. *Electronics Letters*, 50(7), 547–549.
- Zhang,C., Li,W., & Travis,D. (2007) Gaps-fill of SLC-off Landsat ETM+ satellite image using a geostatistical approach. *International Journal of Remote Sensing*, 28(22), 5103–5122.
- Zhang,J. (2010) Multi-source remote sensing data fusion: status and trends. *International Journal of Image and Data Fusion*, 1(1), 5–24.
- Zhang,X., Friedl,M.A., & Schaaf,C.B. (2009) Sensitivity of vegetation phenology detection to the temporal resolution of satellite data. *International Journal of Remote Sensing*, 30(8), 2061–2074.
- Zhu,Z. & Woodcock,C.E. (2014) Continuous change detection and classification of land cover using all available Landsat data. *Remote Sensing of Environment*, 144, 152–171.
- Zhu,Z. & Woodcock,C.E. (2012) Object-based cloud and cloud shadow detection in Landsat imagery. *Remote Sensing of Environment*, 118, 83–94.
- Zhu,Z., Woodcock,C.E., & Olofsson,P. (2012) Continuous monitoring of forest disturbance using all available Landsat imagery. *Remote Sensing of Environment*, 122, 75–91.
- Zink,M., Fiedler,H., Hajnsek,I., Krieger,G., Moreira,A., & Werner,M. (2006) The TanDEM-X Mission Concept. In *Proceedings of the 2006 IEEE International Symposium on Geoscience and Remote Sensing (IGARSS 2006)*. Denver, USA: Ieee, p. 4.
- Van Zyl,J.J., Chapman,B.D., Dubois,P., & Shi,J. (1993) The effect of topography on SAR calibration. *IEEE Transactions on Geoscience and Remote Sensing*, 31(5), 1036–1043.

## Summary

Tropical forests are the largest of the global forest biomes and play a crucial role in the global carbon, hydrological and biochemical cycles. Increasing demand for resources rapidly increases the pressure on tropical forests. As a result tropical regions have been undergoing rapid changes in forest cover in recent decades. These changes are the second largest contributor of greenhouse gas emissions in the atmosphere. Spatially and timely consistent detection of tropical deforestation and forest degradation is fundamental to reliably estimate greenhouse gas emissions, and to successfully implement climate mechanisms like reducing emissions from deforestation and forest degradation (REDD+).

To assess historical and future changes in forest cover, satellite remote sensing at medium resolution scale constitutes a powerful tool. Reviewing satellite-based optical and Synthetic Aperture Radar (SAR) efforts for tropical forest monitoring revealed that operationalised optical-based approaches exist, but frequent cloud cover limits their applicability in the tropics. SAR remote sensing has also demonstrated its capability, but the observation frequency of SAR imagery and appropriate time series methods are limited. Research has indicated there is potential for multi-sensor approaches to overcome the limitations of the single-sensors, but so far developments are restricted to mapping approaches. This thesis addressed the need for advancing multi-sensor methods that combine time series imagery from medium resolution SAR and optical satellites to improve tropical forest monitoring. The main scientific contributions include the introduction of three novel SAR-optical approaches, two of them capable of exploiting the full observation density of time series. Furthermore, an approach for multi-model land cover dependent SAR slope correction was proposed.

Chapter 2 introduced an approach for feature level fusing of multi-temporal L-band SAR and optical forest disturbance information. Using Landsat and ALOS PALSAR imagery from 2007 and 2010, we applied the approach to map forest land cover and to detect deforestation and forest degradation of a persistently cloud covered mining region in Central Guyana. By making use of the complementarities of Landsat and ALOS PALSAR, we demonstrated the reduction of Landsat (cloud cover, Landsat 7 scan line corrector error) and PALSAR data gaps (SAR layover and shadow in mountainous area) to a negligible amount.

Chapter 3 described a practical approach for multi-model land cover dependent slope correction of SAR images that can handle a wide range of terrain and topographic conditions. We corrected ALOS PALSAR images of two topographically complex sites in Fiji (study site of Chapter 4 and 5) and Brazil and showed that the remaining slope effects for the multi-model case are marginal for all land cover types. Particularly, this improves the detection of forest degradation and biomass changes. Considering the large change in the L-band backscatter signal caused by the removal of forest, however, remaining slope effects are already sufficiently small after applying a single-model approach already.

Chapter 4 presented a novel multi-sensor time series correlation and fusion (MultiFuse) approach that was applied to fuse Landsat NDVI and ALOS PALSAR time series. The fused Landsat-PALSAR time series was used in a change detection framework to detect deforestation at a managed forest site in Fiji for the period 01/2008 - 09/2010. We tested the impact of persistent cloud cover in the tropics by increasing the per-pixel missing data percentage of the Landsat time series in a stepwise manner. The results were evaluated against three-monthly reference data that covered the entire study area. For the Landsat-only case, a very strong decrease in spatial and temporal accuracies were observed for increasing Landsat missing data. This highlights the vulnerability of tropical forest monitoring systems that rely only on optical data. In contrast, the results for the fused Landsat-PALSAR case remained high with increasing missing data and were observed to be always above the accuracies for the Landsat- and PALSAR-only cases.

To address the need for near real-time monitoring systems at medium resolution scale, Chapter 5 introduced a Bayesian change detection approach to combine SAR and optical time series for near real-time deforestation detection. We applied the approach in a simulated near real-time scenario using Landsat NDVI and ALSO PALSAR time series already used in Chapter 4. Once a new image of either of the two time series was available, the probability of deforestation was calculated immediately and deforestation events were indicated. These near real-time capabilities are essential to support timely action against illegal forest activities. Spatial and temporal accuracies for the fused Landsat-PALSAR case were consistently higher than those of the Landsat- and PALSAR-only cases, even for increasing Landsat missing data.

With these studies we demonstrated the potential of SAR-optical time series approaches to use the historical and upcoming streams of medium resolution optical and SAR satellite image time series for improving forest monitoring in the tropics.

## Samenvatting

Tropische bossen behoren tot's werelds grootste ecosystemen en spelen een cruciale rol in de mondiale koolstof-, hydrologische en biochemische cycli. De toenemende vraag naar grondstoffen vergroot de druk op de tropische bossen steeds verder. Als gevolg hiervan hebben de bossen in tropische gebieden in de afgelopen decennia snelle veranderingen ondergaan. Deze veranderingen hebben geresulteerd in de op een na grootste component van de broeikasgasemissie naar de atmosfeer. Ruimtelijk en temporeel consistente detectie van tropische ontbossing en bosdegradatie is van fundamenteel belang om een betrouwbare schatting te kunnen maken van de uitstoot van broeikasgassen, en om instrumenten voor de aanpak van klimaatverandering, zoals REDD +, succesvol te kunnen implementeren.

Om historische en toekomstige veranderingen in bosbedekking vast te kunnen stellen, is aardobservatie vanuit satellieten op een midden-resolutie een zeer geschikt middel. Uit literatuuronderzoek van de op satelliet-gebaseerde optische en Synthetische Apertuur Radar (SAR) benaderingen voor monitoring van tropische bos bleek dat er op optische technieken gebaseerde operationele benaderingen bestaan, maar dat hardnekkige bewolking de toepasbaarheid hiervan in de tropen beperkt. Ook de op SAR remote sensing gebaseerde technieken hebben blijk gegeven van toepasbaarheid, maar de observatie frequentie van SAR en de technieken voor de verwerking van tijdreeksen hebben beperkingen. Uit onderzoek blijkt verder dat er mogelijkheden zijn om meerdere sensoren te combineren en daarmee beperkingen die het gebruik van een enkele sensor met zich mee neemt te vermijden, maar deze ontwikkelingen beperken zich tot kartering. Dit proefschrift richt zich op de verdere ontwikkeling van multi-sensor methoden voor tropische bosmonitoring, die tijdreeksen van optische en radarsatellietbeelden met een midden-resolutie combineren. Tot de belangrijkste wetenschappelijke bijdragen van dit proefschrift behoren de introductie van drie nieuwe SAR-optische methoden waarvan er twee in staat zijn de volledige waarnemingsdichtheid van de tijdreeksen te benutten. Een andere bijdrage is de introductie van een verbeterde aanpak van de hellingcorrectie in SAR beelden door middel van een landbedekkingsafhankelijke twee-stappen benadering.

In hoofdstuk 2 is een benadering geïntroduceerd voor de fusie op kenmerk-niveau van multi-temporele informatie over bosverstoring, verkregen uit L-band SAR en optische data. Gebruik makend van Landsat en ALOS PALSAR beelden uit 2007 en

2010 is deze benadering toegepast in een mijnbouwgebied met hardnekkige bewolking in Centraal Guyana voor de kartering van bosland en de detectie van ontbossing en bosdegradatie. Door gebruik te maken van de complementariteit van Landsat en ALOS PALSAR is aangetoond dat ontbrekende karteringsresultaten ten gevolge van missende Landsat data (bewolking, Scan Line Corrector (SLC) -off) en PALSAR data (radar 'layover' en radarschaduw in bergachtig gebied) tot een verwaarloosbaar kleine hoeveelheid konden worden beperkt.

In hoofdstuk 3 is een praktische aanpak beschreven voor hellingcorrectie in SAR-beelden door middel van een bodembedekking afhankelijk twee-stappen model dat geschikt is voor een breed scala aan terrein- en topografische omstandigheden. Voor twee topografisch complexe sites in Fiji (studiegebied van hoofdstuk 4 en 5) en Brazilië werden ALOS PALSAR beelden gecorrigeerd en werd aangetoond dat de resterende hellingeffecten marginaal zijn voor alle soorten bodembedekking. Dit verbetert met name de mogelijkheden voor detectie van bosdegradatie en de veranderingen in biomassa. Aangezien de verandering in de L-band radarechosterkte ten gevolge van ontbossing groot is ten opzichte van de resterende fout in de hellingcorrectie na toepassing van een simpel enkelvoudig hellingcorrectiemodel, is toepassing van het twee-stappen hellingcorrectiemodel niet nodig gebleken voor ontbossingsdetectie.

In hoofdstuk 4 is een nieuw ontwikkelde methode voor correlatie en fusie van tijdreeksen (MuTiFuse) besproken die werd toegepast op Landsat NDVI en ALOS PALSAR tijdreeksen. De gefuseerde Landsat-PALSAR tijdreeks werd gebruikt voor de detectie van verandering veroorzaakt door ontbossing in beheerd plantagebos op Fiji voor de periode 01/2008 - 09/2010. Het effect van aanhoudende bewolking in de tropen werd gesimuleerd door het percentage missende pixels in Landsat tijdreeksen stapsgewijs te vergroten. De resultaten werden geëvalueerd door vergelijking met driemaandelijke referentiegegevens die het hele studiegebied bestreken. Als alleen Landsat data werden gebruikt, werd een zeer sterke afname waargenomen bij toenemende percentages missende data. Dit wijst op de kwetsbaarheid van tropisch bosmonitoringsystemen die alleen optische data gebruiken. Dit staat in sterk contrast met de resultaten voor de gefuseerde Landsat-PALSAR tijdreeks die goed bleven met toenemende ontbrekende gegevens en die altijd boven de nauwkeurigheid van zowel de Landsat-tijdreeks als de PALSAR-tijdreeks bleven.

Vanwege de behoefte aan monitoringsystemen op midden-resolutie voor snelle en actuele (near real-time) ontbossingsinformatie is in hoofdstuk 5 een Bayesiaanse methode voor veranderingsdetectie geïntroduceerd die SAR en optische tijdreeksen combineert. De methode is toegepast voor een gesimuleerd scenario voor snelle en actuele detectie gebruik makend van dezelfde Landsat-NDVI en ALOS-PALSAR tijdreeksen als eerder gebruikt in hoofdstuk 4. Zodra een nieuw beeld van een van de twee tijdreeksen beschikbaar kwam werd de waarschijnlijkheid van ontbossing

onmiddellijk berekend en nieuwe gevallen van ontbossing aangegeven. Deze mogelijkheden voor snelle en actuele detectie van ontbossing zijn van essentieel belang ter ondersteuning aan tijdige actie tegen illegale boskap. De ruimtelijke en temporele nauwkeurigheden in het geval van de gefuseerde Landsat-PALSAR tijdreeksen waren consequent hoger dan die van Landsat- en PALSAR-tijdreeksen apart, zelfs in het geval van toenemende percentages missende data in de Landsat data.

De onderzoeksresultaten hebben de mogelijkheden voor het gebruik van SAR-optische benaderingen aangetoond, zowel voor de historische als voor de toekomstig te verwachten grote stroom van midden-resolutie optische en SAR van satellietbeeldtjdsseries voor verbetering van bosmonitoring in de tropen.

## Acknowledgments

Completing a PhD is truly a marathon event full of personal and scientific challenges. But alongside the challenges, there is the joy of the journey itself and the many interesting and inspiring people encountered along the way. Their support and friendship have helped me endure the tough parts and without them, I surely would not have passed the finish line. Most importantly, many of these people will stay a part of my life far beyond the end of my unforgettable PhD marathon experience.

First and foremost, I would like to express my sincere thanks to my promoter, Martin Herold, who provided me the opportunity to undertake this PhD research at Wageningen University. Martin, I am very grateful for the guidance, freedom and trust you gave me to find my own path during the last four years. I am really looking forward to continuing working together with you here in Wageningen.

This thesis would not have been possible without the support and guidance of my daily supervisors, Dirk Hoekman and Jan Verbesselt. It has been an honour to have had you both as supervisors for this PhD research. Your patience, scientific experience and preciseness played a key role in the completion of this thesis and has truly shaped me for my future scientific life. Dirk, I will never forget the private radar lectures I received during our joint fieldtrip to Guyana. Jan, thanks for introducing me to the scientific wonders of time series analysis, and for showing how to smartly sail against strong winds.

I am indebted to many of all my colleagues at the Laboratory of Geo-information Science and Remote Sensing who provided me not only scientific support and the needed food for thought, but also with the necessary distraction and more importantly friendship and companionship throughout my PhD marathon. When talking about companionship, I am in particular thankful to the PhDs of the *“first generation”* - Arun, Ben, Richard, Michi, Niki, Roberto, Loïc and Kim. By quoting Earl Wilson who said that “science may never come up with a better office communication system than the coffee break”, I would also like to thank Laure, Sarah, Mathieu, Valerio, Jose, Erika, Johannes, Giulia, Nandika, Manos, Benjamin, Marcio, Peter, Eliakim, Eskender, Yang, Kalkidan, Simon, Rosa Maria, Astrid, Alvaro, Konstantin, Jessica, Brice, Arnold, Sytze, Lammert, Willy, Harm, Ron, Arend, Juha, Jan, Wim and John. Special thanks go to Truus and Antoinette for providing endless administrative support and for never being annoyed when I appeared with another

urgent request. I also thank my M.Sc. students, Johannes, Jonas, Robert, Thijs, Vincent and Anika for their great work in Wageningen and during their internships in Fiji. All the members of the PE&RC PhD council are thanked for two great council years during which I enjoyed many discussions about the PhD program. Martin Vissers and all staff from SAR Vision are thanked for assisting in data pre-processing and for fruitful scientific exchange. Finally, I would like to thank Tina, Ben, Alice and Sarah for many hours of proofreading.

Fiji and its kind people played a special role in my PhD. I am grateful to everybody from Fiji Forestry Department, GIZ Fiji, SOPAC, Fiji Pine Limited, Fiji Hardwood, Fiji Lands Department, University of South Pacific for contributing to this PhD in manifold ways. Special thanks go to Samuela Legataki, Christine Fung, Karl-Peter Kirsch-Jung, Bjoern Hecht, Wolf Forstreuter, Akosita, Vili, Jale for endless support, unbeatable hospitality, data sharing, and after work Fiji Bitters during my several stays in Fiji. Tarei, Roderic and the fantastic staff of the Five Princess Hotel are thanked for always providing a home away from home.

Carlos Souza and João, Marcio and the rest of the Imazon staff are thanked for scientific exchange, technical assistance and their hospitality during my work stay in Brazil. I am grateful to Pradeepa Bholanath, Jagdesh Singh and Haimwant Persaud from Guyana Forestry Commission for their support during our joint field trip in Central Guyana. I am also very thankful to Tuomas Häme, Ben de Jong, Joerg, Fabian, Pawan, Donata, Tuomo and Jarno for three very fruitful and enjoyable years during the EU ReCover project.

My PhD journey, however, began before my time in Wageningen. I am very grateful to Christiane Schmuilius for sharing her passion for radar remote sensing and for her never-ending support during my Master and undergraduate education at Jena University that provided the foundation to start this PhD. Maurizio Santoro and Christian Thiel are thanked for teaching me radar remote sensing, scientific advice and for their friendship.

All my friends are thanked for their manifold support and many joyful moments throughout the past four years. Volker and Kai, thank you for motivating me to move to the Netherlands and for your unbelievable support during the first months. Robs, Gregor, Jule, Franzi, Normi, Isa, Keule, Maria, Claudi, Mart, Reik and Nicolas, thanks for many good parties, great reunions and most important your friendship. Robs, Gregor and Normi, thanks for sharing the special beauty of lactate legs during our annual bike tour – can't wait for the next one to come. Thanks to Andre and Cata for being the best host that one can imagine when traveling into the Amazon. I feel very lucky that I met many new friends in Wageningen, Utrecht and Amsterdam that have made me feel at home in the Netherlands. Thanks to Davi, Carlos, and Amandine for populating the Niemeijerstraat with me. Gareth and Alice, what a great pleasure it has been over the past years ... all starting in the bars of Wageningen. Tina, Marvin,

Margriet, Fiona, Gordon, Richard, Daan, Wouter, Ing, Matheus, Sarah, Rob, and Gemma, thank you for the well spent hours at lunch, coffee and bar time and at the slopes of Winterberg. My running mates, Roel, Art, Chris, Robert, Maud and Nathalie are thanks for many hours running in and around Utrecht and of course during a real Marathon.

When speaking of relaxation and recharging my battery, I am very grateful to the members of the travel group "*Mittleres Nesselal*". Lisbeth, Olli and Thomas, thank you for unforgettable trips we enjoyed together in Germany, India, Portugal, Morocco, Turkey and Greece, but also for sharing many happy and difficult moments. Us enjoying the sunset on the mountain temple in Pushkar is etched on my mind, and so are many other moments with you. I am so grateful for this unique friendship that connects four such diverse personalities and lives.

My dear parents, Dietrich and Angelika Reiche, receive my deepest gratitude and love for the many years of endless support and encouragement that provided the foundation for this work. I am very grateful to my brother Matthias for the far too few, but very homelike moments we shared together over the past years. Matthias, thank you for inspiring me more often than you imagine and more importantly for being an amazing brother. Thanks to Susi, and my nieces Hanna and Martha, spending time with you always makes me realise what the real beauty of life is. Opa Erich and the rest of my greater family is thanked for their inspiration.

Although my PhD marathon ends with the defence, a more important journey that started more than three years continues: my life journey with Vief. And with meeting Vief, I got to know a new family and many, many great friends. Marja, Peter and Maarten, thank you for the warm welcome to the Segers. Vief, thank you so much for sharing the same life attitude and fascination for sports, for mastering the *Sci Club 18*, dining out at the *Whale's Tale* and for the many other great moments we shared travelling the world. You must know that this PhD would have not been possible without you on my side. I would like to express something that I cannot put in words – my love for you.

Thank you all!

Johannes  
Utrecht, 28. April 2015

## List of publications

### Peer reviewed journals

- Reiche, J.**, de Bruin, S., Hoekman, D. H., Verbesselt, J. & Herold, M. (2015): A Bayesian Approach to Combine Landsat and ALOS PALSAR Time Series for Near Real-Time Deforestation Detection. *Remote Sensing*, 7, 4973-4996. DOI:10.3390/rs70504973.
- Reiche, J.**, Verbesselt, J., Hoekman, D. H. & Herold, M. (2015): Fusing Landsat and SAR time series to detect deforestation in the tropics. *Remote Sensing of Environment*. 156, 276-293. DOI: 10.1016/j.rse.2014.10.001.
- Hoekman, D. H. & **Reiche, J.** (2015): Multi-model radiometric slope correction of SAR Images of complex terrain using a two-stage semi-empirical approach. *Remote Sensing of Environment*, 156, 1-10. DOI: 10.1016/j.rse.2014.08.037.
- Reiche, J.**, Souza, C., Hoekman, D. H., Verbesselt, J., Haimwant, P. & Herold, M. (2013): Feature level fusion of multi-temporal ALOS PALSAR and Landsat data for mapping and monitoring of tropical deforestation and forest degradation. *IEEE Journal of Selected Topics in Applied Earth Observations and Remote Sensing*, 6, 5, 2159–2173. DOI: 10.1109/JSTARS.2013.2245101.
- Ling, F., Li Z. Y., Chen, E. X., Huang, Y. P., Tian, X., Schmullius, C., Leiterer, R., **Reiche, J.** & Santoro, M. (2012): Regional forest and non-forest mapping using Envisat ASAR data. *Journal of Remote Sensing*, 16, 5, 1101–1114.
- Reiche, M., Funk, R. Zhang, Z., Hoffmann, C., **Reiche, J.**, Wehrhan, M., Li, Y. & Sommer, M. (2012): Application of satellite remote sensing for mapping wind erosion risk and dust emission-deposition in Inner Mongolia grassland, China. *Grassland Science*, 58, 8-19. DOI: 10.1111/j.1744-697X.2011.00235.x.
- Thiel, Ca., Ch. Thiel, **J. Reiche**, R. Leiterer & Schmullius, C. (2009): Großflächige Waldüberwachung in Sibirien unter Verwendung von ALOS PALSAR Winter Kohärenzen und Sommer Intensitäten. *Photogrammetrie, Fernerkundung, Geoinformation*, 18, 377-386.
- Leiterer, R., **J. Reiche**, Thiel, C., Schmullius, C. & Dodo, A.K. (2008): Application of Multi-Temporal MERIS-FR and ASAR-WS data for large scale vegetation monitoring in the west African Sahel zone. *Geo Observateur*, 17, 37-46.
- Reiche, J.**, Hese, S., Schmullius, C. (2007): Objektorientierte Klassifikation terrestrischer Ölverschmutzungen mittels hoch aufgelöster Satellitendaten in West-Sibirien. *Photogrammetrie, Fernerkundung, Geoinformation*, 4/2007, 275-287. DOI: 1432-8364/07/2007/0275.

## Other scientific publications

- Birkholz, R., **Reiche, J.** & Forstreuter, W. (2015): Forest Stratification of REDD+ Sites in Fiji using Very High Resolution Satellite Imagery in support of REDD+. *SPC/GIZ Regional Project 'Climate Protection through Forest Conservation in Pacific Island Countries'*, Suva, Fiji, 33p.
- Duijvenbode, J., **Reiche, J.** & Forstreuter, W. (2014): Forest Stratification in Fiji using High Resolution Satellite Imagery. *SPC/GIZ Regional Project 'Climate Protection through Forest Conservation in Pacific Island Countries'*, Suva, Fiji, 46p.
- Eberenz, J. & **Reiche, J.** (2014): Republic of Fiji: Reference Database and Validation Concept for Remote Sensing based Forest Cover Change. *SPC/GIZ Regional Project 'Climate Protection through Forest Conservation in Pacific Island Countries'*, Suva, Fiji, 36p.
- Häme, T., Sirro, L., Cabrera, E., Enssle, F., Haarpaintner, J., Hämäläinen, J., de Jong, B., Paz Pellat, F., Pedrazzani, D. & **Reiche, J.** (2013): RECOVER: A concept for tropical forest assessment for REDD. *ESA Living Planet Symposium 2013*, Edinburgh, United Kingdom, 8p.
- Reiche, J.** & Herold, M. (2012): Concepts and processing techniques for a global Sentinel 1-3 Land Cover Dynamics and Change (LCDC) product. ESA SP-707. *Sentinel 2 Preparatory Symposium*, Frascati, Italy, 8p.
- Ling, F., Leiterer, R., Huang, Y., **Reiche, J.** & Li, Z. (2011): Forest Change Mapping in Northeast China using SAR and INSAR Data. *34th International Symposium on Remote Sensing of Environment 2011 (ISRSE34)*, Sydney, Australia, 3p.
- Reiche, J.** (2011) Parameterisation of growing stock volume of dense forest in support of the BIOMASAR algorithm, utilising satellite-based height-volume allometry. *MSc thesis*, Jena, Germany: Department for Earth Observation, Friedrich-Schiller University Jena, 117p.
- Reiche, J.**, Leiterer, R., Cartus, O., Santoro, M., Schmullius, C. & Li, Z.Y (2010): FOREST DRAGON 2: Large-Area Forest Growing Stock Volume Mapping in China, using Spaceborne Radar. ESA SP-686. *ESA Living Planet Symposium 2010*, Bergen, Norway, 7p.
- Leiterer, R., **Reiche, J.**, Cartus, O., Santoro, M., Thiel, Ch., Herold, M. & Schmullius, C. (2010): A Multiscale Approach for Semi-Automatic Comparison Assessment of Large Scale Forest Maps. ESA SP-686. *ESA Living Planet Symposium 2010*, Bergen, Norway, 7p.
- Santoro, M., Schmullius, C., Beer, C., Cartus, O., Eriksson, L., Leiterer, R., **Reiche, J.**, Thiel, Ca. & Thiel, Ch. (2010): Forest Mapping of the Northern Hemisphere with Spaceborne Radar. ESA SP-686. *ESA Living Planet Symposium 2010*, Bergen, Norway, 7p.
- Schmullius, C., **Reiche, J.**, Leiterer, R., Cartus, O., Santoro, M., Wegmüller, U., Li, Z.Y., Tian, X. & Ling, F. L. (2010): FOREST DRAGON 2: Mid-Term Results of the European Partners. ESA SP-684. *DRAGON 2 Mid-Term Results Symposium 2010*, Guilin, China, 10p
- Cartus, O., **Reiche, J.**, Leiterer, R., Santoro, M. Schmullius, C. & Zengyuan, Li (2009): Generation and cross-comparison of large-area forest stem volume maps for Northeast and Southeast China, using ERS-1/2 tandem coherence. *6th International Symposium on Digital Earth*, Beijing, China, 8p.

- Reiche, J.**, Leiterer, R., Cartus, O., Santoro, M. & Schmullius, C. (2009): FOREST DRAGON 2: Cross-validation and quality assessment of large-area forest stem volume maps for Northeast and Southeast China. *2009 Dragon 2 Symposium*, Barcelona, Spain, 5p.
- Reiche, J.**, Hese, S. & Schmullius, C. (2009): An Object-Oriented Classification Method for the Quantification of Terrestrial Oil Spill Contamination in West Siberia using High-Resolution Satellite Data. *33th International Symposium on Remote Sensing of Environment 2009 (ISRSE33)*, Stresa, Italy, 4p.
- Leiterer, R., **Reiche, J.**, Thiel, C. & Schmullius, C. (2009): Intra-annual Vegetation Dynamic as potential Indicator for Environmental Change in the West African Sahel Zone. *33th International Symposium on Remote Sensing of Environment 2009 (ISRSE33)*, Stresa, Italy, 4p.
- Thiel, Ch., Thiel, Ca., **Reiche, J.**, Leiterer, R., Santoro, M. & Schmullius, C. (2008): ALOS Palsar Winter Coherence and Summer Intensities for Large Scale Forest Monitoring in Siberia. *The Second Joint PI symposium on ALOS Data Nodes for ALOS Science Program*, Rhodes, Greece, 4p.
- Leiterer, R., **Reiche, J.**, Thiel, C., Schmullius, C. & Dodo, A.K. (2008): Analysis of ASAR and MERIS Data for large scale Water and Vegetation Monitoring in the lullemeden Aquifer, West African Sahel Zone. *3rd International Conference on Managing Shared aquifer Resources in Africa*, Tripoli, Libya, 6p
- Thiel, Ch., **Reiche, J.**, Leiterer, R. & Schmullius, C. (2007): Synergistic usage of ASAR WS and MERIS data for large scale water and vegetation monitoring in Africa. – a science product of the AQUIFER project. *Envisat Symposium 2007*, Montreux, Switzerland, 6p.
- Thiel, Ch., Thiel, Ca., **Reiche, J.**, Leiterer, R. & C. Schmullius (2007): Analysis of ASAR and PALSAR data for optimising Forest Cover Mapping - A GSE Forest Monitoring Study. *ForestSat 2007*, Montpellier, France, 5p.
- Thiel, Ch., Thiel, Ca., **Reiche, J.**, Leiterer, R. & Schmullius, C. (2007): Service Portfolio Evolution – The Instrument for keeping the Service of GSE Forest Monitoring up to date. *ForestSat 2007*, Montpellier, France, 5p.
- Thiel, Ch., Thiel, Ca., **Reiche, J.**, Leiterer, R., Santoro, M. & Schmullius, C. (2007): Polarimetric PALSAR SAR data for forest cover mapping in Siberia. *The First Joint PI symposium of ALOS Data Nodes for ALOS Science Program*, Kyoto, Japan, 4p.

## Book chapter

- Häme, T., Sirro, L., Cabrera, E., Haarpaintner, J., Heinzl, J., Hämäläinen, J., de Jong, B., Paz Pellat, F., Pedrazzani, D. Sirro, L., Cabrera, E., Haarpaintner, J., Heinzl, J., Hämäläinen, J., de Jong, B., Paz Pellat, F., Pedrazzani, D. & **Reiche, J.** (2012): ReCover: Services for the Monitoring of Tropical Forest to Support REDD+. In: Let's embrace space, European Commission, 8p. DOI: 10.2769/31208.

## Short biography

Johannes Reiche was born in Gotha, Germany, on October 27, 1983 and spent his childhood in the village of Brüheim. He attended primary school at *Grundschule Sonneborn*, and later completed secondary school in 2002 at *Arnoldi Staatliches Gymnasium* in Gotha with a major in mathematics and informatics. His spare time was dedicated to sports and outdoor activities, which remains the source of energy and creativity he uses to balance his work life.

Johannes commenced a Bachelor of Science degree in Geography in 2003 at the Friedrich-Schiller University Jena. Over the course of his studies he developed a strong interest in remote sensing. Upon completing his degree in 2006, he stayed in Jena where he worked at the Department of Earth Observation as a research assistant for several ESA funded projects. During this period his passion for radar remote sensing arose. In 2008, he started his Masters of Science in Geoinformatics, while continuing his work as a research assistant focusing on SAR-based forest monitoring. Over the course of his Masters, he attended several workshops and summer schools, including hyperspectral remote sensing, POLinSAR, SAR processing and interferometric point target analysis. In 2011, he completed his Masters with a thesis on the parameterisation of growing stock volume of dense forest in support of the BIOMASAR algorithm, using height-volume allometry.

After his graduation, Johannes moved to the Netherlands to start his PhD at Wageningen University where he focused his research on combining SAR and optical satellite image time series for tropical forest monitoring. Alongside his PhD, Johannes gained project management experience, initiated and led a MSc student exchange program with Fiji, and became engaged in the Global Forest Observation Initiative.

Johannes' current research interest are SAR and InSAR techniques for land applications, and the integration of optical and SAR time series for ecosystem monitoring. He will continue his work as postdoctoral researcher at Wageningen University.

## PE&RC Training and Education Statement

With the training and education activities listed below the PhD candidate has complied with the educational requirements set by the C.T. de Wit Graduate School for Production Ecology and Resource Conservation (PE&RC) which comprises of a minimum total of 32 ETCS (= 22 weeks of activities)



### **Review of literature (6 ECTS)**

- Radar and Optical remote sensing time-series to support REDD (2011)

### **Post-graduate courses (5.9 ECTS)**

- Sampling in space and time; WUR (2012)
- REDD Governance workshop; WUR (2012)
- Analysing spatial data; Bergen, Norway (2012)

### **Laboratory training and working visits (4.5 ECTS)**

- Mapping deforestation and degradation with Landsat time series; IMAZON, Belem, Brazil (2011)
- Monitoring deforestation over pine plantations with Landsat time series data; SOPAC, Suva, Fiji (2013)
- Mapping forest densities, using very high resolution satellite data; SOPAC, Suva, Fiji (2014)

### **Invited review of (unpublished) journal manuscript (2 ECTS)**

- JSTARS: radar-based biomass mapping (2014)
- Remote Sensing of Environment: radar based mapping for peat land (2014)

### **Deficiency, Refresh, Brush-up courses (2.5 ECTS)**

- Forest ecology MSc course (2012)
- Fundamentals of electrical engineering I, Coursera (2014)

### **Competence Strengthening / Skills courses (2.1 ECTS)**

- Improve your writing; WUR (2012)

- Entrepreneurship in and outside science; WUR (2014)
- Last stretch of the PhD program; WUR (2014)

**PE&RC annual meetings, seminars and the PE&RC weekends (1.5 ECTS)**

- PE&RC PhD Weekend (2011)
- PE&RC Days (2013, 2014)

**Discussion groups / local seminars / other scientific meetings (7.5 ECTS)**

- Remote sensing thematic group meeting (2011 - 2015)
- REDD discussion group (2011 - 2015)
- Discussion group REDD actions in Fiji, with GIZ, SOPAC and Fiji Forestry (2012 - 2014)
- R User meeting; WUR (2013 - 2014)
- GFOI Expert meeting sensor interoperability; Boston (2014)
- GFOI Expert meeting forest degradation; WUR (2014)

**International symposia, workshops and conferences (9 ECTS)**

- 1<sup>st</sup> EARSEL SIG Forestry workshop: operational remote sensing in forest management (2011)
- IGARSS; Munich, Germany (2012)
- IGARSS; Melbourne, Australia (2013)
- ESA Living planet symposium; Edinburgh, United Kingdom (2013)
- RS/GIS User conference of the South Pacific; Suva, Fiji (2013)
- ForestSAT conference; Riva del Garda, Italy (2014)
- RS/GIS User conference of the South Pacific; Suva, Fiji (2014)

**Supervision of 3 MSc students**

- Anika Paschalidou: optical TS analysis for LC change in Fiji (2013)
- Jonas van Duijvenbode: OBIA based forest stratification in Fiji (2014)
- Johannes Eberenz: near-real time fusion optical and SAR time series (2014)